HOLLOW FIBER SORBENTS FOR POST-COMBUSTION CO_2 CAPTURE

A Dissertation
Presented to
The Academic Faculty

By

Ryan P. Lively

In Partial Fulfillment
Of the Requirements for the Degree
Doctor of Philosphy in the School of
Chemical & Biomolecular Engineering

Georgia Institute of Technology

May 2011

HOLLOW FIBER SORBENTS FOR POST-COMBUSTION CO_2 CAPTURE

Approved By:

Dr. William J. Koros
School of Chemical &
Biomolecular Engineering
Georgia Institute of Technology

Dr. Ronald Rousseau
School of Chemical &
Biomolecular Engineering
Georgia Institute of Technology

Dr. John Muzzy
School of Chemical &
Biomolecular Engineering
Georgia Institute of Technology

Dr. Chris Jones
School of Chemical &
Biomolecular Engineering
Georgia Institute of Technology

Dr. Ronald Chance
Department of Chemistry &
Biochemistry
Georgia Institute of Technology

Date Approved: December 21st, 2010

We are at the very beginning of time for the human race. It is not unreasonable that we grapple with problems. But there are tens of thousands of years in the future. Our responsibility is to do what we can, learn what we can, improve the solutions, and pass them on.

—Richard Feynman, 1988

DEDICATION

To my supporting and loving parents, Tanya Murphy and Mike Bengtson

ACKNOWLEDGEMENTS

There are many people I have to thank for supporting me throughout the ordeal that is graduate school. While I always had an inkling that I would go to graduate school, I have to thank my mom for nudging me in that direction. Of course, once in graduate school, I turned to her quite often to sort out the maze that is academia. My dad also helped guide me through, with equal helpings of technical advice, interpersonal advice, and football talk. Thanks to my sisters Claire and Chloe for constantly making fun of me, reminding me not to take myself too seriously. My grandparents, Belle & Paul Murphy deserve a lot of credit for not only keeping me fed, but also to remind me that a simple experiment can be much more powerful than pages of calculations.

Dr. Koros was really my inspiration for pushing myself as hard as I did. Despite my best efforts, no other Georgia Tech-level graduate school would give me a chance to join their departments. Dr. Koros gave me a chance to work in his lab—I knew he was taking a risk by doing this, so I consistently worked as hard as I could to justify his decision. Without him, I would most certainly not have the opportunities that I do today. His style of academic guidance, sense of friendship, and belief in principles are things that I will always carry with me.

Of course, graduate school is not graduate school without many heated scientific discussions. It was always my pleasure to participate in these with J.R. Johnson, Ryan Adams, Jason Ward, Jeff Drese, Rich Moore, Eric Ping, Josh Thompson, Imona Omole and Dhaval Bhandari. Thanks to these guys for the good times, both scientific and non-scientific (though, the line between these two blurred on occasion). My other friends always kept me level and down-to-earth, if not slightly distracted, and I thank them: Tyler, Matt, Keith, David, Hal, Gina the "One mg Wonder," Greg, Nathan, Darby, and Josephine.

Finally, I would like to thank my committee, Ron Chance, Chris Jones, John Muzzy, and Ron Rousseau for their technical assistance and guidance. Thanks to Ron Chance, especially, for giving me chances and for reminding me that I am bad at golf. Also thanks to Chris Jones for technical discussions as well as the reminder that I need to work like I have something to prove. I would also like to thank my collaborators at ExxonMobil for their generous funding of this project, as well as the continuous feedback on the project. To have such a close working experience with industrial researchers was an experience I am truly thankful for. Thanks to Harry Deckman, Rusty Kelley, Dan Leta, Hans Thomann, and Bruce DeRites.

Table of Contents

List of Tables

List of Figures

Summary

As concerns mount about the rise in atmospheric CO_2 concentrations, many different routes to reduce CO_2 emissions have been proposed. Of these, post-combustion CO_2 capture from coal-fired power stations is often the most controversial, as the CO_2 capture system will *remove* generating capacity from the grid whereas many of the other solutions involve increasing the generating capacity of the grid with low CO_2-emission plants. Despite this, coal-fired power stations represent a major point source for CO_2 emissions, and if a consensus is reached on the need to reduce CO_2 emissions, a low-cost method for capturing and storing the CO_2 released by these power plants needs to be developed. The overarching goal of this research is to design and develop a novel hollow fiber sorbent system for post-combustion CO_2 capture.

To achieve this goal, three objectives were developed to guide this research: *i*) develop a conceptual framework for hollow fiber sorbents that focuses on the energetic requirements of the system, *ii)* demonstrate that hollow fiber sorbents can be created, and a defect-free lumen layer can be made, *iii*) perform proof-of-concept CO_2 sorption experiments to confirm the validity of this approach to CO_2 capture. Each of these objectives is addressed in the body of this dissertation.

Work on the first objective showed that fiber sorbents can combine the energetic advantages of a physi-/chemi-sorption process utilizing a solid sorbent while mitigating the process deficiencies associated with using solid sorbents in a typical packed bed. All

CO_2 capture technologies—including fiber sorbents—were shown to be highly parasitic to a host power plant in the absence of effective heat integration. Fiber sorbents have the unique advantage that heat integration is enabled most effectively by the hollow fiber morphology: the CO_2-sorbing fibers can behave as "adsorbing heat exchangers."

A dry-jet, wet-quench based hollow fiber spinning process was utilized to spin fibers that were 75wt% solid sorbent (zeolite 13X) and 25wt% support polymer (cellulose acetate). The spinning process was consistent and repeatable, allowing for production of large quantities of fibers. The fibers were successfully post-treated with an emulsion-based polymer (polyvinylidene chloride) to create a *defect-free* lumen side coating that was an excellent barrier to both water and gas permeation. A film study was conducted to elucidate the dominant factors in the formation of a defect-free film, and these factors were used for the creation of defect-free lumen layers. The work discussed in this thesis shows that the second objective of this work was definitively achieved.

For the third objective, sorption experiments conducted on the fiber sorbents indicated that the fiber sorbents CO_2 uptake is simply a weighted average of the support material CO_2 uptake and the solid sorbent uptake. Furthermore, kinetic experiments indicate that CO_2 access to the sorbents is not occluded noticeably by the polymer matrix. Using the fiber sorbents in a simulated rapid thermal swing adsorption cycle provided evidence for the fiber sorbents ability to capture the sorption enthalpy released by the CO_2-13X interaction. Finally, a slightly more-pure CO_2 product was able to be generated from the fiber sorbents via a thermal swing/inert purge process.

Chapter 1

Introduction to CO_2 Capture

1.1 Presentation of Climate Change Problem

Since the Industrial Revolution began in the late 19th century, mankind's use of fossil fuel has ballooned along with its population at an exponential rate. For over two hundred years, beginning with the wide-spread use of coal and then oil after the invention and adoption of the internal combustion engine, fossil fuels have been the dominant form of energy supply. Technological advances provided better standards of living, longer life expectancy, and a better understanding of the physical world. The 1973 Oil Crisis shook the world and began a period of searching for a good replacement for oil. As coal again became the preferred source for power production, and high oil prices receded, the United States again increased fossil fuel consumption and abandoned its quest for an alternative fuel. Unfortunately, the current rate of growth and consumption that has led to today's way of living is likely not sustainable—from a climate perspective and an energy supply perspective. Efficient CO_2 capture technology described in this thesis can mitigate this problem.

1.1.1 United States Energy Portfolio

Currently, the energy portfolio for the United States heavily favors the three major fossil fuels: oil, natural gas, and coal. Oil has a 37.1% share of total energy supply, while natural gas and coal have 23.8% and 22.4%, respectively[1] . On the demand side, electric power is responsible for the most energy consumed, with 40.0% of the United States total energy being dedicated to electric power. Supplying that 40.0% total energy use is mainly coal, in the form of coal-fired power stations[1].

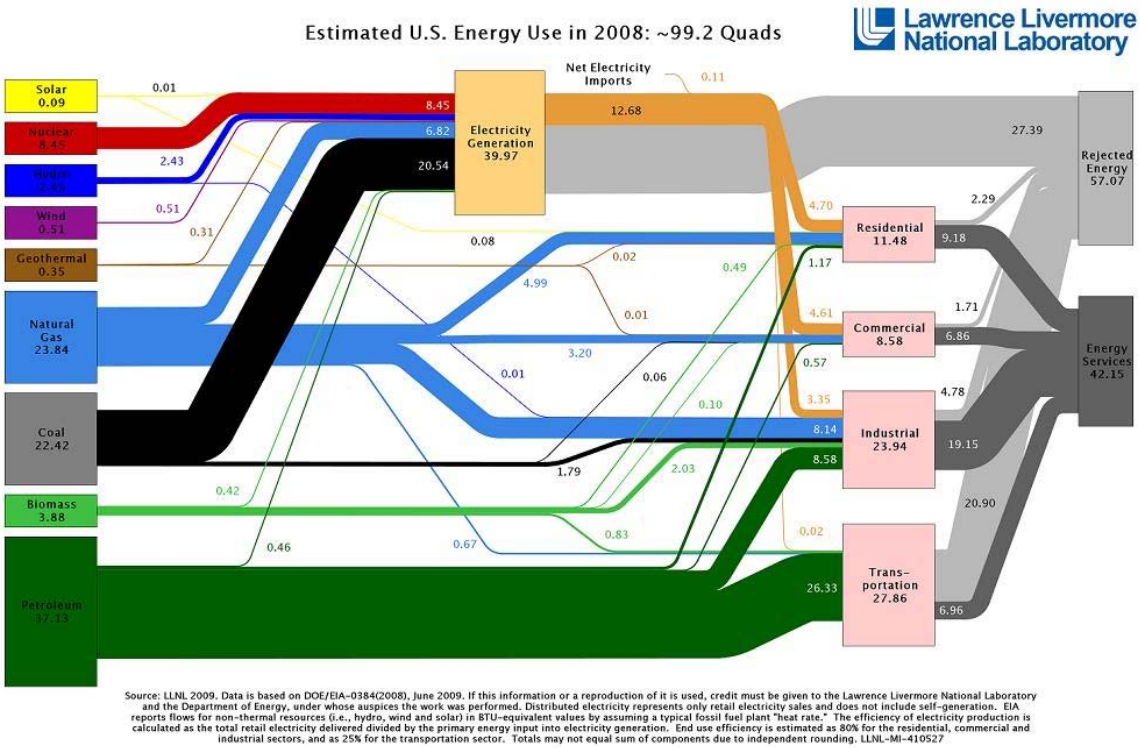

Figure 1.1: Sankey diagram for the energy supply and consumption within the United States for 2008. The left side of the figure tabulates the energy supply from various sources, while the right side of the figure illustrates the demand for energy. The area of the boxes and arrows scale with the amount of energy being transferred from source to sink. As can be seen in the middle of the figure, electricity generation accounted for 40% of total energy consumption in 2008. Source: Lawrence Livermore National Laboratory.

From these numbers, which are displayed in Figure 1.1, it is clear that electric power production from coal is the biggest point source of energy consumption; this can be logically extended to the fact that electricity generated from coal is the biggest point source of CO_2 emissions[2].

Furthermore, the energy portfolio is expected to favor the three major fossil fuels for the foreseeable future, as can be seen in Figure 1.2. While fossil fuel production is not limitless—projections for oil reserves range from 50-100 years[3]—some of the fossil fuels have long life expectancies. Known coal reserves are expected to last anywhere between 200 and 700 years[4]. While the United States long ago lost oil independence, the U.S. does possess the largest known coal reserves[4]. These enormous reserves imply that coal will be a significant part of the energy portfolio for a long time.

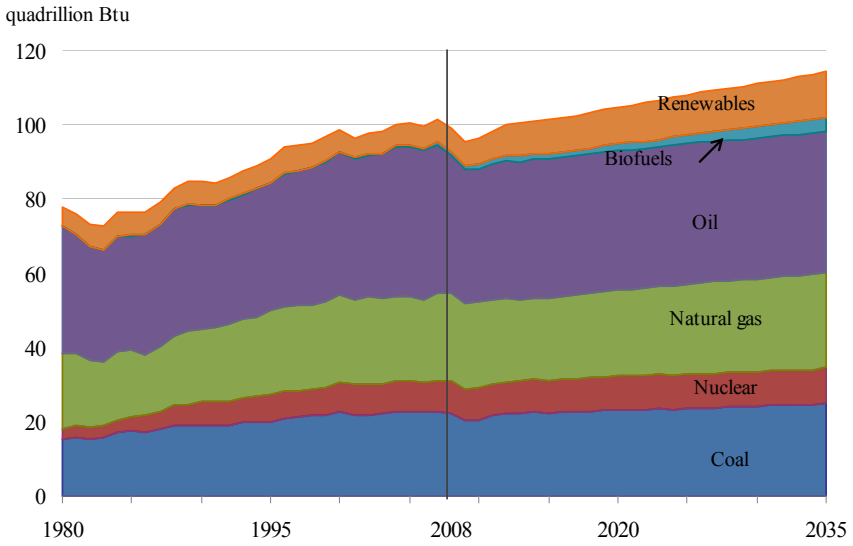

Figure 1.2: United States energy portfolio, in quadrillion BTU's from 1980 projected to 2035 (projection starts from 2010). Source: Energy Information Administration, Annual Energy Outlook 2010.

1.1.2 Evidence of Climate Change & Mitigation Strategies

A direct by-product of the heavy dependence on fossil fuels is the rise in global CO_2 emissions, as well as the global CO_2 concentration in the atmosphere. CO_2 emissions are expected to rise correspondingly with the expected increased dependence on fossil fuels, a developing trend which can be seen in Figure 1.3.

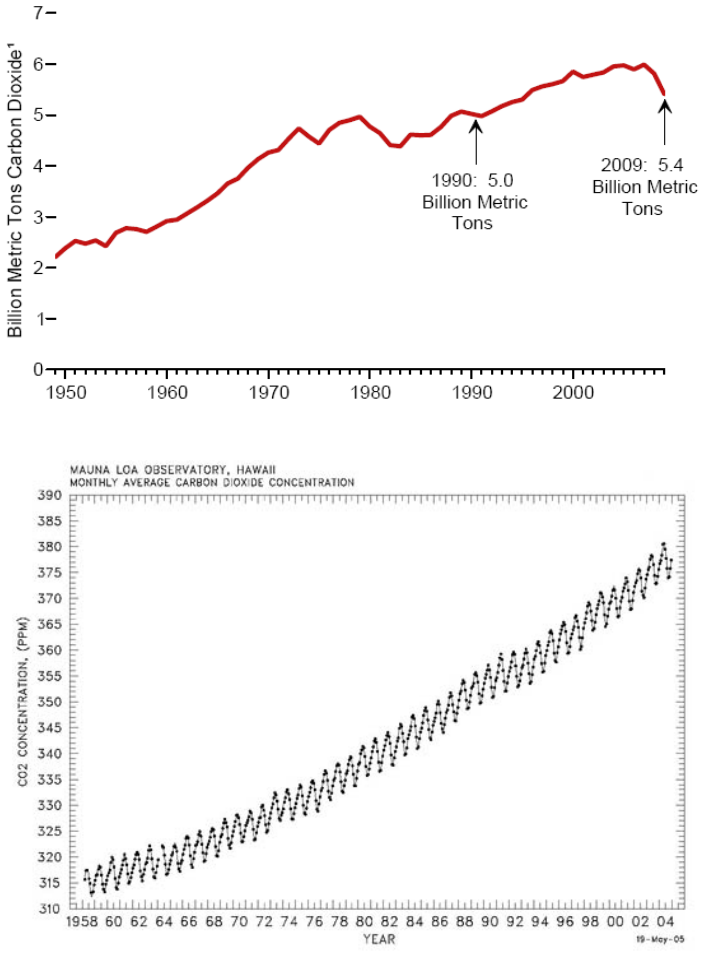

Figure 1.3: *(top)* CO_2 emissions for all U.S. sectors from 1950 to present day in billion metric tons of CO_2. Source: Energy Information Administration, Department of Energy, Annual Energy Review (2009). *(bottom)* Atmospheric concentrations of CO_2 from 1958 to 2005, showing a continuous rise from 315 ppm to 380 ppm. Source: National Ocean & Atmospheric Administration, Earth System Research Laboratory

In comparison to pre-Industrial Revolution CO_2 levels, the global CO_2 atmospheric concentration has been increasing steadily since the Industrial Revolution. Though there is much debate as to what the effects of this increased atmospheric CO_2 concentration will have on the Earth's climate[5,6], it is clear that the burning of fossil fuels essentially serves as a short-circuit to the Earth's natural climate cycle. The increase in the number of vehicles on the road as well as the explosive population growth requiring power in developing countries can be pointed at as two main culprits in the growth in annual CO_2 emissions[1,7].

If there is a consensus on the need to reduce or level global CO_2 emissions, a worldwide effort is required. Pacala and Socolow[8] famously framed the challenge in terms of seven CO_2 emission "wedges," where each wedge represents 50 gigatons of CO_2 avoided over 25 years, as illustrated in Figure 1.4.

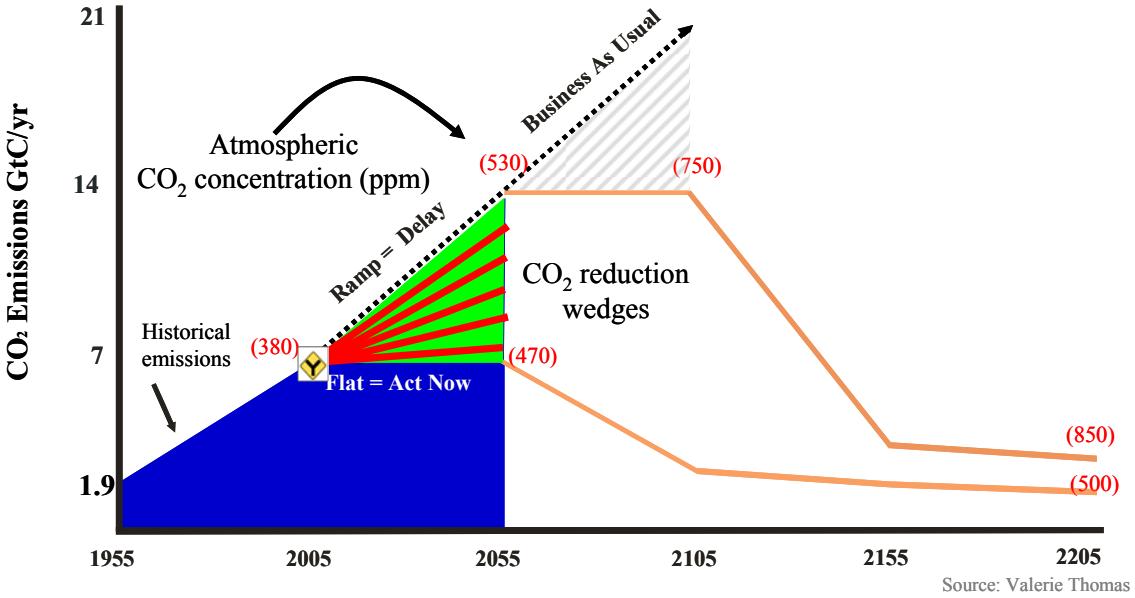

(Values) in parentheses are atmospheric ppm levels of CO_2

Figure 1.4: CO_2 emissions from 1955 projected to 2205, illustrating the concept of CO_2-emission-reducing wedges. The numbers in red indicate the CO_2 atmospheric concentration depending on what action (or inaction) is taken to reduce CO_2 emissions. The green triangles represent different strategies that can be used to remove 50 gigatons of CO_2 over 25 years, and include various measures such as increased use of nuclear power, increased use of renewable energy, increased efficiency of the transportation fleet, and implementation of CO_2 capture from power stations.

Since there is no one "silver bullet" for reducing or even leveling CO_2 emissions, a variety of strategies were considered by the authors that can remove one wedge apiece; if all seven wedges start in 2010, global CO_2 emissions will stabilize by 2060. The wedges include such drastic measures as improving the fuel efficiency of vehicles in the fleet from 30 miles per gallon to 60 miles per gallon, building 400 new 1 gigawatt (GW) nuclear power plants, and installing 90% CO_2 capture on 90% of the coal-fired power plant infrastructure. This last wedge has resulted in serious debate, as out of all of the possible CO_2 emission reduction platforms, the capture of CO_2 from power stations is the only strategy that does not result in increased installed generation capacity or increased

energy efficiency, but instead energetically taxes the power station due to the parasitic load of the added CO_2 capture step.

1.1.1 The SO_X Analogy

The power industry has faced a similar situation before. The United States first initiated an in-depth research program into acid rain in 1980, and by 1990 had amended the Clean Air Act to mandate that power stations must remove sulfur oxides (SO_X) and nitrogen oxides (NO_X). The 1990 amendment established a cap and trade system for SO_X and NO_X with several phases of compliance required from the power stations. The program was mostly successful, reducing SO_X and NO_X emissions by 40% from their original levels, as can be seen in Figure 1.5[9]. Furthermore, the total cost estimates of this reduction were approximately a quarter of the original congressional estimates.

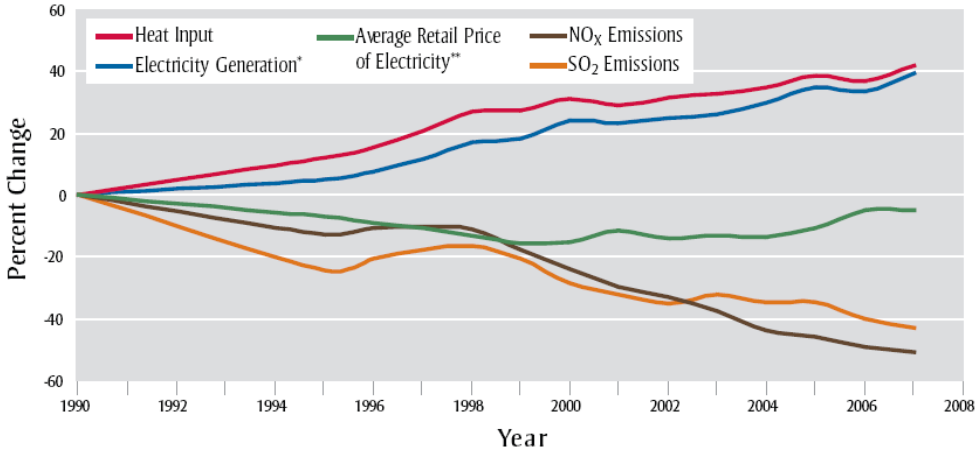

Figure 1.5: Percentage change in electricity generation, combustion of fossil fuels ("heat input"), price of electricity, and NO_X and SO_X emissions. Source: Energy Information Administration and Environmental Protection Agency, 2008.

While the "SO_X Analogy" gives hope for a cheap and timely CO_2 capture system for power stations, the realities of the CO_2 challenge become apparent in comparison between the SO_X problem and the CO_2 problem. First, the typical concentrations of SO_X in coal-fired power stations were approximately 0.20-0.25 vol%, while the approximate CO_2 concentrations in similar power stations are 9-14 vol%[10]. Both scenarios require 90% total capture, and the difference in the Gibb's Energy of Demixing (for complete capture) can be seen, viz.[11],

$$\Delta G_{DM} = -nRT\left(x_1 \ln x_1 + x_2 \ln x_2\right)$$
$$\frac{\Delta G_{DM}^{CO2}}{\Delta G_{DM}^{SO2}} = \frac{\left(0.1 \ln 0.1 + 0.9 \ln 0.9\right)}{0.0021 \ln 0.0021 + 0.9979 \ln 0.9979} = 21.6 \qquad \textbf{(1)}$$

This simple calculation demonstrates that an order of magnitude more energy is required to separate CO_2 from N_2 than SO_2 from N_2.

Second, it is possible to combust coal with lower sulfur contents[12]; the lower sulfur content can be achieved by either mining different coals, or pre-treating the coal to remove as much sulfur as possible[13]. Of course, it is not possible to remove the carbonaceous material from coal, so this route is only available to SO_X removal. Finally, since there is so much less sulfur produced by coal—by two orders of magnitude—the disposal of the captured SO_X is much less of an issue than the disposal of astronomical amounts of CO_2 will be. While the lessons learned from the SO_X analogy will be useful in tackling the CO_2 capture issue, there are still many large challenges that must be overcome for this "carbon wedge" to be removed.

1.2 CO_2 Capture from Coal-fired Power Stations

The underlying challenge for reducing CO_2 emissions from coal-fired power stations is the removal of approximately 9.0 tons of CO_2 per minute from the power station (for 90% capture from a typical 500 MW_e unit). Two broad routes have been proposed: non-point source CO_2 capture[14] and point source CO_2 capture[15]. Non-point source CO_2 capture is often considered as a way to offset the CO_2 emissions from a power plant by capturing CO_2 from the atmosphere, which avoids any need to alter the power station itself. There are a variety of ways to do this[16], but all suffer from a serious disadvantage in terms of driving force. In order to offset CO_2 emissions from a coal-fired power station, an equivalent amount of CO_2 should be captured by the non-point source device. However, the driving force for capture from the atmosphere is only, at best, 400 parts per million (ppm) CO_2, whereas in a power station the CO_2 driving force is the aforementioned 9-14 vol%. Essentially this means that in order to capture an equivalent amount of CO_2, a non-point source device must process approximately 250 times more CO_2-containing gas than a point-source emitter! While non-point source capture is a useful technology to reduce global atmospheric CO_2 concentrations, only point-source capture can truly address the magnitude of the problem.

1.2.1 Oxy-fuel Combustion

There are three general routes for CO_2 capture from coal-fired power stations. The first capture route, often referred to as "oxy-fuel" combustion, shown in Figure 1.6, involves combusting the coal in an enriched-oxygen and carbon dioxide atmosphere[17].

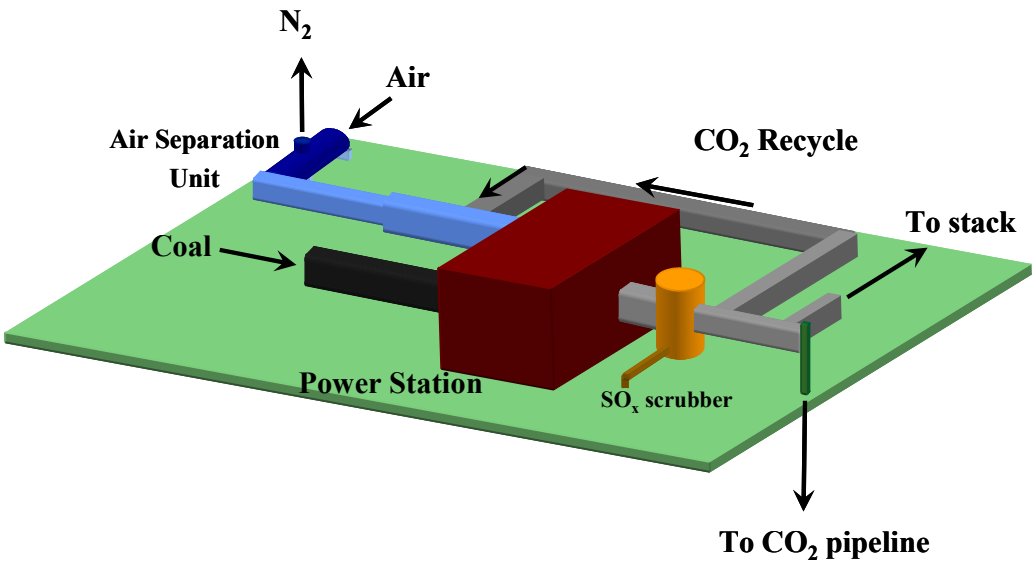

Figure1.6: Overview of a coal-fired power station fitted with an oxy-fuel combustion system. An air separation unit splits the incoming 1.2 MMSCFM (for a 500 MW_e unit) into oxygen and nitrogen. The oxygen is mixed with a flue gas CO_2 recycle. During combustion, the coal is combusted completely in the presence of oxygen, creating a pure CO_2 stream after SO_X removal. This CO_2 stream can then be simultaneously recycled back to the feed of the plant, or compressed and sent to the sequestration pipeline.

The main advantage of this technique is the resulting flue gas is almost all CO_2, requiring minimum clean-up and purification thereby allowing the flue gas to be sent directly to an existing CO_2 pipeline for sequestration. The disadvantage of this technique is that the incoming air to the furnace must be separated into oxygen and nitrogen, effectively

moving the energetic burden on the plant towards this separation. Due to the need for the large air separation unit, and the likely need for new combustion equipment, oxy-fuel plants have not been demonstrated commercially, it is essentially impossible to retrofit coal-fired existing plants with this technology.

1.2.2 Integrated Gasification Combined Cycle

The second route often considered is integrated gasification combined cycle (IGCC, Figure 1.7) combustion, wherein the feed coal is gasified to synthesis gas (syngas), and shifted along the water-gas shift reaction, seen in Scheme 1, to produce a high pressure, high CO_2 partial pressure gas stream with hydrogen.

Scheme 1: $CO_{(g)} + H_2O_{(v)} \rightarrow CO_{2(g)} + H_{2(g)}$

The CO_2 can be easily removed at this point using a physical absorbent such as Selexol®, and the pure hydrogen is sent to the combined cycle turbines for electricity generation[18].

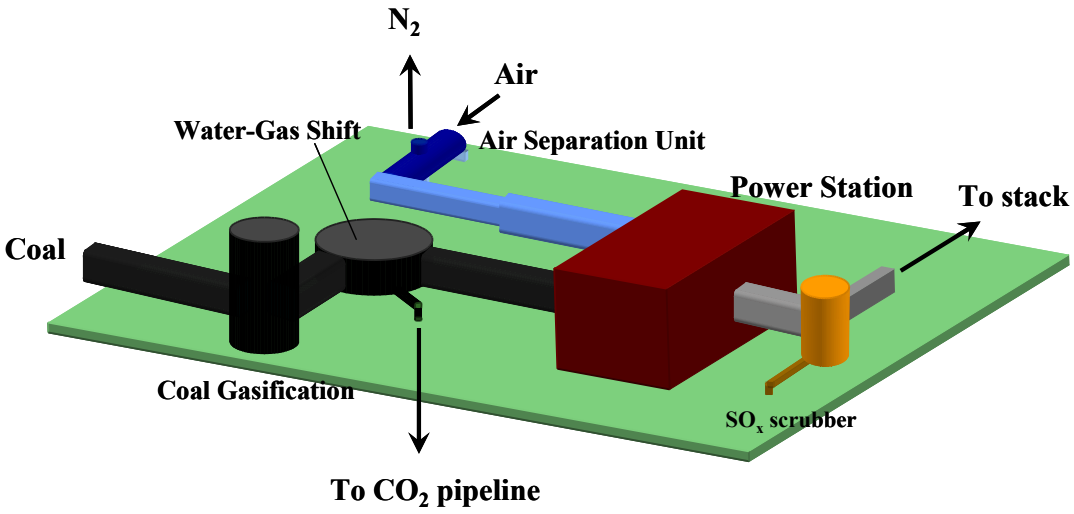

Figure 1.7: Overview of an integrated gasification combined cycle power plant. In this system, feed coal is gasified to generate CO and H_2O. The gasified coal is shifted to CO_2 and H_2, where the CO_2 is captured via a physical solvent and sent to the sequestration pipeline.

The main advantages of IGCC plants are the capture of CO_2 at very high pressure and purity, thus making the CO_2 "sequestration ready", and the higher thermal efficiencies achieved through the combined cycle. The main disadvantages of IGCC power plants are the extremely high installed capital costs[18], as well as the inability to retrofit existing power stations with IGCC technology. In order to make significant headway towards reducing CO_2 emissions from the power generation fleet, the large amount of existing power stations need to have a CO_2 capture technology that is easily retrofitted onto the existing flue gas treatment train.

1.2.3 Post-combustion CO_2 Capture

Post-combustion CO_2 capture is the main route considered for reducing CO_2 emissions from the existing power plant fleet. This route typically involves adding

another system to the flue gas treatment train after the sulfur removal systems, which is illustrated in Figure 1.8.

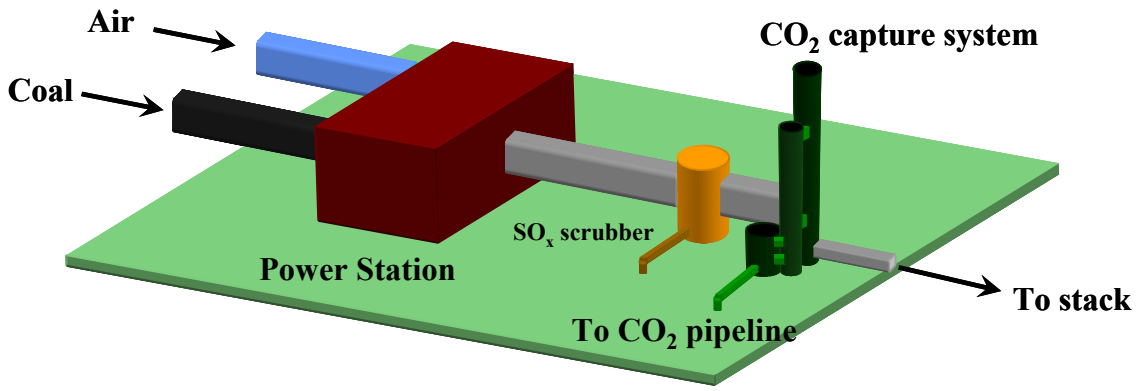

Figure 1.8: A typical coal-fire power station outfitted with a post-combustion CO_2 capture unit. In this arrangement, coal is combusted in the presence of air, and the resulting low pressure flue gas is sent through a flue gas desulfurization unit and then through a CO_2 capture system. The CO_2 captured in the unit is then sent to the sequestration pipeline.

As a result, the feed gas to the CO_2 capture system is typically low pressure (1.05-1.2 atm), low temperature (30°C to 60°C), saturated with water, and comprised mainly of nitrogen and carbon dioxide; the flue gas stream properties are tabulated in Table 1.1[10]. Furthermore, in a typical 500 MW_e coal-fired power station unit, there is an enormous quantity of gas that must be processed; approximately 1,000,000 standard cubic feet per minute (MMSCFM)! As such, there is very little thermal or pressure-driven driving forces for separation; nor is there a significant chemical potential driving force for separation.

Table 1.1: Typical flue gas composition, temperature, and pressure

Parameter/Component	Typical Values
Temperature	30-60°C
Pressure	1.05-1.2 atm
N_2	76.4 vol%
CO_2	12.6 vol%
H_2O	7.1 vol%
O_2	3.7 vol%
SO_X	0.21 vol%

In order to perform the required CO_2/N_2 separation, there is the potential for a large energetic drain on the host power station. By again using the Gibb's free energy of demixing, a rough estimate of the minimum amount of power required by the power station can be found, viz.,

$$\Delta G_{DM} = -nRT\left(x_1 \ln x_1 + x_2 \ln x_2\right)$$
$$\Delta G_{DM} = -\frac{21{,}000mol}{s} \cdot \frac{8.314J}{mol \cdot K} \cdot 308K \cdot \left[0.1 \cdot \ln(0.1) + 0.9 \cdot \ln(0.9)\right] \approx 17.5MW \quad \textbf{(2)}$$

This shows that at the very minimum, 17.5 MW of a power station's produced 500 MW must be used to separate CO_2 from N_2 (this does not take into account sequestration). Of course, approaching the Gibb's free energy of demixing minimum energy requirement is a daunting task. Despite these myriad disadvantages, post-combustion CO_2 capture from coal-fired power plants represents the best opportunity for reducing global CO_2 emissions by attacking the single largest point-source of CO_2 emissions.

1.3 Methods for Post-combustion CO_2 Capture

There are three main tactics for capturing post-combustion CO_2 from a power station: absorption, membranes, and adsorption. Absorption strategies rely on a strong chemical interaction between an absorbent and carbon dioxide. These systems typically involve bubbling the flue gas through a strong amine-based solvent for CO_2, and then heating the solvent to high temperatures to release the CO_2. The main advantage of this technology is the wealth of experience associated with using these systems in other fields[19], and as such, absorption systems are a "go-to" technology for CO_2 capture. However, these systems often have very high energy expenditures due to the thermal nature of the separation. An alternative method of CO_2 capture involves using membranes that are selective for CO_2 over N_2, purifying the CO_2 by allowing it to permeate through the membrane faster than the N_2. Membrane separations avoid the thermal requirements of other CO_2 capture strategies—a marked advantage. One of the main challenges facing membrane separations for post-combustion CO_2 capture is processing the large quantities of gas with little CO_2 driving force present. As such, enormous compressors or vacuum pumps (or some combination thereof) are required to perform the separation, and can exhibit a similar, if not larger, energy penalty than absorption systems. Finally, a third class of systems, based on adsorption into microporous materials, has been proposed as a low-cost alternative for CO_2 capture. These systems rely on (typically) physical adsorption of CO_2 into the pores of a microporous material; the energy required to drive the CO_2 out of the materials is considerably less than that required to reverse the chemical reaction present in the

absorption systems. The lower theoretical energy requirements are offset by the realities associated with utilizing and processing the microporous solids required for capturing the CO_2. Typically these systems are arranged in packed bed form, and as a result, suffer from a wide range of problems that offset the advantages of adsorption. These range from exceedingly high pressure drops through the bed, exceedingly long bed cycling times, and poor utilization of all of the microporous solids.

1.4 Research Objectives

The overarching goal of this work is to develop a new form of structured sorbent that utilizes the energetic advantages of adsorbents while mitigating the processing difficulties of solids and minimizing the energy penalties associated with using solid sorbents. This goal will be pursued via the creation of a polymer-sorbent composite in the form of a hollow fiber with an impermeable barrier on the inside (lumen or bore side) of the fiber, as seen in Figure 1.9.

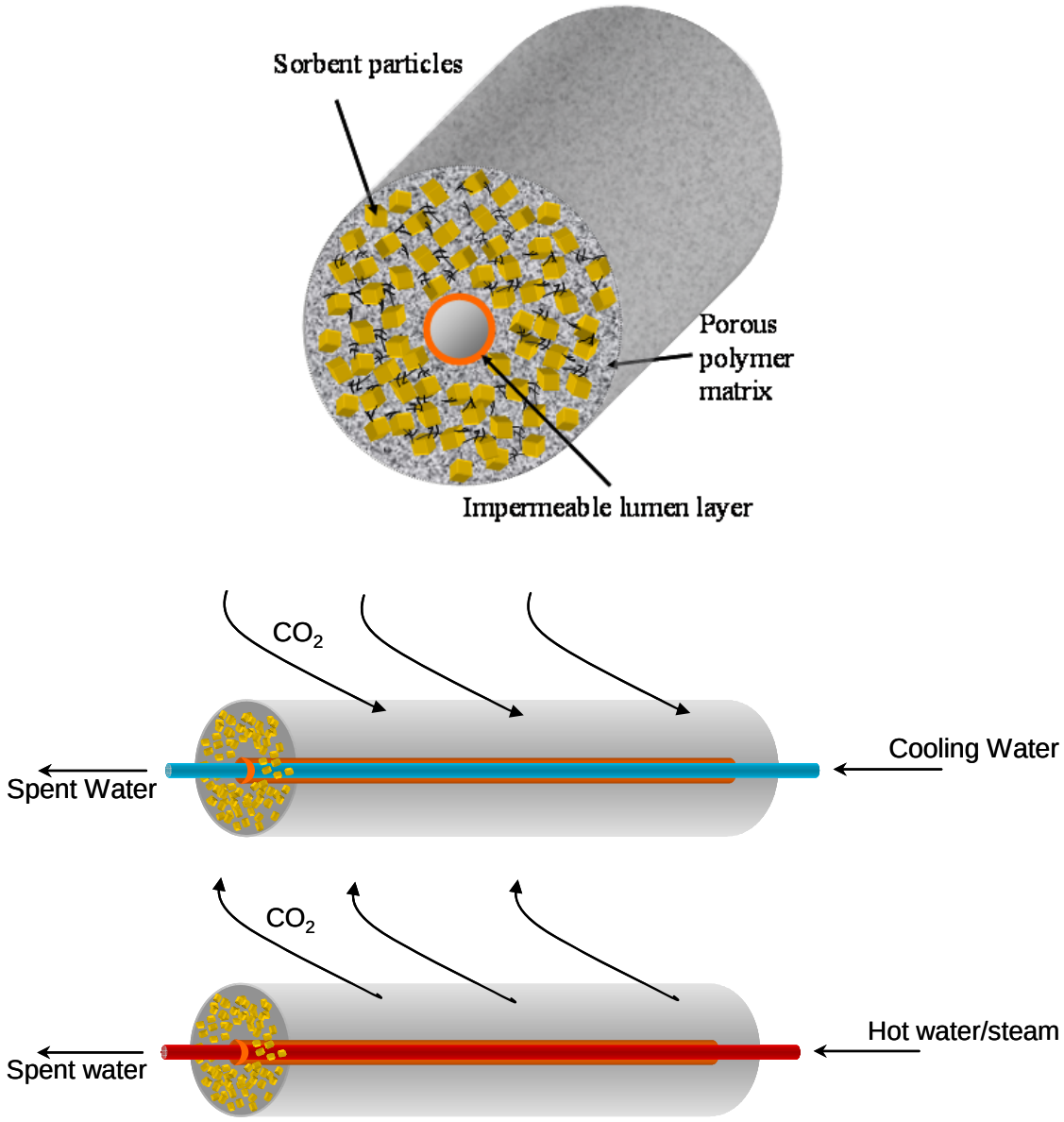

Figure 1.9: ***(top)*** **Cross-sectional schematic of a fiber sorbent, illustrating a microporous solid sorbent suspended within a fiber-shaped porous polymer matrix that has an impermeable lumen layer.** ***(middle)*** **Schematic of fiber sorbents being actively cooled during the CO_2 sorption step.** ***(bottom)*** **Schematic of fiber sorbents being heated with steam or hot water to drive the CO_2 out of the microporous sorbents.**

By bundling the fibers together and passing the CO_2-laden flue gas on the outside (shell side) of the fibers, the total pressure drop across the bed can be reduced significantly in comparison with a packed bed sorbent system. Secondly, the hollow fiber morphology,

coupled with the impermeable lumen layer, allows for rapid heating and cooling of the thin walled fibers via hot and cold water coursing through the fibers; thus allowing for quicker cycling times and more completely utilizing the sorbents contained with the fiber. The objectives of the research presented in this dissertation are:

1. *Develop a conceptual framework for the capture of CO_2 via hollow fiber sorbents, and compare it against existing and emerging CO_2 capture technologies.*

This work seeks to develop the hollow fiber sorbent platform. As the platform itself is new, much of the work is exploratory. Therefore, the essential concepts behind a fiber sorbent system first need to be developed to guide current and future research. Secondly, the new system needs to be compared to traditional and emerging technologies to determine whether the system as imagined is worthy of developing into a full-fledged platform. This comparison will primarily be judged on the basis of total energy consumed by the CO_2 capture system. While other parameters, such as total installed cost and system footprint, are important, as mentioned above, CO_2 capture from power stations is the only "carbon wedge" that actually *removes* capacity from the grid to avert CO_2 emissions. Therefore, it is paramount that the CO_2 capture systems use as little energy as possible.

2. *Develop methods for the creation of high-sorbent-loaded composite hollow fibers and the formation of an impermeable lumen layer*

In order for the fiber sorbent platform to be meaningful in comparison to traditional packed bed systems in terms of CO_2 uptake capacity, the composite fibers need to be primarily the microporous solid, yet still strong enough to be able to be formed, handled, and used in an actual CO_2 capture device. Furthermore, the fiber sorbent structure should be optimized to have an open, continuous structure around the contained solids, such that the exterior CO_2 will have limited obstructions from the fiber itself en route to the microporous solids. Of course, for the fiber sorbent platform to work most effectively, an impermeable lumen layer needs to be created; something that has never been reported before in the literature.

3. *Demonstrate proof-of-concept CO_2 capture experiments using simulated flue gas*

Once the fiber sorbents have been created, CO_2 capture experiments utilizing the fiber sorbents will need to be performed. This will include equilibrium uptake measurements, kinetic uptake measurements, cyclic measurements and demonstration rapid thermal swing CO_2 adsorption (RTSA) measurements. These sorption measurements will help confirm the viability of fiber sorbents as a CO_2 capture platform.

1.5 Dissertation Organization

After the introduction provided in Chapter 1, the thesis will expand in Chapter 2 into background material associated with gas transport in microporous and polymeric materials, chromatography, and hollow fiber spinning fundamentals. Chapter 3 will summarize all of the materials used in the experiments contained within the thesis, as well as all of the methodology associated with those experiments. Chapter 4 will develop and expand upon the conceptual fiber sorbent platform, as well as discuss energetic comparisons with other CO_2 capture technologies, and possible power plant heat integration strategies. Chapter 5 will discuss the creation of the hollow fiber sorbents in the desired morphology, and the conditions required to achieve said desired morphology. Chapter 6 is devoted to the formation of a lumen side barrier layer, as well as developing an understanding for the formation mechanisms at play. Once the fiber sorbents have been fully formed, Chapter 7 will detail the CO_2 uptake capabilities of the fiber sorbents in a variety of situations. Finally, Chapter 8 will discuss conclusions and potential paths forward to expand the hollow fiber sorbent platform.

1.6 References

1. Annual Energy Outlook 2010, Energy Information Administration, Report # DOE/EIA-0383, May 11, **2010**
2. Carbon Dioxide Emissions from the Generation of Electric Power in the United States, Energy Information Administration/Environmental Protection Agency, July **2000**

3. Owen, N.A.; Inderwild, O.R.; King, D.A. The status of conventional world oil reserves—hype or cause for concern? *Energy Policy*, **2010**, 38(8), 4743-4749.
4. Mohr, S.H.; Evans, G.M. Forecasting coal production until 2100. *Fuel*, **2009**, 88, 2059-2067.
5. Anderegg, W. R. L.; Drall, J.W., Schneider, S.H. Expert Credibility in Climate Change. *Proceedings of the National Academy of Sciences of the USA,* April 9, **2010.**
6. Climate Change and Society Governance, *The Professional Geologist*, March **2010**, pg 33.
7. Holtz-Eaken, D.; Selden, T.M. Stoking the fires? CO_2 Emissions and economic growth. *Journal of Public Economics*, **1995**, 57(1), 85-101.
8. Pacala, S.; Socolow, R. Stabilization Wedges: Solving the climate problem for the next 50 years with current technologies. *Science*, **2004**, 305, 968-972.
9. Acid Rain Program 2007 Progress Report, United States Envirnomental Protection Agency, January **2009**.
10. Townley, D. Electrochemical Concentration of Sulfur Oxides from Flue Gas, Georgia Institute of Technology, GA, *PhD Dissertation**,*** **1981.**
11. Smith, J.M.; Van Ness, H.C.; Abbott, M.; *Introduction to Chemical Engineering Thermodynamics*. McGraw-Hill, New York, NY, **2000**.
12. U.S. Coal Reserves: An Update by Heat and Sulfur Content. Report #: DOE/EIA-0529, February **1995**.
13. Kargi, F.; Robinson, J.M. Removal of organic sulphur from bituminous coal: use of the thermophilic organism *sulfolubus acidocaldarius*. *Fuel*, **1986**, 65(3), 397-399.
14. Zeman, F.S.; Lackner, K.S. Capturing Carbon Dioxide from the Atmopshere. *World Resource Review*, **2004**, 16(2), pg 157.
15. White, C.M.; Straziser, B.R.; Granite, E.J.; Hoffman, J.S.; Pennline, H.W. Separation & Capture of CO_2 from Large Stationary Sources & Sequestration in Geological Formations. *Journal of the Air & Waste Management Association*, **2003**, 53(6), 645-705.

16. Keith, D.W.; Ha-Duong, M. CO_2 capture from air: Technology assessment and implications for climate policy. *Proceedings of the 6th Greenhouse Gas Control Conference*, Kyoto, Japan, **2003**, 187-197.
17. Singh, D.; Croiset, E.; Douglas, P.L.; Douglas M.A. Techno-economic study of CO_2 capture from an existing coal fired power plant: MEA scrubbing vs. O_2/CO_2 recycle combustion. *Energy Conv Mgmt,* **2003**, 44, 3073–91.
18. Damen, K.; van Troost, M.; Faaij, A.; Turkenburg, W. A comparison of electricity and hydrogen production systems with CO_2 capture and storage. *Progress in Energy & Combustion Science*, **2006**, 32, 215-246.
19. Rochelle, G.T. Amine Scrubbing for CO_2 Capture, *Science*, **2009**, 235, 1652-1654

Chapter 2

Background & Theory

This chapter discusses the background knowledge related to creation and characterization of hollow fiber sorbents. There exist a myriad of gas transport pathways within fiber sorbents, and the chapter first focuses on the differing mass transfer phenomena that can occur along these pathways. The chapter will then focus upon the mechanisms at play during the hollow fiber sorbent formation process, which give rise to the transport pathways. Finally, emulsion casting for the creation of a dense lumen layer will be considered to complete the framework needed for the reader to understand the subsequent chapters.

2.1 Hollow Fiber Sorbents

In the context of this thesis, fiber sorbents begin as hollow fiber polymer/zeolite composites spun using a wet phase inversion process[1] at high zeolite-to-polymer loadings. After spinning, the preferred fiber sorbents are finished by post-treatment to create a lumen-side barrier layer using either Neoprene® or polyvinylidene dichloride (PVDC). The critically important barrier layer allows for heat transfer fluids to be carried through

the bore of the fibers while flue gas flows over the outside of the fibers, transforming the fiber sorbents into "adsorbing heat exchangers" (a concept expanded upon in Chapter 4 of this dissertation). Water is considered as the heat transfer fluid for cooling and hot water or steam as the heat transfer fluid for heating. Fiber sorbents for post-combustion CO_2 capture are intended for use in a rapid thermal swing adsorption (RTSA) cycle, with the rapid cycles allowing minimum device volumes and more effective use of the sorbent.

Fiber sorbents offer several advantages over conventional solid sorbent-based systems, since the hollow fiber bed acts as a structured sorbent system. Pressure drops through these beds will be correspondingly lower than those of packed or fluidized solid sorbent beds, which reduces draft fan costs and operating expenses.

Since fiber sorbents can support small (100 nm-5 micron) sized sorbents, very rapid mass equilibration times are possible, thereby allowing for smaller device volumes and more efficient use of a given amount of sorbent. This efficient use of sorbent is further leveraged by the rapid thermal equilibration times of the fiber sorbents, which can be seen in Figure 2.1 for a demonstration case where the fiber/packed bed initial temperature is 100°C and the final temperature is 25°C. The fibers are cooled with water in the bores (constant boundary condition), whereas the packed bed is cooled with inert gas (moving temperature front).

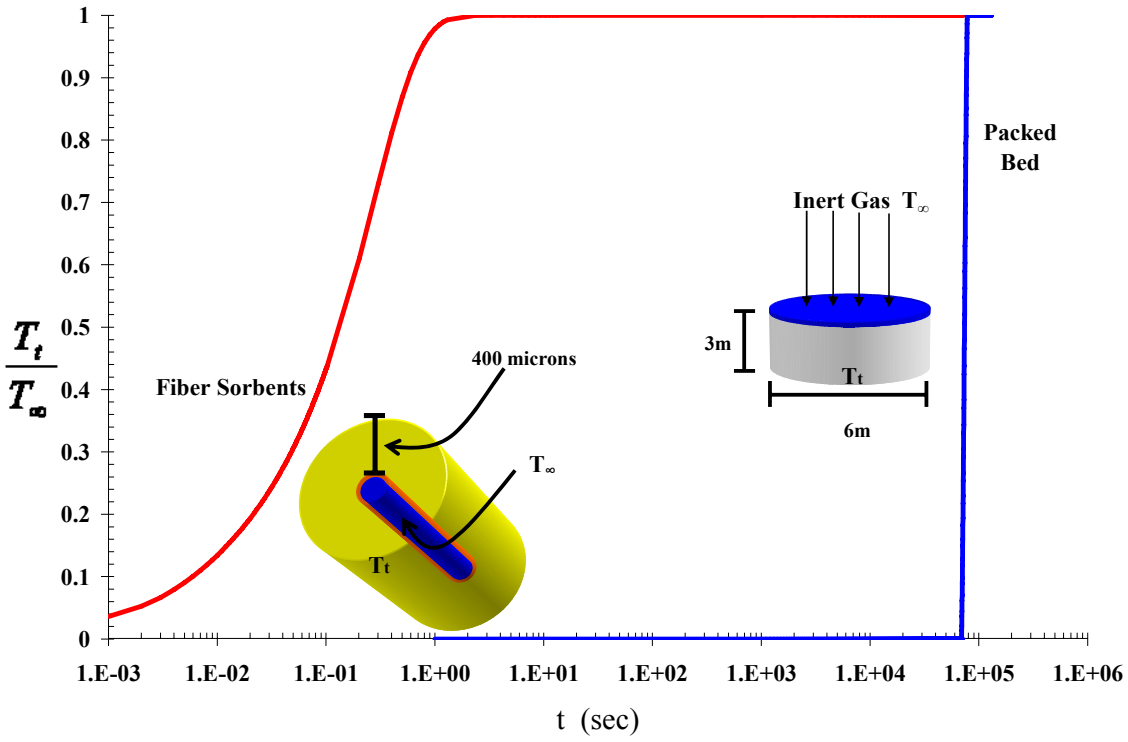

Figure 2.1: Thermal equilibration times of fiber sorbents and packed beds using 25°C cooling water and 25°C inert purge, respectively. Initial bed/fiber temperature is 100°C. The ordinate represents the percentage of cooling achieved, where 0 is no cooling and 1.0 is complete cooling. The abscissa is shown logarithmically due to the very different time scales of the two processes. The rapid response for the hollow fibers can be estimated via transient uptake equations[2], primarily based on responses scaling with the square of the wall /bed thickness. For the packed beds, a more accurate response time can be determined by using the Schumann model for unsteady-state heat transfer in packed beds[3]; however, similar long equilibration times would still be observed in such packed beds.

The thermal cycling mode for sorption-desorption is an ideal match for a hollow fiber sorbent system for several reasons. The bore of the fiber, with an impermeable lumen layer, shown in Figure 2.1, allows for thermal contacting—but not mass transfer—between the sorbent and the heat transfer fluid on much smaller scale than packed bed designs. Furthermore, the power station has an established supply system for the necessary heat transfer fluids, namely, cooling water and steam. Thermal cycling is preferred since, operating in a pressurization-depressurization mode would likely be too costly in this application due to the low flue gas pressures and the enormous flow rates.

2.2 Gas transport in polymers

In polymeric materials, three types of gas transport are common: solution-diffusion, Knudsen diffusion, and bulk diffusion. In a well-functioning fiber sorbent, all three phenomena can occur. In the defect-free lumen layer, solution-diffusion should dominate, while in defective lumen layers and small pores within the fiber sorbent, Knudsen diffusion will be exhibited. Finally, within the larger pores in the fiber bulk gas phase diffusion may be observed. These three types of transport can be characterized by a characteristic gas permeation coefficient, which are an area and thickness normalized flowrate further normalized by the driving force across the material in question, viz.[4],

$$P_i = \frac{Q_i \cdot \ell}{A_s \cdot \Delta p_i} \qquad \textbf{(1)}$$

where P_i is the permeability, l is some characteristic path length, Q_i is a molar flow rate, Δp_i is the pressure drop across the layer and A_s is the surface area of the medium.

2.2.1 Gas Transport Domains within the Fiber Sorbent

The various gas transport domains that can possibly exist within the polymer structure of the fiber sorbent are listed in Table 2.1 according to the range of diffusion coefficients that are usually exhibited, as well as qualitative permeation rates through the material at near ambient temperature and pressure. Figure 2.2 gives an illustration of the various gas transport domains that are discussed in this section.

Table 2.1 Gas Transport Domains within various domains within a fiber sorbent

Gas Transport Domain	Typical Diffusion Coefficients (cm^2/s)	Typical Selectivities, CO_2/N_2
Solution Diffusion	10^{-8} - 10^{-11}	15-30
Knudsen	10^{-5} - 10^{-2}	0.8
Transition	10^{-2} - 0.1	0.8-1
Bulk	0.1 - 0.9	1

As can be seen, solution-diffusion diffusion coefficients are typically much lower than Knudsen, transition or bulk counterparts. As such, the desired morphology for the fiber sorbent lumen layer (which is ideally "impermeable") is a dense structure that requires the solution-diffusion mechanism for permeation to minimize communication between the lumen stream and the interstitial gas feed stream. Any defects in the layer result in a large decrease in the layer selectivity and an increase in permeability. For instance, if the lumen layer is mostly defect-free with a few Knudsen level defects, the resulting measured selectivity will be between the solution-diffusion and Knudsen selectivities. Due to the much more permeable nature of Knudsen defects, the layer cannot support many of these defects (~1 out of 10^5 area fraction) before becoming completely Knudsen defective. If the lumen layer allows free gas phase exchange between the bore and interstitial or external shell side gas feed, bulk diffusion applies. Only solution-diffusion transport offers the required control of transport to make a useful lumen barrier layer. While the desired lumen layer gas transport mechanism is the low flux solution-diffusion, rapid access to the CO_2-capturing sorbents dispersed in the polymer matrix is desired, and as such, the higher flux mechanisms are preferred for exchange between the external shell side feed gas and the interstitial and zeolite pores.

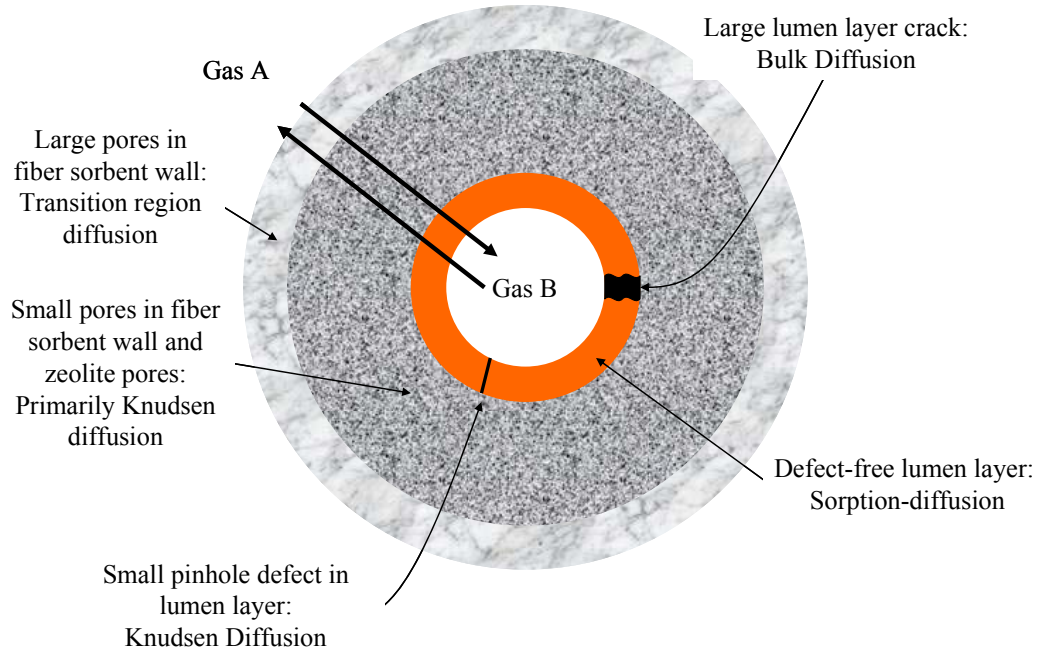

Figure 2.2: Cartoon of a fiber sorbent cross-section that illustrates the various gas transport domains that occur within a fiber sorbent.

2.2.2 Solution-Diffusion

Both Knudsen diffusion and bulk diffusion in fiber sorbents rely on an open channel through the area which a gas molecule is transporting. However, solution diffusion (or sorption-diffusion, as the gas does not necessarily have to "dissolve" within the polymer) gas permeation relies on the combined effects of gas sorption into the polymer film and the subsequent diffusion of the gas molecule through the dense polymer. Permeability in this case is defined as[4],

$$P_i = D_i \cdot S_i \qquad \textbf{(2)}$$

where D_i is the diffusion coefficient of a gas through the polymer and S_i is the sorption coefficient. Gas molecules can diffuse through a dense polymer layer by "jumping" through molecularly sized windows in the randomly fluctuating polymer matrix. The gas molecules diffuse through the polymer in a random walk, which can be represented by[5],

$$D_i = \frac{1}{6} \cdot f_i \cdot L_i^2 \qquad \textbf{(3)}$$

where f_i is the molecule jump frequency and L_i is the jump length. The factor of six takes into account the random nature of the jump by accounting for the six possible directions the molecule can jump in a homogenous medium. In regards to the sorption coefficient, gas molecules typically can dissolve (or 'sorb') into two types of sites within the glassy polymer. In one mode of sorption, the gas molecules sorb into densely packed polymer chain regions, while in the other mode, the gas molecule can fit into molecularly sized holes between the polymer chains, known as free volume. This filling of free volume is known as the Langmuir regime, while the dissolution into the densely packed regions is known as the Henry's Law regime. Rubbery polymers typically do not exhibit Langmuir-like behavior, but they do follow sorption-diffusion transport. The Langmuir region is characterized by the total Langmuir capacity, C_H' and the Langmuir affinity constant b_A. The Langmuir capacity in glassy polymers derives from penetrant-scale packing defects between the rigid glass segments. Since rubbery polymers have flexible backbones, they lack packing defects. The solubility coefficient in glassy polymers can be defined in terms of these two modes by using the dual-mode model[6]:

$$S_i = k_{D,i} + \frac{C'_{H,i} \cdot b_{A,i}}{1 + b_{A,i} \cdot p_i} \quad \textbf{(4)}$$

The first term represents the Henry's Law regime, which dominates at higher gas pressures, and the second term represents the Langmuir regime which dominates at lower pressure due to the lower energy requirements faced by the gas to fill the free volume within the polymer. The solubility coefficient can also be expressed as the ratio of the gas concentration sorbed within the polymer to the total partial pressure of the gas, as seen by[6],

$$S_i = \frac{C_i}{p_i} \quad \textbf{(5)}$$

where C_i is the concentration of the gas penetrant and p_i is the partial pressure of the gas penetrant. The quality of the dense layer can be characterized by the ideal permselectivity of the layer for two different gases, which is defined as[7],

$$\alpha_{ij} = \frac{P_i}{P_j} \quad \textbf{(6)}$$

This ideal selectivity is important for this research as it gives a measure of the overall quality of the lumen layer. Finally, the permeability of a gas through a dense film is often expressed in units of Barrers,

$$\text{Barrer} \equiv 10^{-10} \cdot \frac{cm^3(STP) \cdot cm}{cm^2 \cdot s \cdot cmHg}$$

Often times it is difficult to determine the thickness of the film, and as such only the pressure normalized flux ("permeance") equal to *P/l,* is used to characterize transport, rather than *P* in Equation 1. Permeance has units of Gas Permeation Units (GPU), defined as,

$$1\,\text{GPU} \equiv 10^{-6} \cdot \frac{cm^3(STP)}{cm^2 \cdot s \cdot cmHg}$$

2.2.3 Knudsen Diffusion

The wall of a porous fiber—as well as a defective lumen layer and even the pores in the zeolite—contains many passages with pore radii that are smaller than the mean free path (λ) of gas molecules[8],

$$\lambda = \frac{1}{\sqrt{2} \cdot \pi \cdot d_A^2 \cdot \left[\frac{p_A \cdot \text{N}}{R \cdot T}\right]} \qquad \textbf{(7)}$$

In this case, the dominant mode of transport through the wall will be Knudsen diffusion; d_A is the effective diameter of the molecule, and N is Avogadro's Number. In this case, the normal mean free path of the gas molecule is much longer than the pore diameter, $2r_p$,

causing the molecule to undergo free flight down the pore, with the only collisions primarily being those with the pore wall.

In any case, the porous polymer wall between zeolites, mesoporous diffusion comprising only Knudsen, bulk, or transition diffusion controls. Which mode dominates is determined by the relationship between the pore size of interest and the mean free path. The mean free path, λ, can be defined in terms of the average kinetic gas velocity over the collision frequency,

$$\lambda = \frac{2 \cdot \overline{U}}{f} \tag{8}$$

where $\overline{U}$ is the mean molecular speed and is defined as[9],

$$\overline{U} = \left[\frac{8 \cdot R \cdot T}{\pi \cdot M_w} \right]^{1/2} \tag{9}$$

allowing the general diffusion coefficient to be defined as[5]

$$D_i = \frac{1}{3} \cdot \overline{U} \cdot \lambda \tag{10}$$

In the absence of pore walls, the jump length of an individual diffusion step, L, is the mean free path, λ. Inside narrow pore walls, however, the jump frequency is determined by the collision frequency of the gas molecules colliding with the walls, rather than each

other. Therefore, the diffusion length, L can be roughly estimated as twice the pore radius (or the pore diameter, d_p), yielding the following equation for estimating Knudsen diffusion:

$$D_K \approx \overline{U} \cdot d_P \tag{11}$$

which is more commonly seen as[10],

$$D_{i,K}\left[cm^2/s\right] = 9.7x10^{-3} \cdot r_p \cdot \left[\frac{T}{Mw_i}\right]^{1/2} \tag{12}$$

While selective separation of a gas pair in polymers, as described above, is dependent on the relative sorption of the gas pair within the polymer or within zeolite pores and the diffusion coefficients through the polymer, selective separation through Knudsen defects relies only on the ratio of the molecular weights, viz. (which effects $\overline{U}$ in Equation 11),

$$\alpha_{ij,K} = \frac{D_{i,K}}{D_{j,K}} = \left(\frac{Mw_j}{Mw_i}\right)^{1/2} \tag{13}$$

2.2.4 Bulk Diffusion

Finally, in severely damaged lumen layers and in large pores within the fiber sorbent, bulk diffusion can exist. Bulk diffusion occurs due to one gas molecule

randomly colliding with other gas molecules to cause a random trajectory with no molecular selectivity per se. By again going to the general definition of the diffusion coefficient (Equation 10), and substituting the definitions of the average kinetic velocity of the gas and the mean free path of the gas, the mutual bulk diffusion coefficient for two gases can be given by[10],

$$D_{ij} = \frac{2}{3} \cdot \left(\frac{R \cdot T}{\pi} \right)^{3/2} \cdot \left(\frac{d_i + d_j}{2} \right)^{-2} \cdot \left(\frac{1}{2} \cdot Mw_i + \frac{1}{2} \cdot Mw_j \right)^{1/2} \cdot \left(\frac{1}{p_T \cdot \mathrm{N}} \right) \qquad \textbf{(14)}$$

where d_i is the kinetic diameter of one gas species, d_j is the kinetic diameter of the other, M_i is the molecular weight of the first gas species, M_j is the molecular weight of the second species, and N is Avogadro's number. In larger pores, it is possible for gas molecules to collide with each other as well as with the pore walls. This "transition" situation arises when the gas mean free path is within an order of magnitude (larger or smaller) than the pore radius, as seen in Table 2.2[10,11].

Table 2.2: Diffusion Regimes

Diffusion Regime	Mean Free Path relative to Pore Size
Knudsen	$\lambda > 10\ r_p$
Bulk	$\lambda < 0.1\ r_p$
Transition	$10\ r_p > \lambda > 0.1\ r_p$

To account for this complexity in which the diffusing molecule encounters resistance from both the wall and bulk collisions,, the transition region diffusion coefficient is estimated using a series resistance, which can be seen, viz.,

$$\frac{1}{D_{i,T}} = \frac{1}{D_{i,K}} + \frac{1}{D_{ij}} \quad \textbf{(15)}$$

where $D_{i,T}$ is the transition region diffusion coefficient. Finally, the path through the porous medium is usually not straight, nor is all of the area in the porous medium available for diffusion, so the diffusion coefficient is adjusted by the pre-factor[10,12],

$$D_{i,e} = \frac{\varepsilon}{\tau} \cdot D_i \quad \textbf{(16)}$$

where ε is the porosity of the material, and τ is the tortuosity of the material. The tortuosity factor represents the tortuous path a molecule must take through the material; the higher the factor, the more tortuous the path is. The mutual binary bulk diffusion coefficient, $D_{ij}=D_{ji}$ is non-selective, so if bulk diffusion occurs in a porous material (e.g., a highly defective fiber sorbent lumen layer), the material will display no selectivity for the gas pair (in a mixed gas experiment).

2.2.5 Permeation Porosimetry

In single gas permeation through porous materials, it is possible to decouple the Knudsen effects from the pressure-driven flow (Poiseuille flow), which can aid in the estimation of an effective pore size in the porous material. If a pressure driving force is supplied to one side of a porous material, and Poiseuille and Knudsen flow are assumed to be the only modes of permeation, then the total flow measured downstream of the porous material is[13],

$$\dot{Q}_{Total} = \dot{Q}_{Knudsen} + \dot{Q}_{Poiseuille} \tag{17}$$

where Knudsen flow and Poiseuille flow (for less than 10 atm) are defined as[14],

$$\dot{Q}_{Knudsen} = \frac{2 \cdot \varepsilon \cdot \overline{U} \cdot r_p}{3 \cdot \tau \cdot R \cdot T \cdot \ell} \tag{18}$$

$$\dot{Q}_{Poiseuille} = \frac{\varepsilon \cdot r_p^2 \cdot p_{avg}}{8 \cdot \mu \cdot \tau \cdot R \cdot T \cdot \ell} \tag{19}$$

where p_{avg} is the average pressure across the porous material, and μ is the gas viscosity. If permeation through the porous material is performed at several different pressures, a linear dependence on total flow versus pressure results. The intercept of this line corresponds to the Knudsen contribution to the total flow, while the slope of the line corresponds to the Poiseuille contribution to the total flow, as can be seen in Figure 2.3. With these two flow contributions known, the pore radius can be deduced by taking the ratio of the two contributions[15].

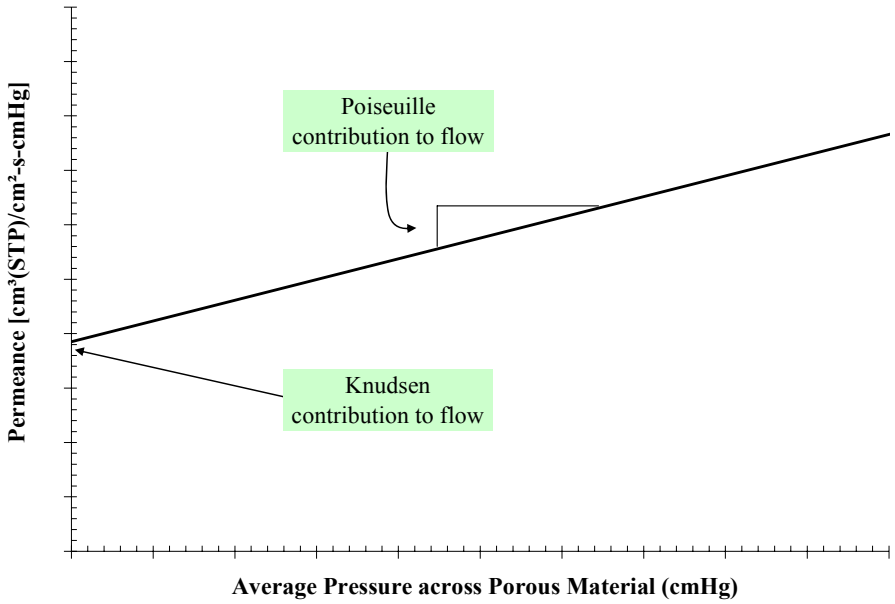

Figure 2.3: Representative plot for permeation porosimetry. By measuring the total flux through a material at varying pressures, the Poiseuille and Knudsen contributions to the flow through the porous material can be estimated.

2.3 Adsorption in Microporous Materials

Another phenomenon within the fiber sorbents comprises adsorption and diffusion of gas molecules within the microporous solid sorbents held within the polymer matrix. Any solid sorbent material can be used within a fiber sorbent structure, but one class of microporous material in particular has been focused on in this research, and that is a class of crystalline materials known as zeolites. A schematic of a zeolite is shown in Figure 2.4. Fortunately, due to the very small characteristic dimensions of the crystalline zeolite sorbents used here, the characteristic diffusion time, X^2/D, is always orders of magnitude larger for the porous fiber wall (typically 100-400 μm) versus the zeolite crystals (typically 0.1-1 μm) even when the diffusion coefficients in the zeolite are as

small as 10^{-6}-10^{-7} cm^2/sec. This fact notwithstanding, the processes related to transport in and out of zeolites are touched on here for completeness.

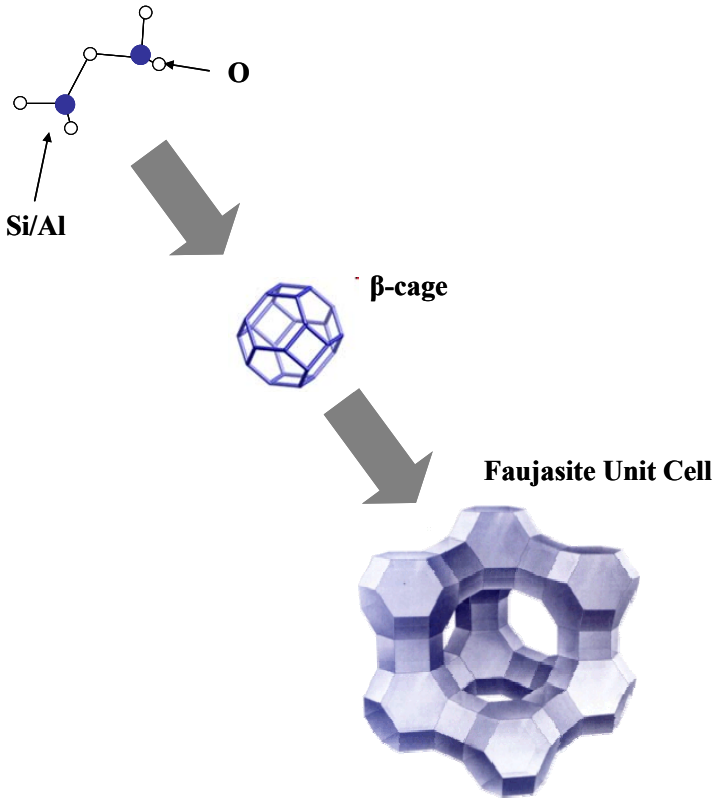

Figure 2.4: Schematic of a zeolite unit cell and its building blocks. The top of the figure shows the silica or alumina "T-atoms" linked together. The T-atoms are organized into a β-cage, which is the constituent building block of most zeolites. Finally, the β-cages are organized into the zeolite unit cage. The aperature size within the faujasite unit cell is 7.4 angstroms. Source for Faujasite unit cell: International Zeolite Association

Zeolites are comprised of "T-atoms," metallic or silicon centers that are tetrahedrally coordinated with oxygen atoms and exhibit high surface area to volume ratios as well as uniform micropore sizes. The uniform micropore sizes—which arise from the crystal structure of the zeolite—allow for size discrimination between different gas molecules[16] if the minimum pore diameter approaches the characteristic kinetic

diameter of the penetrant gases. Zeolite permeability can be estimated by a sorption-diffusion mechanism[16,17],

$$P_i = D_i \cdot S_i \tag{20}$$

where D_i is the diffusion coefficient of penetrant *i* through the zeolite, and S_i is the sorption coefficient of penetrant *i* into the zeolite.

Diffusion in zeolites is assumed to happen under an activated diffusion mode, wherein an adsorbed gas molecule will not desorb from the sorption site and diffuse through the zeolite cage without a sufficient activation energy being supplied. This is represented by the Arrhenius relationship[16,18],

$$D_i = D_0 \cdot \exp\left(\frac{-E_A}{R \cdot T}\right) \tag{21}$$

where D_o is the diffusion pre-factor (cm^2/s), and E_A is the activation energy for diffusion within the zeolite (J/mol).

More importantly for CO_2 capture is the equilibrium attraction between the adsorbate (CO_2) and the adsorbent (the zeolite), which is characterized by the sorption coefficient S_i in Equation 20. Different gas molecules will have different interactions with the sorption site of a zeolite. Aluminosilicate zeolites, by far the most common form of zeolite, typically have very polar surfaces[16], which attracts molecules with high

dipole moments and high polarizability. A charge imbalance exists in aluminosilicate zeolites[16,19], and as such, zeolites contain a counter-balancing ion to ensure overall charge neutrality. The counter-balancing ions generate electric field gradients that attract adsorbates with high quadropole or dipole moments[19]. In terms of CO_2 capture, zeolites will strongly adsorb CO_2 over N_2 due to the much higher quadropole exhibited by CO_2. However, water within the flue gas will more strongly adsorb over CO_2 due to the stronger dipole moment of water. The pressure-dependent gas uptake at constant temperature within a zeolite can be estimated using a Langmuir-type isotherm[20],

$$C_i = \frac{C_{H,i}^{i} \cdot b_i \cdot p_i}{1 + b_i \cdot p_i} \qquad \textbf{(22)}$$

where C_i is the amount of sorbate in the molecular sieve, $C_{H,i}^{'}$ is the pore saturation parameter of the molecular sieve sorbent (cc[STP]/cm^3 sorbent), b_i is the pore affinity for the sorbate (psi^{-1}), and p_i is the sorbate partial pressure (psi).

2.3 Chromatography in mixed-matrix materials

As mentioned above, fiber sorbents for CO_2 capture are based on an equilibrium separation of the shell-side flowing CO_2 and N_2. As the fibers are parallel packed into a column, the CO_2/N_2 separation will occur chromatographically (a cross flow module is also possible, and is considered in Chapter 4). Here, the fiber sorbents are the stationary phase and the flue gas acts as the mobile phase. The difference in carbon dioxide and

nitrogen's affinity for the fibers will result in a partitioning of the two gases, where the CO_2 moving through the bed is retained longer than the N_2. In lab-scale experiments, the effluent from the column is measured in real time; typically a sweep gas is fed over the sample, followed by a tracer input in either a square wave or perfect impulse[21]. This tracer will move down the column at a speed that is entirely dependent on the affinity of the absorbate for the adsorbent, and the output tracer signal will spread based on the rate of diffusion from the mobile gas phase to the stationary zeolite phase, shown in Figure 2.5[22].

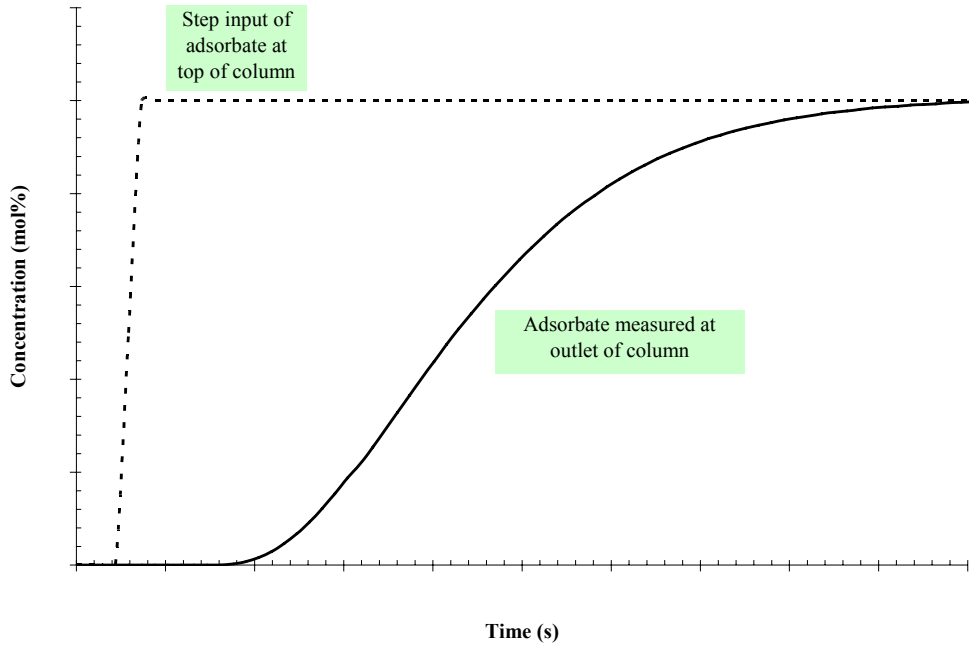

Figure 2.5: Representative plot of the response of an adsorption column to a step input. The spreading of the outlet curve is a result of dispersive forces as well as kinetic limitations within the adsorbent. The lag time in the outlet response is due to the adsorbates affinity for the adsorbent.

In an ideal situation, the spreading of the curve can be used to analyze kinetic information about the fiber sorbents. However, non-idealities such as channeling and axial dispersion

down the column often limit the accuracy of the approach unless great care is taken to minimize these factors. One way to account for the bed non-idealities is to use a mixed gas tracer, with one gas being strongly adsorbing and the other being non-adsorbing. The non-adsorbing tracer will progress through the bed at the mean retention time of the system, essentially capturing the "background" information in the column, which can then be easily factored out. By integrating the non-adsorbing tracer signal and the adsorbate signal with respect to time, the area bounded by the two resulting curves yields the equilibrium sorbed concentration (when the sample mass is accounted for), as demonstrated in Figure 2.6. Breakthrough capacities can also be measured by integrating only to the point of breakthrough.

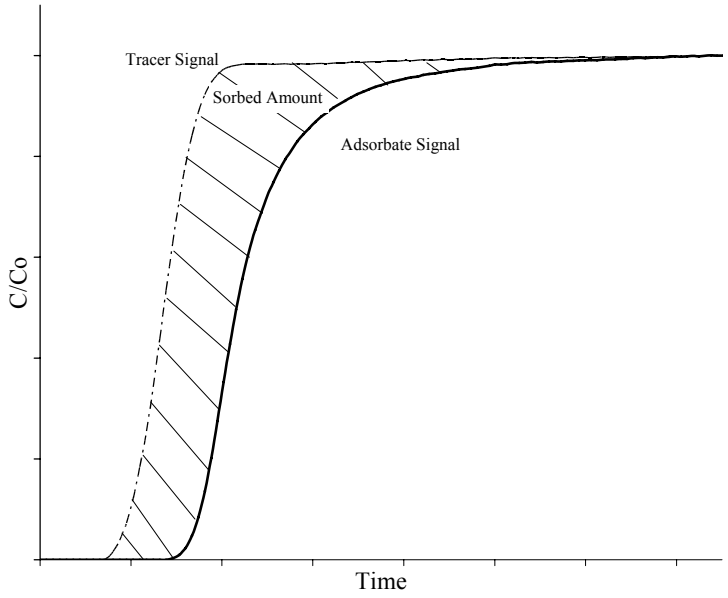

Figure 2.6: Example plot of a typical adsorption run, where an equimolar mixture of non-adsorbing tracer and adsorbing component are flowed past a packed bed. The non-adsorbing tracer accounts for the bed "background," or mean retention time, while the adsorbate signal is delayed due to affinity of the adsorbate for the sample in the bed. The area between the tracer signal and the adsorbate signal represents the total molar amount of adsorbate sorbed into the sample.

2.3.1 Kinetic Resistances

While the retention time of the adsorbate within the chromatography column is a result of the adsorbate's affinity for the stationary phase, the spread of the adsorbate front through the bed is a result of kinetic resistances that exist between the mobile phase and the stationary phase. The spread of the exit signal away from its mean retention time is measured as μ_2'(s^2), the second moment of the signal relative to its mean[22]:

$$\mu_2' = \frac{\int_0^\infty (t-\bar{t})^2 \cdot C(L,t)dt}{\int_0^\infty C(L,t)dt} \qquad \textbf{(23)}$$

where $\bar{t}$ is the mean retention time of an adsorbate, and *C(L,t)* is the concentration of the adsorbate measured at the end of the bed as a function of time. μ_2' is directly proportional to the dispersive resistances within the bed, which are comprised of external film resistance, the internal mesopore resistance, and the internal micropore diffusion resistance[22,23], which can be seen, viz.,

$$\frac{\mu_2' \cdot u}{2L_{bed}\varepsilon_b} = \delta_d + \frac{\varepsilon_b}{(1-\varepsilon_b)} \cdot (\delta_f + \delta_M + \delta_\mu) \qquad \textbf{(24)}$$

where L_{bed} is the length of the sorbent bed, u is the superficial velocity through the bed, ε_b is the bed porosity, δ_d is the axial dispersion contribution, δ_f is the film resistance contribution, δ_M is the mesopore resistance contribution, and δ_μ is the micropore

resistance contribution. The axial dispersion, film, mesopore and micropore contributions are defined, viz.,

$$\delta_d = \frac{D_L \varepsilon_b}{u^2} \qquad \delta_f = \frac{R_f \varepsilon^2}{3 \cdot k_f}$$
$$\delta_M = \frac{R_P^2 \varepsilon}{15 \cdot D_p} \qquad \delta_\mu = \frac{r_c^2}{15K \cdot D_c} \tag{25}$$

Here, D_L is the axial dispersion coefficient (cm^2/s), r_c is the radius of zeolite particles (cm), D_c (cm^2/s) is the micropore diffusivity of sorbate through the particle, R_P is the pore radius (cm) within the fiber sorbent, D_P is the binary diffusion coefficient through the pores of the fiber (cm^2/s), , ε is the fiber porosity, R_f is the radius of the fibers (cm), k_f is the external mass transfer coefficient (cm/s), and K is the dimensionless Henry's Law constant between the adsorbate-adsorbent pair.

2.3.1.1 External Resistances

Many kinetic resistances are present during the fiber sorbent sorption step. Depending on the flue gas velocity past the fiber, an external film resistance can form. A film resistance is a result of a turbulent free stream approaching a rough surface[24]. The viscous drag forces exerted by the surface are concentrated in a thin film next to the surface (Figure 2.7), while shear forces are mainly negligible above the film. In the absence of the boundary layer turbulent eddies maintain a flat concentration profile and adsorbates in the free flowing stream could simply diffuse into the porous substrate

below without having to diffuse through the boundary layer. However, when the film exists, adsorbates must diffuse through the film to reach the substrate below—a significant kinetic resistance.

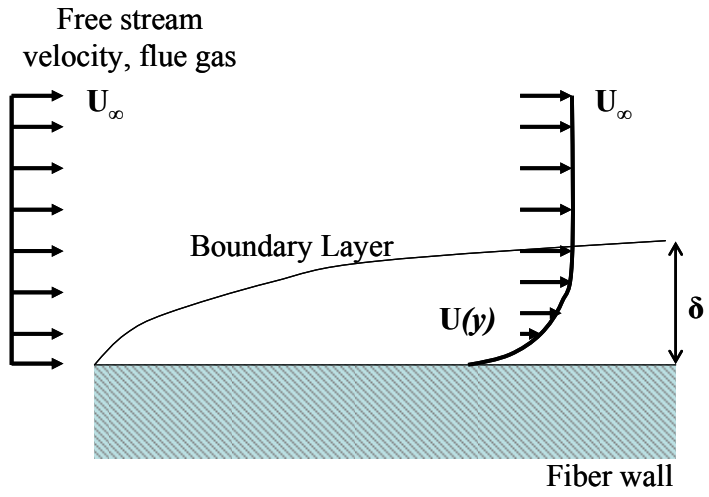

Figure 2.7: Boundary layer created by viscous drag forces between externally flowing flue gas and fiber wall. The boundary layer thickness is given by δ, while the flue gas velocity outside the boundary layer is U_∞, and the gas velocity within the boundary, $U(y)$, is dependent on its proximity to the fiber wall.

Once fully developed, the thickness of the boundary is inversely proportional to the square root of the fluid Reynolds number[10], and the diffusion time through the layer is proportional to the square of the thickness of the layer,

$$\delta \approx \frac{1}{\sqrt{\mathrm{Re}}} \tag{26}$$

$$t \approx \frac{\delta^2}{D_{ij}} \tag{27}$$

As such, increasing the velocity of the free flowing fluid significantly impacts the magnitude of the external boundary layer.

2.3.1.2 Internal Resistances

Within the fiber sorbent structure there are two internal resistances to adsorbates reaching adsorption sites: mesopore diffusion resistance and micropore diffusion resistance, which are seen in Equation 25[22]. The porous polymer support is responsible for the mesopore resistance; essentially the adsorbate must diffuse through the inert sweep gas (or other gas tracers) contained within the pores to reach the zeolites. Increasing the porosity within the polymeric support would have the effect of reducing internal mesopore resistances.* As mentioned above, the adsorbate must diffuse through the zeolite pores in order to reach the appropriate adsorption sites. This resistance is dependent on the diffusion coefficient of the adsorbate through the zeolite pores and is proportional to the square of the crystal size[25]. As noted earlier, fiber sorbents offer the ability to support any small size zeolite crystal, which can allow for low micropore resistances relative to mesopore resistances.

2.3.1.3 Length of Unused Bed

For an efficient separation, care must be taken to optimize the fiber sorbent bed to minimize the kinetic resistances so a sharp front is obtained. A sharp front is desired so that the length of unused bed (LUB) can be minimized, as demonstrated in Figure 2.8[10,26]. With a perfectly sharp front, the necessary fiber length can be decided from equilibrium

* Decreasing the pore size will also help reduce the mesopore resistance as long as the pores are large enough for bulk diffusion. Decreasing the pore size such that diffusion moves into the transition or Knudsen regime will severely decrease the diffusion coefficient, thereby increasing the mesopore resistances.

sorption values; any kinetic resistances will increase the necessary length of the bed/fibers.

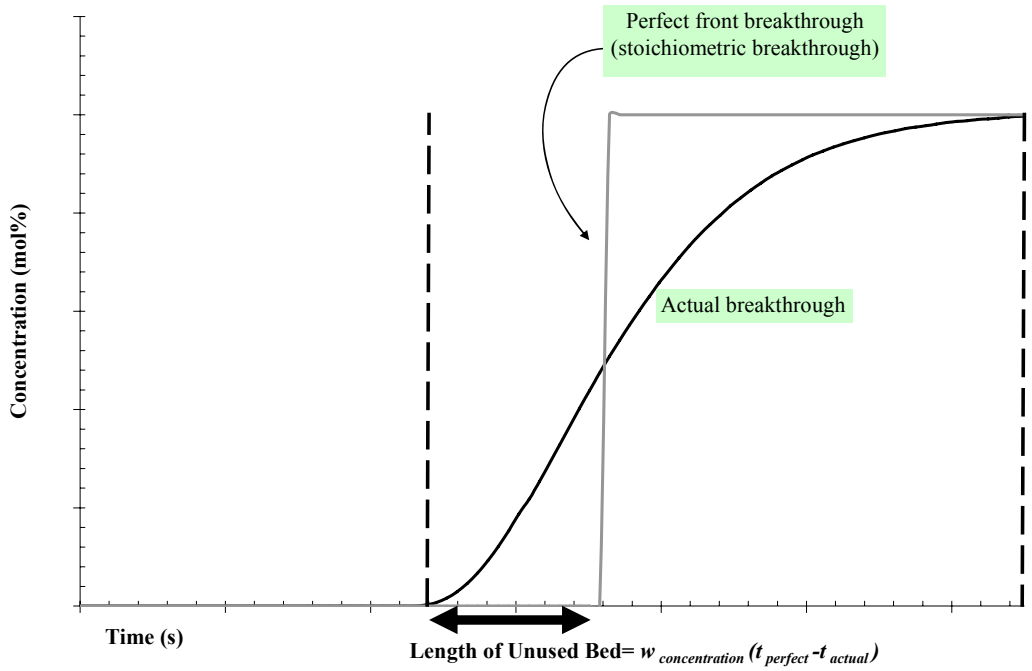

Figure 2.8: Demonstration of a perfectly sharp front and an actual breakthrough front. The more disperse the breakthrough front is, the longer the length of unused bed will become, essentially increasing device volume and decreasing separation efficiency.

2.3.2 Wave Propagation

2.3.2.1 Concentration Front Propagation

The equilibrium behavior of the sorbent not only affects the retention time of the adsorbate in the column, it also affects the shape of the adsorbate breakthrough front in the column. The velocity of the concentration front through the column is defined as[27],

$$w_{c,i} = \frac{v}{1 + \frac{1-\varepsilon}{\varepsilon} \cdot \left(\frac{\partial q_i}{\partial c_i} \right)_T} \tag{28}$$

where v is the superficial gas velocity, ε is the bed void volume fraction, and dq_i/dc_i is the slope of the isotherm. For Langmuir-type isotherms (also known as "favorable isotherms"), the slope of the isotherm decreases with increasing adsorbate concentration, resulting in an increase in the wave velocity at higher adsorbate concentrations. This results in a "self-sharpening" phenomenon, wherein the concentration front begins to sharpen as it moves down the length of the column, as seen in Figure 2.9[27].

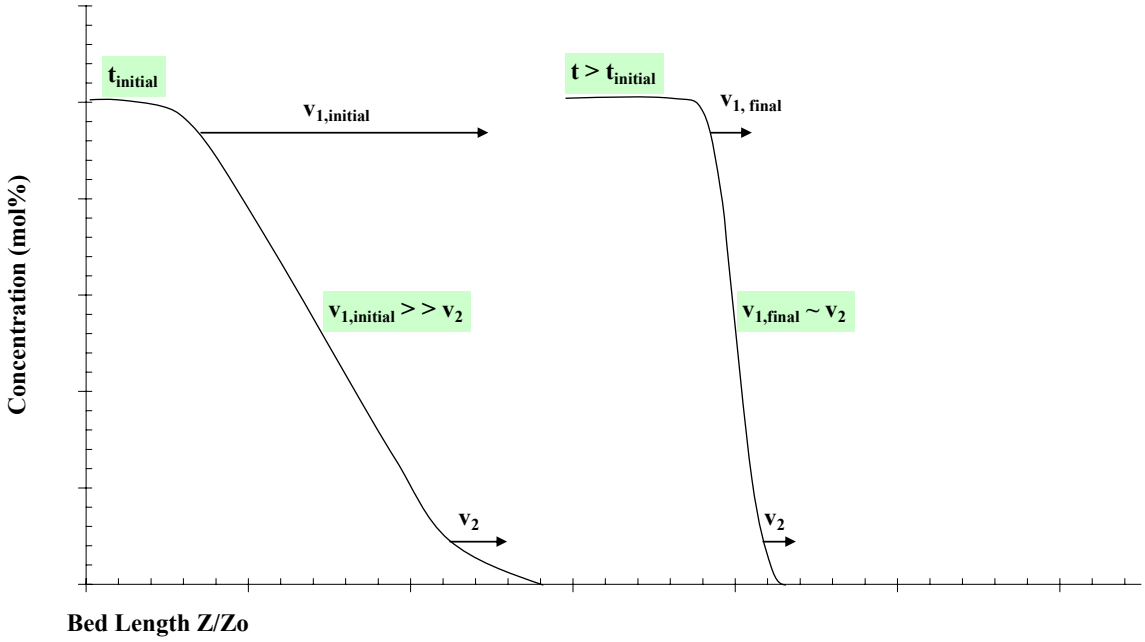

Figure 2.9: Concentration front as a function of bed position. At early times, the concentration front will spread across the bed due to kinetic resistances. However, as the lagging edge develops, the velocity of that edge will increase relative to the leading edge velocity as a result of its location on the sorption isotherm (Equation 28). This causes the lagging edge to accelerate, thereby "self-sharpening" the concentration front.

For unfavorable isotherms (Figure 2.10), the opposite phenomena is true, resulting in a self-spreading wave over the length of the column. Linear isotherms do not exhibit this phenomena. However, for desorption the reverse occurs as the column begins to remove the adsorbate—favorable isotherms self-spread and unfavorable isotherms self-sharpen[27].

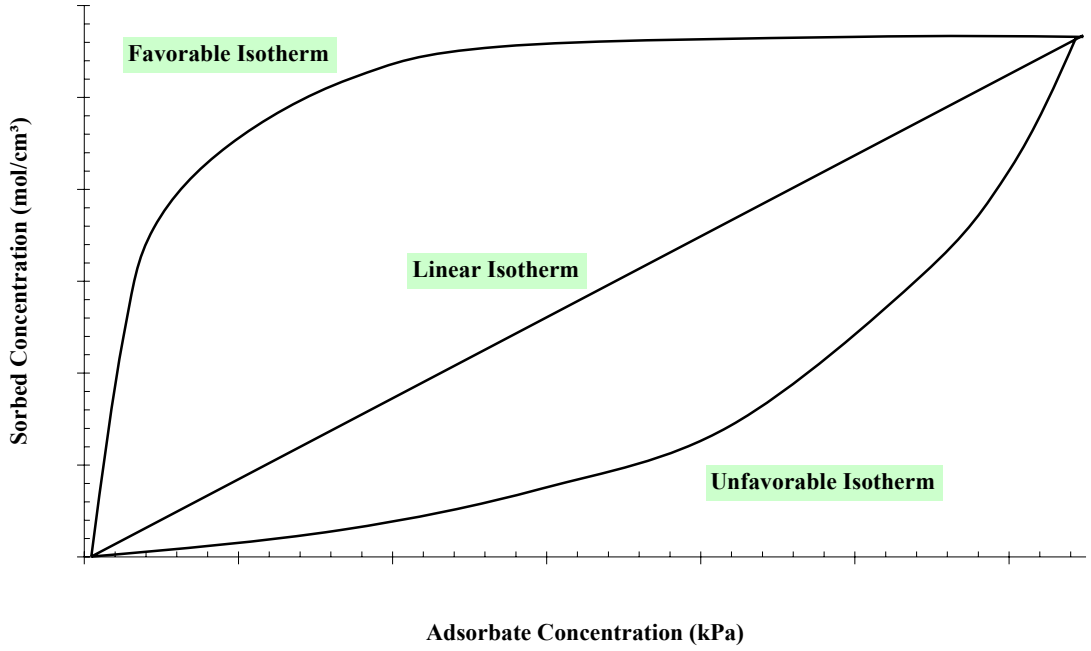

Figure 2.10: Representative plot illustrating the difference between favorable, linear, and unfavorable sorption isotherms.

Due to this self-spreading phenomenon, it can be difficult to recover a pure adsorbate product from a regenerating bed using only an inert purge gas or a pressure swing. Fortunately, strongly sorbing species often have very temperature dependent favorable sorption isotherms[28], and the linear region of the favorable isotherm is extended to higher pressures at higher temperatures, thereby removing the self-spreading phenomena at higher temperatures.

2.3.2.2 Thermal Front Propagation

As mentioned above, the sorption of CO_2 into the zeolites is an exothermic process which releases a significant amount of heat. This heat will progress through the bed in a thermal front, similar to the concentration front discussed in the previous section. The thermal wave propagation velocity is defined as[29],

$$w_{T,i} = \frac{v}{1 + \frac{1-\varepsilon}{\varepsilon} \cdot \frac{C_{P,s}}{C_{P,f}} - \frac{1-\varepsilon}{\varepsilon} \cdot \left(\frac{-\Delta H_s}{C_{P,f}} \right) \cdot \left(\frac{\partial q_i}{\partial T} \right)_C} \qquad \textbf{(29)}$$

Where $C_{P,s}$ is the heat capacity of the solids, $C_{P,f}$ is the heat capacity of the gas and ΔH is the heat of sorption. For a Langmuir-type isotherm, the $\Delta q/\Delta T$ term (as an approximation) is often quite small, and can usually be neglected[30]. When comparing Equation 29 to Equation 28 it is clear that the thermal wave will lead the concentration wave when the heat capacity ratio is less than the concentration step ratio $\Delta q/\Delta c$ (as an approximation), or the waves will coincide when the two ratios are similar, or the concentration wave will lead the thermal wave when the concentration step is greater than the heat capacity ratio. For zeolites, which sorb CO_2 strongly at low pressures, and have heat capacities similar to CO_2/N_2[31,32], the thermal wave will almost always lead the concentration wave. As will be discussed in Chapter 4, a key factor for using fiber sorbents efficiently is the ability to transfer the thermal wave effectively to the cooling water flowing in the bores of the fiber. Similar to mass transfer through the fiber sorbents, heat transfer mainly occurs through thermal diffusion—both through the solid

and gas phase—and the heat transfer rate scales with the inverse square of the wall thickness.

2.5 Wet Quench Fiber Spinning

To form the fiber sorbents, a process known as dry-jet, wet-quench fiber spinning is used[33]. A homogenous polymer solution, known as a 'dope', with suspended zeolites is extruded through an annular die, whereupon the solution undergoes phase separation either thermally or via a non-solvent coagulant. Typically, the added zeolites are assumed to not interfere with the thermodynamics of the polymer solution; as such, one phase solutions refer to the polymer/solvent/non-solvent system existing as one phase and two phase solutions refer to a separation between polymer and liquid phases. For thermally-induced phase separation, a two phase solution is made, and subsequently heated until it becomes a one phase solution; upon cold quench in a liquid the one phase solution will return to a two phase solution[34,35]. More commonly, a stable one phase (polymer solution/zeolite) solution is made at low temperature (20-55°C) conditions and has its composition abruptly changed by non-solvent invasion to shift to the two phase region. The process is referred to as dry-jet, wet-quench spinning due to the nascent fibers residence time in the air gap, and a schematic of the process can be seen in Figure 2.11. In the current work, however, the use of low volatility solvents makes the process essentially the same as a purely wet quench process with no solvent evaporation. It is simply more convenient to avoid immersion of the spinneret in the quench bath, so it is called a dry-jet, wet-quench process.

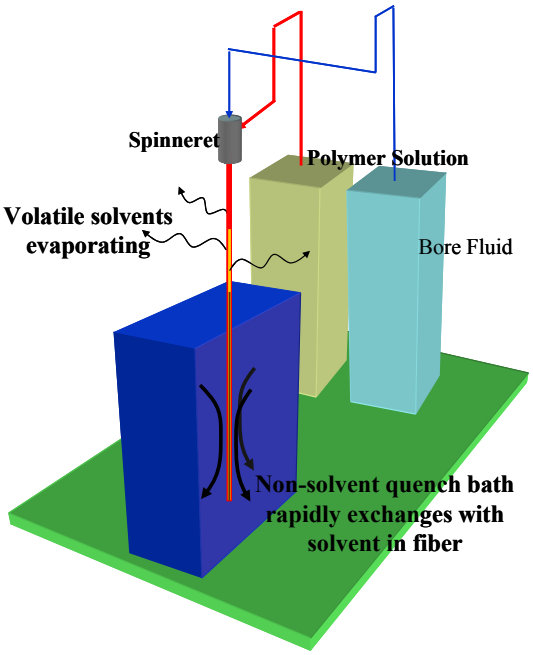

Figure 2.11: Simplified representation of a fiber spinning experiment. A polymer solution and bore fluid are co-extruded through an extrusion die, known as a spinneret, through an air gap and into a non-solvent quench medium. As illustrated in the diagram, volatile solvents evaporate from the fiber during the air gap, while the non-solvent quench medium rapidly diffuses into the fibers to remove the solvent contained within.

2.5.1 Dope Development

The polymer solution is comprised of the polymer, a solvent, and a non-solvent: this ternary system is shown in Figure 2.12. As can be seen, there are three primary regions: one phase regime, two phase regime, and the meta-stable regime[36]. The envelope between the one phase regime and two phase regime is known as the binodal line, while the lines separating the two phase regime and the meta-stable regimes are known as the spinodal lines. The spinodal lines meet the binodal line at the critical point. The polymer/zeolite solutions start in the one phase regime, and by rapid addition of non-solvent are moved past the binodal line into either the meta-stable regime or the two

phase regime. The rapid phase separation leads to a porous polymer network supporting the zeolites.

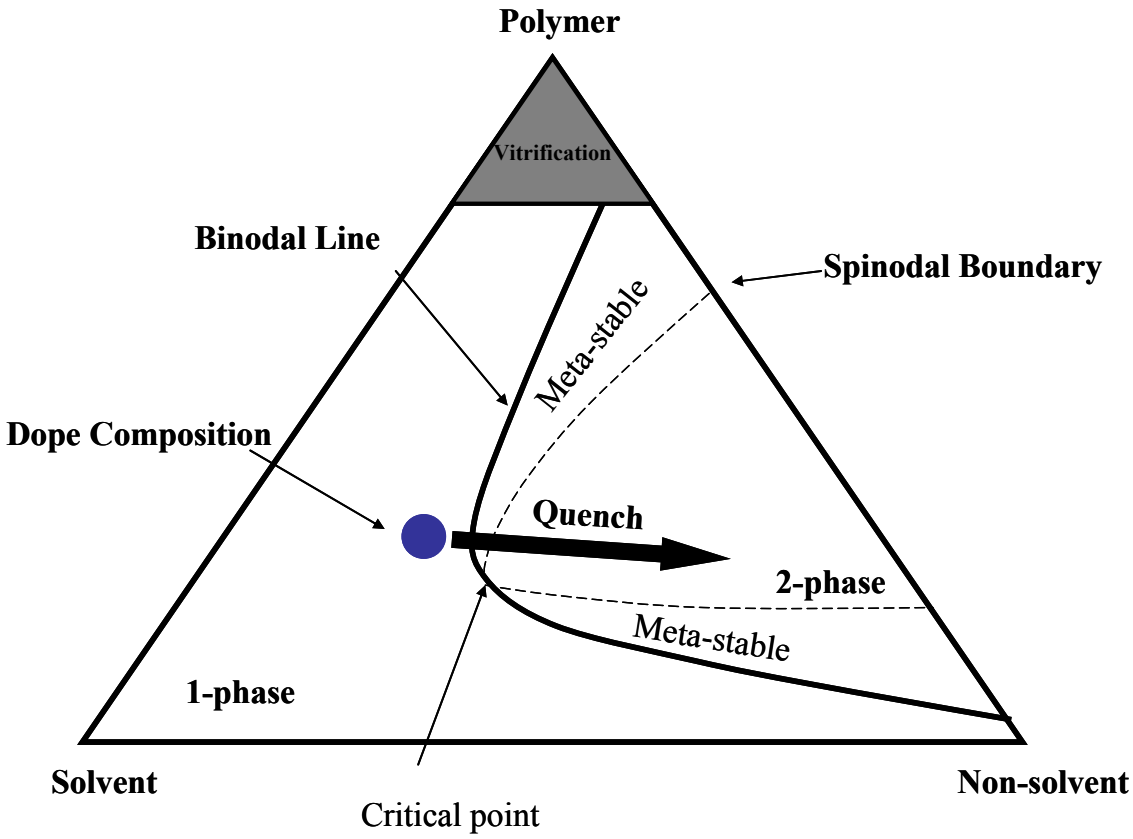

Figure 2.12: Ternary phase diagram for a polymer/solvent/non-solvent system. The 1-phase/2-phase boundary is shown as the binodal line, and the spinodal boundary, which separates the 2-phase region and the meta-stable region, is also shown. The blue point is a representative dope composition; upon non-solvent quenching, the dope will ideally move rapidly into the 2-phase region.

2.5.1.1 Nucleation and Growth

If the solution composition of the polymer solution is in the meta-stable region, phase separation occurs according to a nucleation and growth mechanism[36]. Within the unstable polymer solution, polymer-lean nuclei randomly form, and if the nuclei size is

above some critical size, the nuclei will grow. If the nuclei are below the critical size, they will dissolve back into the unstable polymer solution. The nuclei growth is relatively slow, yielding closed-cell support structures, with the only interconnection between pores coming from ruptured cell walls (cell walls rupture if they grow too large). This is undesirable for fiber sorbents, as a closed-cell porous support will hinder CO_2 diffusion through the support.

2.5.1.2 Spinodal Decomposition

If the phase separation in a region of the polymer solution is in the unstable regime, phase separation occurs according to a spinodal decomposition mechanism. This phase separation mechanism involves essentially instantaneous polymer and solvent demixing, leading to an open, bi-continuous pore structure in the polymer support[36,37]. This support structure is the more desirable support structure for fiber sorbents, as it allows for more rapid CO_2 transport through the polymer walls.

2.5.2 Fiber Spinning

The polymer-zeolite dope is coextruded through a co-annular die with a bore fluid comprised of a solvent and non-solvent. The bore fluid maintains the hollow structure of the fiber during the wet quench process and also can aid in the phase separation process from the inside of the fiber. The nascent fibers pass through an "air gap" above the quench bath, where any volatile solvents or non-solvent evaporate, thereby increasing the

polymer concentration in the dope. The fiber then descends into the non-solvent quench bath, which is typically made up with water. Here, the non-solvent diffuses into the polymer dope whilst the solvent diffuse out. Depending on the phase separation mechanism occurring, the polymer-lean and polymer-rich phases will either rapidly demix—causing the polymer-lean phase to be washed out of the fiber while the polymer-rich forms the solid support—or will undergo nucleation and growth. Finally a pulley and drum system guides and collects the fibers at some set take-up rate. The take-up rate over the extrusion rate is known as the draw ratio. Control over the draw ratio allows for control over the fiber outer diameter, while control over the bore fluid extrusion rate allows for control of the inner fiber diameter.

2.5.3 Solvent Exchange

Finally, after the fibers have been spun, residual solvent and residual coagulant needs to be removed from the polymer support structure. If water is used as a coagulant, the fibers usually cannot be dried directly, as the evaporating water results in strong capillary forces which may collapse the pore structure of the fiber sorbent if the modulus of the polymer is low due to residual solvent still present to plasticize it[38]. The strength of the capillary forces is proportional to the surface tension of the fluid. Therefore, to minimize the capillary forces, the fibers are washed with miscible non-solvent fluids that steadily decrease in surface tension. Once a fluid with a low enough surface tension is filled into the pores of the fiber—typically a volatile hydrocarbon—the fibers can then be

air dried to remove the non-solvent, and finally high temperature (~110°C) vacuum drying can be used to remove the residual non-solvent.

2.6 Formation of Dense Layers from Emulsion-based Polymers

A convenient way to create the lumen side barrier layer is to use a post-treatment technique based on a polymer latex. A polymer latex is defined as an aqueous colloidal suspension of spherical polymer particles, and is created by an emulsion polymerization. The latex serum (the aqueous dispersion containing the polymer particles) contains electrolytes, surfactants, plasticizers, emulsifiers, initiators and other species[39]. The polymer particles themselves carry surface functionality that serves as stabilizing agents to allow the aqueous dispersion to stay dispersed. When the latex is cast over a substrate and the aqueous dispersion evaporates, a continuous thin film of polymer is left behind. By washing a latex through the bores of the fiber, a polymer layer is deposited on the lumen side of the fiber.

In order for the lumen layer to be defect free, the cast latex needs to form a continuous, dense film. Latex film formation occurs through three main phases: I) water evaporation/drying, II) particle deformation, and III) polymer interdiffusion[40].

2.6.1 Nascent Film Drying

The drying stage (Stage I) occurs initially through a constant loss of water that is similar to simple water evaporation. As the water evaporates, the meniscus of the aqueous colloidal dispersion shrinks, densifying and ordering the polymer particles within[41]; at this point the water evaporation rate slows due to a decrease in surface area of the meniscus as well as an increase in polymer concentration[42]. One hypothesis is that at a critical polymer concentration, the particles on the outer edges and outer surface of the meniscus will begin to form a dense skin via Stage II and III[43]. Finally, the hypothesis posits that the residual water trapped under the forming skin layer must diffuse through the polymer itself[43] or through existing pores between the particles[44] to complete the film formation. Figure 2.13 gives an overview of this film formation procedure.

2.6.2 Particle Deformation and Polymer-Polymer Diffusion

Directly linked to the water evaporation from the film is the polymer particle deformation. Once the particles are close enough to be in contact, a neck is formed with some radius of curvature (Figure 2.13c). The interfacial tension between the polymer and water can be estimated using the Young-Laplace equation[45],

$$\Delta p = \frac{2 \cdot \gamma}{r_p} \qquad \textbf{(29)}$$

where γ is the surface tension of the latex serum, and r_p is the radius of the necking region. These interfacial forces begin to deform the polymer particles and allow the process of sintering the particle network into an FCC packing while reptation across the interface proceeds.

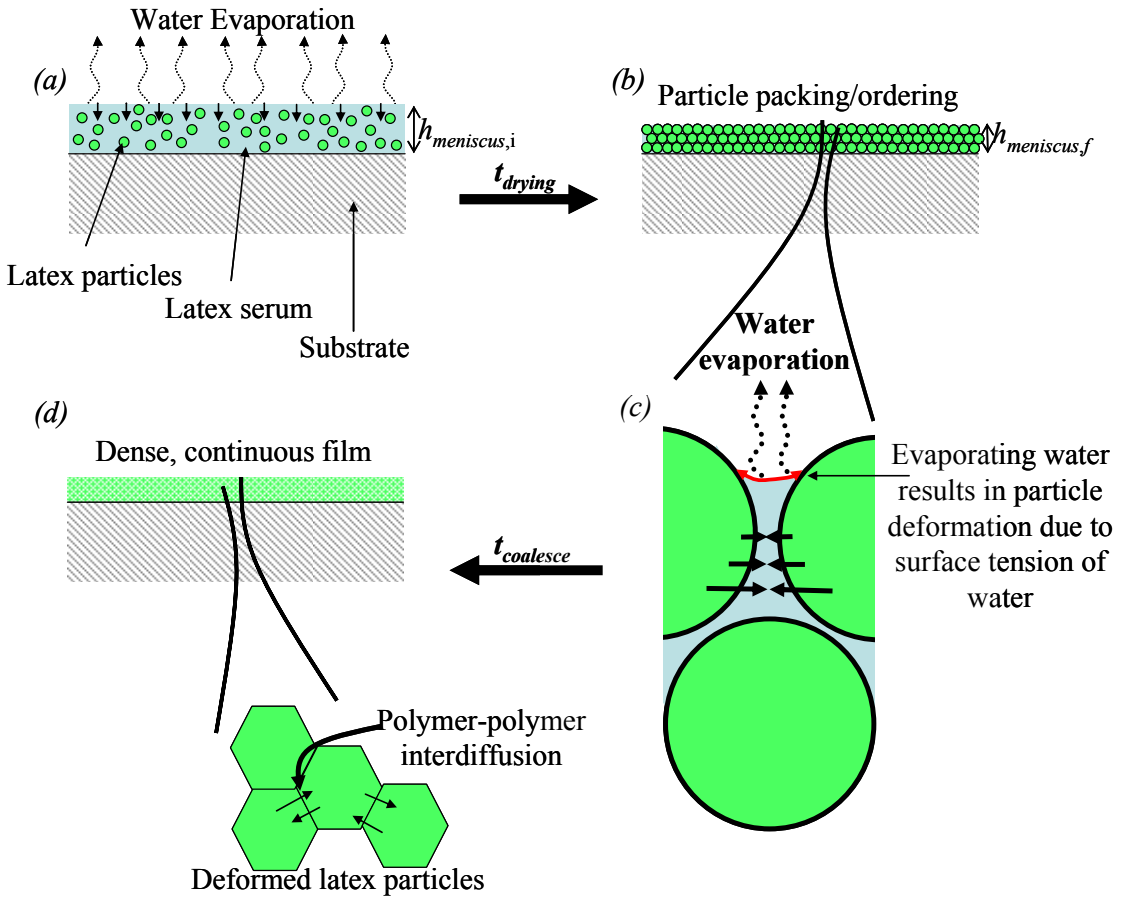

Figure 2.13: Overview of latex film formation on a dense substrate. ***(a)*** **After casting, bulk water evaporates slowly from the nascent film, causing the meniscus to shrink (Stage I).** ***(b)*** **As the meniscus shrinks, the particles are given ample time to close pack and order as the last of the bulk water evaporates.** ***(c)*** **At a critical polymer concentration, the strong surface tension of the evaporating water pulls the particles close together, finally causing them to deform (Stage II).** ***(d)*** **After deformation, the particles (which are now in intimate contact) begin to undergo polymer-polymer interdiffusion to create a dense, continuous film (Stage III).**

As the remaining water in the wet film diffuses out to the atmosphere, a moving front of particle deformation will occur from the bottom of the film towards the top.

Once deformed, the polymer particles are believed to form a rhombic dodecahedral structure[46]. Finally, once the polymer particles are deformed and in the rhombic dodecahedral structure, polymer chain interdiffusion (Stage III) can occur and "lock in" the deformations, resulting in a dense continuous film.

2.7 Summary

Ideal hollow fiber sorbents allow for rapid CO_2 access to the zeolites contained within, and have a dense, defect-free lumen layer that allows cool and hot water to carry away and provide thermal waves in the fibers, respectively. Various modes of gas transport occur both outside and inside the fiber sorbents, and have been discussed in this chapter. A non-solvent-induced phase separation, dry-jet, wet quench spinning process has been described for the formation of fiber sorbents, with the ideal phase separation mechanism being spinodal decomposition. Finally, an overview of film casting from polymer laticies has been presented, wherein the latex first undergoes evaporative drying, followed by particle deformation and finally forming a dense film after polymer-polymer interdiffusion occurs.

2.8 References

1. McKelvey, S. A.; Clausi, D. T.; Koros, W.J. A guide to establishing hollow fiber macroscopic properties for membrane applications. *J. Membr. Sci*. **1997**, 124 (2) 223– 232

2. Hines, A.L.; Maddox, R.N. *Mass Transfer: Fundamentals and Application*. Prentice-Hall, New Jersey. **1985**.
3. Wakao, N.; Kaguei, S. *Heat and Mass Transfer in Packed Beds*. Gordon and Breach, New York, NY. **1982**
4. M. Mulder, *Basic Principles of Membrane Technology*. (Kluwer Academic Publishers Group, Norwell, MA, **2003**), 2nd ed.
5. Paul, D.R.; Yampolskii, Y. *Polymeric Gas Separation Membranes*; CRC Press: Boca Raton, FL, **1994**
6. Michaels, A.S.; Vieth, W.R.; Barrie, J.A. Diffusion of Gases in Polyethylene Terephthalate, *Journal of Applied Physics*, **1963**, 14(1), 13-20
7. Ghosal, K.; Freeman, B.D. *Polymers for Advanced Technologies*, **1994**, 5, 673.
8. Baker, R.. *Membrane Technology and Applications*. John Wiley & Sons, Hoboken, NJ, **2004**.
9. Maxwell, J.C. Molecules, *Nature*, **1873**, 417, 903.
10. Hines, A.L.; Maddox, R.N. *Mass Transfer: Fundamentals and Application*. Prentice-Hall, New Jersey. **1985**.
11. Tomadakis, M.M.; Sotirchos, S. Ordinary, transition, and Knudsen regime diffusion in random capillary structures, *Chem. Eng. Sci.*, **1993**, 48(9), 3323-3333.
12. Mason, E.A.; Malinauskas, A.P. *Gas transport in porous media: The Dusty Gas Model*, Elsevier, New York, NY, **1983**
13. Uchytil, P. Gas permeation in ceramic membranes, *Journ. Memb. Sci.*, **1994**, 97(27), 139-149.
14. Burggraaf, A.J.; Cot, L. *Fundamentals of Inorganic Membrane Science & Technology*, Elsevier, New York, NY, **1996**.
15. Schofield, R.W.; Fane, A.G.; Fell, C.J.D. Gas & vapour transport through microporous membranes. I. Knudsen-Poiseuille Transition, *Journ. Memb. Sci.*, **1990**, 53(1), 159-171
16. Karger, J.; Ruthven, D.M. *Diffusion in Zeolites*, John Wiley & Sons, Hoboken, NJ, **1992**

17. Burggraaf, A.J. Single gas permeation of thin zeolite (MFI) membranes: theory and analysis of experimental observations, *Journ. Memb. Sci.*, **1999**, 155(1), 45-65.
18. Chen, Y.D.; Yang, R.T. Concentration Dependence of Surface Diffusion & Zeolitic Diffusion, *AIChE Journal*, **1991**, 37(10), 1579-1582.
19. Yang, R.T. *Adsorbents: Fundamentals & Applications*, John Wiley & Sons, Hoboken, NJ, **2003**.
20. Yang, R.T. *Gas Separation by Adsorption Processes*, Butterworth Publishers: Stoneham, MA, **1987**.
21. Hicks, J.C.; Drese, J.H.; Fauth, D.J.; Gray, M.L.; Qi, G.; and Jones, C.W. Designing Adsorbents for CO_2 Capture from Flue Gas-Hyperbranched Aminosilicas Capable of Capturing CO_2 Reversibly . *Journal of the American Chemical Society* **2008**, 130, 2902.
22. Do, D.D.; *Adsorption Analysis: Equilibria and Kinetics*, Imperial College Press, London, UK, **2008**.
23. Li, P.; Tezel, F.H.; *Journal of Colloid and Interface Science*, **2007**, 313, 12-17.
24. Blausius, H. The Boundary Layers in Fluids with Little Friction, *Journal of Math & Physics*, **1908**, 56(1), 1-37.
25. Delmas, M.P.F.; Ruthven, D.M. Measurement of intracrystalline diffusion in NaX zeolite by capillary column gas chromatography, *Microporous Materials*, **1995**, 3, 581-592.
26. Ruthven, D.M. *Principles of Adsorption & Adsorption Processes*, Wiley-Interscience, **1984**.
27. Ruthven, D.M..; *Encyclopedia of Separation Technology Volume 1,* John Wiley and Sons, Inc., New York, NY, **1997**.
28. Barrer, R.M.; Gibbons, R.M. Zeolitic Carbon Dioxide: Energetics & Equilibria in Relation to Exchangeable Cations in Faujisite, *Trans. Faraday Soc.*, **1965**, 61, 948-961.
29. Farooq, S.; Ruthven, D.M. Heat Effects in Adsorption Column Dynamics, *Ind. Eng. Chem. Res.*, **1990**, 29, 1076-1084

30. Pan, C.Y.; Basmedjian, D. An Analysis of Adiabatic Sorption of Single Solutes in Fixed Beds: Pure Thermal Wave Formation & its Practical Implications, *Chem. Eng. Sci.*, **1970**, 25, 1653
31. Chue, K.T.; Kim, J.N.; Yoo, Y.J.; Cho, S.H.; Yang, R.T. Comparison of Activated Carbon and Zeolite 13X for CO_2 recovery from Flue Gas by Pressure Swing Adsorption. *Industrial & Engineering Chemistry Research* **1995**, 34, (2), 591-598.
32. Felder, R.M.; Rousseau, R.W. *Elementary Principles of Chemical Processes*, John Wiley & Sons, Hoboken, NJ, **1986**.
33. Loeb, S.; Sourirajan, S. Sea Water Demineralization by Means of an Osmotic Membrane, *Advances in Chemistry*, **1963**, 38, 117-132.
34. Lloyd, D.; Kim, S.; Kinzer, K. Microporous membrane formation via thermally induced phase separation, *Journ. Memb. Sci*., **1991**, 64, p. 1.
35. Matsuyama, H.S.; Berghmans, S.; Batarseh, M.T.; Lloyd, D.R. Formation of anisotropic membranees via thermally induced phase separation, *Polymer*, **1999**, 40, 2289-2301
36. van de Witte, P.; Dijkstra, P.J.; van der Berg, J.W.A.; Feijen, J. Phase separation processes in polmer solutions in relation to membrane formation, *Journ. Memb. Sci.*, **1996**, 117, 1-31.
37. Koros, W.J.; Fleming, G.K. Review: Membrane-based gas separation, *Journ. Memb. Sci.*, **1993**, 83, 1-80.
38. Park, H.C.; Moon, Y.S.; Rhee, H.W.; Won, J.; Kang, Y.S.; Kim, U.Y. Effect of solvent exchange on the morphology of asymmetric membranes, in *Membrane Formation & Modification*, I. Pinnau & B. Freeman, Editors. **2000**, ACS: Washington, D.C., 110-129.
39. Padget, J.C. Polymers for water-based coatings—a systematic overview, *Journal of coatings technology,***1994**, 66(839), 89-103.
40. Keddie, J.L. Film formation of latex, *Materials Science & Engineering*, **1997**, 21, 101-170.
41. Everett, D.H. *Basic Principles of Colloid Science*, Royal Society of Chemistry, Cambridge, **1998**.

42. Vanderhoff, J.W.; Bradford, E.B.; Carrington, W.K. The transport of water through latex films, *Journal of Poly. Sci.*: *Polymer Symposia*, **1973**, 41(1), 155-174.

43. Sheetz, D.P. Formation of films by drying of latex, *Journal of Applied Polymer Science*, **1965**, 9(11), 3759-3773.

44. Brown, G.L. Formation of films from polymer dispersions, *Journal of Poly. Sci.*, **1956**, 22 (102), 423-434.

45. Rousseau, R. W. *Handbook of Separation Process Technology*. (pp. 917). John Wiley & Sons.

46. Wang, Y.; Kats, A.; Juhue, D.; Winnik, M.A.; Shivers, R.R.; Dinsdale, C.J. Freeze-fracture studies of latex films formed in the absence of surfactant, *Langmuir*, **1992**, 8(5), 1435-1442.

Chapter 3

Materials & Methods

This work is based on spinning polymeric fiber sorbents with embedded inorganic zeolites, coating the fibers with a polymer latex, and characterizing the fibers sorption and permeation properties. The chapter will first introduce the materials used for the experiments in this research, followed by the experiments developed for this research as well as details on supporting experiments. The selection of materials will be discussed, especially the choice of zeolite, as the sorption performance of the fibers is strongly related to the abilities of the zeolite.

3.1 Materials

All of the materials in this work are commercially available and are used with little to no modification to promote scalability. As will be discussed in Chapter 4, the magnitude of CO_2 capture from coal-fired power stations requires materials that are readily available industrially and do not require many energy intensive steps to synthesize and purify. Furthermore, the fiber spinning and post-treatment techniques discussed below are extensions of regularly practiced spinning and post-treating techniques in industry.

3.1.1 Polymers

Cellulose acetate (CA) (MW 50,000, Sigma-Aldrich) and polyvinylpyrrolidone (PVP) (MW 55,000, Sigma-Aldrich) were the polymers used in the spinning process. PVP was chosen as a known pore former and macrovoid suppression agent[1]. All polymers were dried in vacuum at 110°C for one day to remove sorbed atmospheric water and used directly to form solutions. Cellulose acetate was chosen as a model glassy polymer due to its ease of availability, wealth of research performed on the polymer, and the industrial relevance of the polymer. Furthermore, cellulose acetate has an adequately high T_g (185-210°C dry[2]) which will allow it to withstand the rapid thermal cycles associated with the RTSA system. The T_g of cellulose acetate in humid conditions drops considerably, limiting its use in high temperature steam or water drying applications[3]. The structure of cellulose acetate can be seen in Figure 3.1.

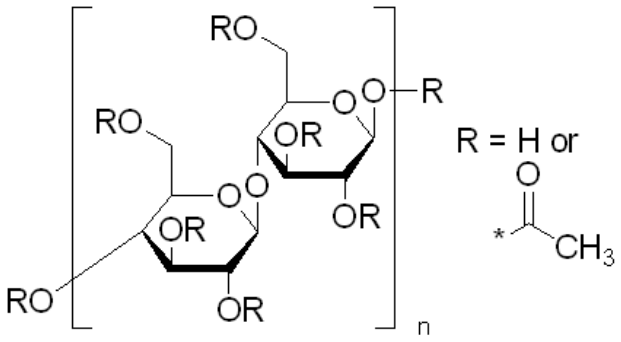

Figure 3.1: Repeat unit of cellulose acetate. Source: Sigma-Aldrich.

If the R groups on the backbone are completely comprised of hydrogen, the polymer is referred to as cellulose; if the R groups are instead exclusively acetate groups, the

polymer is commonly referred to as cellulose triacetate. The cellulose acetate in this work has 39.7wt% acetyl content, which corresponds to a degree of substitution of 2.5.

Polymers chosen for the creation of the dense lumen layer were Neoprene® and polyvinylidene chloride (PVDC) laticies. PVDC latex for application in the lumen layer was supplied by SolVin Chemicals (Northwich, UK), batch name XB 202. Neoprene® latex was supplied from DuPont Elastomers (Wilmington, DE), batch name 571. According to SolVin Chemicals, the PVDC latex is 55% by volume solids, the latex serum is anionic with a pH of 1.5. It has a glass transition temperature near -17°C[4]. Finally, this batch of PVDC latex has copolymer components of polymethylmethacrylate (PMMA) to improve the temperature resistance of the polymer. According to DuPont Elastomers, the Neoprene® latex is 50% by volume solids, is a copolymer of neoprene and sulfur (to aid in future crosslinking), is a cationic dispersion and has a pH of greater than 12. The glass transition temperature of neoprene is approximately -50°C[4,5]. PVDC was chosen for its remarkable properties as a barrier, while Neoprene® was chosen for its high temperature performance once crosslinked[5]. A curing package for Neoprene® latex was kindly supplied by Tiarco Chemicals (Dalton, GA). The structures of PVDC and neoprene can be seen in Figure 3.2. The permeability of the two polymers is listed in Table 3.1.

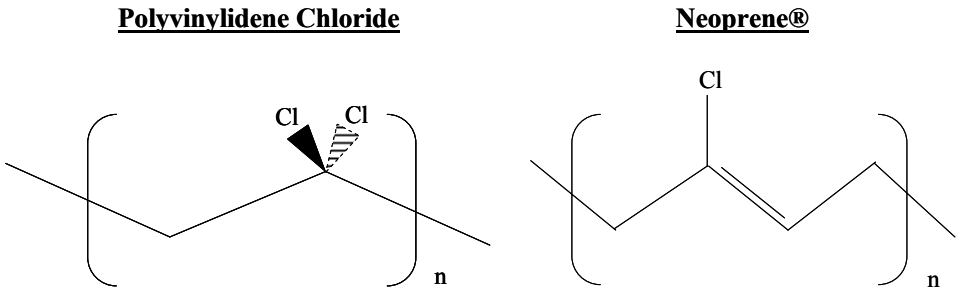

Figure 3.2: Repeat unit of polyvinylidene chloride and Neoprene®

Table 3.1: Permeabilities of PVDC and Neoprene® to some common gases[6]

All values in Barrers	P_{H2O}	P_{CO2}	P_{N2}	P_{He}	P_{O2}
Polyvinylidene Chloride	3.0	0.012	0.001	0.066	0.002
Neoprene®	914	26.0	1.17	--	4.0

3.1.2 Adsorbents

Zeolite 13X (1-3 micron particles, Sigma-Aldrich) was chosen as the model adsorbent for suspension within the polymer matrix. The zeolites were dried at 230°C to remove any potential contaminants. After drying, the zeolites were saturated with water in a humidifying chamber, thereby filling the pores with water, which was the quench medium in the spinning process. This procedure sets the sieves as "passive" fillers during the water bath quench step of the fiber spinning process (as opposed to being dehydrated fillers which can sorb solvent and non-solvent out of the polymer dopes, thereby changing the composition). In comparison with other sorbents, the capacity of dehydrated 13X for CO_2 is high and its heat of sorption (~36 kJ/mol)[7] is relatively low;

however, its hydrophilic nature makes it only useful for dry feeds[7] (coal-fired flue gas is saturated with water). While it is recognized that a more water-resistant sorbent may ultimately be preferable, 13X allows for a useful idealized discussion of the key concepts for fiber sorbents.

3.1.3 Solvents

Several solvents and non-solvents were used in this work for preparation of the fiber sorbent dopes and subsequent dehydration. *N*-methyl-2-pyrrolidone (NMP) (*ReagentPlus™ 99%*, Sigma-Aldrich, Milwuakee, WI) was used as the solvent in the polymer solutions due to its miscibility in water and solvency for cellulose acetate. Methanol (99.8%, ACS Reagent, Sigma-Aldrich) and hexane (ACS Reagent, >98.5%, Baker) were used for solvent exchange after fiber spinning. Methanol was used to remove excess water from the fibers, and hexane was used to exchange excess methanol from the fibers. This standard procedure replaces high surface tension fluids with lower surface tension fluids to prevent capillary forces from collapsing the pore structure during drying[8]. All solvents and non-solvents were used as-received with no purification or modification.

3.1.4 Penetrants

Pure gases (He, N_2, O_2, CO_2) and special made mixed gases (10mol% CO_2/90mol% N_2, 10mol% CO_2/10mol% He/80mol% N_2) were all obtained from Air Products (Allentown, PA).

3.2 Experimental Procedures

3.2.1 Fiber Sorbent Formation

3.2.1.1 Cloud-point Technique

Polymer solutions of varying solvent, non-solvent, polymer concentration and zeolite loading were made to determine the boundary between one-phase and two-phase polymer solutions using the cloud point technique. First, pure polymer solutions were made to determine the binodal line separating the single phase and two phase regimes. Once this was determined, the polymers-to-liquids ratio was held constant, and the NMP-to-H_2O ratio was held constant as the "passive" zeolites were added in. These small sample solutions were extruded through syringes into de-ionized water to determine qualitatively the speed of phase separation and fiber spinnability.

3.2.1.2 Hollow fiber sorbent spinning

Hollow fiber sorbents were created via the well-known non-solvent phase inversion technique, which is also known as "dry-jet wet-quench spinning"[9]. The aforementioned polymer solutions were extruded through a spinneret into a non-solvent quench bath (typically water). A schematic of the spinning setup is shown in Figure 3.3.

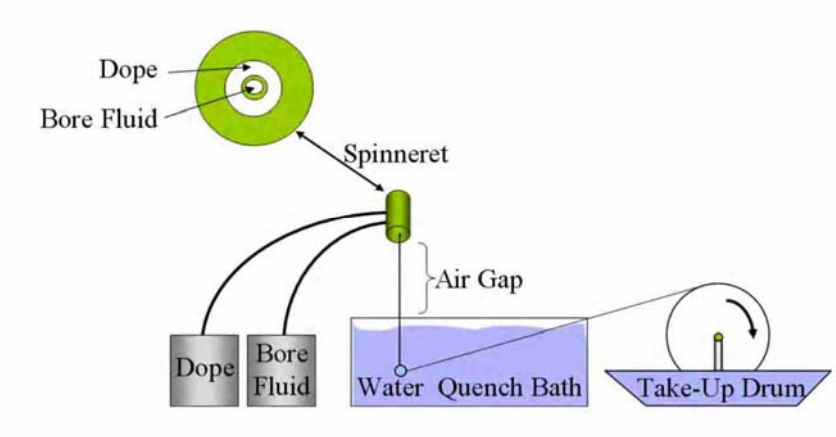

Figure 3.3: Layout of typical fiber spinning apparatus

The non-solvent in the quench bath invades the nascent fiber and displaces the solvent within, allowing for the formation of a porous fiber exhibiting a continuous polymer pore network structure with sorbent particles suspended within the porous polymer network[10]. The polymer-sorbent solutions were prepared by first mixing 80% of the required amounts of NMP and de-ionized water into a 1L glass jar sealed with a PTFE cap. The remaining 20% of the solvent and non-solvent were mixed with 20% of the required amounts of cellulose acetate and PVP in a 500mL glass jar with a PTFE cap to form a priming dope in order to aid particle dispersion within the solution. The prime dope solution was slowly mixed on a roller at 50°C until complete dissolution was observed (usually around 24 hours). Zeolite 13X, saturated with water, was added to the NMP/H_2O dispersing solution, and sonicated (1000 W max horn, Dukane, Leesburg, VA) 3 times for 1 minute with 30 second breaks. The polymer prime dope was then added to the dispersing solution, and two more sonication cycles were performed. Finally, the remaining dried cellulose acetate and PVP were mixed via impeller at high shear rates for 5 hours, or until complete dissolution was observed.

3.2.1.3 Barrier layer formation

Creation of the lumen layer via a post-treatment method is straightforward in practice. By using a latex, the need for an organic solvent is removed and allows for multiple latex "washes" if needed, followed by a drying step to remove the excess aqueous solution. This method also has the advantage of being quite tunable: latex concentration, drying gas humidity, length and number of washes, and pressure of the feed latex are all parameters that can be varied.

The fiber sorbents were assembled into standard shell and tube modules with a length of 15-24 cm[8]. Fiber modules were attached to the post-treatment system and flowing humid N_2 pre-saturated the pores of the fiber with water vapor. Fibers were then post-treated by flowing diluted PVDC or Neoprene® through the bores of the fiber at 600 mL/hr-fiber with 30mL of fluid using a 1L ISCO® syringe pump while the fiber ends were submerged in a hexane bath to prevent any rapid latex drying and subsequent fiber plugging at the tips of the fibers. The layer was then dried in several different ways which are tabulated in Table 3.2.

Table 3.2: Summary of drying procedures

Drying Method	Drying Procedure
Dry	6 hours dry nitrogen, 15 hours 71°C vacuum
Wet	6 hours saturated nitrogen, 15 hours 71°C vacuum
Graded	6 hours saturated nitrogen, 15 hours 25%RH at 25°C
Toluene-assisted	6 hours water-and-tolune-saturated nitrogen, 15 hours 25% RH at 25°C

"Dry" drying used dry nitrogen immediately after the latex deposition to dry the nascent latex film followed by vacuum drying at 71°C, while "Wet" drying used water-vapor saturated N_2 to dry the latex film followed by vacuum drying at 71°C, "Graded" drying again uses wet N_2 to initially dry the layer followed by 15 hours of ambient air drying, and finally, "Toluene-assisted" drying uses toluene-saturated and water-saturated N_2 to dry the fibers before 15 hours of ambient air drying. The module was then flipped over and the experiment was repeated. Finally, PVDC latex of two different ages were used—2 years old and fresh.

3.2.1.4 Formation of Dense Films from PVDC Latex

PVDC film formation was studied by casting PVDC films from the latex (old and new) on a variety of substrates. Cellulose acetate/13X composite films were formed by

casting excess polymer dope from the spinning experiments onto a glass plate and immediately quenching into DI H_2O followed by the standard dehydration techniques. Other substrates studied were smooth glass, etched glass, porous nylon 6,6 (Whatman International Ltd., Maidstone, England, 0.2 μm pore), and porous PVP-free polycarbonate (Poretics Corporation, Livermore, CA, 0.1 μm pore). The glass substrates were cleaned with acetone and soap water before use, while the porous substrates were used as-is. The substrates were placed on a leveling base (Paul Gardener Company, Pompano Beach, FL) and set to be perfectly level using a bubble leveler. The substrate and leveling agent were placed into a glove bag (Aldrich, Milwaukee, WI) along with a doctor knife (Paul Gardener Company, Pompano Beach, FL), sealed off and filled with the appropriate atmosphere (dry N_2 or wet N_2) and purged three times with that atmosphere. The casting knife was then placed at one end of the plate as ~4mL of latex was poured onto the substrate. Finally, the knife was drawn across the substrate to evenly distribute the latex. After the same amount of drying time that the fibers were given, the films were removed from the bag and either sent to the vacuum oven for 71°C drying or allowed to dry in ambient air for 15 hours.

3.2.2 Barrier Layer Performance Testing

3.2.2.1 Gas permeation

After the fiber sorbents were post-treated, the gas transport properties of the bare fiber sorbents were probed via N_2/He permeation using an isobaric system (constant

pressure, variable volume) with bore-side feed pressures of 20-100 psig at 35°C. This gas pair was chosen due to the separation between bulk and Knudsen selectivities (1 and 2.67, respectively), and due to the fact that both of these gases are inert towards CA and PVDC. Gas flow on the shell-side of the module was measured using a bubble flow meter every 45 minutes until the readings were within 5% of the previous reading. The volumetric flowrate can then be readily converted to molar flow rate, and along with knowledge of the barrier layer inner diameter, the permeance of the layer can be readily calculated.

The PVDC films were first tested using an isobaric system in the same fashion as described above. If the films were defect-free, they were then moved to a constant volume—or isochoric—system. The PVDC films were masked into a custom built permeation cell comprised of two stainless steel plates with a sintered steel disk placed on the bottom plate to serve as a support for the film[11]. The cell is then installed into a constant temperature permeation box by attaching it to a feed and permeate volume. A simple schematic is given in Figure 3.4[12].

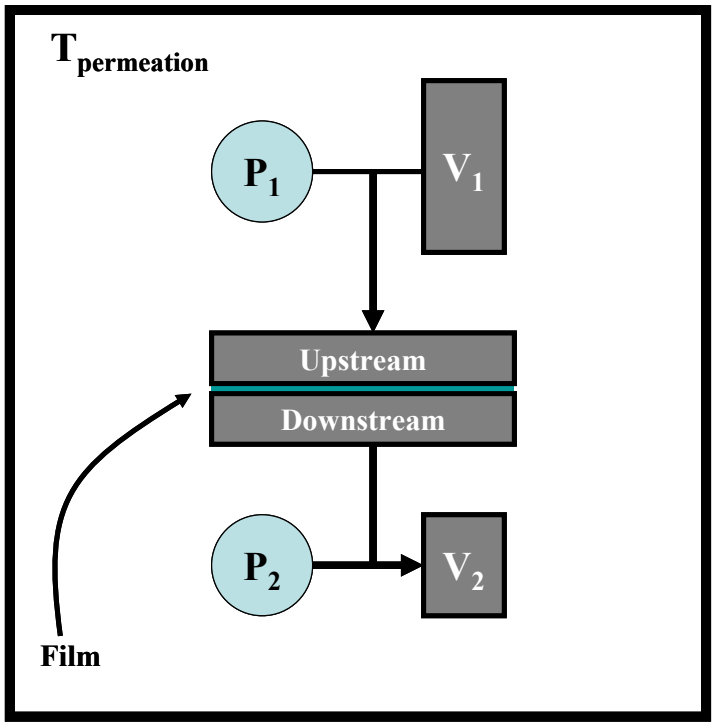

Figure 3.4: Simplified schematic of an isochoric permeation system. P_1 represents the upstream pressure transducer, while V_1 represents the upstream volume. P_2 and V_2 represent the downstream pressure transducer and volume, respectively. Typically, $V_1 >> V_2$. The system is held at constant temperature, $T_{permeation}$. Schematic based on original figure by J.R. Johnson.

A constant feed pressure is supplied to the upstream volume, while the downstream volume is kept under high vacuum. Leak rates in the system are monitored, and are usually of the order of 10^{-6} torr/sec. A permeation experiment begins when the downstream vacuum is closed, and the upstream feed valve is opened. The pressure rise in the downstream volume is monitored via a 10 torr transducer (MKS Instruments, Andover, MA). Knowledge of the downstream volume as well as the pressure rise in the volume allows for calculation of the molar flux of gas across the PVDC film.

3.2.3.2 Water permeation

Water permeability of the PVDC lumen layer was tested by attaching a backpressure regulator to the end of the fiber module and pressurizing water in the bore of the fiber via a 100mL ISCO pump to 40 psig. While water was pressurized in the bore, nitrogen at 300 sccm flowed on the shell side of the module and was sent to a Pfeiffer Vacuum QMS 200 Omnistar Mass Spectrometer. From these data, the water content in the nitrogen could be found, allowing for the calculation of the molar flow rate of water permeating through the fiber sorbent. Water permeability of the Neoprene® layers were not tested due to the known high water permeability of neoprene.

3.2.3 Fiber Sorbent Characterization

3.2.3.1 Permeation porosimetry

After spinning, bare fiber sorbents were potted into 8" modules and installed into the isobaric system described above. Helium was used as the penetrant gas, and the feed pressure was systematically varied from 20 psig to 100 psig in 20 psig steps. Due to the extreme flux through the fiber walls, helium must be used to avoid the Joule-Thomson effect. The pressure-dependent flux through the porous fiber walls allows for determination of the Knudsen contribution and the Poiseuille contribution to the overall flux in the fibers.

3.2.3.1 Pressure-decay sorption

To characterize sorption of CO_2 in the fiber sorbent as a function of CO_2 pressure at constant temperature, a simple pressure decay method developed for polymers is useful[13]. The time required to reach equilibrium in the system can also be measured to provide insight into fiber sorbent response times (without thermal moderation in the bore of the fibers). Despite its utility, such sorption kinetic approaches are only useful as preliminary kinetic and equilibrium characterization techniques, since sorption-generated heat effects cannot be effectively mediated inside this sorption system. Moreover, as a batch system, convective mass transfer resistances within the fiber wall cannot be accurately probed. Finally, since only pure gases can be used, the effects of competitive sorption or humidity in the feed cannot be assessed.

The aforementioned pressure-decay sorption method was used to determine the sorption isotherms and sorption kinetics of the fiber sorbents[14]. The sorption cells, shown in Figure 3.5, were immersed in constant temperature oil baths and zeolite crystal samples were held in a porous stainless steel filter element and capped with aluminum foil while fiber samples were loosely packed in the cell for their respective tests. After loading the fiber sorbent or crystal samples, the oil baths were set to 115°C and vacuum was pulled on the sample cells for one day to completely evacuate the cell and the fiber sorbents. After the drying step the oil bath was set to 45°C or 100°C and CO_2 was introduced to the reservoir and allowed to equilibrate. After thermal equilibrium, the sample valve was opened briefly to introduce the CO_2 to the fiber sorbent or crystal

sample. The pressure decay over time was recorded for each expansion, allowing for the determination of sorption kinetics and generation of sorption isotherms. Constraints of this simple experiment preclude moderation of local thermal heat effects within the sample cell. Those effects can be avoided in the actual RTSA system.

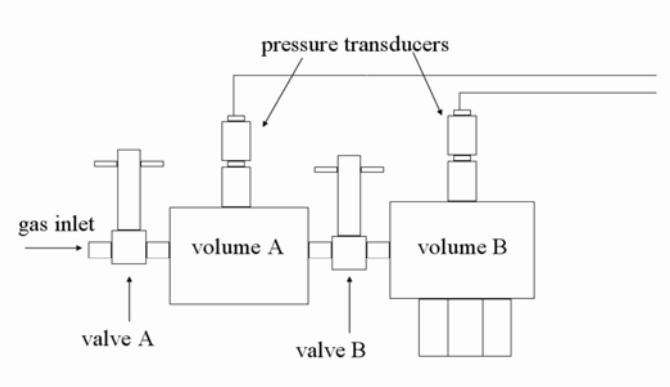

Figure 3.5: Schematic of a pressure-decay sorption cell. Volume A is the empty reservoir, and Volume B is the sample reservoir. After thermal equilibration, gas in Volume A is quickly dosed into Volume B, and the pressure decrease in Volume B is monitored.

3.2.3.2 Thermal gravimetric analysis sorption

TGA (thermogravimetric analysis) was used to analyze the stability of the fiber sorbents in a cyclic thermal environment in a series of experiments described below. A Netzsch STA 409 TGA was used, which could be programmed to control heating and cooling ramp rates and thermal soak times. Liquid nitrogen dried helium gas was set as the TGA purge and protective gas for the in-TGA drying (36 hours, 115°C or 400°C), as seen in Figure 3.6. As the drying step was completed, the TGA was cooled to 100°C, and the purge and protective gases were switched using a three-way valve to CO_2. For

thermal cycling, CO_2 gas was used to determine the regenerability and response rates of the sorbents under cyclic conditions. Separate fresh zeolite 13X samples were run at two activation temperatures, 400°C and 115°C. The 400°C activation was performed to check the validity of the results from this technique when compared to more traditional sorption characterization methods. The 115°C activation was performed to analyze the effect of low temperature activation on pure 13X. Finally, the same activation and thermal cycles were performed on the fiber sorbents.

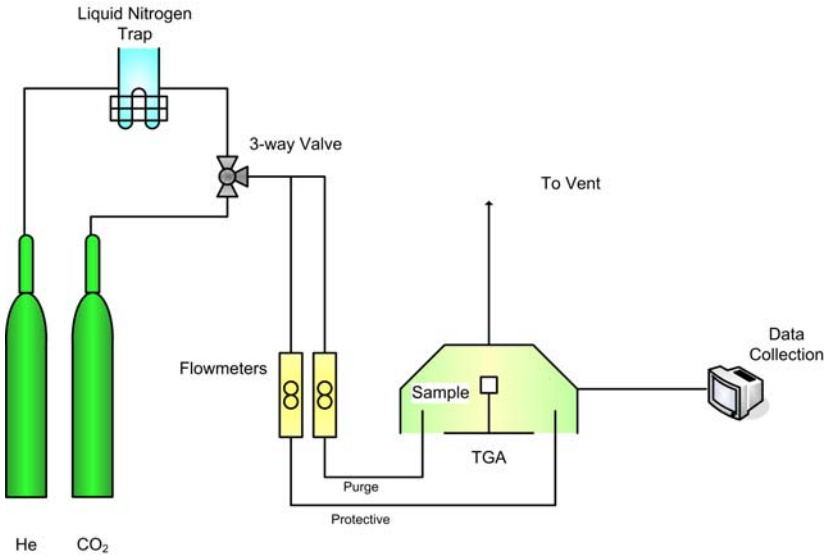

Figure 3.6: TGA adapted for cyclic sorption studies.

3.2.3.3 Column chromatography sorption

3.2.3.3.1 Un-cooled fiber sorption

A multicomponent competitive adsorption system was built to test the fiber sorbent modules in dry simulated flue gas feeds. A detailed schematic of this system is

given in Figure 3.7. The system was designed to have the ability to test saturated flue gas feeds, though these experiments are not discussed here.

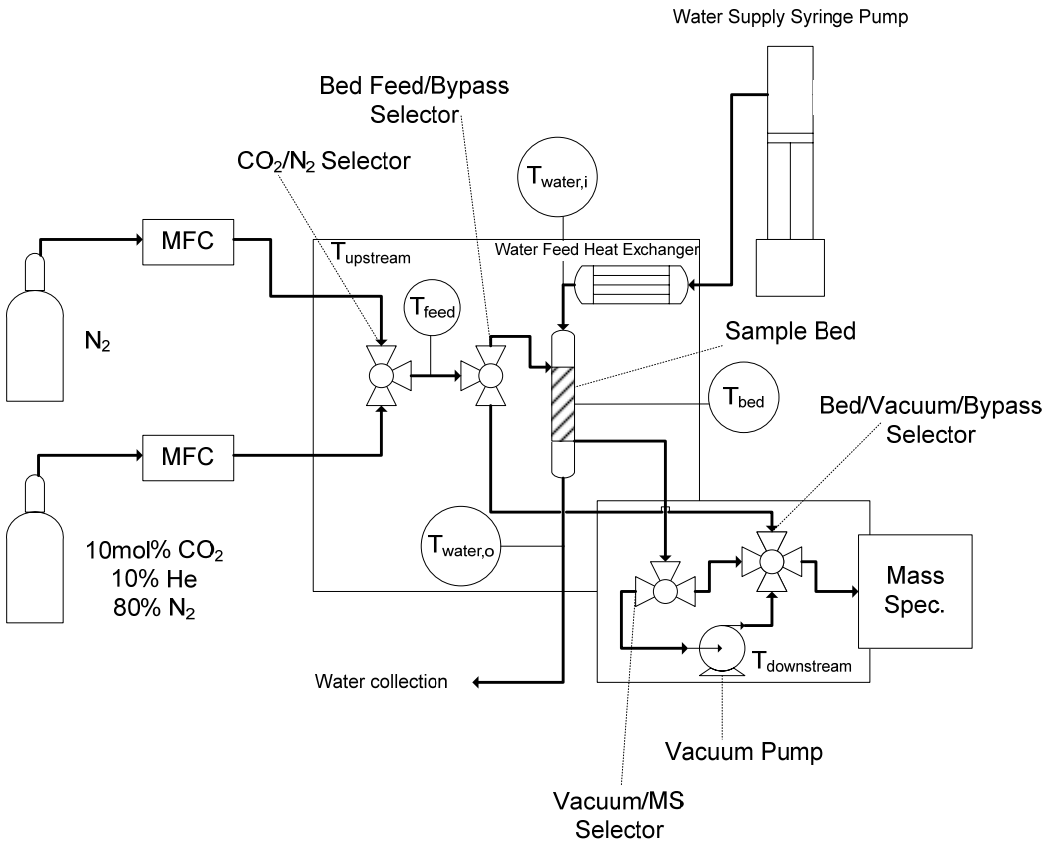

Figure 3.7: Schematic of multi-component rapid thermal swing adsorption system. The system is partitioned into an upstream and downstream that are at different temperature (Tdownstream>>Tupstream). The temperatures denoted are all measured continuously, as is the gas concentration.

Fiber sorbent modules were dried at 125°C for 2 days under vacuum in the system. After drying, the fiber bed was purged with 20.0 sccm of dry nitrogen and brought to the adsorption temperature, 37°C in these studies. The fiber bed was then rapidly switched to a 10 mol% He/10 mol% CO_2/80 mol% N_2 feed at varying flowrates to investigate sorption uptake kinetics. In this protocol, He acts as the inert tracer, N_2 acts as the carrier

gas, and CO_2 is the adsorbate of interest. The fiber bed effluent composition was determined with a Pfeiffer Vacuum QMS 200 Omnistar Mass Spectrometer. After the sorption run was complete, the bed was heated at 110°C under 20.0 sccm of flowing N_2. Mass flow controllers were used to precisely hold the purge and feed gases at the flowrates in this study. The upstream of the fiber modules was held at a constant temperature of 37°C via heaters, while the fiber module was wrapped in heat tape and held at the desired experimental temperature. The immediate downstream of the module was held at 130°C to prevent any condensation of water on the walls of the tubing. This procedure was adopted, since in the absence of downstream heating, water vapor desorbing from zeolites tends to condense on the non-heated walls.

3.2.3.3.2 Cooled fiber sorbent experiments

The multicomponent system described above was modified to allow hot or cold water to be pumped through the bores of the fibers. A 100mL ISCO pump attached to 1 meter of ¼" copper inch tubing wrapped in heat tape and controlled via heat controllers supplied the cold or hot water to the fibers (the modification is shown in Figure 3.7). Furthermore, the fiber modules were assembled using nylon PFA fittings from Swagelok® with a hypodermic needle thermocouple (Omega Instruments) nested in the middle of the fibers (Figure 3.8), which minimized the thermal mass of the module and allowed for measurement of the thermal waves moving through the fiber bed, respectively.

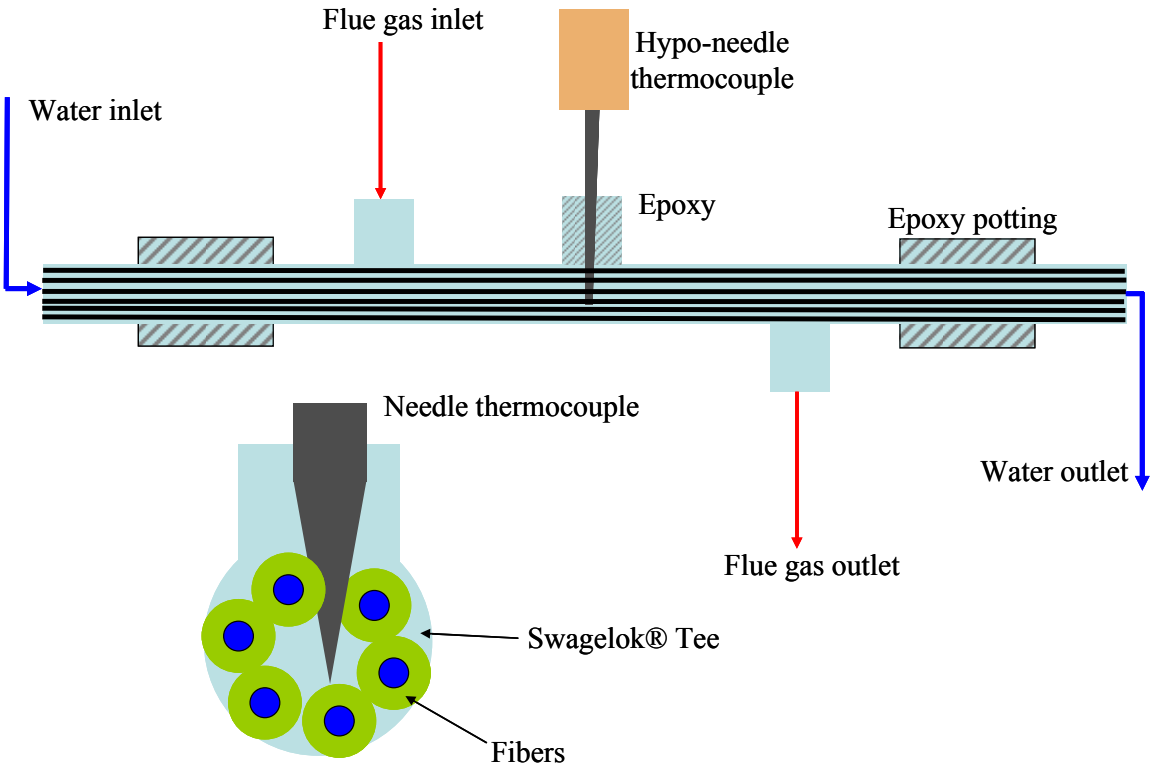

Figure 3.8: Overview of module assembly for hollow fiber sorbents. Typically, six fibers are fit into approximately 18 cm of PFA tubing, and sealed into the two ends via epoxy. Three tees are attached to the tubing, two for gas inlet/outlet, and one for a hypo-needle thermocouple. This thermocouple is nested among the fibers, and epoxied into the tee.

The sorption procedure described in the previous section was slightly modified by allowing the cooling water to begin running through the bores for 30 seconds before the sorption experiment was started. The effect of the water flow rate on the sorption capacity as well as well as the magnitude of the water and fiber thermal waves was studied.

3.2.3.3.3 Desorption experiments

Desorption experiments were performed by allowing either the bed to come to CO_2 saturation, or by stopping the CO_2 sorption experiment as 1mol% CO_2 was observed in the mass spectrometer (corresponding to 90% CO_2 capture). The feed valve to the module was then closed as 90-105°C hot water was pushed through the fiber bores. The module was then swept with nitrogen; the flow rate of the sweep gas and the timing of opening the feed valve were varied.

3.3 Supporting Experiments

3.3.1 Scanning electron microscopy

Scanning electron microscopy (SEM) was used to evaluate fiber sorbent pore structure, polymer-filler interfaces, and probe for lumen layer defects. Solvent exchanged fibers were soaked in hexane for 2 minutes, transferred to liquid N_2, and sheared in half using two fine point tweezers. This procedure ensured sharp fiber breaks, and the fibers were then sputter-coated with a 10-20nm thick gold coating (Model P-S1, ISI, Mountain View, CA), and transferred to a high resolution Field Emission Scanning Electron Microscope, Leo 1550 (Leo Electron Microscopy, Cambridge, UK). The same procedure was repeated for the PVDC films.

3.3.2 X-ray diffraction

X-ray diffraction was used to investigate the crystal structure of the 13X used in this study as well as search for any crystallinity in the PVDC films. All of the data in this study were collected via Ni-filtered Cu Kα radiation on a PanAlytical X'Pert PRO machine. The zeolite powder samples were pressed into the sample holder with a clean glass slide while the film samples were stacked and supported with a clip into the sample holder. A step-scanning protocol was used, where 0.02° 2θ steps were taken from 5° to 70° 2θ at 1 second per step. θ is the Bragg angle.

3.3.3 Differential scanning calorimetry

Differential scanning calorimetry (DSC) was employed to demonstrate the difference in morphology between aged and fresh PVDC films cast on smooth glass. It is well known that the presence of crystallinity increases glass transition temperature compared to non-crystalline sample. The instrument for this characterization was model Q800 from TA Instruments. Glass transition temperature was determined from the first scan by taking the half height of heat increment. Each run was made at 10°C from -50°C to 170°C. Nitrogen flow at 50 ml/min was maintained to prevent any oxidation of polymer during run.

3.4 References

1. Qin, J.J.; Li., Y.; Lee, L.S.; Lee, H. Cellulose acetate hollow fiber ultrafiltration membranes made from CA/PVP 360 K/NMP/water. *Journal of Membrane Science* **2003**, 218, 173-183.
2. Barker, R.E.; Thomas, C.R. Glass Transition & Ionic Conductivity in Cellulose Acetate, *Journal of Applied Physics*, **1964**, 35(1), p. 87
3. Malldi, D.P.; Scherer, J.R.; Kint, S.; Bailer, G.F. Water in polymer membranes. Part III: Water sorption & pore volume in cellulose acetate films, *Journ. Memb. Sci.*, **1984**, 19(2), 209-231.
4. Ahareni, S.M.; On free volume of polymers above the glass transition, *Journal of Applied Polymer Science*, **1979**, 23(1), 223-228.
5. Kauffman, G.B.; Mason, S.W.; Seymour, R.B. Happy and Unhappy Balls: Neoprene and Polynorbornene, *Journal of Chemical Education*, **1990**, 67(3), 198- 199.
6. Sweeting, O.J. *The Science and Technology of Polymer Films*, John Wiley & Sons, Inc.: New York, NY **1971**
7. Chue, K.T.; Kim, J.N.; Yoo, Y.J.; Cho, S.H.; Yang, R.T. Comparison of Activated Carbon and Zeolite 13X for CO_2 recovery from Flue Gas by Pressure Swing Adsorption. *Industrial & Engineering Chemistry Research* **1995**, 34, (2), 591-598.
8. McKelvey, S. A. Formation and characterization of hollow fiber membranes for gas separation (fiber breaks, macrovoids). University of Texas, Austin, *Ph.D. Dissertation* **1997**.
9. McKelvey, S.A.; Clausi, D.T.; Koros, W.J.; A guide to establishing hollow fiber macroscopic properties for membrane applications, *Journal of Membrane Science* **1997**, 124, (2), 223-232.
10. Husain, S. Mixed Matrix Dual Layer Hollow Fiber Membranes for Natural Gas Separation. Georgia Institute of Technology, GA, *Ph.D. Dissertation* **2006**.
11. T. Moore, "Effects of Materials, Processing, and Operating Conditions on the Morphology of Gas Transport Properties of Mixed Matrix membranes," *PhD Dissertation*, University of Texas - Austin, **2004**.

12. Moore, T.; Damle, S.; Williams, P.; Koros, W.J. Characterization of Low Permeability Gas Separation Membranes and Barrier Materials: Design and Operation Considerations, *Journal of Membrane Science,* **2004**, 245 (1-2), 227-231 .
13. Koros, W.J.; Paul, D.R.; Design considerations for measurement of gas sorption in polymers by pressure decay, *Journal of Polymer Science, Polymer Physics Ed.* **1976**, 14, 1903.
14. Chandra, Preeti. Multi-component Transport of Gases and Vapors in Poly(Ethylene Terephthalate). Georgia Institute of Technology, GA, *Ph.D. Dissertation* **2006**.

Chapter 4

Hollow Fiber Adsorbent System Design and Comparisons

In order to guide the creation and testing of hollow fiber sorbents for CO_2 capture, a basic system and process design calculation was performed. Parallels to existing hollow fiber membrane technology were used to guide what was feasible in the design of the hollow fiber sorbent system. The scale of the process was estimated, and its energetic requirements were calculated. Finally, a comparison to other CO_2 capture systems is presented.

4.1 Overview of Hollow Fiber Adsorbent Process Configuration

As discussed in Chapter 1, a post-combustion CO_2 capture system attached to a 500 MW_e coal-fired power station must process approximately one million standard cubic feet per minute, with anywhere from 9-14vol% CO_2 contained within. For this analysis, all systems are assumed to have 10vol% CO_2 within the flue gas for simplicity. Fiber sorbents for post-combustion CO_2 capture are intended for use in a rapid thermal swing adsorption (RTSA) cycle, with the rapid cycles allowing minimum device volumes and more effective use of the sorbent. In order for an effective separation to occur, the RTSA system needs to maximize CO_2 recoveries during the sorption step. As such, the

bed void fraction should be no higher than 60% to mitigate dilution of the desorbing CO_2 with interstitially held flue gas. There exists an intrinsic tradeoff here: at higher void volumes, flue gas pressure drops are decreased, but CO_2 recoveries also decrease; the cross flow pressure drop is given, viz.[1],

$$\Delta P_{Flue} = \frac{4 f_f N_r \rho_{flue} v_{Max}^2}{2 g_c} \left(\frac{\mu_s}{\mu_b} \right)^{0.14} \quad \textbf{(1)}$$

where f_f is the friction factor between the gas and the fibers, N_r is the typical number of obstacles a "packet" of gas may encounter on its flight through the module, v_{max} is the superficial velocity at the front of the bed, g_c is the gravitational constant, and μ_s and μ_b are the laminar and bulk viscosities, respectively.

As such, a maximum of 60% void volume has been determined to keep CO_2 recovery purities over 90 mol%. For this study, the void volume is assumed to be 50%, and the CO_2 recovery purity is assumed to be 90mol%. An integral mechanism for capturing a pure CO_2 product is configuring the bed such that the CO_2 outlet is placed at the bottom of the bed, while the heating agent for desorption is fed from the top. This essentially drives the CO_2 out of the sorbents held within the fibers, displacing the interstitial gas in plug flow fashion, thereby generating a pure "wave" of CO_2 which can be then sent to the compression station via an inert (N_2) purge (Figure 4.1).

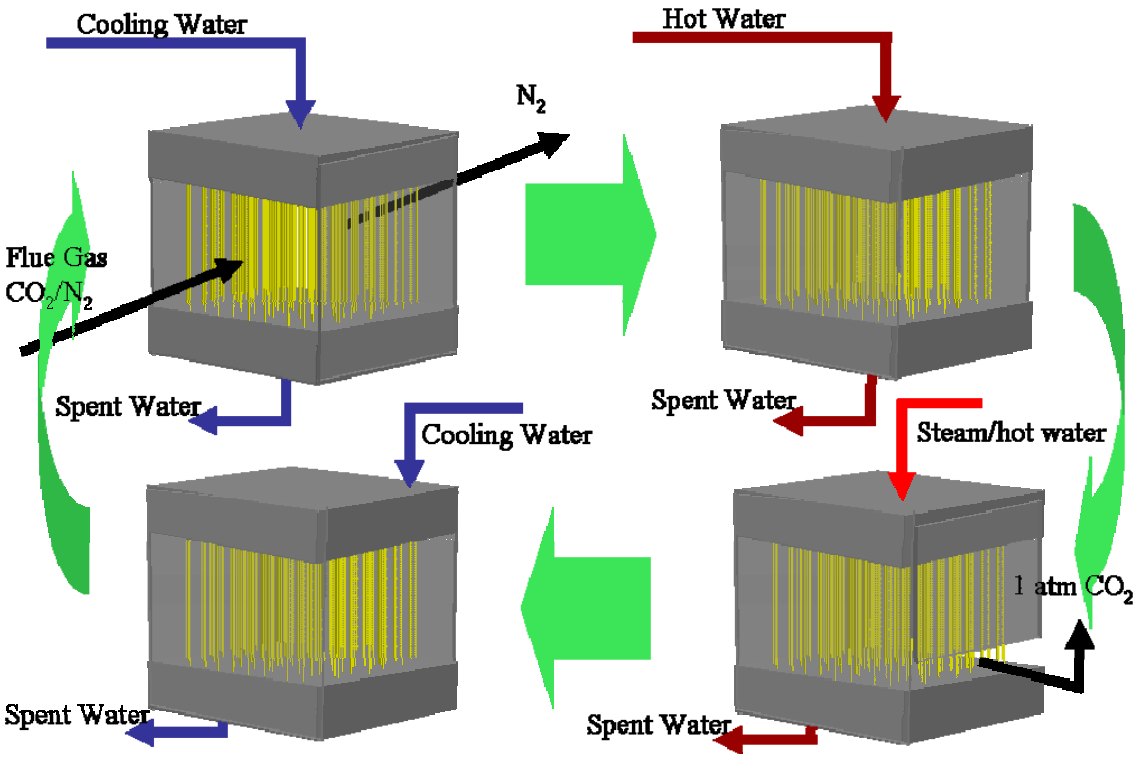

Figure 4.1: Overview of fiber sorbent RTSA operation. Four beds are assumed in this study, with each bed operating in phase with the others. During the sorption step (top left), CO_2-containing flue gas flows on the shell side of the fibers (in cross-flow configuration), while cooling water runs through the bores of the fibers carrying away the released heat of sorption. After the sorption step, the bed is heated using hot water with all exits to the bed closed, allowing CO_2 pressure to build. After the heating step, the bottom of the bed is cracked open as hotter water or steam is sent through the bore to supply the heat of desorption. A thermal wave in the fibers results in a corresponding CO_2 wave, thereby displacing the interstitial gas. The CO_2 can be recovered by an inert sweep (not shown). After the desorption step, the fiber sorbents are returned to the sorption temperature via cooling water.

In parallel flow configuration, the fibers are arranged into a shell and tube module. Here, the shell-side flue gas flows in the same direction as the lumen-side cooling water during the sorption step. In this way, the thermal wave—which moves axially through the bed—can be transferred to the cooling water running in the bores of the fibers, thereby heating the water, allowing it to be used elsewhere in the plant. As discussed in Chapter 2, the thermal wave propagates much faster than the concentration front; if the

cooling water velocity matches the thermal wave velocity, the fibers will remain isothermal at the concentration front. For the desorption step, hot water or steam can be driven through the bores of the fibers, which will drive the CO_2 out of the embedded zeolites in a plug that matches the thermal front through the fibers. A delayed nitrogen purge can then be used to push out the plug of purified CO_2 and sweep the bed in preparation of the next sorption step. In a parallel flow configuration, the shell-side flue gas can support a higher loading fraction of fibers (which results in higher purity CO_2) at similar or lower pressure drops than its cross-flow equivalent due to its linear velocity scaling, which can be seen, viz.[2,3,4],

$$\Delta P_{flue} = 32 \cdot \frac{1}{\varepsilon_m} \cdot \left\{ \frac{d_f}{d_m} + \left(1 - \varepsilon_m\right) \right\}^2 \cdot \frac{\mu_b \cdot v_{\max} \cdot L_{bed}}{d_f^2} \qquad \textbf{(2)}$$

where d_f is the fiber diameter, d_m is the module inner diameter, ε_m is the void fraction in the module, and L_{bed} is the length of the fibers (the fiber length is equivalent to the bed length).

Parallel flow and cross flow configurations each have various advantages and disadvantages. Cross flow modules are envisioned as much larger, singular entities, whereas parallel flow modules are much smaller and will likely require many modules to be assembled together to complete one phase of the RTSA cycle. Parallel flow modules have much lower pressure drops than cross flow modules for equivalent loading and superficial gas velocity, as can be seen in Table 4.1.

Table 4.1: Comparison between cross flow and parallel flow modules

	Fiber module arrangement	
	Parallel Flow	**Cross Flow**
External Mass Transfer Resistance	Boundary layers create significant external resistance	Bluff body effect shears away external resistance
Thermal Wave/Cooling Water Matching	Cooling water and thermal wave flow in same direction, allowing for easy matching	Cooling water and thermal wave flow orthoganal to each other, making matching difficult
Bed Size	6m x 1m (*LxR*)	12 x 6 x 25 m^3 (*LxHxW*)
Number of Beds Required	200	4
Packing Fraction	0.50-0.72	0.30-0.40
Pressure drop scaling	v	v^2

A main advantage of cross flow modules is the reduction of external mass transfer limitations via the "bluff body" effect[5]; this will allow for sharper fronts moving through the bed in comparison to parallel flow modules (for similar gas velocities), which can lead to smaller bed sizes, as the LUB can be reduced. On the other hand, parallel flow modules more readily allow for a pairing of the thermal waves propagating through the solids and the cooling water in the bores. In cross flow pattern, the gas flowing in the *x*-direction through the bed pairs poorly with the cooling water flowing in the *y*-direction.

Table 4.1 highlights the differences between the two module configurations, and lists the number of beds that are required for the entire process.

Finally, the fiber characteristics need to closely match system demands to minimize operational costs. In that regard, the amount of sorbent per fiber cross-section should be maximized, i.e., the fiber should have both a small ID and a large OD. Approximately 320 microns and 1200 microns, respectively, are used in this study. There are several factors that determine the final fiber dimensions: fiber spinnability, pressure drop of water and steam in the bore of the fiber, pressure drop of the flue gas on the shell side of the fiber (Appendix A), and the amount of sorbent contained per cross-section of the fiber. For a base case of 1M SCFM flue gas feed at 10 vol% CO_2, 1.1 atm and 45°C, a 70 second cycle time (70 second sorption time) is assumed. These parameters are used as the base feed case for all the technologies considered herein.

In determining the fiber sorbent system size, several objectives should be kept in mind: minimizing superficial velocity of flue gas, maximizing CO_2 recoveries during the desorption step, and maximizing CO_2 sorption capacity per fiber. In this analysis, long fibers (6m) are envisioned in a cross-flow pattern, with a 15m x 6m opening to the cross flow module. The module is assumed to operate in cross-flow mode during the sorption step. While 6m fibers are longer than the standard hollow fiber modules in use today, special module designs with supports to aid in fiber handling could certainly be envisioned. Furthermore, longer fibers will increase the bore-side fluid pressure drop,

but this can be largely mitigated by increasing the bore size of the fibers. Appendix A gives a rough estimate of the fiber sorbent system size.

4.3 Estimation of Energy Penalties of the Fiber Sorbent System and Comparison to other Technologies

This section analyzes each CO_2 capture device on a basis of 1 tonne of CO_2 captured (unless otherwise noted), at effectively 99% capture. This high capture rate, relatively to the normal 90% capture rate, was chosen to more fairly compare the technologies in question, as some technologies benefit more from lower capture efficiencies than others. With this basis, the energetic costs can scale linearly with the capture rate chosen, and the results of the chapter can be easily adjusted to differing capture rates. However, it should be noted that capital costs do not scale linearly with the capture rate. As will be shown in the chapter, even at these high capture rates, a low energy cost path exists with the use of effective plant heat integration. The findings discussed herein are not the result of a rigorous process design, but rather, a high-level approach that considers the primary energy requirements (and to some extent the secondary energy requirements) that more transparently reveal the potential for low-cost CO_2 capture. Throughout the chapter, the parasitic load of each CO_2 capture system is used as a means of comparison, which is defined as

$$\%Parasitic = \frac{\left(\frac{\text{GJ consumed, by capture}}{\text{tonne of } CO_2 \text{ captured}}\right)}{\left(\frac{\text{GJ generated, plant, no capture}}{\text{tonne of } CO_2 \text{ released (no capture)}}\right)} \quad \textbf{(3)}$$

This metric is used in favor of the more common *levelized cost of electricity* (LCOE)[6,7], due to the ease of determining the energetic parasitic load (a major focus of the chapter), whereas the LCOE requires full process descriptions, which as indicated above, can distract from the high-level energetic analysis presented herein. Throughout the chapter, the energy consumed by the capture process (in GJ/tonne) is thermal energy, not electrical energy.

4.3.1 Comparisons of CO_2 Capture Technologies without Heat Integration

4.3.1.1 Intrinsic Heats

Drawing comparisons between different CO_2 capture technologies that rely on different mechanisms of capture can be difficult due to process configuration, heat integration strategies, differing CO_2 recoveries and feed basis, among many other factors. A useful starting metric for comparing CO_2 capture processes is the thermodynamic cost associated with the CO_2 capture mechanism. In the absence of heat integration strategies (discussed later), these thermodynamic costs are usually expressed as heats that the CO_2 capture system must process and pay for.

4.3.1.2 Solid Sorbent Systems

In the case of solid adsorbent systems, such as packed beds (Figure 4.2) and fiber sorbents, the intrinsic cost of the system is related to the heat released during adsorption and the heat required for desorption. For physical adsorption (often referred to as

"physisorption") cases, such as adsorption by zeolites[8], the mechanism for CO_2 capture can be visualized in Scheme 1,

Scheme 1:

$$CO_2 + Surface \Leftrightarrow (CO_2)\cdot(Surface)$$

where the CO_2 is weakly attracted to the zeolite surface due to various effects—typically induced dipole attractions. Heats of reaction are generally in the 25–50 kJ/mole range for the physisorption cases.

Zeolite 13X is often used as a standard in terms of CO_2 capture due to its high CO_2 sorption capacity in the region of interest for post-combustion CO_2 recovery (~0.1atm of CO_2)[9]. Unfortunately, flue gas feeds are often nearly saturated with water, which preferentially adsorbs over CO_2[10,11]. This precludes the use of 13X in post-combustion CO_2 recovery situations, unless the flue gas is dehydrated, or the 13X is modified sufficiently so that it can operate effectively in the presence of a water saturated feed. In this chapter, the costs of dehydration of the flue gas are not considered. It is reasonable to assume that a single guard bed for removing flue gas water could be included into the CO_2 capture process, resulting in no more than two times the cost, as the guard-bed could be imagined as capital and energetically redundant. While this option is possible, there have been reports of flue gas dehydration using high vapor flux membranes (with low CO_2/N_2 gas flux)[12], allowing for lower dehydration costs when compared to an adsorbing guard bed (which must be regenerated).

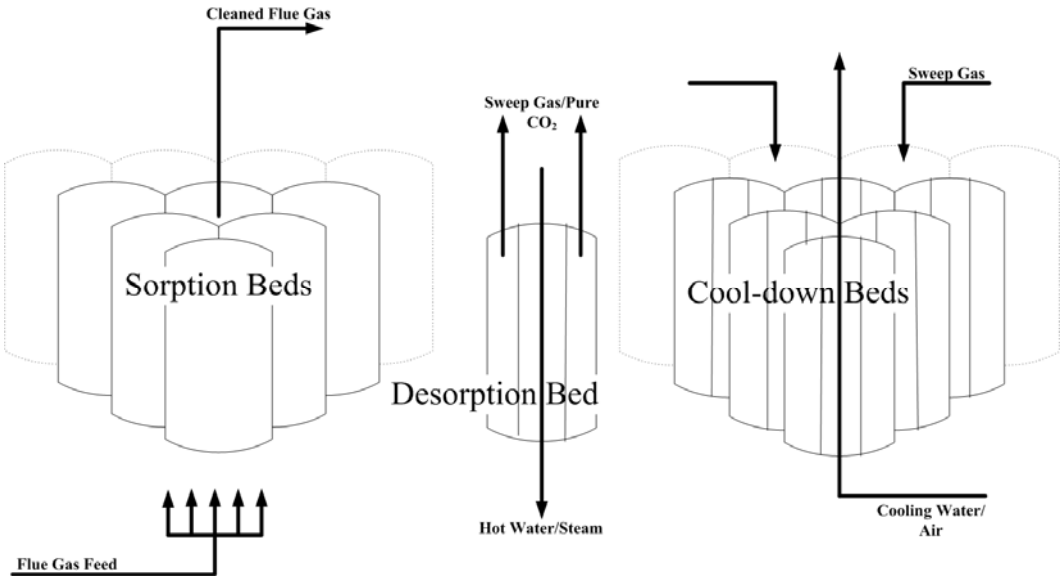

Figure 4.2: Solid sorbent packed bed system in thermal swing mode. Many beds are used in the sorption step to reduce pressure drop costs while one bed is desorbing using hot purges or hot water in heating jacket or heating tube. The beds not desorbing are either queued to desorb, or are finished desorbing and are being cooled by an inert purge or a cooling jacket.

A newly developed field in the solid adsorbent literature is solid supported amines, where amine groups are typically covalently bound to the surface of a mesoporous silica[10], viz.

Scheme 2:

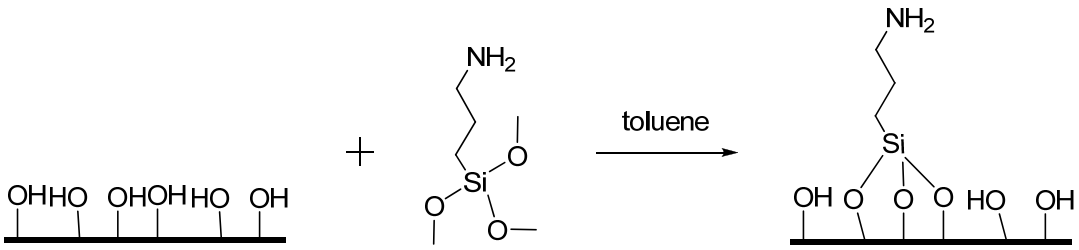

These sorbents offer a distinct advantage in terms of flue gas capture due to the amine-water-carbon dioxide reaction to form bicarbonates, effectively allowing the sorbent to operate in humid feeds, as illustrated by:

Scheme 3:

$$2 \cdot (R - NH_2) + CO_2 \Leftrightarrow (R - NHCO_2)^- (R - NH_3)^+, \textit{carbamate}$$
$$R - NH_2 + CO_2 \Leftrightarrow (R - NH_3)^+ (HCO_3)^-, \textit{bicarbonate}$$

Furthermore, these amines have high selectivity for CO_2 over nitrogen[13], but at a penalty of a higher thermodynamic cost than physical adsorption; more heat is released from the chemical reaction between CO_2 and the amines, which is often referred to as a chemical adsorption (or "chemisorption"). Heats of reaction for this case are in the range 60-90 kJ/mole. Finally, SO_x and NO_x have been shown to bind irreversibly to most amine groups[14]. This implies that extra stages of flue gas desulfurization will be needed, increasing the costs of using amine-based separation (chilled ammonia and liquid amines included). These costs are not included here, though an increase of 20-50% over the presented costs can be used as an estimate for the total system costs including additional desulfurization[15].

4.3.1.3 Membrane Systems

The main intrinsic energy penalty associated with the use of membranes for CO_2 separation and capture is related to the pressure ratio across the membrane (Figure 4.3).

Favre has determined the optimum membrane/pump configuration to be "as-received" flue gas on the feed side, and a vacuum pump on the downstream side[16]. This bypasses the need to compress the excess nitrogen present in the flue gas by only doing work on the product, thereby minimizing the membrane process energy requirements. In this analysis, an overall pressure ratio ($p_{feed}/p_{permeate}$) across the membrane of 10 is assumed, based on the analysis by Favre[16]. This analysis uses a membrane CO_2/N_2 selectivity of 120 and a CO_2 recovery factor of 80%. The more recent work by Merkel et al[22] in 2009, however, using multi-stage membrane processes shows that membranes have the potential to be a competitive CO_2 capture technique (on an energy consumption basis) within a specific set of constraints that are not considered here.

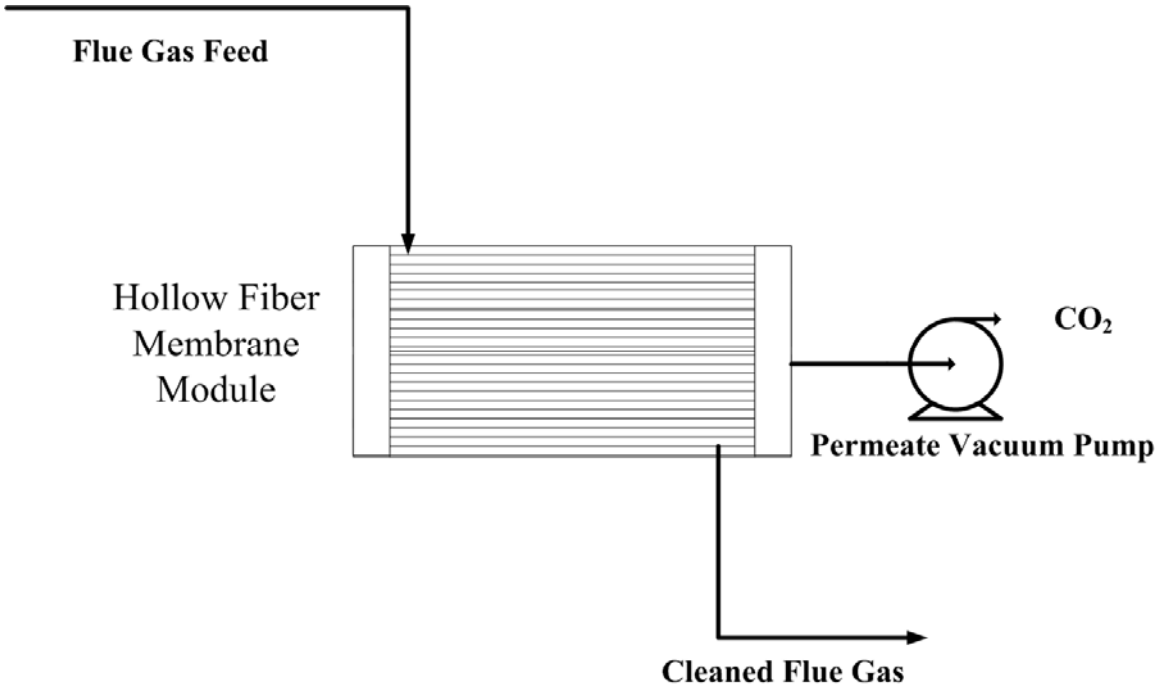

Figure 4.3: Hollow fiber membrane module in vacuum pump arrangement to minimize energetic costs. Flue gas is swept across the shell side of the fibers (to minimize compression costs required to force such large quantities of flue gas through the bores of the fibers), while vacuum is pulled on the bore side to supply the necessary compression ratio across the membrane.

4.3.1.4 Liquid Amine Systems

In the case of the liquid amines (Figure 4.4) there are two thermodynamic costs intrinsically associated with capturing CO_2. The first is the heat of reaction of the CO_2 and amines (similar to that of the solid supported amines). The second is that in order for the reaction to reverse, the amine solution (typically monoethanolamine—MEA—and water), needs to be heated to 100-115°C, which releases the CO_2. Due to the high temperature, the solvent carrying the amines partially evaporates. This solvent vaporization requires extra heat input during the reaction reversal phase, while not contributing to the actual reaction reversal. In this analysis, 5% of the water in the MEA/water solution (30wt% MEA) is assumed to evaporate in the desorption step[17,18], though this number can vary depending on MEA concentration, solvent flowrate, stripper pressure and temperature, and CO_2 loading.

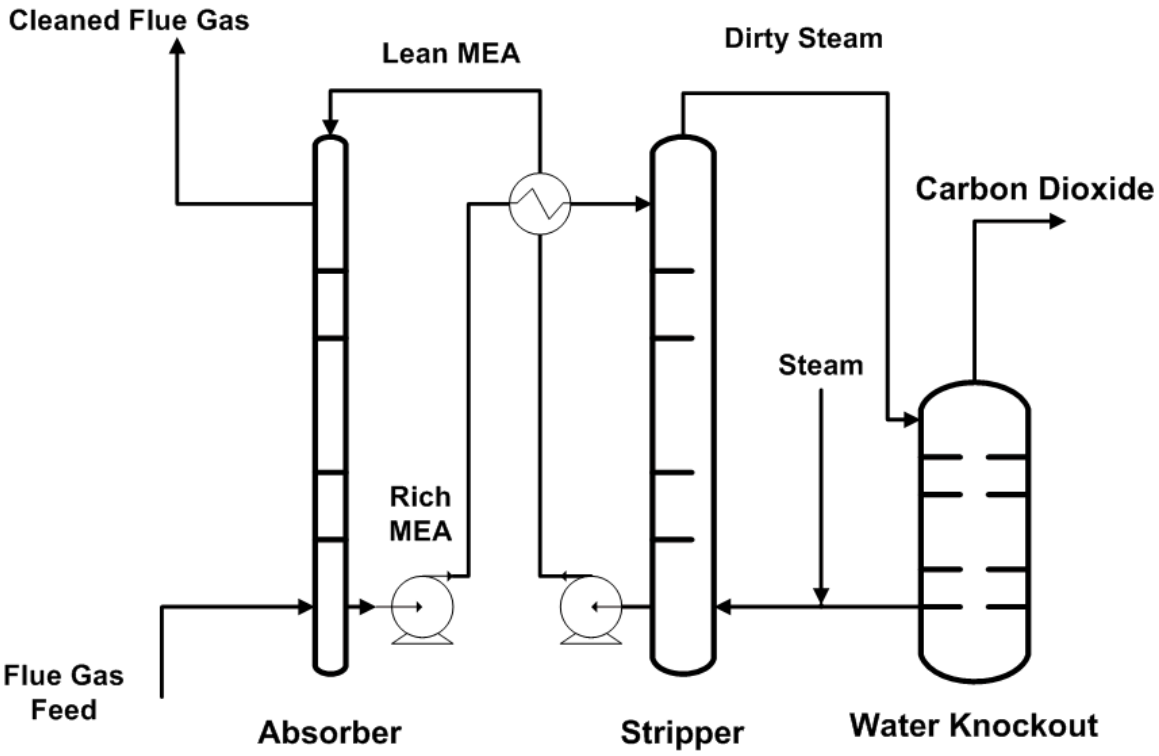

Figure 4.4: Liquid amine stripping based off of monoethanolamine (MEA) and water. CO_2 containing flue gas is bubbled through the absorber while the MEA solution flows downwards, chemically binding to the CO_2. The CO_2 containing MEA solution ("Rich MEA") is heat exchanged with a hot CO_2-absent MEA solution ("Lean MEA") and sent to a stripping column. Steam is supplied to the stripping column to supply the heat of desorption and removes the CO_2 from the MEA. The CO_2 is then separated from the steam in a flash drum.

4.3.1.5 Chilled Ammonia Systems

The final comparison case is chilled aqueous ammonia CO_2 absorption (often referred to as "chilled ammonia") (Figure 4.5). Determination of the intrinsic heat associated with this process requires correct identification of the chemical reactions taking place and their associated thermodynamics. In our analysis, we consider two absorber feed cases: 1) aqueous ammonia, with Scheme 4 being dominant, and 2), a slurry of ammonium carbonate and bicarbonate with Scheme 5 being dominant.

Scheme 4:

$$2 \cdot NH_{3,(aq)} + H_2O + CO_{2,(g)} \Leftrightarrow (NH_4)_2 CO_{3,(aq)}$$

$$NH_{3,(aq)} + H_2O + CO_{2,(g)} \Leftrightarrow NH_4HCO_{3,(aq)}$$

Scheme 5:

$$CO_{2,(g)} + H_2O + (NH_4)_2 CO_{3,(aq)} \Leftrightarrow 2 \cdot NH_4HCO_{3,(aq)}$$

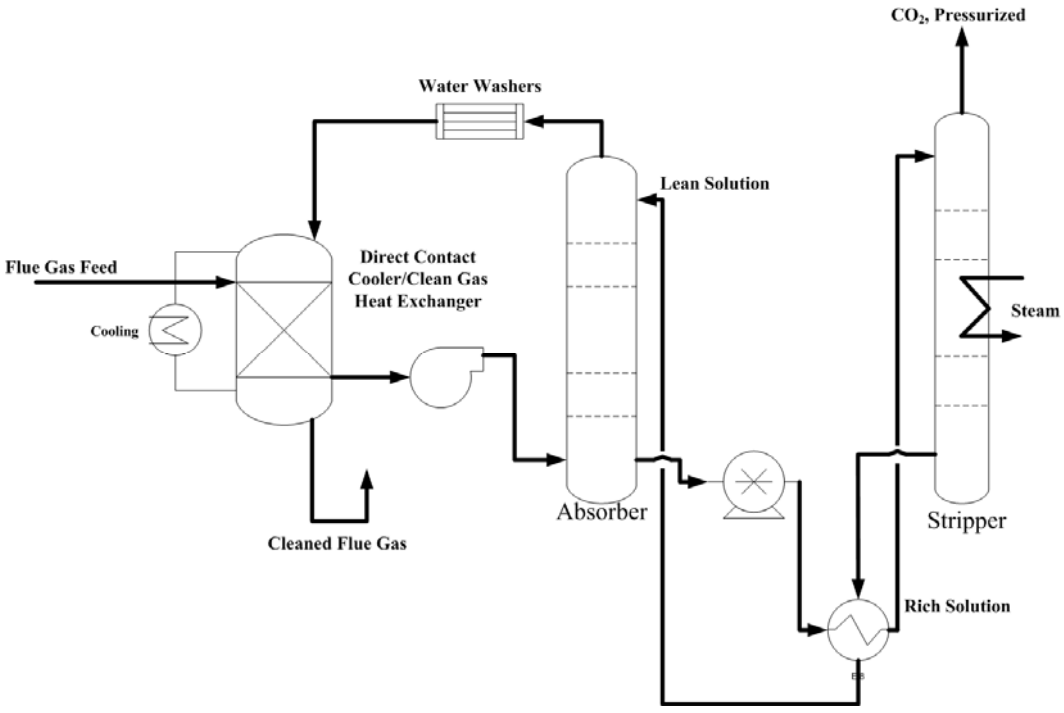

Figure 4.5: Chilled ammonia CO_2 capture system. Flue gas is chilled using direct contact chillers down to the sorption conditions. It is then bubbled through an absorption column while either aqueous ammonia or slurried ammonia (in water) is flowed from the top. The rich ammonia stream is heat exchanged with the lean ammonia stream, pressurized, and sent to a stripping column where the CO_2 is removed. The cleaned flue gas is washed with several water towers to remove any ammonia slippage that may have occurred during the sorption step.

Within the chilled ammonia literature, there is considerable debate as to which mechanism is correct[19,20,21]; the implications can readily be seen in Figure 4.6 in terms of the intrinsic heat penalties due to the differences in heat of reaction and heat of formation of ammonia/CO_2 and ammonium carbonate/bicarbonate, respectively.

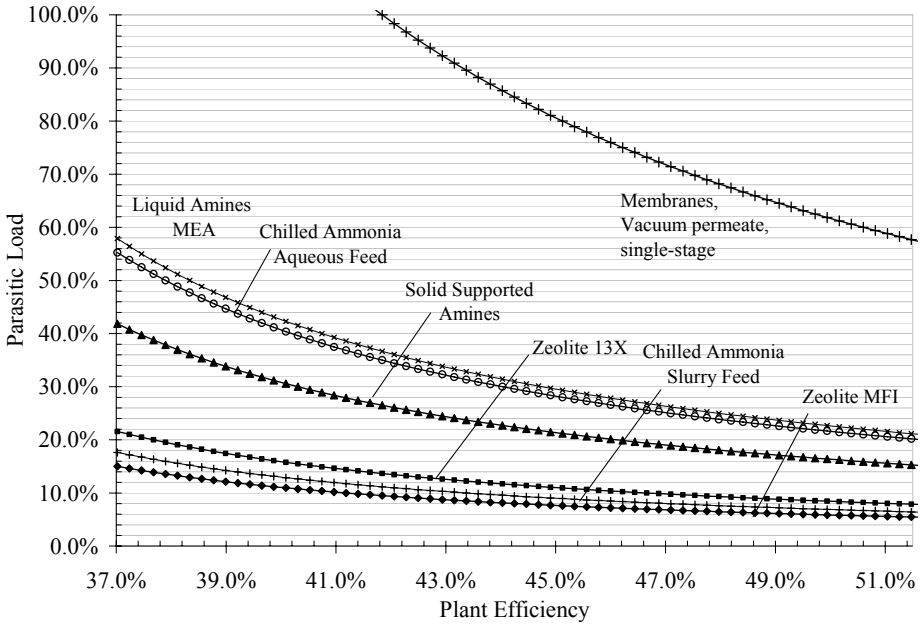

Figure 4.6: Parasitic loads of the various CO_2 capture technologies with intrinsic energy penalties considered only. Plant efficiencies on the abscissa represent the original plant efficiencies before any CO_2 capture equipment is installed.

Table 4.2: Intrinsic energy penalties associated with CO_2 capture technologies

Process	Description of Intrinsic Heat	Energy Penalty of Intrinsic Heat (kJ/mol of CO_2)	Minimum Cost of CO_2 Capture (GJ/tonne of CO_2 captured)
Fiber Sorbents	*Heat of Sorption of the Solids*	36, Zeolite 13X	0.82
		25, Zeolite MFI	0.57
		70, Solid Supported Amines	1.59
Packed Bed	*Heat of Sorption of the Solids*	36, Zeolite 13X	0.82
		25, Zeolite MFI	0.57
		70, Solid Supported Amines	1.59
Single Stage Membrane	*Compression Ratio Across the Membrane*	--	6.00
Liquid Amines	*Heat of Reaction*	70	1.59
	Heat of Vaporization of Solvent	55	0.61
Chilled Ammonia, Aqueous	*Heat of Reaction*	92	2.1
Chilled Ammonia, Slurry	*Heat of Formation*	29	0.67

4.3.1.6 Intrinsic Heat Comparisons

Table 4.2 lists the intrinsic penalties associated with each of the processes in consideration, along with the "minimum energy penalties" in GJ (consumed) per tonne of CO_2 (captured). As will be discussed later, these "minimum" energy penalties can in fact be reduced considerably with efficient heat integration strategies. The choice of GJ per tonne of CO_2 is a useful unit to compare differing technologies for several reasons. First, it sidesteps economic discussions and focuses on the actual process performance. Secondly, it allows the parasitic load of these processes to be computed for any base plant (as seen in Figure 4.6) since a plant performance can be easily couched in terms of GJ (generated) per tonne of CO_2 (released). The plant efficiencies used in Figure 4.6 represent the range of coal fired power plants from conventional generation to advanced generation without CO_2 capture. Plant steam is usually supplied to the process to provide the heat for CO_2 desorption. Figure 4.6 shows that in terms of intrinsic energy penalties, physisorption processes have the potential to be the lowest energy consumers, while chilled ammonia in slurry mode, with the low heat of formation penalties, has the potential to be quite competitive. On the other hand, in the fully aqueous chilled ammonia feed stream, the process is still favorable over an aqueous MEA system but more energy intensive than the solid sorbent physisorption and chemisorption processes. Membrane processes, in the single stage configuration, due to the compression ratio across the membrane and the large amounts of gas being handled, are not competitive—or even possible—in a post-combustion CO_2 capture scenario, as they consume more energy than the plant produces. Recently, Merkel et. al[22], published a method for using

high-flux membranes in a multi-stage apparatus that can significantly drive down costs in comparison to the single-stage process. This analysis is not considered here, though the final parasitic load the authors report is compared to the technologies in this chapter (Table 4.7).

4.3.2 Auxiliary Energy Penalties

The intrinsic heats listed above give a general starting point for process comparisons. However, there are many auxiliary or "non-intrinsic" penalties associated with each process that must be considered for a complete comparison. These auxiliary penalties are necessary for the process to run, but represent areas in which process optimization, heat recovery, and breakthrough technologies can bring costs down. Auxiliary penalties are unit operations such as draft fans, cooling towers and refrigeration systems, which are mainly considered to be the most significant energy penalties that are not directly associated with the intrinsic penalties. Later discussion of heat recovery and heat integration will illustrate the possibility of mitigating some of these auxiliary penalties, but they are first identified here for clarity.

4.3.2.1 Fiber Sorbent Systems, Auxiliary Penalties

The fiber sorbent system has several auxiliary energy penalties associated with it: cooling water for maintaining isothermal operation during the sorption step, draft fans

required to push the flue gas through the fiber bed, and finally heating and cooling water to raise and lower the temperature of the fibers between the sorption and desorption steps.

The first auxiliary energy is the cooling water used to maintain isothermal operation during the sorption step. This cooling water accepts the heat of sorption released during the exothermic reaction between the sorbent and sorbate. The amount of cooling required is directly related to the heat of sorption released, that is, zeolite high-silica MFI ($\Delta H \sim 25$ kJ/mol) will have the lowest cooling water duty, whereas solid-supported amines ($\Delta H \sim 75$ kJ/mol) will have the highest cooling water duty. There are two non-heat integrated ways to return this cooling water to the proper temperature after the cooling step: cooling towers or reservoir cooling. The cooling water is assumed to be fed to the fibers at 25°C, and over the length travelled through the fiber (6m), is assumed to warm to 35°C. An optimization problem exists in tuning the "level of isothermality" (as in, how much fiber temperature drift is acceptable) desired versus the cooling water flow rates (i.e., if thermal drift in the fibers is acceptable, then lower cooling water flow rates can be used, thereby reducing costs). We will not consider that optimization further here. The energy requirements for the cooling tower are assumed to be equivalent to the sensible heat change of the cooling water, and can be seen in Table 4.3, and approximately 20,000 kg of water are required per tonne of CO_2 captured. Reservoir cooling, on the other hand, simply refers to depositing the spent cooling water in a large body of water near the plant (most plants have a large reservoir of water nearby), and drawing the required cooling water from that same reservoir. In this way, the energy required to return the cooling water to the feed temperature can largely be removed from

the energy balance with the exception of water pumping and treatment (negligible compared to the costs of cooling). Since this option is not always possible, the case with and without reservoir cooling is considered here.

A second auxiliary energy penalty for the fiber sorbent beds is the use of a draft fan, or a combination of draft fans, to push the flue gas through the beds. The pressure drop through the bed is estimated using flow across tube banks pressure drop correlations[23], while the fan energy is estimated using a non-isothermal basis[24], where the increase in sensible heat of the flue gas due to compression is used to estimate the energy requirements of the fan (along with a 70% electrical efficiency). Fiber packing density and arrangement can readily affect the pressure drop across the bed; in this study a pressure drop across the bed of 0.1 atm is assumed—easily attainable in a fiber sorbent bed with low fiber packing density.

The final auxiliary penalty considered for the fiber sorbent case is the heating and cooling of the solids contained within the fiber sorbents. Without effective heat recovery between the heating and cooling steps, supplying the necessary change in sensible heat of the solids would render the fiber sorbent process non-competitive. A simple heat recovery strategy is to utilize a simulated counter-current flow through the bed (Figure 4.7a), where the cooling water flowing through the hot bed is heated towards the temperature required to heat the cold bed, and vice versa (Figure 4.7b). The water carrying the sensible heat away from the fibers progresses through the bed in a moving temperature front—the sharpness of the front determines the amount of sensible heat that

can be recovered in this fashion. Once the moving front breaks through the bed, the heating/cooling step ends and the desorption/sorption step begins. Since perfect recovery of the sensible heats is impossible, a small booster on either side of the cycle must be used—using these small boosters rather than large cooling towers or heaters significantly drives down the overall energy penalty. Due to the thin walls of the fiber sorbents, a $\Delta T_{approach}$ of 1°C between the fiber sorbent temperature and the cooling/heating fluid temperature is assumed[25]. Finally, for a given swing capacity (that is, the difference between the sorption capacity at T_{cold} and the sorption capacity T_{hot}), different swing temperatures are required for each sorbent depending on the heat of sorption. As heat of sorption increases, the temperature dependence of the swing capacity decreases, implying that MFI will have the highest sensible heat duty and solid-supported amines will have the lowest sensible heat duty—directly opposite of the cooling water duties listed above. In this study, the 13X fiber temperatures alternate between 100°C and 35°C, the MFI fibers alternate between 135°C and 35°C, and the solid-supported amine fibers alternate between 75°C and 35°C.

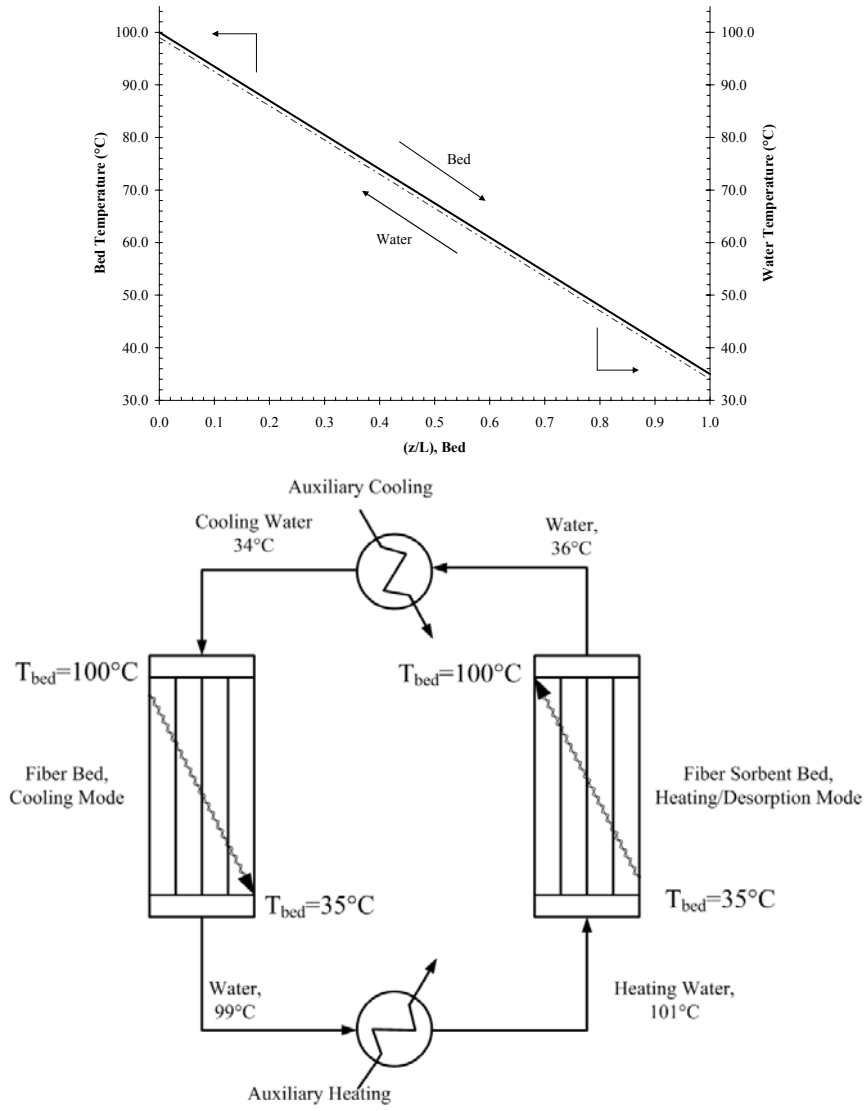

Figure 4.7: ***(a, top)*** **Pseudo-counter-current heat recovery strategy for fiber sorbents using 1°C $\Delta T_{approach}$. The thin walls of the fiber sorbents allow for very rapid heat transfer, creating a sharp "thermal wave" moving through the bed, allowing the counter-current configuration to be assumed.** ***(b, bottom)*** **Process configuration using a water cycle through the beds, where most of the sensible heat of one bed is transferred to the other, while the difference is supplied by "polishing" heaters or coolers.**

4.3.2.2 Packed Bed Sorption Systems, Auxiliary Penalties

In terms of intrinsic energies, solid sorbents in fiber sorbent form and packed bed form were equivalent; however, the auxiliary costs incurred by the packed bed

configuration make it much more energy intensive than the fiber sorbent configuration. Similar to the fiber sorbents, the packed bed configuration includes the auxiliary costs of draft fans and heating and cooling of the solids.

The first auxiliary energy penalty associated with the packed bed configuration is the one most often mentioned as a "show-stopper" for the technology: the cost of pushing the enormous quantities of flue gas through the bed. When considering packed beds for post-combustion CO_2 capture, two routes are possible: employ many duplicate beds to reduce overall flue gas pressure drop, or employ the required number of beds (based on heating and cooling times) at a high pressure drop. In this analysis, the low pressure drop route is used in order to minimize energy costs (while increasing capital costs—not considered in this chapter). In particular, we assume a maximum pressure drop of 69 kPa across a bed with 70vol% packing that is 3.0m tall and 6.1m in diameter. As mentioned above, this route requires many extra beds to keep the pressure drop down. Pressure drop across the bed can also be minimized by decreasing the filling fraction within the bed. However, decreasing the filling fraction also decreases the capacity of the bed, which in turn requires more beds; a full parametric study would be required to find the optimum between capital expenditures and operating costs, and we only consider the low operating cost route here. The number of beds required during the sorption step is approximately 30. With a non-isothermal fan approach similar to the fiber sorbent case, the total energy requirement of the fan can be estimated. As can be seen in Table 4.3, the fiber sorbent bed configuration allows for an order of magnitude in energy savings over a conventional packed bed configuration due to reduction in the flue gas draft fan duty.

Determining the sensible heat requirements for heating and cooling the packed bed system is essentially an optimization problem between operating costs and capital costs. To minimize operating costs, many excess beds are required so that the rate of heating and cooling the beds can be lowered; this system can be described as an out-of-phase system (that is, the length of the sorption step is not equivalent to the length of the heating or cooling step and excess beds are required to make up for this). The only limiting factor in the out-of-phase system is the total footprint required and the amount of capital to be invested into the system. On the other hand, the system can be designed as an in-phase system, where the sorption step is equal in length to the cooling and heating steps. This scheme requires the maximum heating and cooling rates possible. Despite this limitation, the in-phase scheme requires the fewest number of beds. In this analysis, with 30 beds already being needed for the sorption step alone for a conventional packed bed process, the in-phase scheme was chosen so that the number of beds was kept to a (relative) minimum of 90 beds. The same sensible heat recovery strategy used in the fiber sorbent case is also employed in the packed bed analysis, albeit with a 5°C $\Delta T_{approach}$, which is typical of traditional heat transfer equipment[23] and is illustrated in Figure 4.8. As can be seen in Table 4.3, the heating and cooling of the solids (with the in-phase scheme) is an enormous energy penalty for the packed bed system.

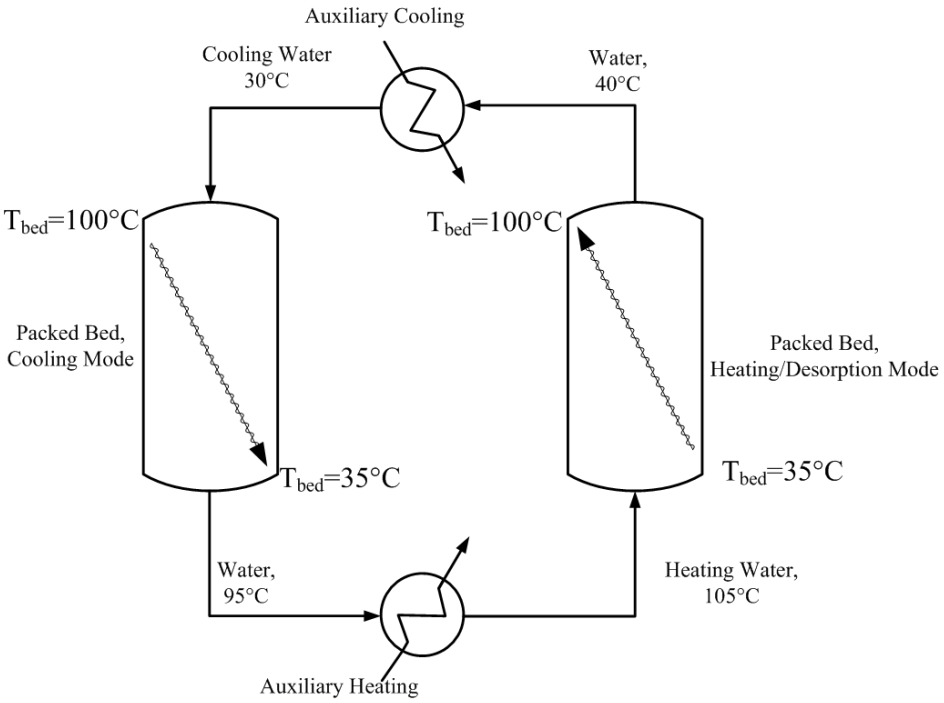

Figure 4.8: Sensible heat recovery strategy in solid sorbent packed beds.

4.3.2.3 Liquid Amine Systems, Auxiliary Penalties

Liquid absorption systems, unlike solid absorption systems, have the majority of the energy penalties contained within the intrinsic heats listed above. For MEA-based liquid absorption systems, the main auxiliary energies are the power for draft fan required to feed the flue gas through the absorber and stripper towers, and the heating and cooling of the amine solutions to the sorption and desorption temperatures. Following the DOE Baseline Report[26], an appropriate pressure drop across each tower is approximately 1.0 psi; the same methods as mentioned above are used to estimate the draft fan duty. Heating and cooling requirements for the amine solutions can largely be recovered in heat exchange between the rich and lean streams as seen in Figure 4.4. A $\Delta T_{approach}$ of

5°C is assumed in this study, as is typical in traditional heat transfer equipment[23]. As can be seen in comparison between Figures 4.6 and 4.9, most of the energetic costs of the MEA-based absorption process are attributable to the high heat of reaction between MEA and CO_2 and the vaporization of water during the desorption process (5% basis).

4.3.2.4 Chilled Ammonia Systems, Auxiliary Penalties

Chilled ammonia, on the other hand, incurs an additional auxiliary cost associated with the cooling of the flue gas down to the sorption conditions—typically 0°C-10°C is used. The draft fan duty for the chilled ammonia system is similar to the MEA-based system, though it will likely have less draft fan duties due to the higher sorption capacities of the chilled ammonia[21] thereby reducing the required column height. In similar fashion, the sensible heat duties for the chilled ammonia process are lower than those of the MEA-based system. Cooling the flue gas down to the sorption conditions requires the use of direct contact chillers[21], usually paired with some heat recovery from the cleaned flue gas (see Figure 4.5). In this study, the flue gas is assumed to be coming into the CO_2 capture system at 50°C, and cooled to 0°C, and leaves the absorber at 10°C, as based on the report by Alstom[20,21]. The sensible heat contained by the cleaned flue gas allows for an upper limit of 30% heat recovery via this method, though it should be noted that if the flue gas is completely cooled to ambient temperatures before the CO_2 capture system, the duties for the direct contact chillers decrease significantly and the heat recovery percentages can increase (within the limits of heat exchange).

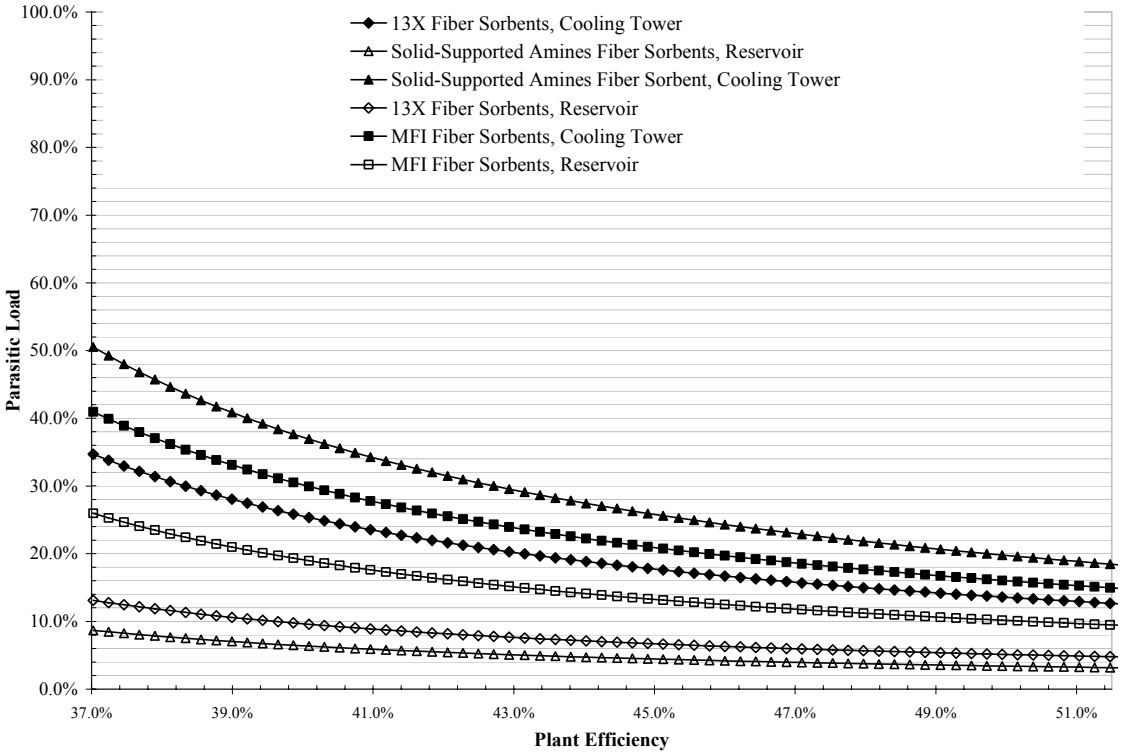

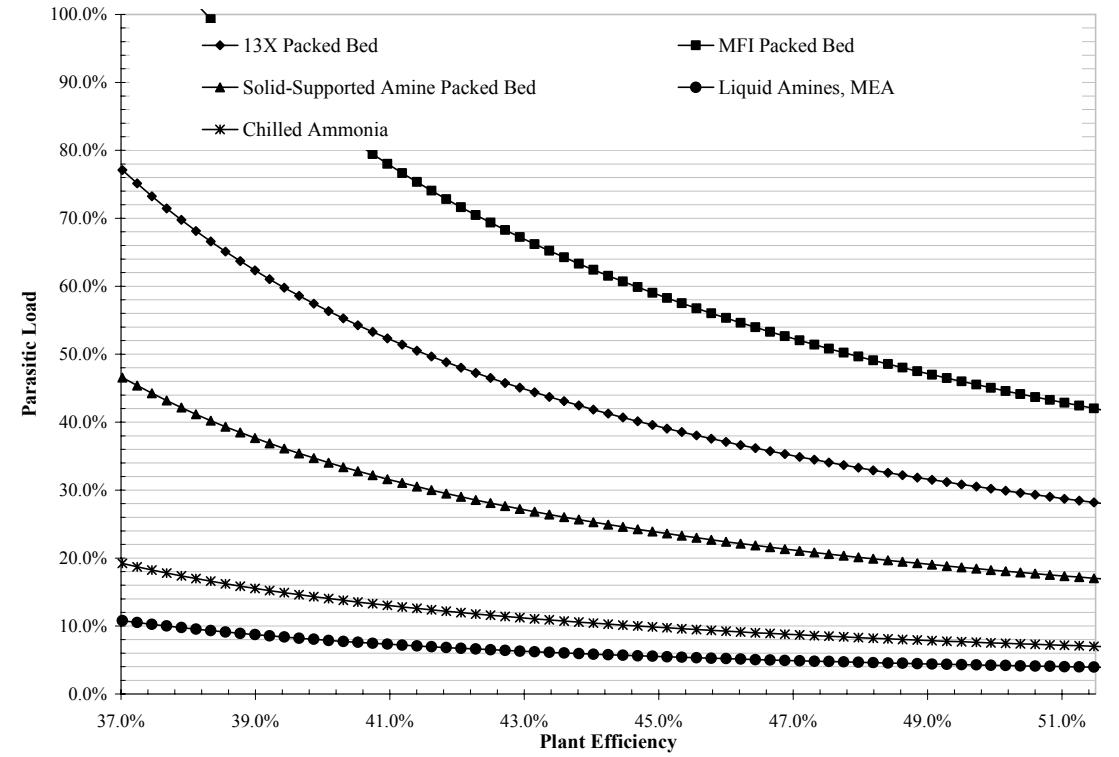

Figure 4.9: Parasitic loads as a result of auxiliary energy penalties of the various CO_2 capture systems. Figure split for convenience.

Table 4.3: Auxiliary Energy Penalties associated with CO_2 capture technologies

Process	Description of Auxiliary Energy	Cost of CO_2 Capture (GJ/tonne of CO_2 captured)
Fiber Sorbents	*Draft Fan*	0.11
	Cooling Water	0.82, Zeolite 13X
		0.57, Zeolite MFI
		1.59, Solid-Supported Amines
		0, Reservoir
	Sensible Heat	0.39, Zeolite 13X
		0.88, Zeolite MFI
		0.22, Solid-Supported Amines
Packed Bed	*Draft Fan*	0.65
	Sensible Heat	2.23, Zeolite 13X
		3.72, Zeolite MFI
		1.12, Solid-Supported Amines
Liquid Amines	*Draft Fan*	0.07
	Sensible Heat	0.34
Chilled Ammonia	*Cooling of flue gas*	0.41
	Draft Fan	0.05
	Sensible Heat	0.27

4.3.2.5 Compression Systems

Another key process variable (considered to be an auxiliary penalty) that can make or break a post-combustion CO_2 capture process is the CO_2 recovery pressure. The costs of compression can be described viz.[24],

$$\frac{T_{Out}}{T_{In}} = \left(\frac{P_{out}}{P_{In}}\right)^{1-1/\gamma_{CO2}}$$
$$W_{required} = \frac{\dot{m}_{CO2} C_{P,CO2} \left(T_{Out} - T_{In}\right)}{\eta_{compressor}} \quad \textbf{(4)}$$

and it can easily be seen that the costs scale exponentially with the CO_2 recovery pressure (the CO_2 compression pressure is constant). Typically, the CO_2 compression is performed in a five-stage, intercooled compression train, with each compressor decreasing significantly in cost from the first.

Table 4.4: CO_2 recovery pressures and costs of CO_2 compression for CO_2 capture

Process	CO_2 Recovery Pressure (bar)	Cost of CO_2 Compression (GJ/tonne of CO_2 captured)
Fiber Sorbents	1.0	0.750
Packed Bed	1.0	0.750
Membranes	1.0	0.750
Liquid Amines	1.5	0.661
Chilled Ammonia	20.0	0.207

Table 4.4 lists CO_2 recovery pressures typically expected in each of the processes considered. Solid adsorbent systems, including fiber sorbents, are engineered so that a "wave" of pure or near-pure CO_2 is captured during the desorption step, while the dilute CO_2 is used as purge stream elsewhere in the system. Membrane systems will recover

CO_2 between 0.1-1.0 bar, depending on vacuum pump type (for instance, a steam ejector will recover the CO_2 at 0.1 bar, but a mechanical pump will discharge the CO_2 from the pump at atmospheric conditions). In the case of liquid absorption systems, the desorption pressure is a function of CO_2 loading and temperature[27]; typically CO_2 is assumed to be recovered between 1.0-1.5 bar for MEA systems (1.5 bar in this study), and 10-20 bar for chilled ammonia systems (20 bar in this study). In the absence of any interstage heat recovery, the high pressures attainable by chilled ammonia give it a distinct energetic advantage over any other sorption process. Figure 4.10 shows the parasitic loads for compression for each CO_2 capture process.

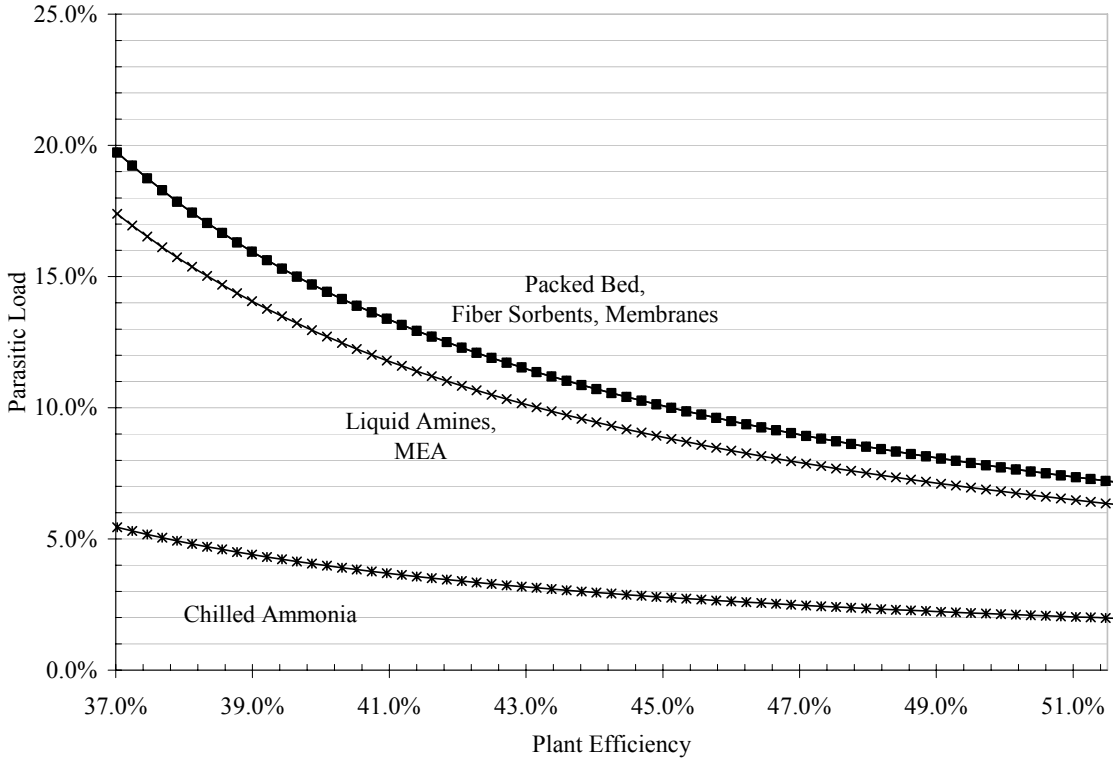

Figure 4.10: Parasitic loads incurred as a result of CO_2 compression for the various CO_2 capture technologies.

4.3.3 Total Parasitic Load without Heat Integration

With the intrinsic energy penalties, auxiliary energy penalties and the costs of compression considered, an overall high-level picture of post-combustion CO_2 capture can be derived (Figure 4.11). As established by the intrinsic energy penalties, it can easily be seen that membranes in a single-stage configuration, even the high performance membranes used in this analysis, are outside of the practical realm for post-combustion CO_2 capture, though it has shown in the literature that at CO_2 concentrations higher than 10 mol%, membranes can become quite competitive[16]. In the same bracket as membranes is the packed bed solid sorption process. The packed bed systems are considered non-competitive by high auxiliary costs resulting from the large amount of solids required and the fans required to push the flue gas through the bed. The MEA-based liquid absorption process, due mainly to high heats of sorption and the loss of water during the desorption step, is quite energetically taxing, especially to lower efficiency plants. This result is well-known[28,29,30], and often serves as the motivation for developing new liquid-based absorbents, such as those by Rochelle et. al[31], which can desorb at lower temperatures or higher pressures, thereby avoiding the excess heat lost to water vaporization. Chilled ammonia, depending on the type of feed possible in realistic situations, has the potential to be the lowest energy user of any known CO_2 capture device. The two chilled ammonia cases represent the best possible case (complete slurry feed) and the perhaps the worst case (aqueous ammonia feed), with the real case likely existing somewhere in between and currently being deployed now[21]. A full slurry feed on the scales required for post-combustion CO_2 capture has yet to be proven in any

analogous industrial process to our knowledge. Finally, depending on which solid sorbent is used, and how the solids are cooled, the fiber sorbents have the potential to be a relatively low energy route comparable with chilled ammonia (slurry feed). In an absolute sense, however, every CO_2 capture route, *without* effective heat integration (next section), represents a significant energy parasite on the power plant, likely rendering all of the technologies marginally viable.

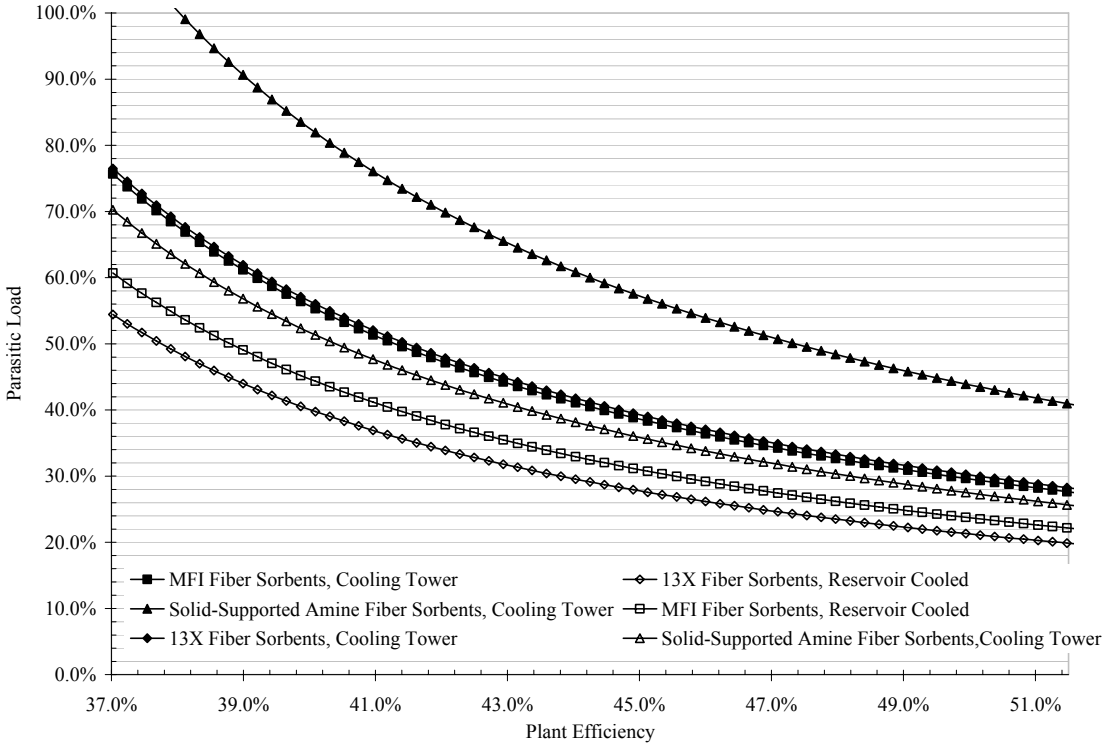

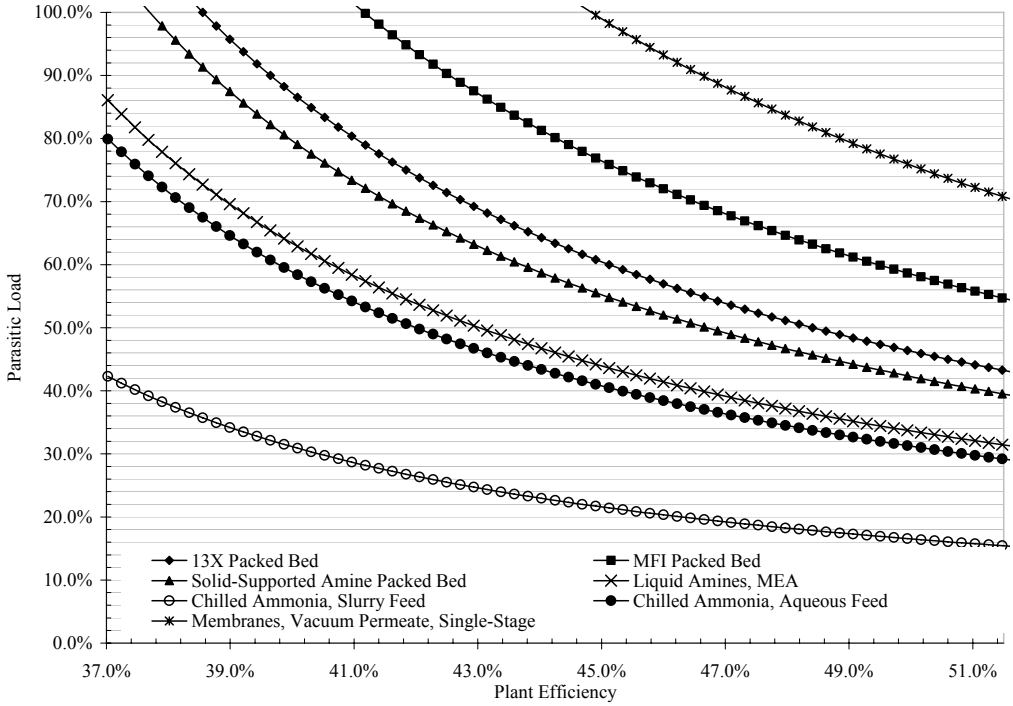

Figure 4.11: Overall parasitic loads incurred by the addition of a CO_2 capture system without the use of plant-wide heat integration. Figure includes intrinsic heats, auxiliary energy penalties, and heats of compression. CO_2 capture rate is 99% capture for all technologies with the exception of membranes, which use an 80% capture rate. Figure split for convenience.

4.3.4 Comparison of CO_2 Capture Technologies with Heat Integration

4.3.4.1 Heat Integration Overview

The previous section established a reference point to guide improvements in CO_2 capture technologies. One of the biggest improvements necessary is heat integration with the power plant. This chapter makes the distinction between heat *recovery* and heat *integration*; that is, heat recovery refers to a unit operation using all of the available heat contained within its own system, and heat integration is linking available heats in the entire plant to an add-on operation (i.e., CO_2 capture). Recovering the sensible heat of the solids or liquids as mentioned above can be considered an example of heat recovery. Figure 4.12 gives a conceptual overview of a CO_2 capture station that is integrated within a power station.

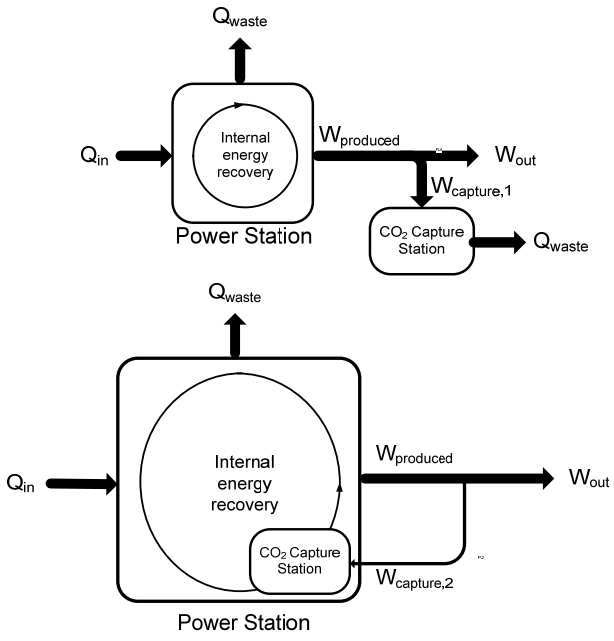

Figure 4.12: *(top)*, CO_2 capture without any effective heat integration with the host power station. *(bottom)* CO_2 capture station effectively integrated into the host power station, making $W_{capture,2}<W_{capture,1}$

4.3.4.2 Heat Integration, Feedwater Preheating

Figure 4.13 shows an overview of a sub-critical coal-fired power plant with plant streams color coded to show the available process heat (not used for generating electricity) at a reference of 25°C and 1.0 atm. For this particular process[26,32], it can be seen that the steam bleeds (from highest pressure to lowest pressure) have significant heating potential; furthermore, the feedwater exiting each of the feed heaters has substantial amounts of low grade heat. These preheaters serve to take the plant process water up from 45°C and 1.0 atm (after the cooling towers) to 220°C before entering the boiler by bleeding steam from different stages within the turbine. This is done to increase the overall efficiency of the plant. From a process perspective, the same effect can be achieved by transferring the heats of sorption and desorption incurred in the CO_2 capture process to the process water, thereby removing these "energy penalties," while maintaining the efficiency boost to the plant from the feedwater preheating. An earlier study by Gibbins and Crane[33] first mentioned the possibility of using the feedwater streams as cooling water to decrease the reflux condenser duties (sensible heat duties) in a liquid amine tower; however, to our knowledge, this is the first mention of directly integrating the feedwater heat exchange system into the sorption system, allowing for the capture of latent heat *and* sensible heat.

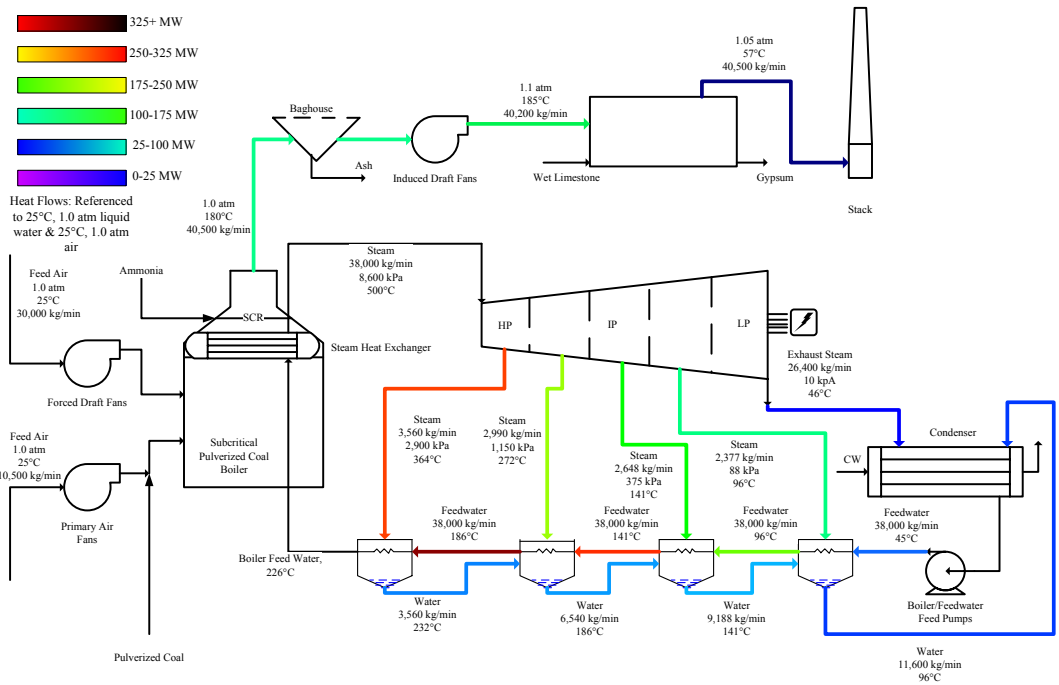

Figure 4.13: Overview of sub-critical pulverized coal power plant with non-essential (non-electricity generating) streams colored depending on the total heat flow contained within the stream referenced to 25°C and 1.0 atm.

In this study, the first two lower temperature feedwater heat exchangers are replaced by sorption equipment, as the remaining heat exchangers likely use process fluids that are too hot for any process (with the possible exception of packed bed sorbents). The steam bleed streams are used in the desorption process, condensed and taken down to 45°C water. The 45°C stream leaving the cooling towers is taken to 91°C, and 141°C water is taken to 45°C. Figure 4.14 gives a conceptual overview (eschewing the necessarily complex piping arrangement required to achieve the benefits) of how the feedwater preheaters may be effectively replaced by a multitude of fiber sorbent beds which transfer sensible and latent heats to and from the feedwater streams. These heats are applied equally to all of the CO_2 capture devices, though the fiber sorbents have the potential to utilize the heat most efficiently for several reasons. First, the fiber sorbents

heat exchange system is already directly integrated into the fibers, whereas the other technologies, notably liquid amines and chilled ammonia, would require new tower designs to allow the feedwater to flow through the absorber and stripper. Secondly, the micro-capillary nature of the fiber sorbents allows for much more effective heat transfer between the sorbents and the fluid in the bore[25]. Finally, the solid sorbents have much more need for additional sources of sensible heat, specifically in the range typically associated with the feedwater preheating train. Table 4.5 shows the total energy recoverable from a feedwater preheating strategy.

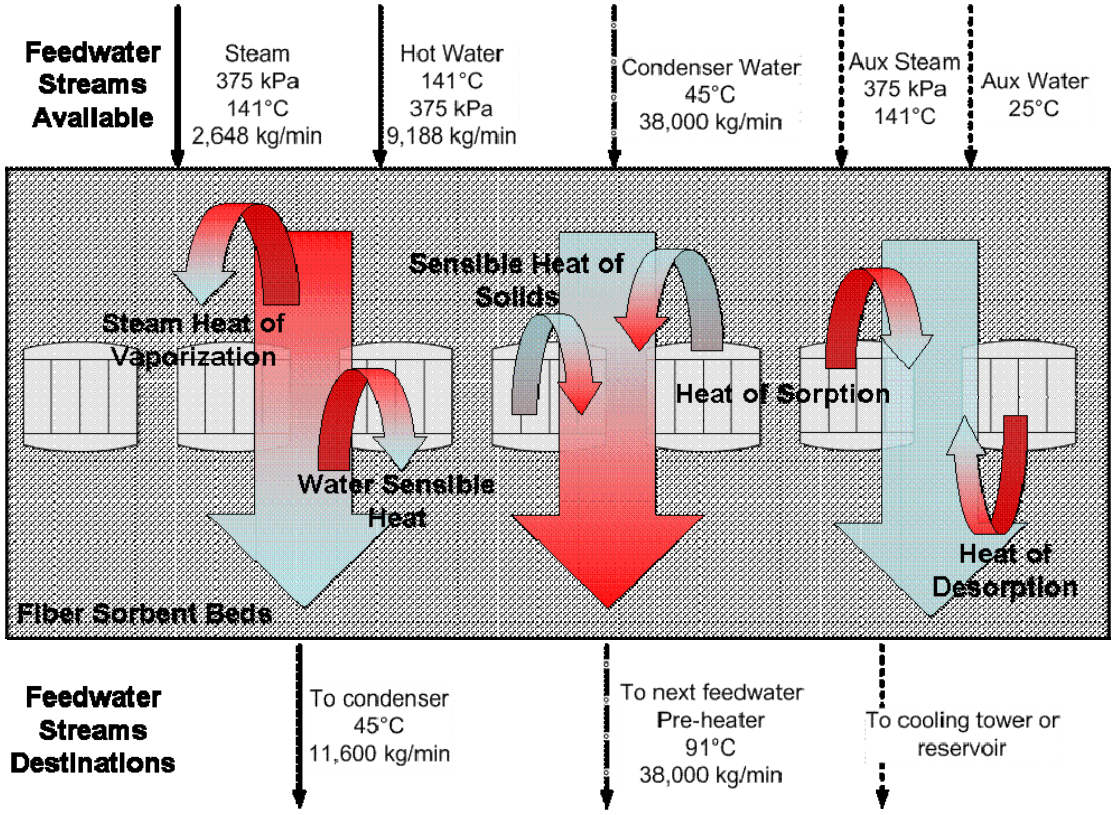

Figure 4.14: Conceptual overview of fiber sorbent bed heat integration into feedwater preheating system. The fiber sorbent beds replace the first two feedwater heat exchangers, effectively creating a system that has the potential to not only adsorb and desorb CO_2, but also achieve the desired heat exchange required for optimal plant efficiency.

4.3.4.3 Heat Integration, CO_2 Compression Intercoolers

As disclosed by Kelley et. al[34], it is possible to use the heat generated by the compression to raise the sensible heat of water, which can then be used elsewhere in the CO_2 capture system or the plant, as seen in Figure 4.15. In this analysis, a 10°C approach across the heat exchanger was considered as well as a worst-case 50°C approach (Table 4.5). The remaining interstage cooling is assumed to be completed using direct contact chillers, and is taken into account in the calculations. The heated process water is then sent to the sorption processes to aid in sensible heat needs. Again, all of the energy generated from this heat integration is credited equally to all processes considered here.

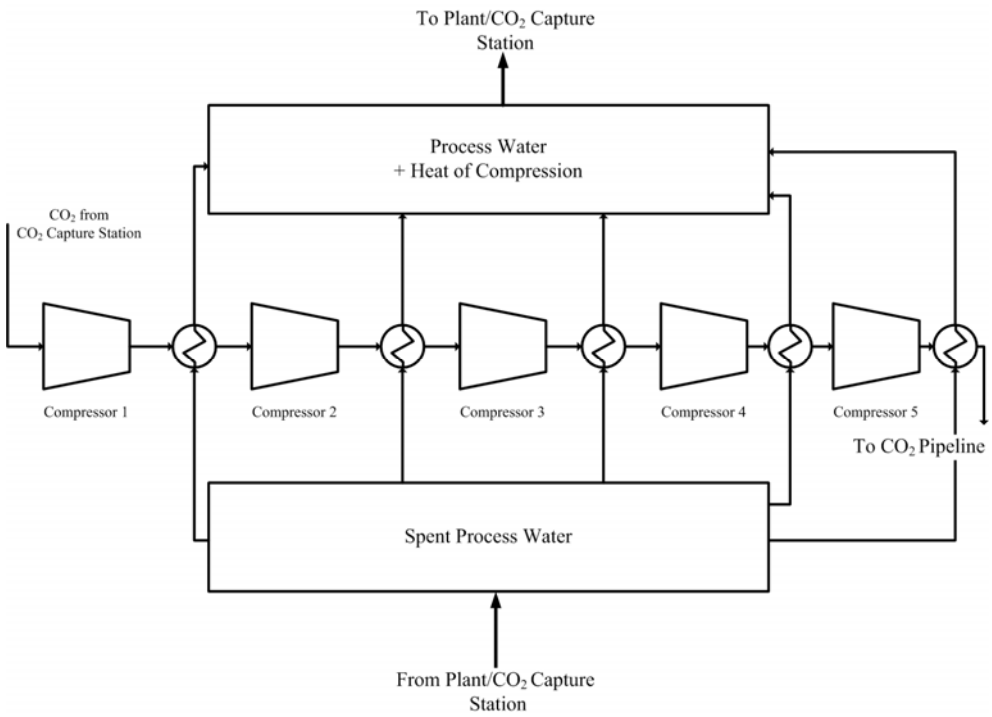

Figure 4.15: Heat integration strategy for recovering heat generated from CO_2 compression. The hot CO_2 is contacted with water in interstage intercoolers. This heated water is then transferred back to the plant or to the CO_2 capture system to aid in sensible heat needs.

Table 4.5: Possible recoverable heats for CO_2 compression heat integration strategy

Process	CO_2 Recovery Pressure (bar)	Cost of CO_2 Compression (GJ/tonne of CO_2 captured)	Possible Recoverable Heat in Interstage Cooling (GJ/tonne of CO_2 captured), 10°C Approach	Possible Recoverable Heat in Interstage Cooling (GJ/tonne of CO_2 captured), 50°C Approach
Fiber Sorbents	1.0	0.750	0.616	0.406
Packed Bed	1.0	0.750	0.616	0.406
Membranes	1.0	0.750	0.616	0.406
Liquid Amines	1.5	0.661	0.543	0.339
Chilled Ammonia	20.0	0.207	0.141	0.039

4.3.4.4 Effects of Heat Integration on CO_2 Capture Costs

Figure 4.16 (and Table 4.6) shows the effects on plant parasitic loads as a result of applying the available heats in the feedwater preheating train and the compression train. As can be seen, the overall parasitic loads decrease dramatically when compared to non-heat-integrated parasitic loads in Figure 4.10. The fiber sorbents, especially with reservoir cooling, have exceptionally low parasitic loads on the power plant; though dehydration costs are not considered here for 13X and additional SO_x clean-up costs are not considered for the solid-supported amine case. Zeolite MFI fiber sorbents, on the other hand, emerge as an ideal route to pursue for several reasons. First, the hydrophobic pure-silica zeolite will dramatically reduce any need for dehydration (if any is needed at

all). Second, SO_x sorbs reversibly[35] unlike in solid-supported amines. Finally, the low heat of sorption exhibited by MFI drives down costs (with heat recovery and heat integration strategies handling much of the sensible heat duties). Chilled ammonia with slurry feed is the lowest parasitic load CO_2 capture device considered, mainly due to the low intrinsic heats (heat of formation) and relatively low auxiliary penalties as well as high CO_2 recovery pressures. Similar to the fiber sorbents scenario, many additional costs are not considered for the chilled ammonia case, such as the addition of several water washing steps to effectively eliminate ammonia slip, and the costs of moving such a large slurry mixture around rapidly between the two towers. The actual cost of chilled ammonia lies somewhere between the two cases considered, most likely towards the lower end, since some slurry formation is inevitable. Liquid-based amines, by comparison, are much more expensive than chilled ammonia, though still on the boundary between plausible and non-starter, mainly due to the high heats of reaction and lost solvent during the desorption step. Finally, packed bed systems as well as single-stage membrane systems can be considered non-starters for this application due to the high parasitic loads.

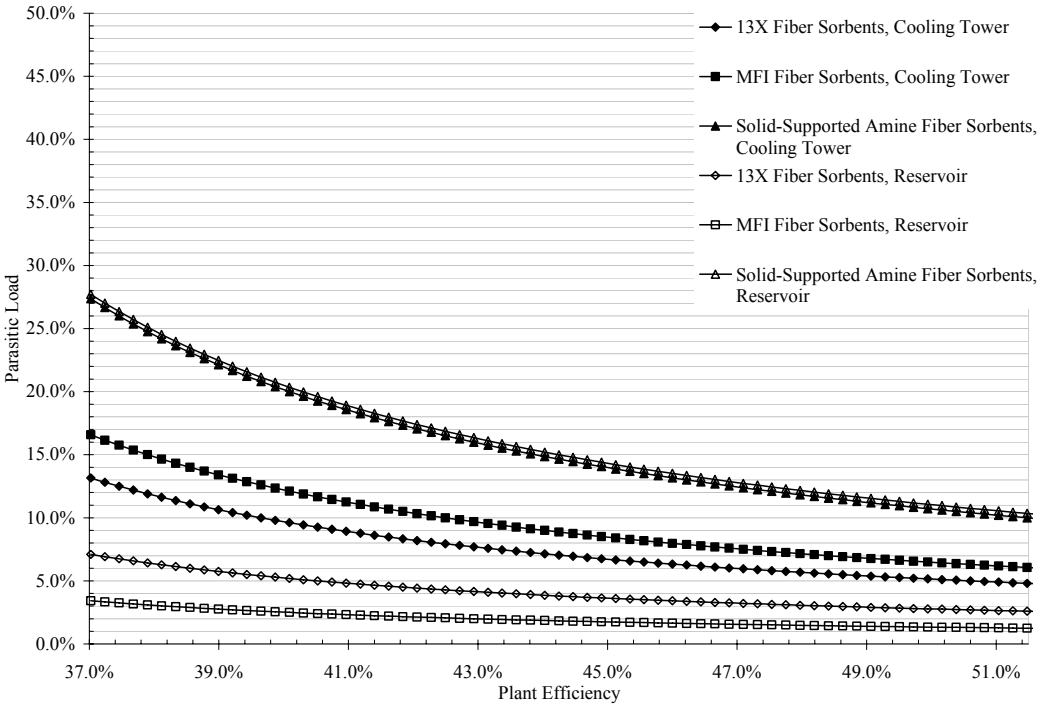

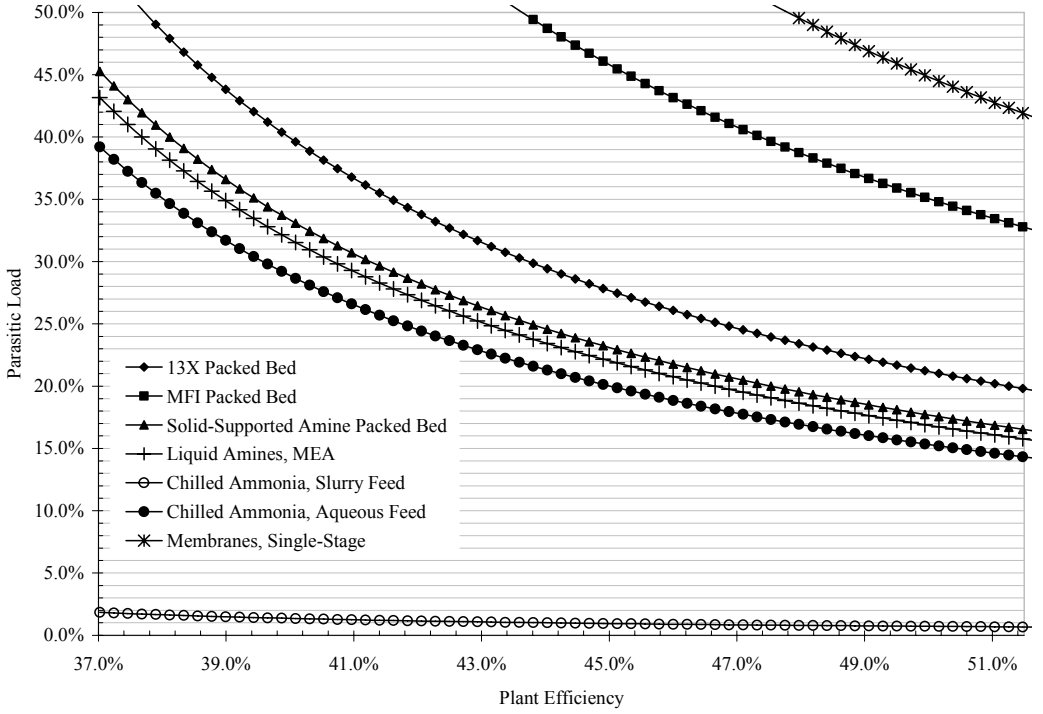

Figure 4.16: Overall parasitic loads incurred by the addition of CO_2 capture system with sensible and latent heats integrated into the power plant system. Specifically, heats available in the first two feedwater preheating stages are used, as well as the heat generated from CO_2 compression. Figure split for convenience.

Table 4.6: Overall energy penalties and energy recoveries from CO_2 capture systems and heat integration

Process	Auxiliary Energy Requirements (GJ/tonne of CO_2 captured)	Available Waste Heat for Auxiliary Loads (GJ/tonne of CO_2 captured)	Work Losses due to Steam Use (GJ/tonne of CO_2 captured)	Available Waste Heat for Desorption (GJ/tonne of CO_2 captured)	Compression Energy Requirements (GJ/tonne of CO_2 captured), 10°C Approach
Fiber Sorbents	1.32 In-house Cooling Water, Zeolite 13X	1.09	0.82	0.68	0.13
	1.59 In-house Cooling Water, Zeolite MFI		0.57		
	0.90 In-house Cooling Water, Solid Supported Amines		1.59		
	0.5 Reservoir Cooling Water, Zeolite 13X		0.82		
	0.99 Reservoir Cooling Water, Zeolite MFI		0.57		
	0.33 Reservoir Cooling Water, Solid Supported Amines		1.59		
Packed Bed	2.88, Zeolite 13X		0.82		0.13
	4.37, Zeolite MFI		0.57		
	1.77, Solid Supported Amines		1.59		
Liquid Amines, MEA	0.41		2.20		0.12
Membranes	6.00		--		0.13
Chilled Ammonia, Aqueous Feed	0.898		2.10		0.07
Chilled Ammonia, Slurry Feed	0.90		0.67		0.07

4.3.4.4 Literature Comparisons

Table 4.7 summarizes and compares the main findings in this work with other reports in the literature concerning similar capture technologies. This work differs from earlier reports[26,37] on the total parasitic load for liquid-based amines by approximately a 10% higher parasitic load than previously reported. This difference is mainly a result of the excess heat lost due to solvent (water) vaporization during the desorption step, which was not accounted for in the earlier studies. The membrane process considered in this chapter is closely in line with the work presented by Favre in 2007[16] which indicates that membrane process should be discarded as a post-combustion capture technology. The more recent work by Merkel et al in 2009[22], however, using multi-stage membrane processes shows that membranes have the potential to be a competitive CO_2 capture technique within a proper set of constraints. The chilled ammonia analysis presented in this work, which took the two extreme cases of a pure slurry feed (heat of formation penalty only) and a pure aqueous ammonia feed (heat of reaction only), bounds the analysis reported by Alstom[21] when heat integration is considered. Without heat integration, the parasitic loads presented here are higher by at least 20%; this could be possibly attributed to the CO_2 recovery used in this study as compared to the Alstom study, which is not specified. In the case of solid sorbents in packed bed configuration, there is relatively little literature available for comparison. A dry carbonate process developed by RTI international[36] has the potential to drive down CO_2 capture costs for solid sorbents due to lower thermal requirements, as well as alleviate water-CO_2 competitive sorption effects normally associated with zeolitic solid sorbents. In that RTI

study, many of the issues associated with the packed bed configuration considered in this study are circumvented by using a fluidized bed (essentially removing the large sensible heat requirements of the packed bed configuration). Indeed, many of the challenges associated with the dry carbonate process[36] are possibly addressed by integrating the dry carbonate into a fiber sorbent morphology, thus capturing the benefits of both processes. Finally, pure-silica MFI-based fiber sorbents with full heat integration and reservoir cooling offer an attractive route to drive down CO_2 capture costs.

Table 4.7: Literature comparisons

Study	Base Plant Efficiency (%)	CO_2 Capture Percentage (%)	Parasitic Load (%)
DOE Baseline, Case 1a, Advanced Amines[26]	35	90	26.4
Rochelle 2006 Case, MEA[37]	Not specified	Not specified	27
This work, MEA, with heat integration	37	90	38.7
Merkel et. al, Two-step countercurrent sweep membrane process[22]	Not specified	95	16
Favre, 2007, single-stage vacuum membrane process[16]	38.5	80	135
This work, single-stage vacuum membrane process	37	80	112
Alstom report, Chilled Ammonia[21]	40.5	Not specified	9.5
This work, chilled ammonia, slurry feed, with heat integration	40.5	90	1.12
This work, chilled ammonia, aqueous feed, with heat integration	40.5	90	24
RTI International Report, Thermal Swing Fluidized Beds, Dry Carbonate[36]	35	90	17.5
This work, Thermal Swing Packed Beds, Solid Supported Amines, with heat integration	37	90	40.7
Fiber Sorbents, MFI Case, Reservoir Cooling, with heat integration, this work	37	90	3.1

4.4 Conclusions

The objective of this chapter was the development of a high-level, but internally consistent, energetic analysis of various CO_2 capture technologies, forgoing many details associated with typical comparison papers in an effort to capture the essence of each technology. In this light, each of the processes were seen to be unduly parasitic on the host plant in the absence of heat integration, likely rendering CO_2 capture not possible, or at least, not economical. The analysis within the chapter used a 99% CO_2 capture rate (except for the membrane process, which used an 80% capture rate, as that has been established as the most optimum capture ratio[16]), which partially accounts for the high parasitic loads in the absence of heat integration. This high capture rate was chosen to illustrate that with appropriate heat integration, a low cost capture route does exist even at high recoveries. When heat integration strategies, such as utilizing heat flows in the feedwater preheating system and heats of compression of CO_2 (among others not addressed in this study), are considered, the CO_2 capture technologies become much more plausible. Specifically, chilled ammonia in slurry mode offers one of the lowest parasitic loads—under 5%—along with Zeolite MFI fiber sorbents (with reservoir cooling) also exhibiting parasitic loads under 5%. These technologies, chilled ammonia and fiber sorbents, are both quite promising in terms of energetics and warrant further research to determine the reality of installing a wide-spread fleet of such systems.

Finally, it should be noted that the overall energetic analysis presented here do not consider a number of practical issues facing CO_2 capture processes: SO_x and NO_x, water,

oxygen, carbon monoxide, and particulates. All of these difficulties will need to be addressed for wide-spread deployment of CO_2 capture systems. However, the biggest hurdle is often considered to be the energy penalties associated with capturing the CO_2, and that is the focus of the present study.

4.5 Nomenclature

T_{Out}	Flue gas temperature exiting the compressor (K)
T_{in}	Flue gas temperature entering the compressor (K)
P_{out}	CO_2 compression pressure (Pa)
P_{in}	CO_2 pressure entering the compressor (Pa)
γ_{CO2}	Adiabatic gas expansion coefficient
$\dot{m}_{CO2}$	Mass flow rate of CO_2 entering compressor (kg/s)
$C_{P,CO2}$	CO_2 specific heat capacity (J/kg-K)
$\eta_{compressor}$	Isentropic compressor efficiency
$W_{required}$	Overall energy consumption by compressor (J)

4.6 References

1. *Perry's Chemical Engineers' Handbook*. 6th ed.; McGraw-Hill, Inc.: **1984**.
2. Wu, J.; Chen, V. Shell-side mass transfer performance of randomly packed hollow fiber modules, *Journ. Memb. Sci*., **2000**, 172, 59-79.

3. Bessho, N. Advanced Pressure Swing Adsorption System with Fiber Sorbents for Hydrogen Recovery. Georgia Institute of Technology, GA, *PhD Dissertation,* **2010.**
4. James R. Welty, C. E. Wicks, Robert E. Wilson, Gregory L. Rorrer, *Fundamentals of Momentum, Heat, and Mass Transfer*. 4th ed.; John Wiley & Sons: New York City, **2001**.
5. Nakamura, Y. Bluff-body aerodynamics and turbulence, *Journal of Wind Engineering and Industrial Aerodynamics,* **1993**, 49(1), 65-78.
6. Bemis, G.R.; DoAngelis, M. Levelized cost of electricity generation technologies, *Contemporary Economic Policy*, **1990**, 8(3), 200-214.
7. Rubin, E.S.; Chen, C.; Rao, A.B. Cost & performance of fossil fuel power plants with CO_2 capture and storage, *Energy Policy,* **2007**, 35(9), 4444-4451.
8. Yang, R.T. *Gas Separation by Adsorption Processes*, Butterworth Publishers: Stoneham, MA, 1987.
9. Chue, K.T.; Kim, J.N.; Yoo, Y.J.; Cho, S.H.; Yang, R.T. Comparison of Activated Carbon and Zeolite 13X for CO_2 recovery from Flue Gas by Pressure Swing Adsorption. *Industrial & Engineering Chemistry Research* **1995**, 34, (2), 591-598.
10. Choi, S.; Drese, J.; Jones, C. *ChemSusChem* 2009, **2**, 796.
11. Brandani, F.; Ruthven, D.M.; *Ind. Eng. Chem. Res.*, **2004**, 43, 8339-8344.
12. Sijbesma, H.; Nymeijer, K.; Marwijk, R.; Heijboer, R.; Potreck, J.; Wessling, M. Flue gas dehydration using polymer membranes. *Journal of Membrane Science,* **2008**, 313, 263-276.
13. Xu, X.; Zhao, X.; Sun, L.; Liu, X.; Adsorption separation of carbon dioxide, methane, and nitrogen on monoethanol amine modified β-zeolite, *Journal of Natural Gas Chemistry,* **2009**, 18, 167-172.
14. Khatri, R.A.; Chuang, S. S. C.; Soong, Y.; Gray, M. *Energy Fuels* 2006, **20**, 1514.
15. van den Broek, M.; Hoefnagels, R.; Rubin, E.; Turkenburg, W.; Faaij, A. Effects of technological learning on future cost and performance of power plants with CO_2 capture. *Progress in Energy and Combustion Science*, **2009**, 35, 457-480.

16. Favre, E. Carbon dioxide recovery from post-combustion processes: Can gas permeation membranes compete with absorption? *Journal of Membrane Science*, **2007**, 294, 50-59.

17. Abu-Zahra, M. R. M.; Schneiders, L. H. J.; Niederer, J. P. M.; Feron, P. H. M.; Versteeg, G. F. CO_2 capture from power plants: Part I. A parametric study of the technical performance based on monoethanolamine. *International Journal of Greenhouse Gas Control*, **2007**, 37-46.

.18. Feng, B.; Du, M.; Dennis, T. J.; Anthony, K.; Perumal, M.J. Reduction of Energy Requirement of CO_2 Desorption by Adding Acid into CO_2-loaded Solvent. *Eneryg & Fuels*, **2009**, In press.

19. Mathias, P.M.; Reddy, S.; O'Connell, J.P. Quantitative evaluation of the chilled-ammonia process for CO_2 capture using thermodynamic analysis and process simulation. *International Journal of Greenhouse Gas Control,* **2009**, In press.

20. Gal, E. **2006**. Ultra cleaning combustion gas including the removal of CO2. World Intellectual Property, Patent WO 2006022885.

21. Gal, E.; Olson, S. **2006**. Chilled ammonium process (CAP) for post combustion CO_2 capture. In: Presented at the 2nd Annual Carbon Capture and Transportation Working Group Workshop, Palo Alto, March 23.

22. Merkel, T.C.; Lin, H.; Wei, X.; Baker, R. Power plant post-combustion carbon dioxide capture: An opportunity for membranes. *Journal of Membrane Science*, **2009**, In Press.

23. Kern, D.Q., *Process Heat Transfer.* McGraw-Hill, New York, NY, **1950.**

24. McCabe, S.; Smith, J., *Unit Operations of Chemical Engineering.* McGraw-Hill, New York, NY, **1993**

25. Kandlikar, S.; Garimella, S.; Li., D.; Colin, S.; King, M.R., *Heat Transfer and Fluid Flow in Minichannels and Microchannels.* Elseveir, LTD. Kidlington, Oxford, **2006.**

26. Cost and Performance Baseline for Fossil Energy Plants. Volume 1: Bituminous Coal and Natural Gas to Electricity, NETL Technical Report Number DOE/NETL-2007/1281, August **2007**. http://www.netl.doe.gov/energy-analyses/pubs/Bituminous%20Baseline_Final%20Report.pdf

27. Darde, V.; Thomsen, K.; van Well, W.J.M.; Stenby, E.H. Chilled ammonia process for CO_2 capture, *Energy Procedia,* **2009,** 1 (1), 1035-1042.
28. Singh, D.; Croiset, E.; Douglas, P.L.; Douglas M.A. Techno-economic study of CO_2 capture from an existing coal fired power plant: MEA scrubbing vs. O2/CO2 recycle combustion. *Energy Conv Mgmt,* **2003**, 44, 3073–91.
29. Alie, C.; Backham, L.; Croiset, E.; Douglas, P.L.; Simulation of CO_2 capture using MEA: a flowsheet decomposition method, *Energy Conversion & Management,* **2005**, 46, 475-487.
30. MIT, **1997**, CO_2 Capture, Reuse and Storage Technologies for Mitigating Global Climate Change, A White Paper. DOE Order No. DE-AF22-96PC01257
31. Freeman, S.A.; Dugas, R.; Wagener, D.V.; Nguyen, T.; Rochelle, G.T. Carbon dioxide capture with concentrated , aqueous piperazine, *Energy Procedia,* **2009**, 1 (1), 1489-1496.
32. Smith, J.M.; Van Ness, H.C.; Abbott, M.M. *Chemical Engineering Thermodynamics*, 6th ed., McGraw-Hill, New York, NY, **2001.**
33. Gibbins, J.R.; Crane, R.I. Scope for reductions in the cost of CO_2 capture using flue gas scrubbing with amine solvents, *Proc. Instn. Mech. Engrs.,* **2004**, 218, 231-239.
34. Kelley, B.T.; Deckman, H.W.; Hershkowitz, F.; Northrop, S.P.; Ravikovitch, P.I. Temperature Swing Adsorption of CO_2 from Flue Gas Utilizing Heat from Compression. U.S. Patent Application 20080314244. May 16, **2008.**
35. Gollakota, S.V.; Chriswell, C.D. Study of an Adsorption Process Using Silicalite for Sulfur Dioxide Removal from Combustion Gases, *Ind. Eng. Chem. Res.,* **1988,** *27*, 139-143.
36. Nelson, T.; Coleman, L.; Anderson, M.; Herr, J.; Pavani, M., March, **2009,** *The Dry Carbonate Process: Carbon Dioxide Recovery from Power Plant Flue Gas,* Presented at: Annual NETL CO_2 Capture Technology for Existing Plants R&D Meeting, Pittsburgh, PA.
37. Rochelle, G.T. Amine Scrubbing for CO_2 Capture, *Science*, **2009**, 235, 1652-1654

Chapter 5

Hollow Fiber Sorbent Spinning

The first step in testing the hollow fiber sorbent platform is the creation of highly loaded polymer/inorganic hollow fibers using a dry-jet, wet-quench spinning process. At the outset of this research, the *main* goal of the work was to develop methods for spinning fibers with high solids loading, as at that time the general wisdom was that fibers of this nature could not be easily made. Initially, the general wisdom prevailed, as many different polymers and spinning conditions were iterated through with no successful spins (these polymers include: polysulfone, PEBAX®, Hydrin-ECO®, and Estane®). Finally, cellulose acetate was chosen as the support polymer for the zeolites, allowing for fiber spinning experiments that were not only easily repeatable—enabling the production of large quantities of fiber sorbents—but also easily tunable, which allowed for attempts at optimizing the fiber sorbent performance in terms of permeation through the porous support. The chapter is divided into three sections: *1)* dope development, *2)* the effect of draw rate and temperature on fiber pore size and permeance, the effect of bore fluid composition on fiber pore size, permeance and lumen side phase separation, and finally, *3)* the fiber spinning parameters used to spin the majority of the fiber sorbents in this work.

5.1 Dope Development

The first step in spinning hollow fiber sorbents is to develop a cellulose acetate/solvent/non-solvent ternary phase diagram for pure polymer solutions. As mentioned in Chapter 3, the zeolites are saturated with water prior to their addition to the dope; this allows the zeolites to be considered "passive fillers" which do not alter the polymer solution's composition. Unlike hollow fiber membranes, ideal hollow fiber sorbents do not have an outer skin layer; as such, no volatile solvents or non-solvents were used in the final dope composition. Therefore, NMP (N-methyl-2-pyrrolidone) was chosen as the solvent due to its very low volatility[1], strong solvency power[2], and the fact that it is relatively benign towards humans and the environment (fiber spinning experiments create significant amounts of solvent waste). The choice of non-solvent, which acts to reduce the solvency power of the solvent, is mainly based on volatility and environmental safety. The clear choice is water, due to its abundance, relatively low volatility (compared to light hydrocarbons and alcohols), and most of all, it's miscibility with NMP.

Once the components have been selected, a map of the ternary phase equilibria needs to be established. Using standard cloud point techniques[3], the final polymer dope solution chosen was 14.3wt% CA/ 5.7% PVP/70.4% NMP/9.6% water; the full phase equilibria map can be found in the theses of Dhaval Bhandari and Naoki Bessho[4,5]. The low polymer concentration (relative to hollow fiber membrane spinning) was chosen in order to maximize the amount of zeolite loading in the solution; polymer solutions with

CA concentrations lower than this were found to extrude poorly. The goal of this work was to spin fibers primarily composed of zeolites; however, there are practical limits. Mainly, the polymer dope solution can only support a certain amount of added zeolites before the solids loading exceeds the dry loading, which is demonstrated in Figure 5.1.

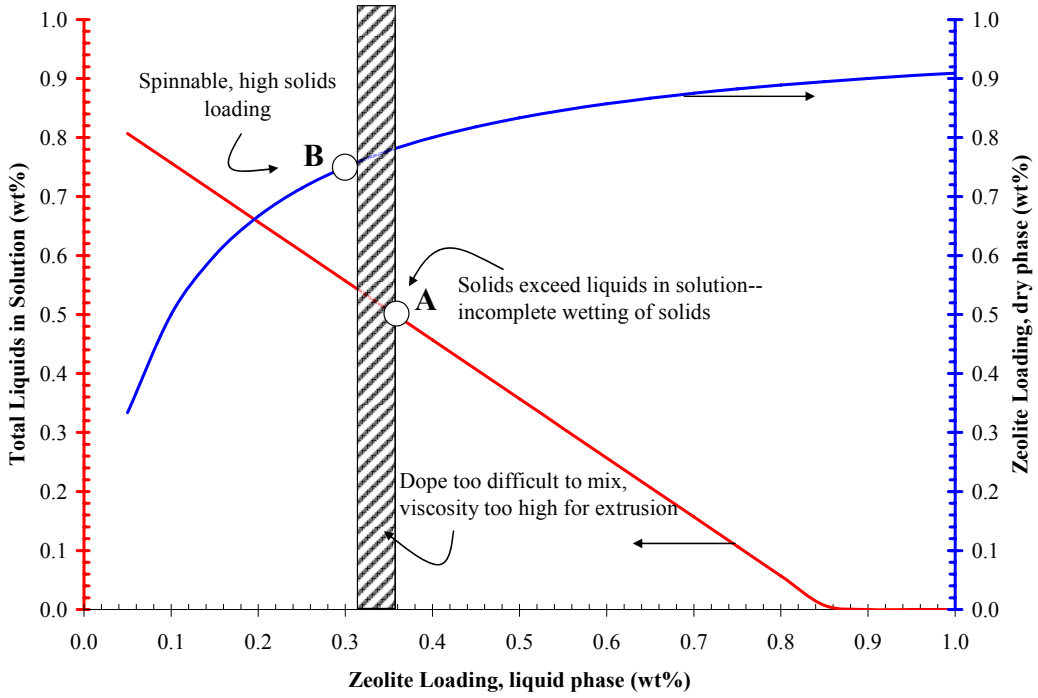

Figure 5.1: Total liquids in solution and dry zeolite loading as a function of zeolite loading in the liquid phase.

At this point (**A**), the polymer/zeolite dope is essentially oversaturated in solids (whether it be zeolites or polymers), and non-wetted powder exists within the solution, making it obviously un-spinnable. The hatched region in Figure 5.1 shows the region in which the polymer/zeolite solution is not in solids excess but is so viscous that it behaves like a thick paste or a solid. Dopes in this region were exceedingly difficult to mix, and were likely un-spinnable. At approximately 30wt% zeolite 13X (**B**), dopes were readily able

to be mixed and were found to be spinnable as well. The dry-fiber loadings correspond to 75wt% zeolite 13X. This loading of zeolites compares favorably with zeolites bound into pellets in traditional packed bed systems; the pellets are typically 70wt% zeolite and 30% binder material[6]. The final polymer dope solution chosen was 10wt% CA/ 4% PVP (pore former)/30% 13X/49.3% NMP/6.7% water.

5.2 Effect of Draw Rate and Temperature on Pore Size and Fiber Permeance

5.2.1 Spin Parameters

Once the spinning dope was prepared, and syringe experiments confirmed the extrudability of the polymer/zeolite solution, the dope was loaded into high pressure 500 mL ISCO® syringe pumps. One of the design parameters for the fiber sorbents was the creation of large OD/small ID hollow fibers; ideally, the fibers would have a 1200 micron OD and a 320 micron ID. Since this is significantly larger than fibers typically spun in the Koros Research Group[7-10], several spins were performed to investigate the effect of the extrusion rate on the fiber outer diameter and the possibility of spinning such large fibers. Furthermore, to reduce internal mass transfer resistance during the sorption step, a highly permeable pore structure is desirable. In addition to the effect of draw ratio (which will affect the phase separation kinetics), the effect of temperature (which will affect the kinetics and equilibrium of phase separation) on pore formation was studied.

The spinning conditions that were varied were extrusion rates of 400 mL/hr, 700 mL/hr and 1000 mL/hr at a constant take up rate of 11.7 meters per minute (which corresponds to a draw ration of 1.7, 1.0, and 0.7, respectively), and spinning temperatures of 25°C, 37°C, and 50°C (spinneret and bath were both at these temperatures). A deep coagulation bath (3 ft. depth) was used to provide more time for the nascent fibers to completely phase separate. The air gap was set very low to approach wet-spinning without actually submerging the spinneret, which might cause phase separation in the spinneret annulus. Wet-spinning was desirable to avoid formation of a dense outer resistive skin layer via evaporative solvent loss; this effect would likely be minimal with NMP as the only solvent. The full list of spinning conditions can be seen in Table 5.1.

Table 5.1: Spinning parameters used for temperature/draw ratio experiments

Spin Dope Composition			Spinning Parameters	
Component	**Core Dope (wt%)**		**Parameter**	
CA	10		Core Flow Rate	400, 700, 1000 mL/hr
PVP	4		Bore Flow Rate	100, 175, 250 mL/hr
13X	30		Bore Composition	80/20 NMP/H_2O
NMP	49.3		Operating Temperature	25°C, 37°C, 50°C
H_2O	6.7		Take-up Rate	11.7. m/min
--	--		Air Gap	3 cm

For these experiments, the bore fluid was chosen to be 80% NMP and 20% H_2O. The effects of bore fluid composition on fiber phase separation are complicated, but the

bore fluid is used primarily to occupy space and maintain the hollow structure of the fiber. As such, a neutral solvency bore fluid is chosen, and in this work, 80% NMP and 20% H_2O was found to be readily spinnable—a full discussion of bore fluid composition follows in the next section.

5.2.2 Fiber outer diameter as a function of draw ratio

As can be seen in Figure 5.2, the outer diameter of the fiber scales linearly with the draw ratio at all three temperatures that were investigated, though some deviations from this trend were seen at low draw ratios. Relative to hollow fiber membranes, the draw ratios chosen were quite low (0.7-1.8, as opposed to 2-8)[11].

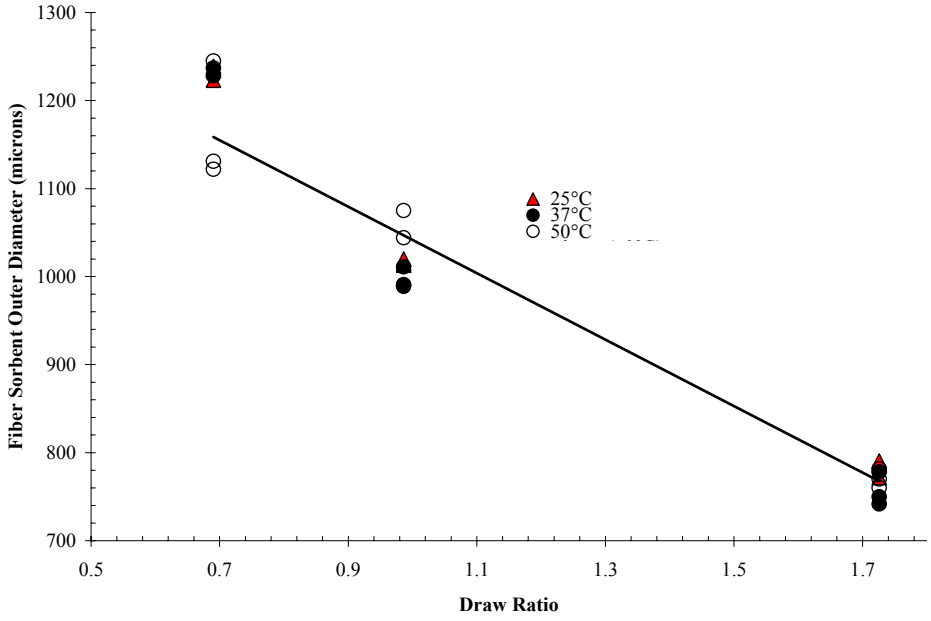

Figure 5.2: Fiber sorbent outer diameter as a function of draw ratio.

Low draw ratios were necessary to achieve the large outer diameter requirements established in the previous chapter. As can be seen, at the lowest draw ratio for all three

temperatures studied, the fiber outer diameter was found to lie approximately between 1150 and 1250 microns, which satisfies the OD requirements. Figure 5.3 shows SEM images of the fibers at constant temperature but varying draw ratio.

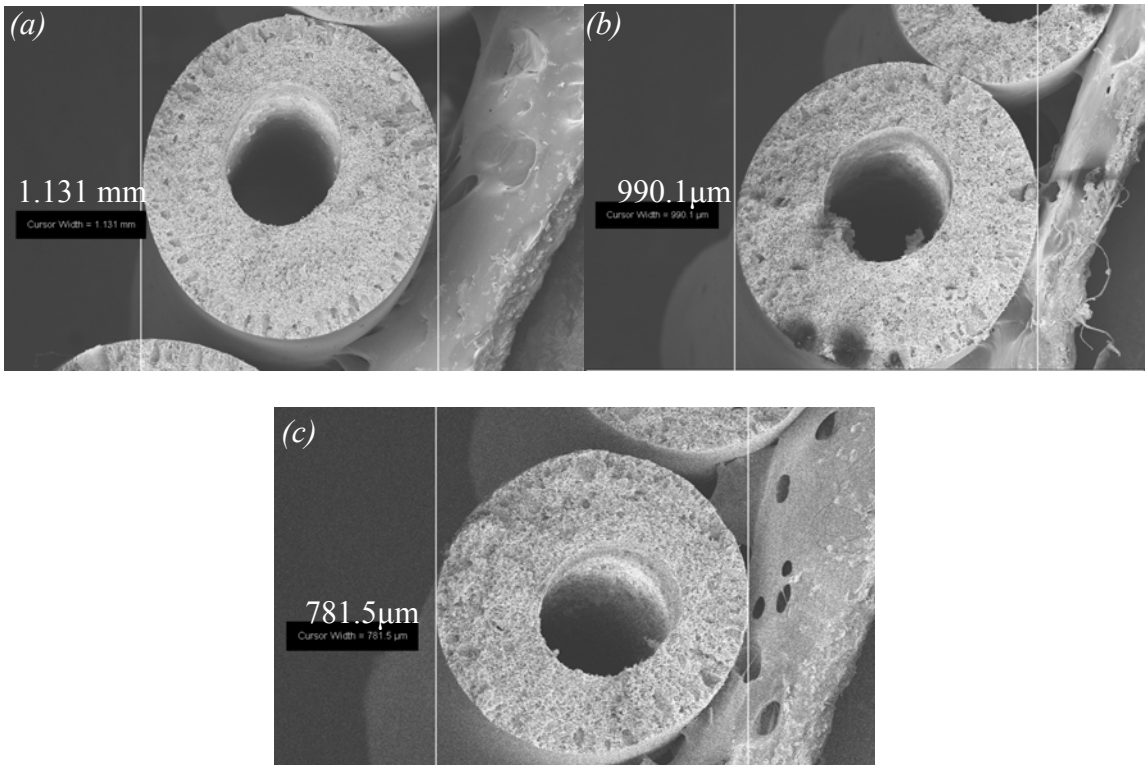

Figure 5.3: SEM images of cellulose acetate/13X fiber sorbents spun at 50°C with a draw ratio of 0.7 *(a)*, 1.0 *(b)*, and 1.7 *(c)*.

For this particular fiber sorbent dope, the following relation can be used to estimate the outer diameter from a known draw ratio,

$$\text{Fiber OD (microns)} = -(390 \pm 20)x(\text{Draw Ratio}) + (1430 \pm 40) \qquad \textbf{(1)}$$

The bore diameter also needs to be set at approximately one quarter of the fiber outer diameter to maximize the sorbent loading in the fiber walls while minimizing feed water pressure drops in the final sorption cycle (Appendix A). Typically, hollow fiber membranes prefer an OD/ID ratio of 2[11], which results in a core fluid/bore fluid extrusion rate ratio of 3[12]. For this work, a core fluid/bore fluid extrusion ratio of 4 was used, which resulted in the inner diameters in the final fibers that were larger than desired, as can be seen in Figure 5.4. The final section of the chapter addresses this issue.

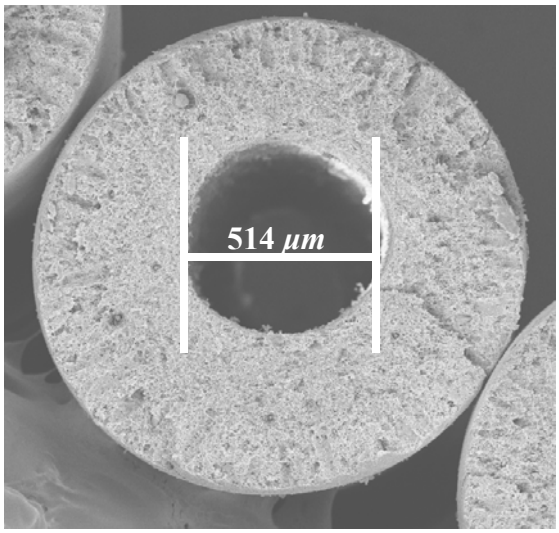

Figure 5.4: Fiber sorbent cross-section showing large bore diameter.

5.2.3 Permeation porosimetry

5.2.3.1 Effect of draw ratio

To investigate the effect of draw ratio on fiber sorbent pore morphology, helium permeation measurements were performed on the fibers that were spun at differing draw

ratios. The permeation pressure was steadily increased and the flux through the fiber was recorded; this increase in flux with respect to pressure gives insight into the Poiseuille contribution as well as the Knudsen contribution to permeation. CO_2 or nitrogen could not be used to perform the necessary calculations due to an observed Joule-Thomson effect on the permeation results, which yielded a negative permeance versus pressure slope. As can be seen in Figure 5.5, as draw ratio is increased at a constant temperature of 50°C, the observed permeance through the fibers increases.

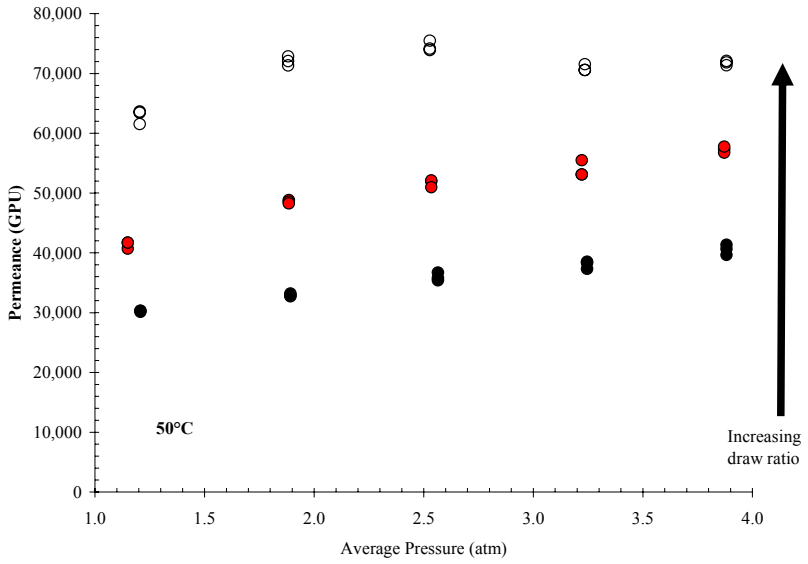

Figure 5.5: Helium permeation porosimetry results for fibers spun at 50°C and draw ratios of 0.7, 1.0, and 1.67

The most likely cause of this phenomenon is the increase in diffusion path length that the non-solvent coagulant must traverse in order to cause full phase separation in the fiber. Thermodynamically, spinodal decomposition may be favored for these fiber sorbent dopes, as they were formulated to be very close to the binodal line. However, kinetic limitations (such as the aforementioned increase in diffusion path length) can push the

phase separation mechanism towards nucleation and growth, thereby reducing the overall permeance of the fibers. While SEM images are inconclusive, some evidence of this can be seen in Figure 5.6, where a morphology possibly reflecting spinodal decomposition is observed in the outermost portion of the fibers (Figure 5.6*a* and Figure 5.6*b*), while denser closed cell regions are observed farther inside the fiber (Figure 5.6*c* and Figure 5.6*d*).

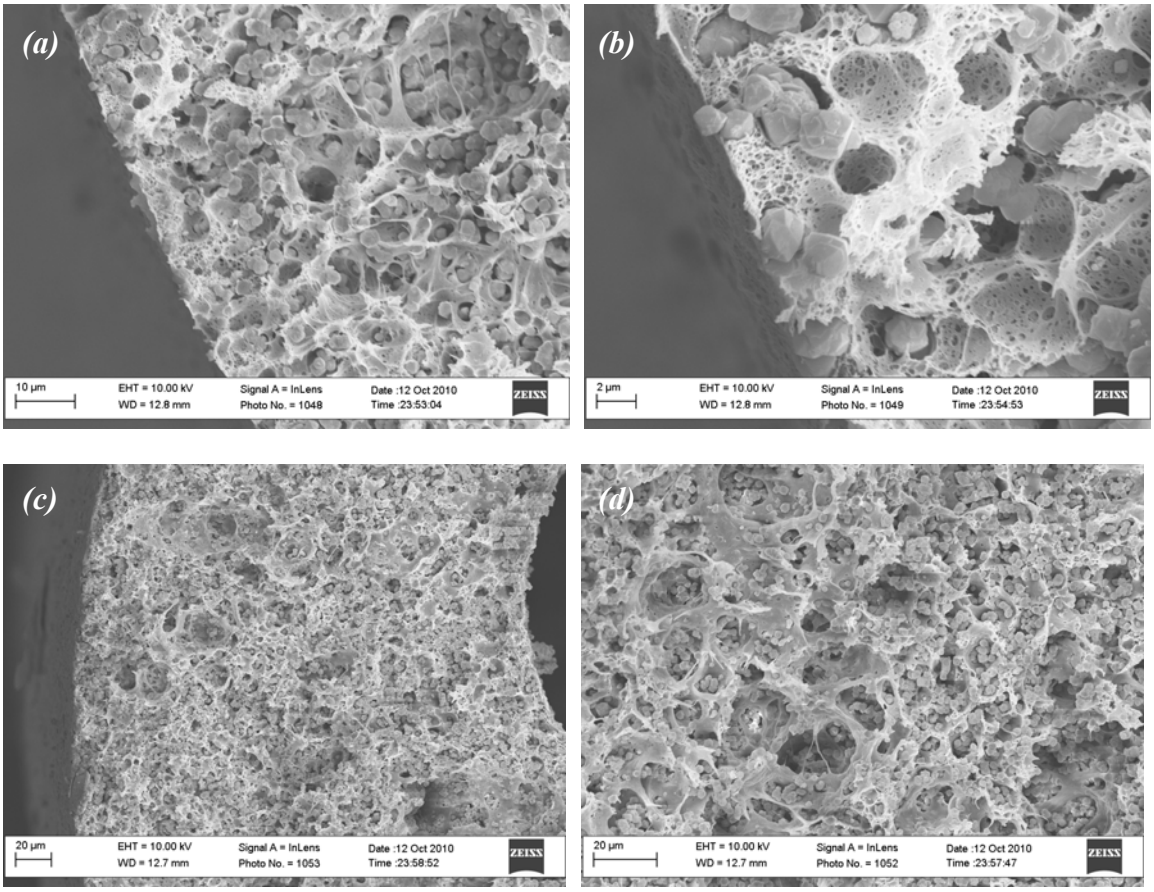

Figure 5.6: ***(a)*** **Possible evidence of spinodal decomposition can be seen on the outer rim of the fiber sorbent.** ***(b)*** **Evidence of spinodal decomposition after magnification.** ***(c)*** **Fiber sorbent wall. Cells from nucleation and growth can be seen in the middle-to-inner portion of the wall.** ***(d)*** **Cells from nucleation and growth are apparent after magnification.**

5.2.3.2 Effect of temperature

While the effect of draw ratio on pore formation is best thought of as a kinetic effect, spinning temperature can have both a kinetic effect as well as an equilibrium effect. As can be seen in Figure 5.7, as temperature is increased at a constant draw ratio, the fiber sorbent permeance decreases.

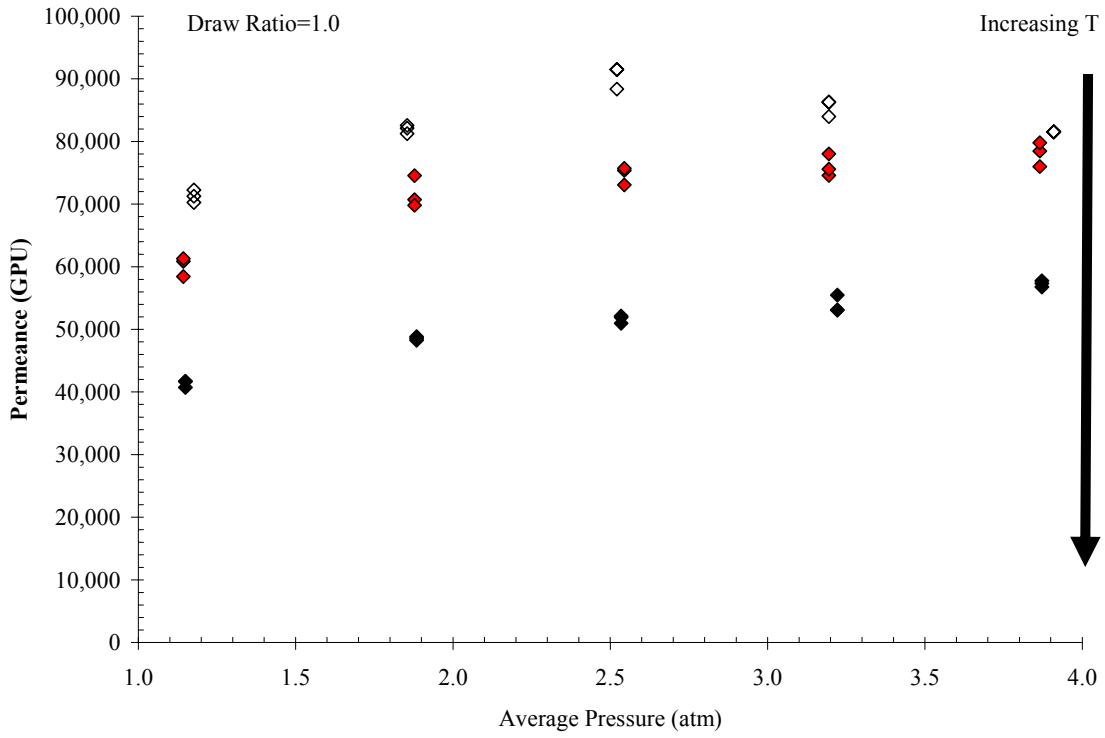

Figure 5.7: Helium permeation porosimetry results. Constant draw ratio of 1.0, spinning experiments conducted at 25°C, 37°C and 50°C.

Initially, this may seem counterintuitive—as the temperature of the spinning apparatus increases (including the quench bath), the diffusion coefficient of non-solvent into the nascent fiber will increase, promoting a more rapid phase separation (i.e., kinetics are

improved with increasing spinning temperature). However, as the spin dope was formulated to be very close to the binodal line at 25°C, increasing the temperature of the dope will actually move the binodal line farther away from the dope composition, as is hypothesized in Figure 5.8 (i.e., causing the phase separation to be more thermodynamically unfavorable). As the nascent fiber traverses through the quench bath, a larger portion of its residence time will be as a one-phase polymer solution: during this period non-solvent will be diffusing in and replacing the existing solvent. This shift will drive the composition upwards on the ternary phase diagram, likely causing portions of the fiber sorbent solution to move into the meta-stable nucleation and growth phase separation regime. It appears from the permeation results that the equilibrium contribution to pore formation is the dominant contribution, at least in terms of spinning temperature.

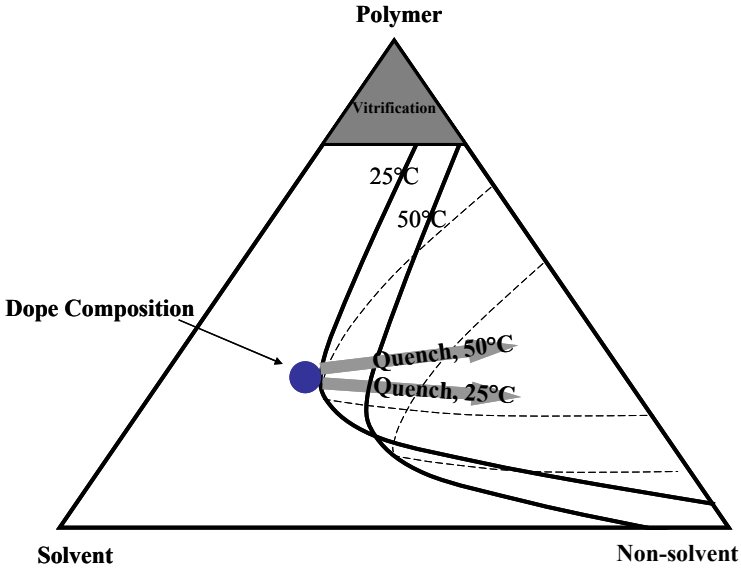

Figure 5.8: Cartoon illustrating how the binodal line shifts to the right of the ternary phase diagram at higher temperatures. For a dope formulated at 25°C and spun at 50°C, this corresponds to a larger portion of the quench residence time being spent in the 1-phase region.

5.2.3.3 Pore formation hypothesis

The previous two sections showed that the pore formation mechanism is affected by both solvent exchange kinetics (effect of draw ratio and spin temperature) and solution equilibrium (spin temperature). Perhaps the most surprising result in this series of experiments is the reversal of temperature dependence once the draw ratio is moved from 1.0 to 1.7, as can be seen in Figure 5.9. At the lower draw ratios, the helium permeance scales negatively with spinning temperature, as shown in the previous section. At the highest draw ratio studied, the permeance scales positively with the spinning temperature, perhaps indicating a shift from a equilibrium-dominated pore formation mechanism (as discussed in the previous section) to a kinetically-dominated pore formation mechanism.

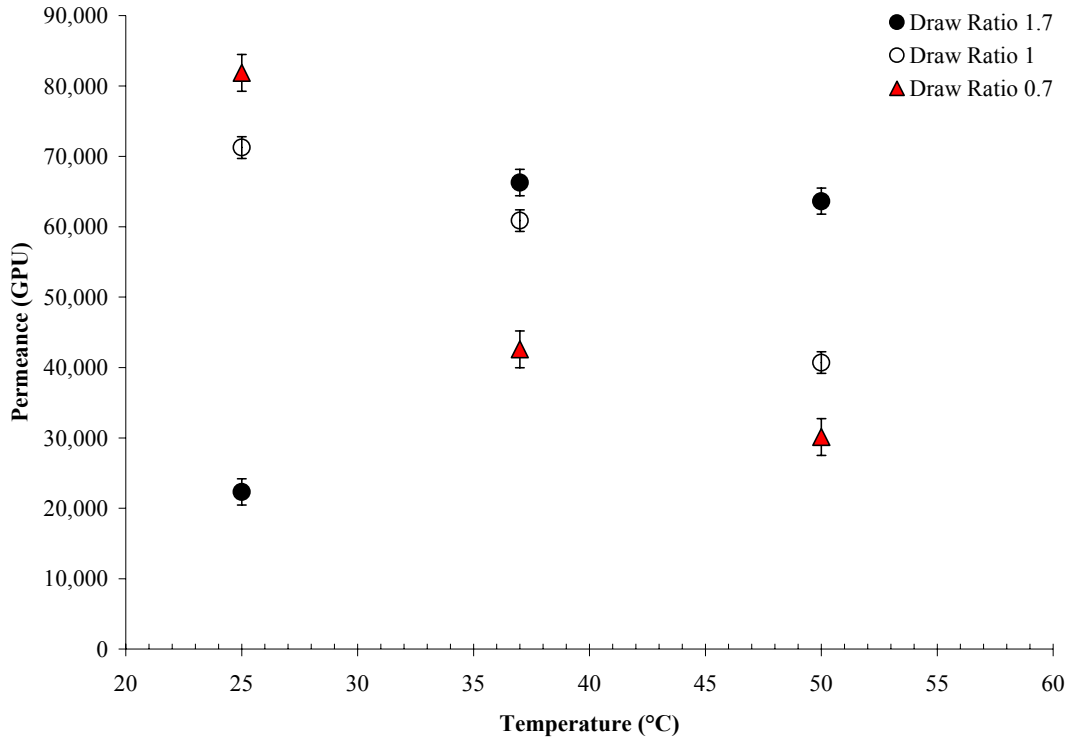

Figure 5.9: Helium permeance as a function of spinning temperature and draw ratio.

This dramatic difference in spinning temperature dependence on helium permeation at higher draw rates could be due to a myriad of factors. These factors include non-linear scaling of temperature dependence on ternary phase equilibrium states, non-linear scaling of temperature dependence on kinetic factors such as diffusion and cell growth, changes in the die-swell due to lower shear rates in the spinneret at higher spinning temperatures, and the contributions of the bore fluid changing with temperature and draw ratio. This last factor in particular was used to develop a hypothesis for a reversal in fiber permeance/spinning temperature dependence. One of the limiting factors of permeation porosimetry is that the method gives only the total flux through the fiber wall[13]; the resistances within the fiber wall will occur in a series resistance mode. Therefore, permeation porosimetry may measure the limiting resistance through the fiber wall. At 25°C, the bore fluid chosen for these experiments is neutral by design. At this spinning temperature, the non-solvent must diffuse from the outer diameter of the nascent fiber to the innermost radius of the fiber for complete phase separation. The innermost portion of the fiber will likely undergo cell wall nucleation and growth. However, with the slower draw ratios, the cells will have much more time to grow due to the increase in wall thickness and will eventually rupture once the cell size is too large. These cell ruptures will allow for a more continuous path and a reduction in the resistance encountered at the innermost wall, as can be seen in Figure 5.10.

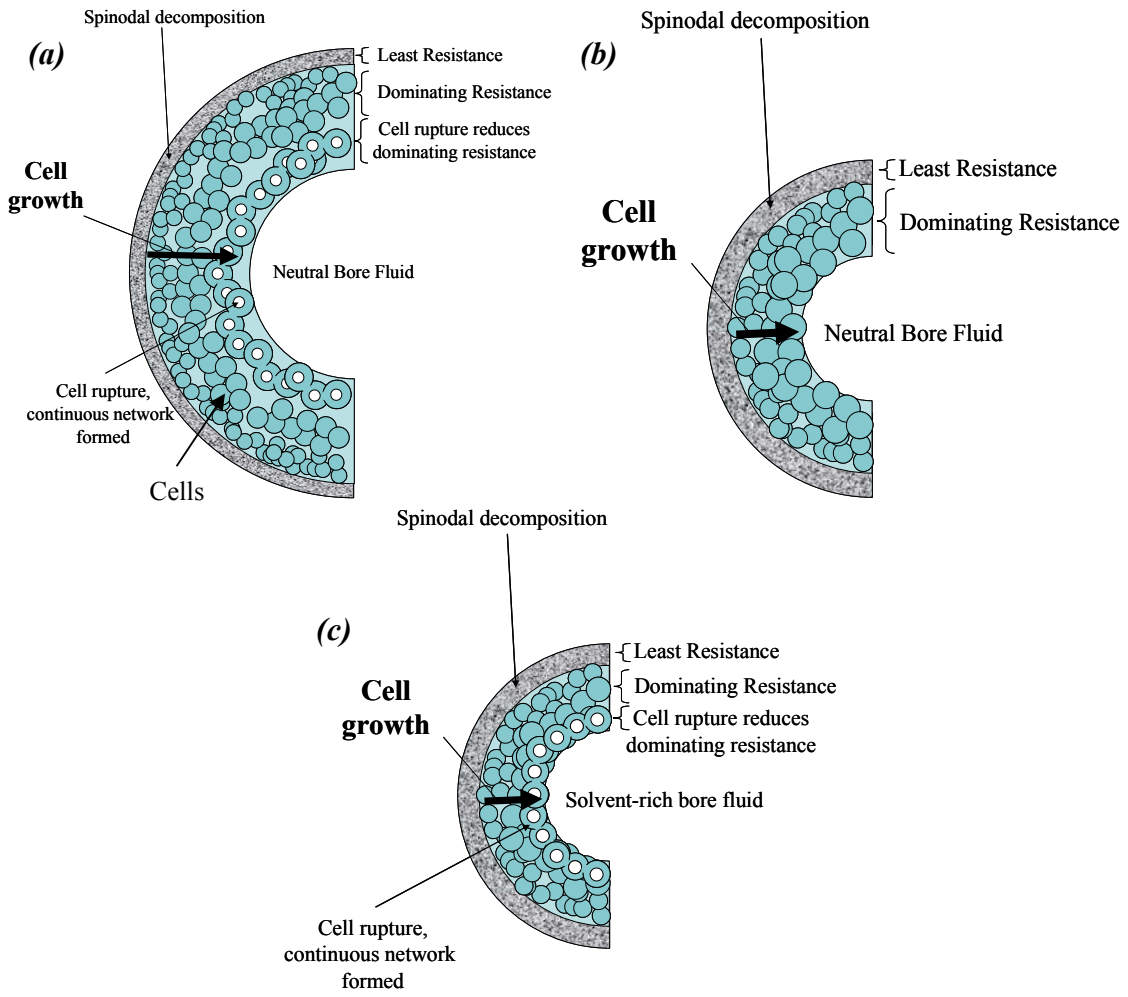

Figure 5.10: Hypothesis for pore formation throughout the fiber wall. Spinodal decomposition likely occurs at outer radius of the fiber, and nucleation and growth proceeds inward. The cells farthest from the outer edge of the fiber have the most time to grow in size. *(a)* Low draw ratios, low temperatures. Cells rupture due to continuous growth near the inner radius of the fiber, thereby reducing the resistance in the fiber wall. *(b)* High draw ratios, low temperatures. Due to shorter non-solvent diffusion path lengths, the cells do not grow to a rupturable size. *(c)* High draw ratios, high temperatres. The now-solvent-rich bore fluid slows down phase separation at the inner radius, resulting in more time for cell-growth and eventual rupture.

As the temperature is increased, the bore fluid becomes more solvent-like and this extra solvent essentially adds to the non-solvent diffusion time (since the extra solvent must also be exchanged with the external non-solvent coagulant), allowing the innermost cells to grow and eventually rupture. The more cell walls that rupture, the more

interconnected and straightforward the path through the "resistance area" will be (Fig. 5.10*a* and 5.10*c*). This hypothesis can be indirectly probed by estimating the tortuosity in the fiber wall; the higher draw ratio should exhibit a negative spinning temperature dependence on tortuosity (as in, the pore channel becomes more connected with an increase in spinning temperature), while the lower draw ratios should exhibit a positive spinning temperature dependence on tortuosity.

5.2.3.4 Pore Size, Porosity, and Tortuosity

To test this hypothesis, the helium permeance data from the above spinning experiments can be decoupled into the Knudsen and Poiseuille contributions to the overall flow. By taking the ratio of the Poiseuille and Knudsen contributions, a rough estimate of the pore size in the fiber sorbent can be obtained. However, many of the highly permeable fibers exhibit a transition in Poiseuille flow (slope) around 2 atmospheres average pressure (Fig. 5.5 and Fig 5.7), making it difficult to estimate this contribution correctly. The most permeable of fibers exhibit this transition, and the most likely cause of this is that the assumption of a complete pressure drop across the fiber wall used in the permeance calculations is no longer valid—the permeate side of the module is likely pressurized. To estimate the Poiseuille and Knudsen contributions, only the points before the observed transition were considered. An example of the Poiseuille and Knudsen contributions to the total flow can be seen in Figure 5.11.

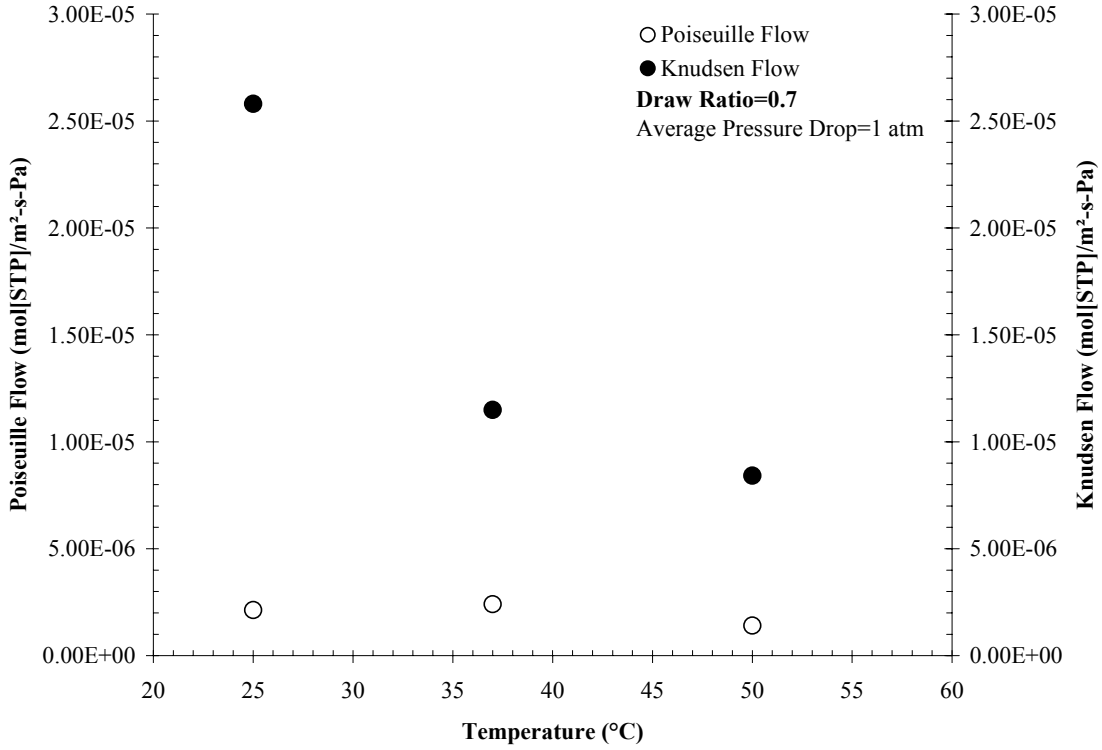

Figure 5.11: Decoupling of helium permeation porosimetry data into Knudsen and Poiseuille contributions at 1 atm.

For all of the fiber sorbents spinning conditions, Knudsen flow is the dominant form of transport measured through the fiber sorbents. This implies that the measured pore sizes in the fiber sorbents are smaller than the mean free path of the helium atoms at the test pressures (2.0 atm upstream, 1.0atm downstream). The mean free path of helium at these conditions can be seen, viz.,

$$\lambda = \frac{1}{\sqrt{2}\cdot\pi\cdot d_A^2\cdot\left[\frac{p_A\cdot \mathrm{N}}{R\cdot T}\right]} = \frac{1}{\sqrt{2}\cdot\pi\cdot\left(2.6x10^{-8}\,cm\right)^2\cdot\left[\frac{1.01bar\cdot 6.023x10^{23}}{83.14\cdot 308K}\right]} = 140nm \quad \textbf{(2)}$$

The Knudsen contributions to flow can be used to estimate the effective Knudsen diffusion coefficient, $D_{K,eff}$ using Fick's first law,

$$N_{He,Knudsen} = -D_{He,Knudsen,effective} \cdot \frac{dC_{He}}{dx} \quad \textbf{(3)}$$

Using the pore size data obtained from the Poiseuille and Knudsen ratio (which is shown later in Figure 5.13), the true Knudsen diffusion coefficient, D_K, can be estimated using Equation 12 in Chapter 2. Finally, by measuring the porosity of the fiber sorbent samples—either gravimetrically or via mercury porosimetry—the tortuosity of the pore structure can be estimated with knowledge of the effective and true Knudsen diffusion coefficients via Equation 16 in Chapter 2. The tortuosity and porosity dependence on temperature can be seen in the following group of figures (Figure 5.12), with each figure representing a different draw ratio.

As can be seen in the figures, the lowest draw ratio results in a tortuosity that is positively dependent on the spinning temperature, and as the draw ratio is increased to 1.7, the resulting fiber tortuosity decreases as a result of an increase in spinning temperature; perhaps lending some credence to the hypothesis in Section 5.2.3.3. Furthermore, the most permeable fibers (T_{spin}=25°C, DR=0.7, & T_{spin}=50°C, DR=1.67) were found to also exhibit the highest porosity and the lowest tortuoisty, again supporting the cell-rupture hypothesis posited in the previous section. The porosity of the fibers pass through a minima at 37°C. As mentioned before, the kinetic factors of phase separation are improved by increasing the spinning temperature, while the dope composition

becomes less favorable for phase separation from an equilibrium perspective as the spinning temperature is increased. This minima could be a result of the two sets of factors scaling with temperature in a non-linear fashion, resulting in a fiber with less voids.

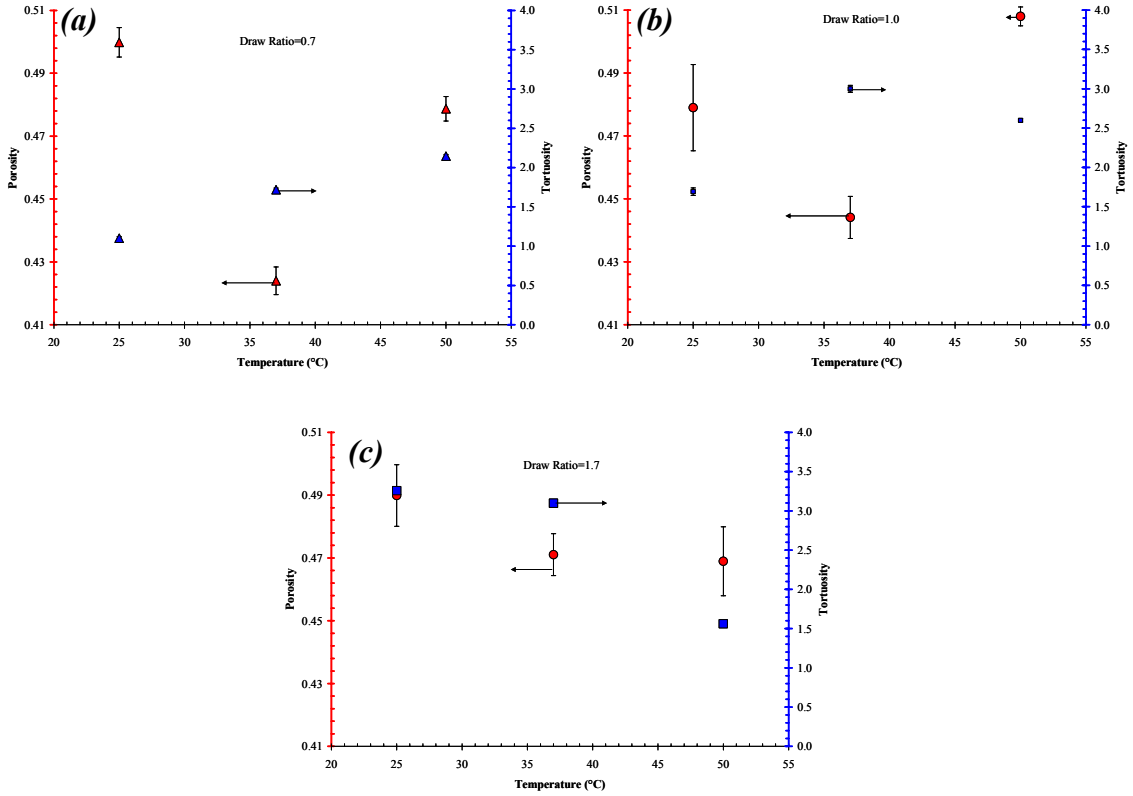

Figure 5.12: Porosity and tortuosity of fiber sorbents as a function of draw ratio and spinning temperature. *(a)* Draw ratio=0.7, *(b)* Draw ratio=1.0, *(c)* Draw ratio=1.7. Porosity measured via gravimetric methods.

To assess the validity of the permeation porosimetry method for determing pore size in fiber sorbents, the pore diameters estimated via permeation porosimetry were compared with those from mercury porosimetry in Figure 5.13. A secondary motivation for this comparison was to investigate the above hypothesis that permeation porosimetry

returns the limiting resistance in the fiber (and therefore the limiting pore size), not the overall resistance (or mean pore size). The mercury porosimetry results shows the full pore size distribution for the fiber sorbents. The most dominating pores are clearly the ~1 micron pores, exhibited in all three samples studied. These large pores are possibly a result of the polymeric cavity that forms around the supported zeolites, as can be seen in many of the SEM images throughout the chapter. An increase in spinning temperature (relative to: DR=1.7, T=25°C) results in these pores becoming even more dominant, while an increase in the draw ratio (relative to the same sample) results in these large pores becoming even larger, as a shift from 1 micron pore diameters to 2 micron pore diameters are exhibited. All three samples exhibit two smaller peaks at approximately 200 nm and 90nm and a broad peak at 30 nm. A simple weighted average of the intrusion volume seems to indicate the zeolites (75wt%, 66vol% loading) are responsible for the 1-2 micron pores, while the smaller pores measured are the intercellular pores within the polymer support. The helium porosimetry results seem to return the average pore diameter out of these three peaks, which is consistent with the hypothesis that helium permeation porosimetry gives insight into the dominating resistance, not necessarily the dominating morphology. However, the previous discussion on pore formation is still valid, as the intercellular pores are the limiting resistance to permeation, and the spinning conditions seem to affect these pores (and their connectivity) the most.

The main pore diameter is approximately 1-2 microns, which is longer than the mean free path of helium (Equation 2), and almost outside of the range of the transition region (Table 2.1), indicating that near-bulk diffusion will be taking place for the

majority of the fiber. This is favorable for rapid diffusion through the fiber wall; a necessity for rapid sorption/desorption cycling.

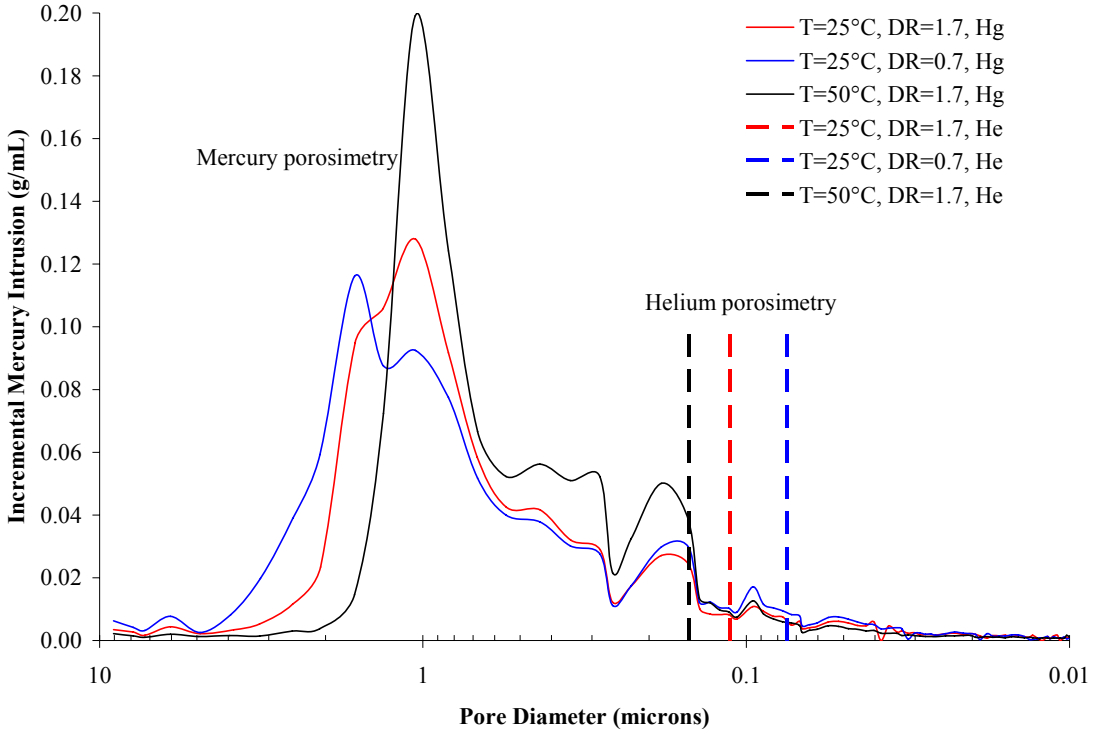

Figure 5.13: Comparison between helium permeation porosimetry and mercury porosimetry for 3 selected fiber sorbent spinning experiments.

5.3 Effect of Bore Fluid Composition on Lumen Side Phase Separation

5.3.1 Spin Parameters

While the bore fluid during spinning is ideally neutral, there are instances where the bore fluid may be unintentionally non-neutral, as in the previous sections. Furthermore, with the need to cast a latex-based polymer onto the lumen side of the fiber,

a smooth surface on the lumen side of the fiber is desired to aid in the film formation of the latex. The next series of experiments served to further test the hypothesis presented in Section 5.2.3.3 on the effect of the bore fluid as well as probe the possibility of creating a smooth lumen side layer via cellulose acetate phase separation. To investigate these factors, the draw ratio and temperature of the spinning experiments were fixed while the bore fluid composition was varied from pure water to pure NMP, as can be seen in Table 5.2.

Table 5.2: Spinning conditions for bore fluid study

Spin Dope	Composition		Spinning Parameters	
Component	**Core Dope (wt%)**		**Parameter**	
CA	10		Core Flow Rate	1000 mL/hr
PVP	4		Bore Flow Rate	250 mL/hr
13X	30		Bore Composition	100% H_2O, 80% H_2O, 60% H_2O, 40% H_2O, 20% H_2O, 0% H_2O, balance NMP
NMP	49.3		Operating Temperature	50°C
H_2O	6.7		Take-up Rate	11.7. m/min
--	--		Air Gap	3 cm

The high extrusion rate (or low draw ratio) was chosen due to the necessity for fibers with large outer diameters, while the higher operating temperature was chosen due to the

relative ease of spinning fibers at 50°C as compared to 25°C[†]. While this sacrifices some of the extremely high permeances that were observed for the 25°C spun fibers (Section 5.2.3.2) the increase in spinning line stability (i.e., a decrease in line breaks) is a more important factor for scaling up to production levels.

5.3.2 Bore fluid-dependent fiber morphology

As can be seen in the series of SEM images in Figure 5.14, the circularity of the fiber bores is improved drastically as the water content in the bore fluid is decreased. As the water concentration in the bore fluid is increased past the neutral point into the non-solvent region, phase separation of the fibers will occur from both the non-solvent quench bath as well as the non-solvent bore fluid. This results in very fast separation times—a consequence of this is that the most rapidly phase separated fibers (bore fluid concentration 0% H_2O-20% H_2O) are not able to be taken up on the drum due to the lack of tensional strength of the mostly-zeolitic fibers. These fibers were simply extruded into the bath and collected from the bath. The non-circular bores are most likely the result of stress points forming in the fiber bore due to the rapid phase separation. As can be seen in the SEM images (Fig. 5.14*a*), at the highest water concentration, the fiber bore forms an elliptical shape due to a collapse within the fiber. An increase in NMP concentration results in the collapse becoming less severe until finally the bores are concentric with the NMP-rich bore fluids. The NMP-rich bore fluid (Fig 5.14*d*) keeps the innermost portion

[†] The relative ease in spinning likely arises from the slower phase separation time of the 50°C dope, as discussed in the previous section. This allows the fiber to remain nascent for a longer period of time, where it is more capable or withstanding tension stresses; the 25°C spun fibers phase separate more quickly, and exhibit more periodic spinning line breaks.

of the fiber solvated for the longest time, essentially allowing the nascent fiber time to develop a perfectly circular structure on the lumen side of the fiber.

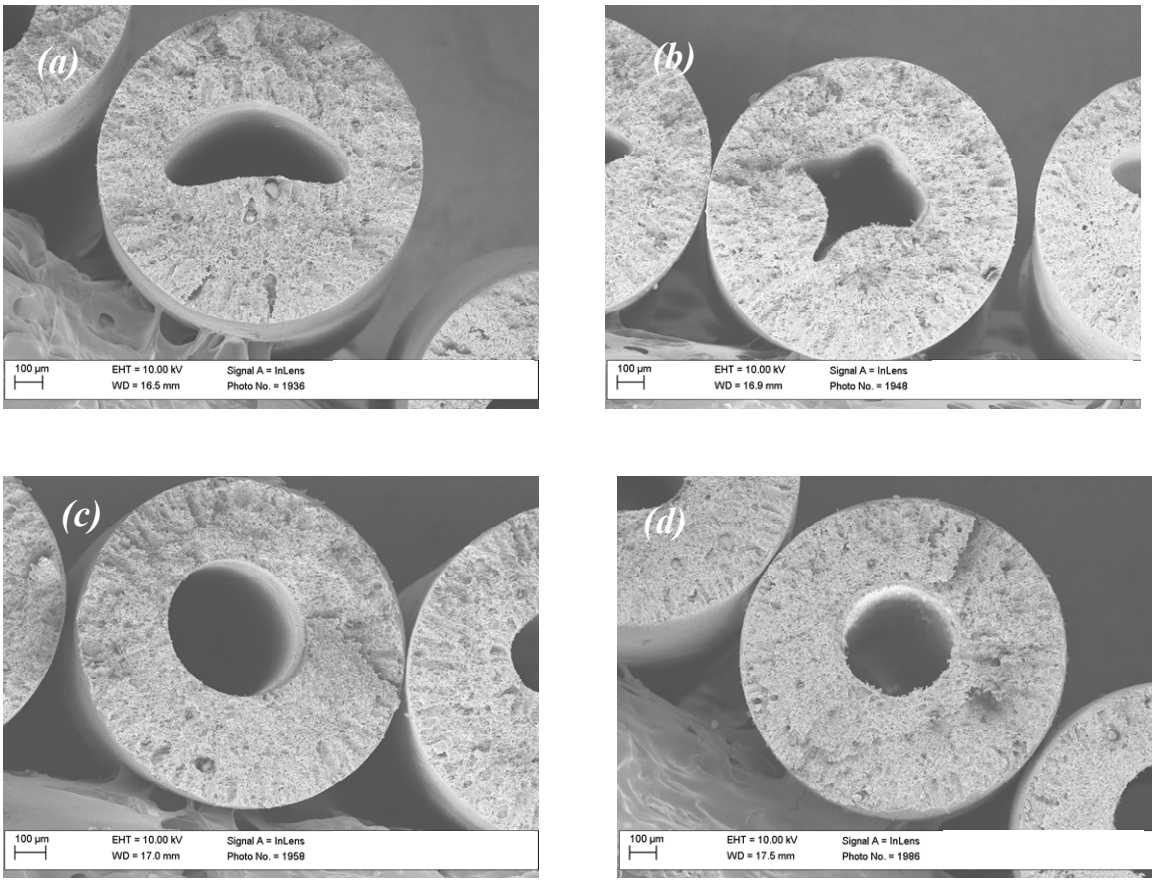

Figure 5.14: Bore circularity as a function of bore fluid concentration. ***(a)*** **100% H_2O,** ***(b)*** **80% H_2O,** ***(c)*** **60% H_2O,** ***(d)*** **0% H_2O; balance NMP.**

5.3.3 Permeation Porosimetry

Helium permeation porosimetry experiments were performed on these fibers to shed light onto the differences in permeance and pore diameter in the fiber sorbents formed with different bore fluids. Section 5.2.3.3 suggested that non-neutral bore fluids

will significantly alter the permeance performance of the fiber sorbents. Figure 5.15 shows the helium permeation results as well as the pore diameters as a function of the water content in the bore fluid.

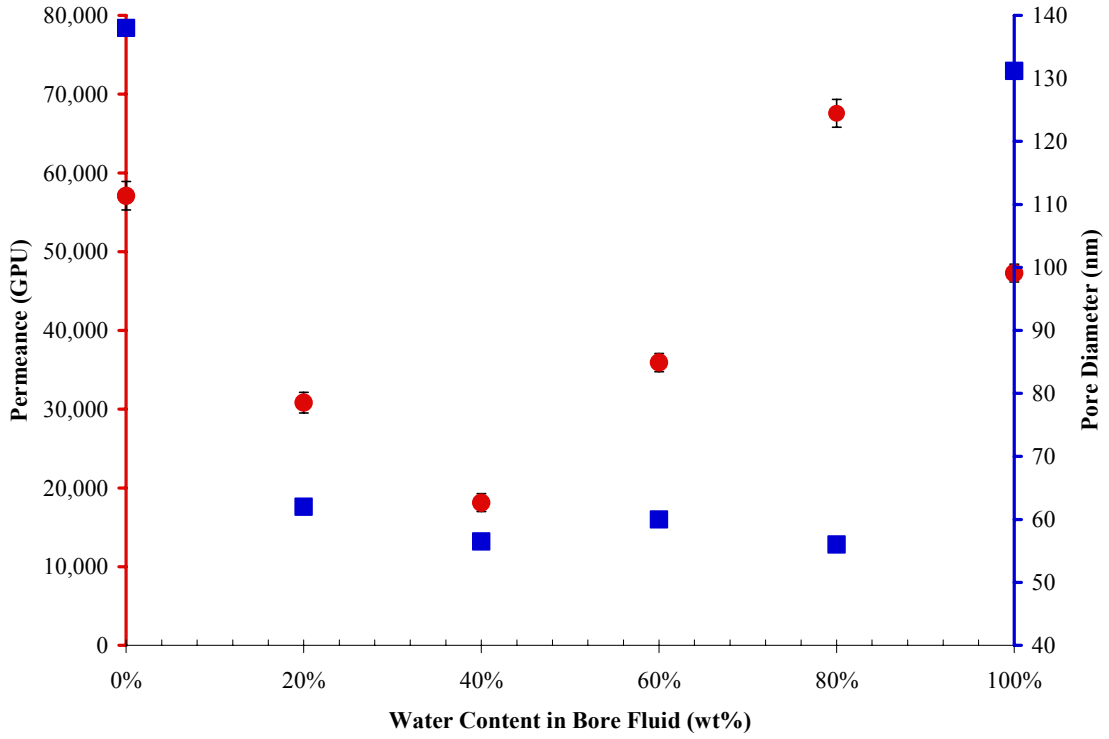

Figure 5.15: Helium permeance and pore diameter as a function of the water content in the bore fluid during spinning.

The helium permeance through the fibers changes significantly depending on the bore fluid used during spinning with a roughly parabolic response being observed. At 50°C, the neutral point bore fluid is most likely near 40% H_2O and 60% NMP. If this bore fluid is at the neutral point, it would yield the lowest permeance according to the hypothesis presented in the previous section (Section 5.2.3.3). Moving away from the neutral point to the more solvent-rich bore fluids yields more permeable fibers; further confirmation

that by delaying the phase separation time via solvent contributions from the bore fluid[‡], cell growth time is increased, thereby resulting in more ruptured pores. Moving away from the neutral point to more non-solvent rich bore fluids also yields an increase in permeance. The effect here is just the opposite: the non-solvent rich bore phase separates the fibers from inside out, removing the innermost region of nucleation and growth speculated about in the neutral and solvent-rich bore fluids (Fig 5.16*b*-*d*) and replacing it with spinodal decomposition (Fig. 5.16*a*)

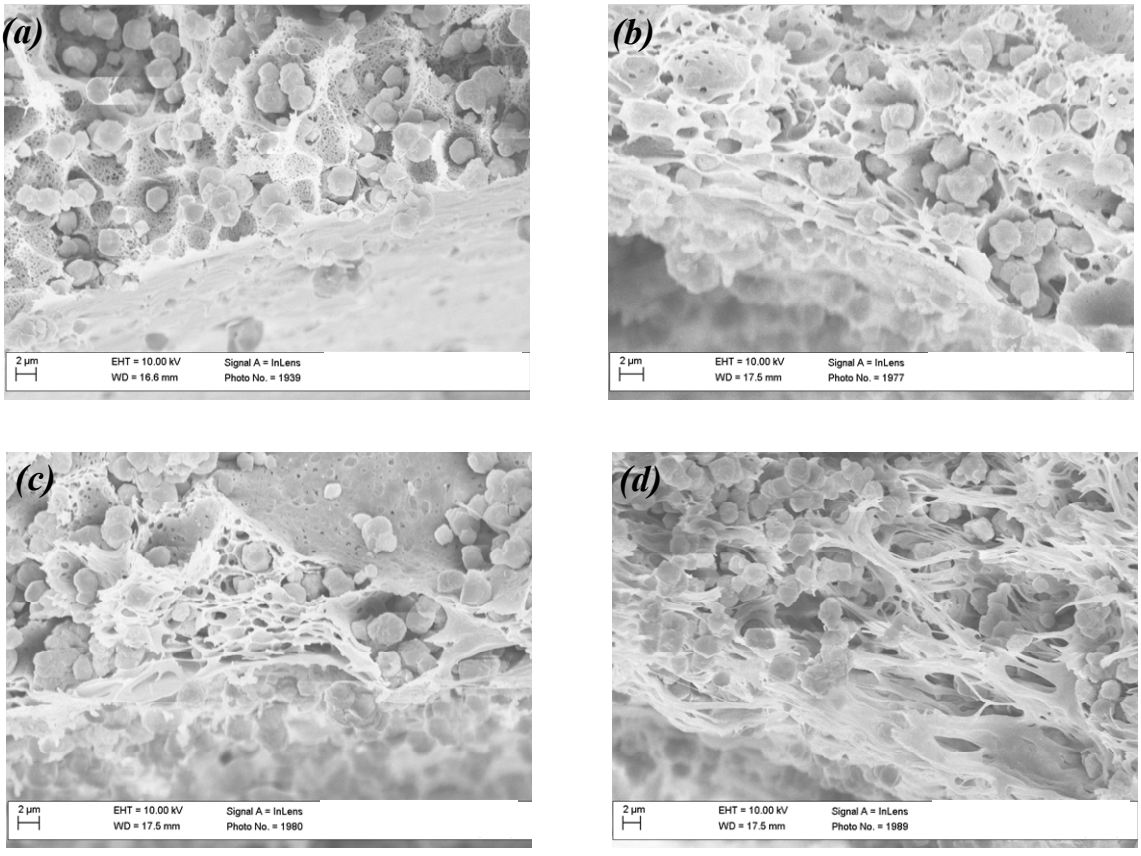

Figure 5.16 Inner lumen smoothness and pore morphology as a result of different bore fluid concentrations used during spinning. *(a)* 100% H_2O (possible spinodal decomposition), *(b)* 40% H_2O (nucleation and growth), *(c)* 20% H_2O (possible nucleation and growth and cell rupture), *(d)* 0% H_2O (severe cell rupture); balance NMP.

[‡] Again, the external non-solvent coagulant must exchange out the extra solvent from the solvevnt-rich bore fluid.

The resulting fiber pore diameter also shows a roughly parabolic dependence on water content in the bore fluid during spinning (Fig. 5.15). The pore diameters were consistent with those observed in Section 5.2.3.4 using helium permeation porosimetry. The parabolic response (Fig 5.15) is consistent with the pore formation hypothesis noted in Section 5.2.3.3—neutral bore fluids result in nucleation and growth at the inner radius with minimal cell rupture (hence the smaller pores). Non-neutral bore fluids allow for either greater cell rupture (solvent-rich bore fluids) and hence larger pores, or spinodal decomposition (non-solvent-rich bore fluids) which also removes the main "resistance area" in the fiber sorbent.

SEM images in Figure 5.16 show that a smoother inner lumen is obtained with non-solvent rich bore fluids. Ideally, this would aid in the latex film deposition—the laticies are formulated to be cast onto smooth substrates, a concept which will be expanded upon in Chapter 6. However, the non-circular bores are unsuited for latex post-treatments and are furthermore not suited for high pressure cooling water due to the weak points where the bore collapsed. Therefore, the rough inner lumen is a non-ideality that will have to be overcome in the creation of a defect-free barrier layer.

5.4 Production of Hollow Fiber Sorbents

The previous sections established the effects that some of the spinning parameters have on the pore morphologies of hollow fiber sorbents composed of cellulose acetate

and zeolite 13X. The spinning experiments were readily repeatable, allowing large quantities of fibers to be produced for further analysis, lumen layer post-treatments and sorption tests. These extra experiments require ample amounts of fiber, so it was necessary to combine the information learned in the previous sections into a "final recipe" for production of large quantities of fibers. One issue that arose was the bore diameter size: a large bore is preferable for reducing cooling water pressure drops, yet a small bore is preferred for increasing the zeolite loading in the cross section of the fiber. As mentioned above in previous sections, a core/bore extrusion ratio of 4 was taken, yet large-bore fibers were the result. In subsequent spins, the extrusion ratio was adjusted to 5, such that the final spinning conditions used in the remainder of the work can be seen in Table 5.3.

Table 5.3: Spinning parameters used to produce the bulk of the fibers for this work

Spinning Parameters	
Parameter	
Core Flow Rate	1000 mL/hr
Bore Flow Rate	200 mL/hr
Bore Composition	80/20 NMP/H_2O
Operating Temperature	50°C
Take-up Rate	11.7. m/min
Air Gap	3 cm

As mentioned previously, a 50°C spinning temperature was chosen due to the decrease in the frequency of spinning line breaks as compared to a 25°C spinning experiments. The decrease in line breaks is most likely a result of slower phase separation times, allowing for the nascent fiber to be drawn more consistently. The 25°C fiber will phase separate more rapidly, and will not always be able to withstand the drawing from the take-up drum. While the decrease in phase separation time results in less permeable fibers, by using a slightly solvent-rich bore fluid at 50°C, some of the decreases in permeance can be recovered via the nucleation-growth and cell rupture mechanism discussed earlier. Of course, these fibers with "lower" permeances still exhibit *extremely* high fluxes (30,000 GPUs), which suggests that the indicating the desired open, continuous pore structure has largely been achieved. SEM images of these fibers reveal that the fiber design objectives were achieved. As can be seen in Figure 5.17, the fiber OD and ID are close to the design goal, with the OD being 1100 microns, and the ID being 300 microns as well as good sorbent dispersion seen throughout the porous polymer matrix. The bottom figure shows that the preferred "sieve-in-a-cage" morphology, needed for rapid mass transport through the fibers, was also achieved.

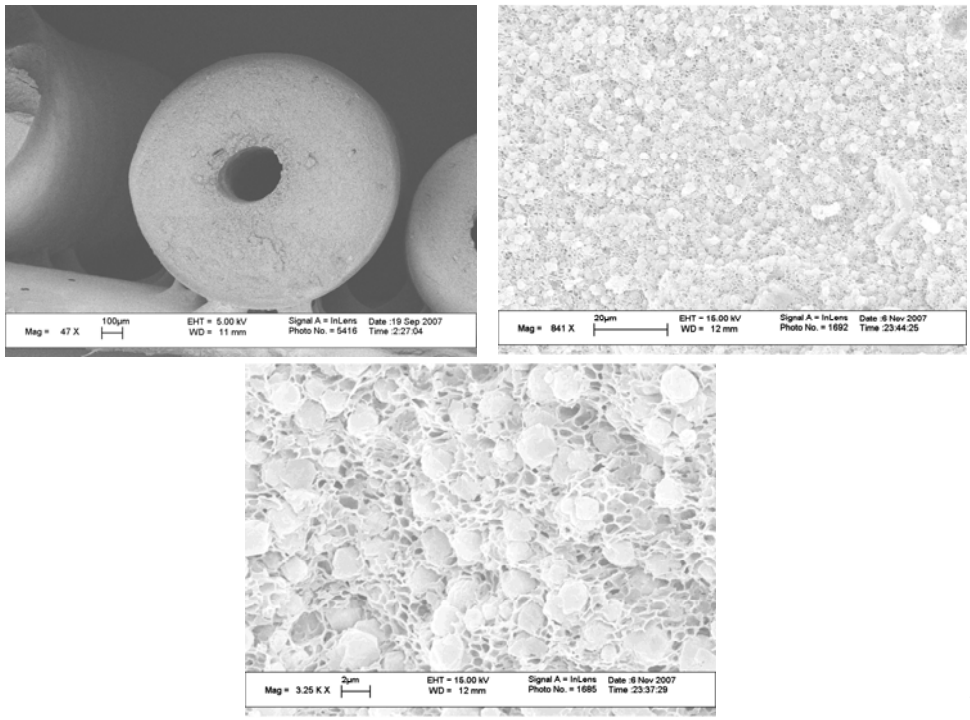

Figure 5.17: (*top left*): SEM image of fiber sorbent. (*top right*): 13X dispersion (75wt%) in cellulose acetate matrix. (*bottom*): 13X particles exhibiting "sieve in a cage" morphology in cellulose acetate matrix.

5.4.1 Fiber sorbent zeolite loading

TGA experiments were performed on these fiber sorbents to estimate the zeolite loading within the fiber. For the TGA studies, a simple three step heat program was used to confirm the predicted loading of zeolite 13X in the fiber sorbents. The first two heating steps removed excess water from the zeolites and cellulose acetate, and the final step burned off the cellulose acetate (Figure 5.18). The final loading of the fiber sorbents was found to be 74.5wt% zeolite 13X.

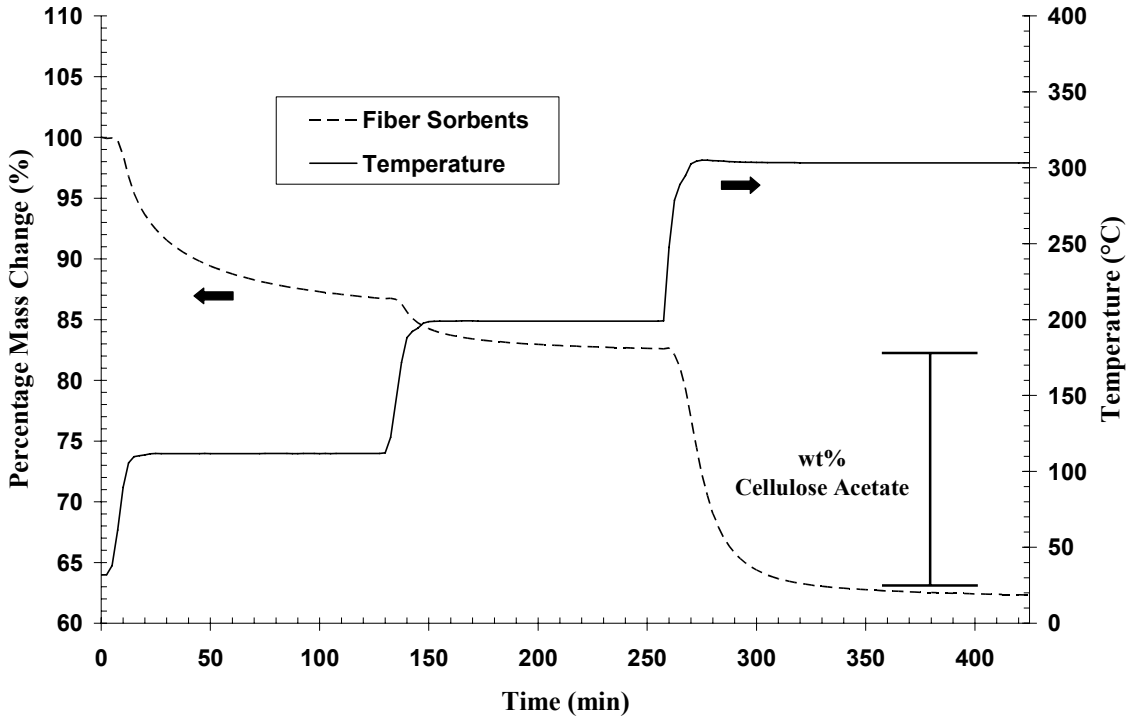

Figure 5.18: TGA results for cellulose acetate/13X fiber sorbents in an air atmosphere to determine zeolite loading.

5.5 Summary

Spinning of highly-loaded hollow fiber sorbents using cellulose acetate has proven to be a repeatable and reliable process. Spinning parameters were varied to determine their effect on the formation of the porous cellulose acetate support. Ideally, low draw ratios, high core-to-bore extrusion ratios, ambient temperatures and solvent-rich bore fluids should be used to achieve fibers with the most porosity and most interconnected pores. The bulk of the fibers produced for this work utilized low draw ratios, high core-to-bore extrusion rates, solvent-rich bore fluids but were spun at higher temperatures than ambient. This sacrifices some permeance in favor of a spinning

process exhibiting less line breaks, which ultimately is a more important factor for scale up. These fibers were then used for the latex post-treatments as well as for sorption testing, and these two extensions will be discussed in Chapters 6 and 7, respectively. Finally, the zeolites were found to be well dispersed within the polymer matrix, and the desired "sieve-in-a-cage" morphology (which is favorable for rapid access to the sorbents) was achieved.

5.6 References

1. Daubert, D.E.; Danner, R.P. *Physical & thermodynamic properties of pure chemicals: data compilation*, **1989**, Taylor & Francis, Washington, D.C.
2. Balashova, I.M.; Danner, R.P.; Pushpinder, S.P.; Duda, J.L. Solubility & diffusivity of solvents and nonsolvents in polysulfone & polyetherimide, *Ind. Eng. Chem. Res.*, **2001**, 40(14), 3058-3064.
3. Husain, S. Mixed Matrix Dual Layer Hollow Fiber Membranes for Natural Gas Separation. Georgia Institute of Technology, GA, *Ph.D. Dissertation* **2006**.
4. Bhandari, D. Hollow fiber sorbents for the desulfurization of natural gas, Georgia Institute of Technology, GA, *PhD Dissertation,* **2010**.
5. Bessho, N. Advanced Pressure Swing Adsorption System with Fiber Sorbents for Hydrogen Recovery. Georgia Institute of Technology, GA, *PhD Dissertation,* **2010.**
6. Ruthven, D.M. *Principles of Adsorption & Adsorption Processes*, Wiley-Interscience, **1984**.
7. Clausi, D.; Koros, W.J. Formation of Defect-Free Polyimide Hollow Fiber Membranes for Gas Separations, *Journal of Membrane Science,* **2000**, 167 (1), 79-89.
8. Kosuri, M. Polymeric Membranes for Super Critical Carbon Dioxide ($scCO_2$) Separations, *PhD Dissertation*, Georgia Institute of Technology, GA, **2009**.

9. Carruthers, S. Integral-skin Formation in Hollow Fiber Membranes for Gas Separations, *PhD Dissertation*, University of Texas - Austin, TX, **2001**.
10. Pesek, S.; Koros, W.J. Aqueous Quenched Asymmetric Polysulfone Hollow Fibers Prepared by Dry/Wet Phase Separation, *Journal of Membrane Science*, **1994**, 88(1), 1-19.
11. Wallace, D. Crosslinked Hollow Fiber Membranes for Natural Gas Purification and Their Manufacture from Novel Polymers, *PhD Dissertation*, University of Texas - Austin, TX, **2004**.
12. Husain, S.; Koros, W.J. Mixed matrix hollow fiber membranes made with modified HSSZ-13 zeolite in polyetherimide polymer matrix for gas separation, *Journal of Membrane Science*, **2007**, 288(1-2), 195-207.
13. Schofield, R.W.; Fane, A.G.; Fell, C.J.D. Gas & vapour transport through microporous membranes. I. Knudsen-Poiseuille Transition, *Journ. Memb. Sci.*, **1990**, 53(1), 159-171.

Chapter 6

Formation of Defect-free Lumen-side Barrier Layer

A unique challenge facing fiber sorbents is the need to create a robust lumen-side barrier layer to allow facile heat exchange between bore and fiber wall without significant mass exchange. This layer can be introduced by post-treatment or direct spinning onto the interior of the fiber. For the fiber sorbent RTSA system to operate effectively, the lumen layer must provide a robust barrier to both gas and water during continuous thermal cycles. The efficacy of the barrier layer can be probed with permeation techniques, as discussed later. Good adhesion between the sorbent layer and the lumen layer is required, and the barrier polymer deposition medium must be a poor solvent or non-solvent for the sorbent layer polymer. This chapter will first present methods and corresponding challenges facing various barrier layer fabrication techniques, followed by results of some experimental trials, and finally moving to a discussion of the experimental observations.

With the above requirements in mind, several different routes were explored to create a defect-free lumen layer: rapid interfacial polymerization, co-spinning, and latex post-treatment. Rapid interfacial polymerization entails placing a reactive liquid into the pores of the fiber, which is followed by a bore side wash with a secondary reactive liquid.

By design, the two liquids will react at their interface, creating a layer with a thickness that is dependent on the rate of reaction as well as the reagent diffusion through the nascent layer created. One of the few literature mentions of a lumen-side permeable layer in hollow fibers uses a rapid interfacial polymerization technique[1], and this technique was adapted to create a dense barrier layer on the fiber sorbents. Ultimately, this technique was unsuccessful, as the layer created was unable to withstand normal permeation experiments. Results from this technique can be found in Appendix B.

The second technique—dual layer fiber spinning—was considered to create the lumen layer during the formation of the fiber sorbent layer, thereby removing the need for further post-treatments. This approach required the design and fabrication of composite spinnerets to enable a thin lumen layer to be directly spun along with the fiber sorbent dope.[2] Ultimately, many issues prevented a successful spin; primarily, the inner lumen layer undergoes non-solvent induced phase separation as a result of contact with the bore fluid, rather than the desired vitrification which can occur for external skins on hollow fiber membranes open to solvent loss into an air gap. Furthermore, the fiber sorbent support polymer (CA) and the barrier polymer (polyacrylonitrile, PAN) were immiscible, leading to barrier layer delamination. Unfortunately, the dual layer fibers will also require post-treatment to remove lumen layer bypass, a concept which is elaborated on in Section 6.2.2. Results from this technique, including spinneret designs, are reported in Appendix C.

Finally, latex-based post-treatments were selected as the method of choice for creating the dense lumen-side barrier layer. This method proved to be a reliable and repeatable technique after an optimization of the process[3]. Initial work focused on developing Neoprene® barrier layers cast from aqueous laticies. It was found that after chemically crosslinking the Neoprene®, the barrier layer was resistant to both high temperatures and oxygen (i.e., retaining permeation properties after extended soaks in air at 141°C), but was too permeable to water. For water-resistant sorbents such as solid supported amines or Silicalite-1, Neoprene® barrier layers will likely be preferred due to the aforementioned temperature and oxidative resistance. However, as this work has focused on using the water-sensitive zeolite 13X as a proof-of-concept, Neoprene® was unsuitable for sorption tests that include cooling water in the bores (Chapter 7). Clearly, the permeating water would reduce the zeolites CO_2 uptake via competitive sorption (Appendix D). Nevertheless, the work performed on Neoprene® established the basic process of post-treating the fiber sorbents and identified some key issues that must be tackled for a successful barrier layer to be formed. The full discussion on Neoprene® barrier layers can be found in Appendix B.

As discussed in Chapter 3, polyvinylidene chloride (PVDC) was chosen as a successor to Neoprene® due to its low water permeability. Compared to Neoprene®, PVDC is approximately 1,000 times less permeable to water[4]. However, arriving at a defect-free PVDC lumen layer proved to be much more difficult Neoprene®, and while many of the lessons learned from the Neoprene® post-treatment experiments could be carried over to PVDC post-treatment experiments, a deeper understanding of latex film

formation mechanisms was required to achieve success with PVDC. Therefore, a series of film-based experiments was used to gauge the effect the film substrate, latex age, and drying rate had on the latex film formation and subsequent permeation properties. These results were then extended to post-treating hollow fiber sorbents; initially in single-fiber modules for permeation experiments (this chapter), and eventually scaling to 6-fiber modules for sorption experiments (Chapter 7).

6.1 Development of PVDC Lumen Layer, Film Studies

6.1.1 Challenges of casting onto fiber sorbent substrates

Chapter 2 discusses some general hypotheses regarding formation of dense films from laticies on smooth, dense, and continuous substrates. While the literature base on this topic has grown substantially in the past twenty years[5], very few attempts have been made to characterize or understand the film formation properties when the latex is cast onto a ***porous substrate***[6,7]. Further complicating this case for fiber sorbent post-treatment applications, the PVDC latex must be forced through a 300-400 micron hollow fiber bore while in contact with a highly porous (~40-50%, as seen in Chapter 5), rough, hydrophilic and inorganic-organic hybrid material, which is then followed by a forced convection drying via a gas sweep through the bores of the fibers. This introduces many new non-idealities into the film formation process and the resulting film can have defects that range from the macroscopic scale down to the nanoscopic scale. For an effective barrier, the layer must be essentially molecularly perfect with few defects, as discussed in

Chapter 2. Due to the myriad of non-idealities that have been introduced by casting the layer onto the cellulose acetate/13X fiber sorbent matrix, several experiments were performed to isolate the most relevant factors dictating the film formation process.

One of the main issues associated with a lumen-side fiber sorbent post-treatment using an aqueous latex is the capillary forces that arise as a result of the porous substructure. These capillary forces are caused by the latex being able to wet the inner surface; once the latex wets the inner surface, the liquid will attempt to minimize its free energy by filling the pores of the fiber[8]. The pore-filling action removes latex serum from the latex, most likely inhibiting defect-free film formation (discussed in Section 6.3). To investigate this capillarity effect, latex films were cast on continuous glass plates (control), porous hydrophobic substrates, porous hydrophilic substrates, and cellulose acetate/13X films. Another non-ideality is the lack of smoothness of the inner surface of the fiber. If there are any large discontinuities in the surface, such as a crevice, the ability of the nascent film to form a continuous layer will be undermined by the inability of the film to coalesce at the discontinuity, an example of which is illustrated in Figure 6.1. This effect was investigated by casting films on a smooth glass plate (control) and a finely etched glass plate, where the etches represent large discontinuities in the film.

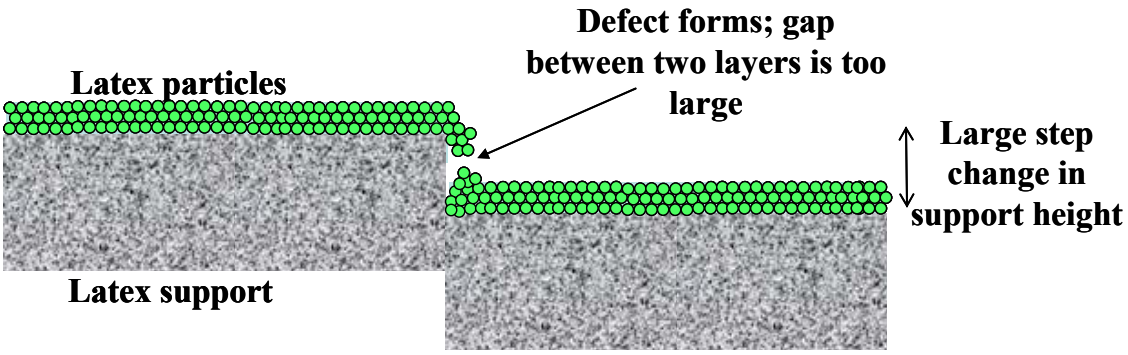

Figure 6.1: Illustration of a large discontinuity on a latex substrate. The discontinuity can disrupt the particle ordering, ultimately leading to a defect in the continuous film.

Once the lumen layer has been successfully cast onto the inner surface of the fiber, the layer must undergo drying. Unlike conventional flat sheet drying, free convection/evaporation drying is difficult to achieve within fiber sorbents, as the remaining latex held within the bore needs to be evacuated after the post-treatment. Therefore, a forced convection gas sweep is used to dry the lumen layer, which—depending on the water vapor content of the gas—has the possibility to be a much more severe drying rate than simple free evaporation at ambient conditions. To investigate this effect, three drying conditions were chosen for PVDC films cast onto cellulose acetate/13X films (Table 3.2): completely dry nitrogen followed by 71°C vacuum ("dry" mode), water vapor-saturated N_2 followed by 71°C vacuum ("wet" mode), and water vapor-saturated N_2 followed by drying at ambient conditions ("graded" mode). Finally, the latex age can have a large impact on the continuity of the final film. To test this effect, the substrate and drying rate experiments were repeated for fresh PVDC latex as well as PVDC latex that was aged for 2 years.

6.1.1 Effect of drying condition

PVDC latex was cast onto cellulose acetate/13X mixed matrix films and dried several different ways, as mentioned above. During the wet phase of the film casting (see Chapter 3 for details), no obvious changes were observed in the nascent films. In the "wet" drying mode the film was moved to a vacuum oven to remove excess water which resulted in very rapid film formation. This rapid film formation resulted in large stress fractures for the aged latex films and bubbles and boils in the fresh latex film (Figure 6.2). When the films were dried in a dry glove bag ("dry" mode) a thin cloudy skin layer could be observed on the outer surface of the nascent film. However, once the film was moved to the vacuum oven, rapid film formation again occurred, resulting in large stress fractures and bubbles in the aged and fresh latex films, respectively. The absence of bubbling in the aged latex films is especially interesting, as it likely indicates that the latex loses some volatile component over time. One hypothesis is that the latex loses a volatile "leveling agent;" this leveling agent serves to reduce the T_g of the PVDC particles, thereby allowing them to more easily coalesce with nearby particles[9]. Finally, films dried with the "graded" drying protocol were found to form an amber colored and crack-free film after approximately 15 hours drying at ambient conditions.

Figure 6.2 show SEM images of the aged and new latex films cast onto the cellulose acetate/13X support dried via the "wet" and "dry" drying method. The figure illustrates the bubbling and cracking effects that were visually observed during the film formation experiments. Closer examination of the non-cracked film areas indicates the

presence of well-formed, dense areas of PVDC when the new latex is used, whereas porous, poorly formed films are found when the aged latex is used, as seen in Figure 6.3. This likely indicates that, at least in the case of the new PVDC, the continuous film forms correctly during the rapid drying, but the necessity for stress relaxation causes the films to crack.

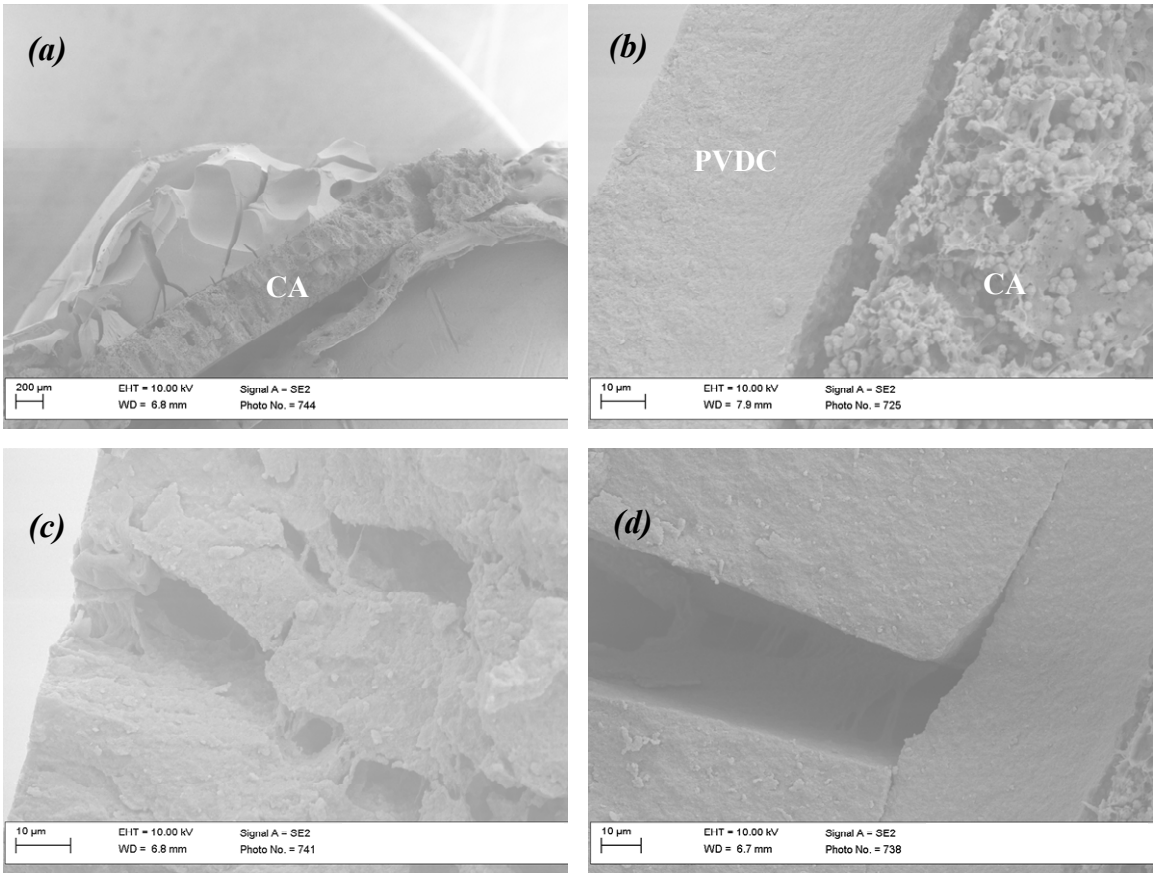

Figure 6.2: PVDC films cast onto cellulose acetate/13X film substrates using the "dry" and "wet" drying methods. ***(a)*** **Large bubbles and cracks are clearly seen in the PVDC film.** ***(b)*** **Delamination between the cellulose acetate/13X support and the PVDC layer.** ***(c), (d)*** **Large cracks in the rapidly dried PVDC film.**

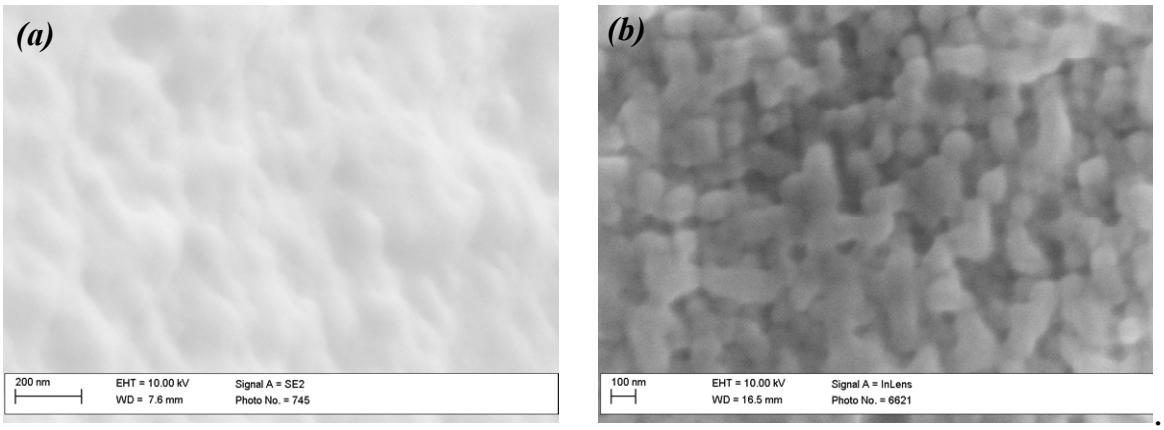

Figure 6.3: High magnification SEM images of "crack-free" areas of PVDC films cast using the "wet" drying method. *(a)* PVDC films cast from the fresh PVDC latex show a lumpy surface with well-adhered, deformed PVDC particles. *(b)* PVDC films cast from the aged latex show a globular structure with poor particle deformation and intercalation.

When the drying rate is markedly slowed via the "graded" drying mode, the film was found to form a dense, level coating on top of the cellulose acetate/13X matrix, as seen in Figure 6.4. The coating appears to be well-adhered to the cellulose acetate/13X matrix, and no cracks or large crazes could be detected in the cross-sectional SEM images. However, the aged latex film was found to have sizable craters found in the cross-sectional images (Fig 6.4*b)*. As can be seen in Figure 6.4*c*, the films cast from the new latex yield a dense PVDC layer with no PVDC globules visible, indicating that the film likely formed correctly. In the case of the films cast from the aged PVDC, a dense layer is also observed, however, the PVDC globules are still slightly visible, but appear to be well adhered to each other. From SEM images alone, the "graded" drying method is clearly preferred for drying the nascent PVDC films. Of course, SEM images alone cannot show nanoscopic defects that a gas molecule might "see", so helium and nitrogen permeation experiments were performed on these six films to elucidate the true extent of proper film formation.

Table 6.1 shows the results from the helium and nitrogen permeation experiments. As expected from both visual observations and SEM images, the films dried via the "wet" and "dry" mode were completely defective, yielding permeances that were similar to the bare fiber permeances discussed in Chapter 5. The He/N_2 selectivity through the films is close to Knudsen selectivities (2.6 for helium/nitrogen), though the bulk selectivity contribution is clearly present. Due to the large PVDC cracks, the dominating resistance to permeation is most likely the CA/13X film, which was found to have pores that would fall into the transition region (Chapter 5), and these selectivities seem to confirm that. The films dried in the "graded" mode—which were visually the most promising—yielded significantly lower permeances than the defective films. It is interesting to note that the old latex yields a helium permeance of ~55 GPUs while the new latex yields a helium permeance of ~5.5 GPUs. Knudsen selectivities of 2.6 are expected if the films exhibit pores radius' is a tenth of the mean free path of either helium or nitrogen, and bulk selectivities are expected if the pore radius is an order of magnitude larger than the mean free path, as discussed in Chapter 2.

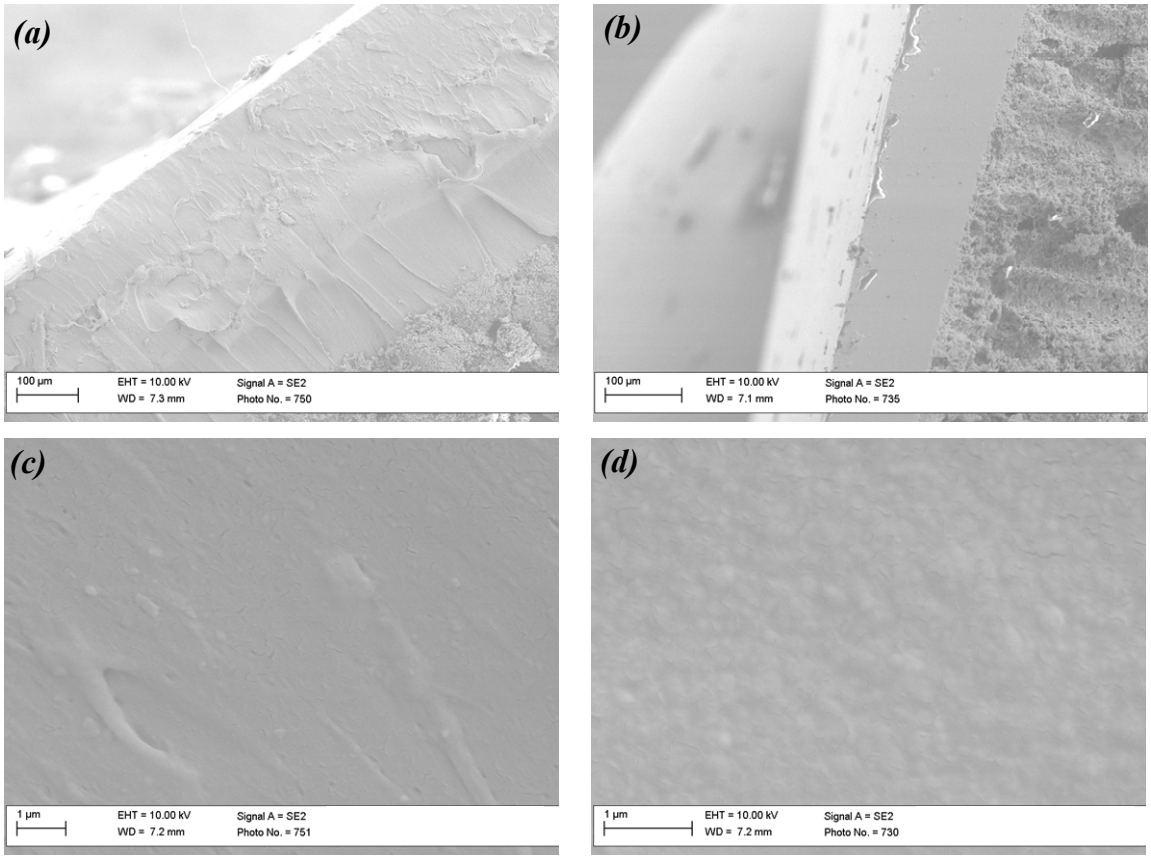

Figure 6.4: PVDC films cast onto a cellulose acetate/13X support using the "graded" drying mode. *(a)* Film cast from new PVDC latex shows good adhesion to CA support. *(b)* Film cast from aged PVDC latex shows good adhesion to CA support, though some cratering is observed in the cross section of the film. *(c)* Enhanced magnification of PVDC film from the fresh latex shows a continuous structure with no globular particles detected. *(d)* Enhanced magnification of PVDC film from the aged latex shows a continuous structure with slightly globular particles detected.

Table 6.1: Effect of drying rate on PVDC film formation (CA/13X substrate)

	Drying Method					
Films	"Dry"		"Wet"		"Graded"	
Latex Sample	**Helium Permeance (GPU)**	**He/N_2 Selectivity**	**Helium Permeance (GPU)**	**He/N_2 Selectivity**	**Helium Permeance (GPU)**	**He/N_2 Selectivity**
2-year aged	4.8 ±0.11 x 10^5	1.76±0.05	5.3±0.28 x 10^5	2.15±0.15	54.7±0.4	1.63±0.05
Fresh	6.9±0.15x10^5	2.5±0.4	2.2±0.19x10^5	2.2±0.03	5.6±0.4	1.87±0.1

T=35°C, feed pressure of 10 psig used for highly defective films (>10^4 GPU), 100psig for slightly defective films (<1000 GPU). Error bars represent 1 standard deviation.

The selectivities observed in these experiments are between 1 (bulk) and 2.65 (Knudsen), indicating that there exists a porous pathway through the film that has a pore radius that allows for both Knudsen and bulk diffusion to contribute. As judged by the higher selectivities and lower permeances of the films cast from the new latex, perhaps the pores that form are fewer and perhaps smaller compared to the aged latex, and the pathway through the film is a more tortuous one. This concept of a "porous" barrier layer is important for the discussion of the film formation mechanism, which is discussed in Section 6.3. The "graded" drying mode and the use of fresh latex is clearly the preferred for forming the barrier layer, though there is much work required to optimize this drying procedure to result in "defect free" films cast onto porous supports.

6.1.2 Effect of substrate

Once a drying rate was established that allowed for adequate film formation (a 10^5 reduction in permeance when compared to the uncoated substrate) on cellulose acetate/13X substrates, the effect of the substrate on the latex film formation properties was studied. Smooth glass (control) and etched glass substrates were used to investigate film formation mechanisms in ideal, non-porous conditions, while porous nylon 6,6 films were used to test hydrophilic porous substrates, and porous PVP-free polycarbonate films were used to test hydrophobic porous substrates. Fresh and aged latex samples were cast onto these four substrates and were dried using the "graded" drying mode investigated in the previous section. For the glass substrates, a water meniscus was observed on the glass plate that slowly receded as the film dried with a milky center and clear edges.

Once dried, the new latex formed a clear and highly flexible film, not unlike common household Saran®; the films cast on the etched glass had the imprint of the etches formed into the film, yet these films were just as flexible. However, the aged latex formed an amber colored film that was highly brittle; again, the shape of the etches on the plate were imprinted into the film. One inch strips of the films from the aged latex/smooth glass were able to be bent approximately 130° before breaking, whereas one inch strips from the aged latex/etched glass were only able to be bent approximately 45° before breaking. Interestingly, the breaks in the etched glass film almost always occurred at the etch imprints of the film where stress concentration points (or lack of film coalescence) exist. The new latex films were not able to be broken via simple bending tests.

Films cast onto the hydrophobic polycarbonate substrate were observed to poorly coat the substrate—the PVDC latex pooled together above the substrate, leaving parts of the substrate uncoated. This was confirmed once the nascent latex was dried, films were poorly formed, brittle and not adhered to the polycarbonate substrate. This was observed in both fresh and aged laticies. While the hydrophobic substrates had incomplete coatings, PVDC films cast onto the hydrophilic nylon substrates were found to make smooth and even coatings from the fresh latex. SEM images of the films cast onto the hydrophilic substrate show a well-adhered, even coating (Figure 6.5*a*), while the films cast onto the hydrophobic substrate exhibit delamination between the PVDC and PC layers (Figure 6.5*b*). Upon closer magnification, the fresh PVDC cast onto the nylon substrate showed partial particle deformation and particle intercalation (Figure 6.5*c*), although a porous structure was still obtained. The aged PVDC cast onto the nylon

substrate showed particle deformation, yet seemingly poor polymer-polymer interdiffusion (Figure 6.5*d* and inset, respectively).

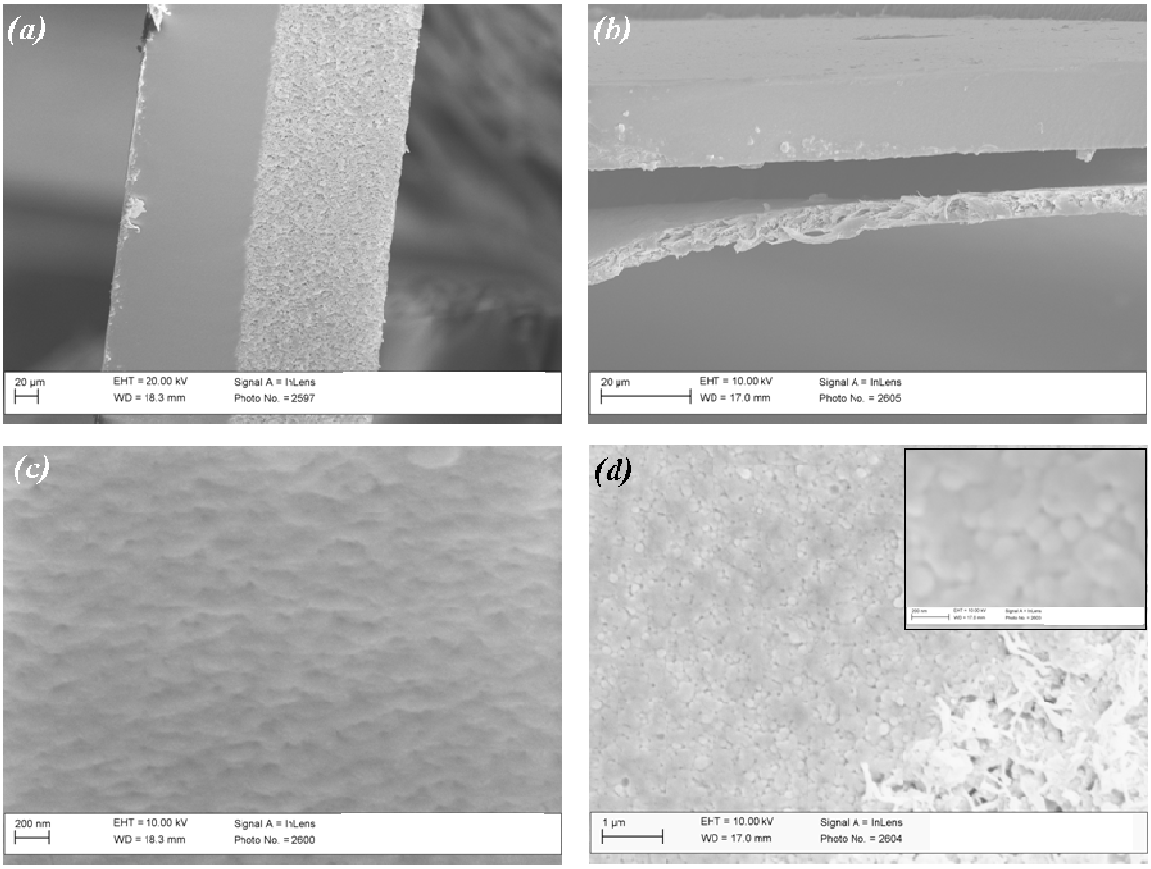

Figure 6.5: SEM images of aged and fresh PVDC latex cast onto nylon 6,6 and PVP-free polycarbonate substrates. *(a)* PVDC (fresh latex) film well adhered to nylon 6,6 substrate. *(b)* PVDC (aged latex) delaminated from polycarbonate substrate. *(c)* High magnification image of PVDC from fresh latex cast onto nylon substrate showing partially deformed, intercalated particles. *(d)* High magnification image of PVDC from aged latex cast onto nylon substrate showing deformed particles that are poorly intercalated. Inset clearly shows lack of particle intercalation.

SEM images in Figure 6.6 of the smooth and etched glass PVDC films reveal a marked difference between the aged and new laticies. The PVDC films from the aged latex were found to exhibit globular morphology in the cross-sectional images for both smooth and etched glass substrates (not shown). Further magnification reveals the individual PVDC particles packed together, with only slight intercalation between the particles observed (Figure 6.6*a*). The face of the film cast on the etched glass substrate

has large discontinuities corresponding to the etch imprints (Figure 6.6*b*), with large cracks clearly present. The films cast onto the smooth glass do not exhibit this phenomenon. The films cast from the fresh latex did not exhibit this severe globular structure in the cross-sectional images, even upon further magnification, though a "lumpy" surface is still exhibited indicating that perhaps the PVDC particles have not *completely* intercalated (Figure 6.6*c*). Finally the outer edge of the film was found to be quite dense, smooth, and free of the aforementioned "lumpy" surface (Figure 6.6*d*). Furthermore, there was no observable discontinuities occurring at the etch lines for the fresh PVDC film cast on the etched glass substrate (not shown).

.

Of course, SEM images do not completely reveal the efficacy of a barrier polymer; helium and nitrogen permeation experiments were again used to probe the PVDC films. Table 6.2 summarizes the permeation results of the films cast onto varying substrates. The films cast onto the hydrophobic polycarbonate films were, as expected, completely defective yielding high fluxes through the film. PVDC films cast from the aged latex onto the porous nylon substrate were found to also be defective, which is easily confirmed via the SEM images in Figure 6.5. Most interestingly, the films from the fresh PVDC latex cast onto the hydrophilic nylon exhibit very low helium permeance of 0.4 GPU, as opposed to the 5.6 GPU permeance exhibited by the cellulose acetate/13X films cast from the same latex (the films were approximately the same thickness). Inference from Figure 6.5 suggests that while the fresh latex exhibited good particle intercalation, the aged latex did not, perhaps explaining the large difference in helium permeance that was observed. The near-bulk selectivity observed likely indicates the

presence of large pores in the PVDC film. If the defects through the film have pore sizes that are larger than 210 nm (an order of magnitude more than the helium mean free path at 100 psig), then bulk selectivities would be expected. The films cast from the aged latex onto the glass substrates—both smooth and etched—were too brittle to mask the films into the permeation cells; films that were able to be successfully masked were broken by the low gas pressures used in these experiments.

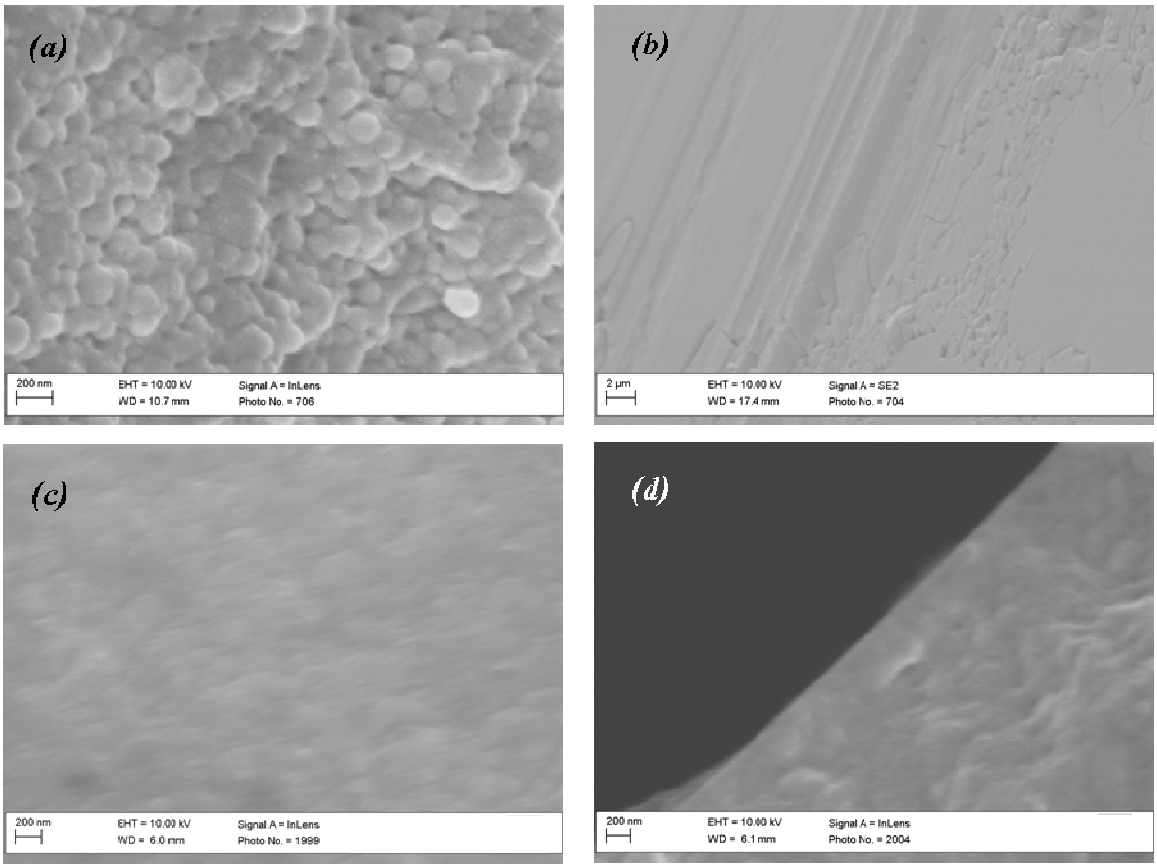

Figure 6.6: SEM images of PVDC films cast onto smooth and etched glass substrates. (a) Aged latex cast onto smooth glass substrate. (b) Aged latex cast onto etched glass substrate. (c) Fresh latex cast onto smooth glass substrate. (d) Fresh latex cast onto etched glass substrate

Finally, the films cast from the fresh PVDC latex onto the glass substrates were not able to be measured on the isobaric system due to their exceedingly low permeances. These

films were installed into the isochoric system and exhibited extremely low helium permeances of approximately 10^{-4} GPU; nitrogen fluxes were much lower than the capabilities of the permeation system (the nitrogen permeation experiments yielded the same results as a typical leak test!). This indicates that given an ideal (or even slightly non-ideal, as in the case of the etched glass) substrate and a reasonable set of drying conditions ("graded" drying mode), the fresh PVDC latex works as designed.

Table 6.2: Effect of substrate on PVDC film formation ("graded" drying)

	Substrate			
	PVP-free Porous Polycarbonate		**Porous Nylon 6,6**	
Latex Sample	**Helium Permeance (GPU)**	**He/N_2 Selectivity**	**Helium Permeance (GPU)**	**He/N_2 Selectivity**
2-year aged	$3.5 \times 10^4 \pm 0.01$	2.28±0.02	121±0.28	1.1±0.05
Fresh	$1.3 \times 10^4 \pm 0.05$	2.2±0.05	0.41±0.02	1.2±0.13
	Smooth Glass		**Etched Glass**	
Latex Sample	**Helium Permeance (GPU)**	**He/N_2 Selectivity**	**Helium Permeance (GPU)**	**He/N_2 Selectivity**
2-year aged	--	--	--	--
Fresh	1×10^{-4}	∞	1×10^{-4}	∞

T=35°C, feed pressure of 10 psig used for highly defective films (>10^4 GPU), 100psig for slightly defective and defect-free films (<1000 GPU). Nitrogen permeance for defect-free films were too low to measure. Aged latex films cast onto glass were too brittle to test. Error bars represent 1 standard deviation.

6.1.3 Effect of Latex Age

As observed in the previous sections, the age of the latex has a marked effect on the film formation properties and subsequent permeation results. To investigate this, the two latex samples cast onto the smooth glass substrate (the control substrate) using the "graded" drying mode were analyzed via XRD and DSC. XRD results, in Figure 6.7, show a typically amorphous diffraction pattern for the film from the fresh PVDC latex, as expected. The films cast from the aged latex show a distinct shift in the diffraction pattern towards high angles. Using Bragg's Law[10],

$$n\lambda = 2d \sin\theta \qquad \textbf{(1)}$$

the d-spacing of the aged PVDC sample is estimated to be approximately 1.6 angstroms. While there is a significant amount of spread in the diffraction pattern, this indicates that there exists a small fraction of crystallinity in the aged PVDC.

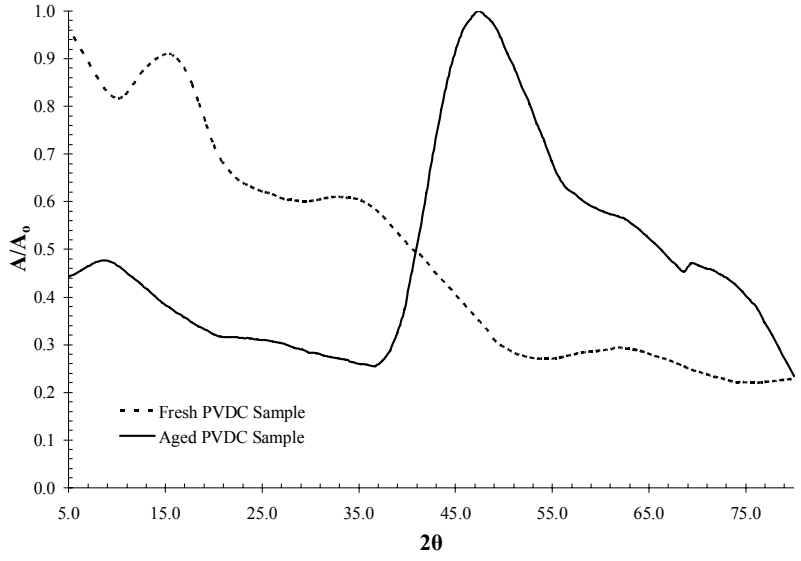

Figure 6.7: XRD plot of PVDC sample fresh from supplier *(dotted line)* and PVDC sample aged for 2 years *(solid line)*.

DSC further confirms this inference, as seen in Figure 6.8, where the fresh latex sample exhibits a small cold crystallization peak (at ~75°C) while the aged sample does not exhibit this peak. This implies that the fresh sample has more amorphous phase than the aged sample (or, the aged sample possesses more crystallinity than the fresh sample)[11]. Furthermore, the T_g of the aged latex is shifted higher (+ 5-7°C higher T_g) than that of the fresh latex, reflecting the presence of additional crystallinity in the aged latex. The effect of this crystallinity will be discussed in a Section 6.3.

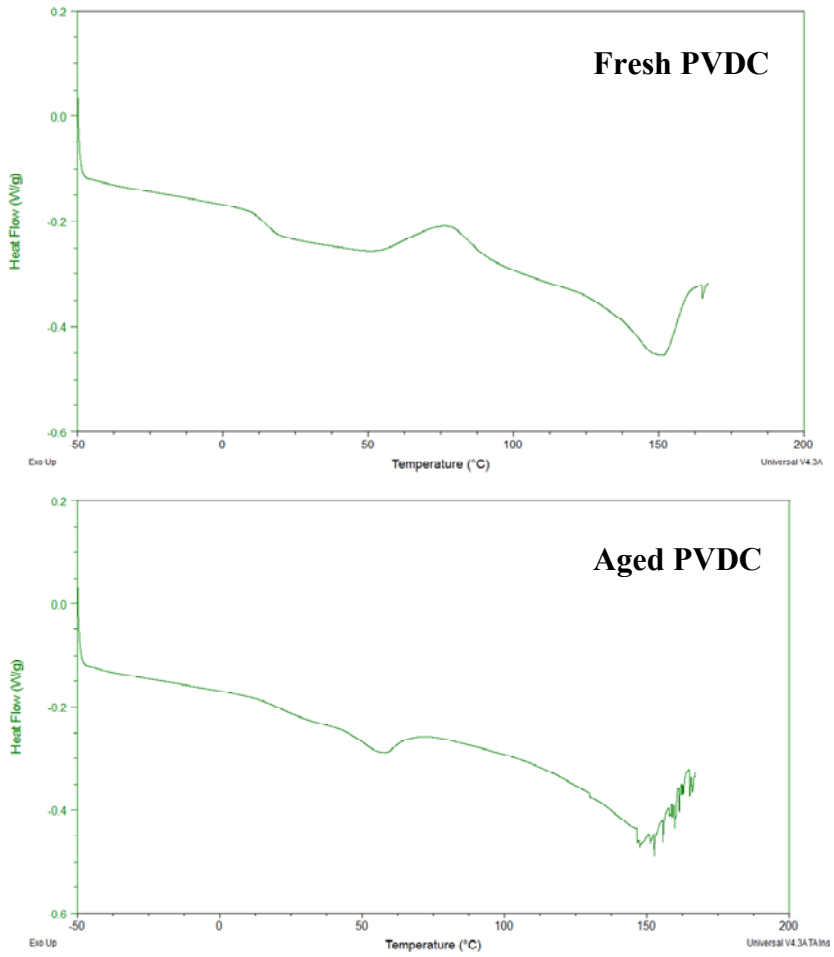

Figure 6.8: DSC on PVDC latex samples that were fresh from the supplier *(top)*, and PVDC latex that was aged for 2 years *(bottom)*

6.2 Development of PVDC Lumen Layer, Fibers

The film experiments were conducted to gain insight into the latex film formation mechanism on porous supports, with the ultimate goal being extension to lumen-side coating of fiber sorbents. Fiber sorbents from the previous chapter were potted into 8" one fiber modules. The fibers were dried in "dry," "wet," and "graded" modes. In order for the fibers to be tested in RTSA mode, the lumen side PVDC layer must be defect free. Any defects in the lumen layer will allow water to rapidly bypass the barrier layer, reducing the CO_2 capacity of the zeolite 13X contained within the cellulose acetate support.

6.2.1 Necessity for dilution of latex

Initial experiments used the PVDC latex as received and attempted to post-treat it directly onto the lumen side of the fiber. Unfortunately, this always resulted in a solid plug of latex forming in the middle of the fibers, effectively blocking the bore of the fiber, as seen in Figure 6.9. Pre-saturating the pores in the fibers with wet nitrogen was found to reduce the plugging that occurred in the fiber bores. However, the incidence of fiber plugs was still unacceptably high. Deionized water was used to dilute the latex, as well as to decrease the viscosity of the latex. Furthermore, the extra water allows the latex dispersion to remain stable in the face of the strong capillary forces exhibited by the porous support, which is discussed at length in Section 6.4. At 40vol% H_2O/60vol%

PVDC latex, the latex post-treatment process was found to never plug the fiber sorbents with latex. As such, this diluted latex was used for all subsequent experiments.

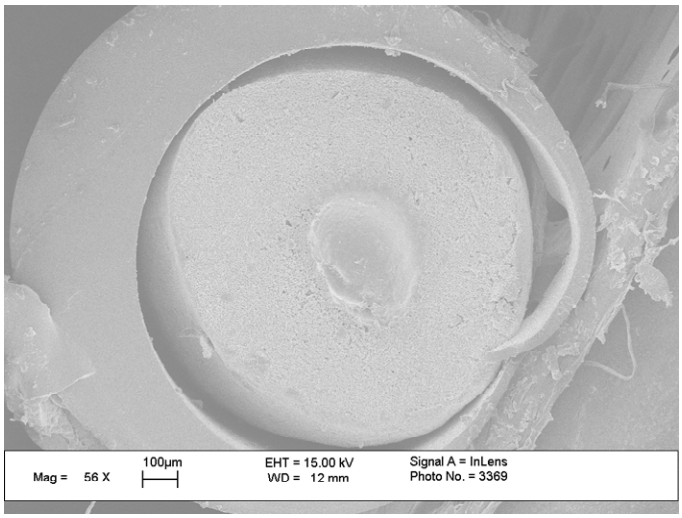

Figure 6.9: SEM image of a PVDC-plugged fiber as a result of insufficient latex dilution.

6.2.2 Lumen Layer Bypass

An additional issue that had to be overcome with fiber sorbents involved *lumen layer bypass*. In a typical selective hollow fiber membrane, the outer selective skin seals against the potting material (typically an epoxy[12]), thereby forcing feed streams to pass through the selective portion of the fiber (Figure 6.10, *top*). In a fiber sorbent, however, with the barrier layer on the interior of the fiber, no such seal exists between the epoxy and the lumen-side barrier layer. As such, water and steam that are introduced on the bore-side can bypass through the highly permeable core structure of the fiber into the shell-side of the manifold. Furthermore, flue gas from the shell-side feed could escape into the water and steam systems (Figure 6.10, *bottom*). This problem, if not remedied,

would render the RTSA system ineffective.[§] To counter this, a simple method of "capping" the fibers at the potting seals was developed. During the post-treatment experiment, capillary forces present at the face of the fiber pull the latex into the top face of the fiber (the bottom face is submerged in hexane); the subsequent gas drying step must be carefully chosen to assist in the formation of a defect-free cap layer as well as a defect-free lumen layer.

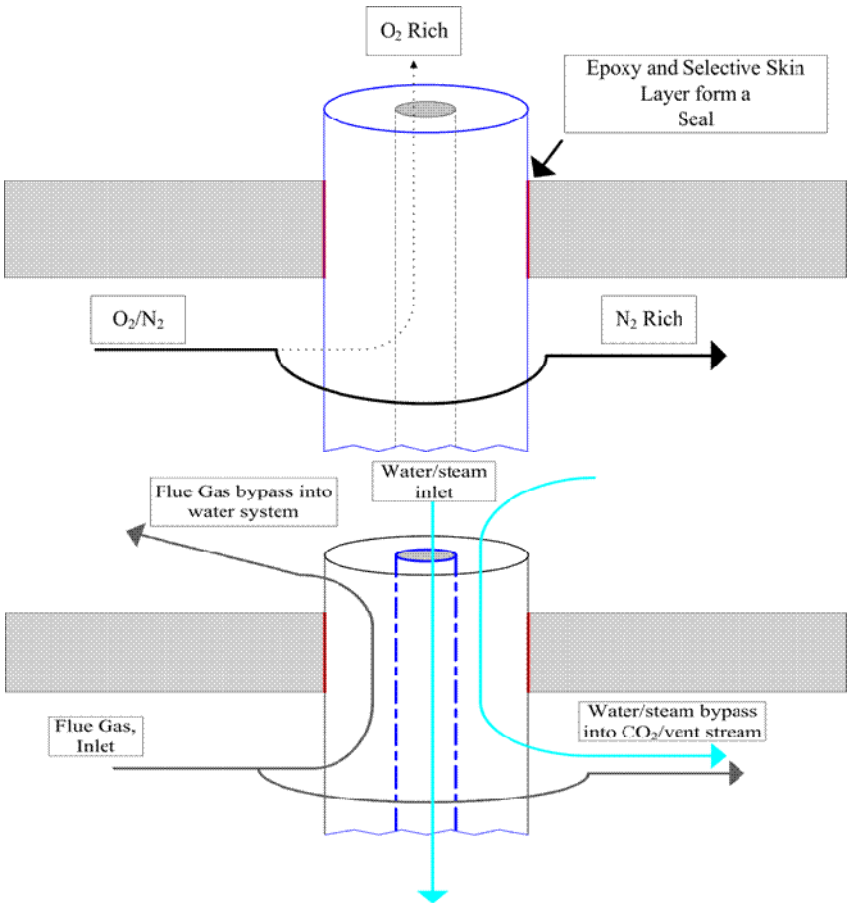

Figure 6.10: Illustration of lumen layer bypass. ***(top)*** **Typical potting of a hollow fiber membrane separates the feed and permeate side.** ***(bottom)*** **Typical potting in a hollow fiber sorbent does not effectively separate the feed and permeate sides of the fiber.**

[§] From a laboratory perspective, if lumen layer bypass is not addressed, the true permeance of the barrier layer will never be known, as the defective end caps would dominate permeation through the fiber sorbent.

6.2.3 Effect of drying rate and latex age

6.2.3.1 "Dry" Mode

Fibers dried using the "dry" mode were found to be the most defective; SEM images in Figure 6.11 show the fiber lumen layer as well as a cracked fiber face that exhibited matted, poorly formed PVDC; likely due to rapid stress-relaxation at the face of the fiber (Fig 6.11*a*). Higher magnification reveals the PVDC particles have not even deformed or intercalated significantly for the aged latex (Fig 6.11*c*), while the new latex shows only marginal improvement in terms of particle deformation and intercalation (Fig. 6.11*d*). Permeation experiments (Table 6.3) on fibers from the aged and new latex show a four order of magnitude reduction in permeance over the bare fibers, and a further reduction in permeance by using the fresh latex. However, both fibers are still four to five orders of magnitude away from a defect free layer; most likely the fissures in the face of the fiber as well as the porous nature of the lumen layer are responsible for these high-than-expected fluxes.

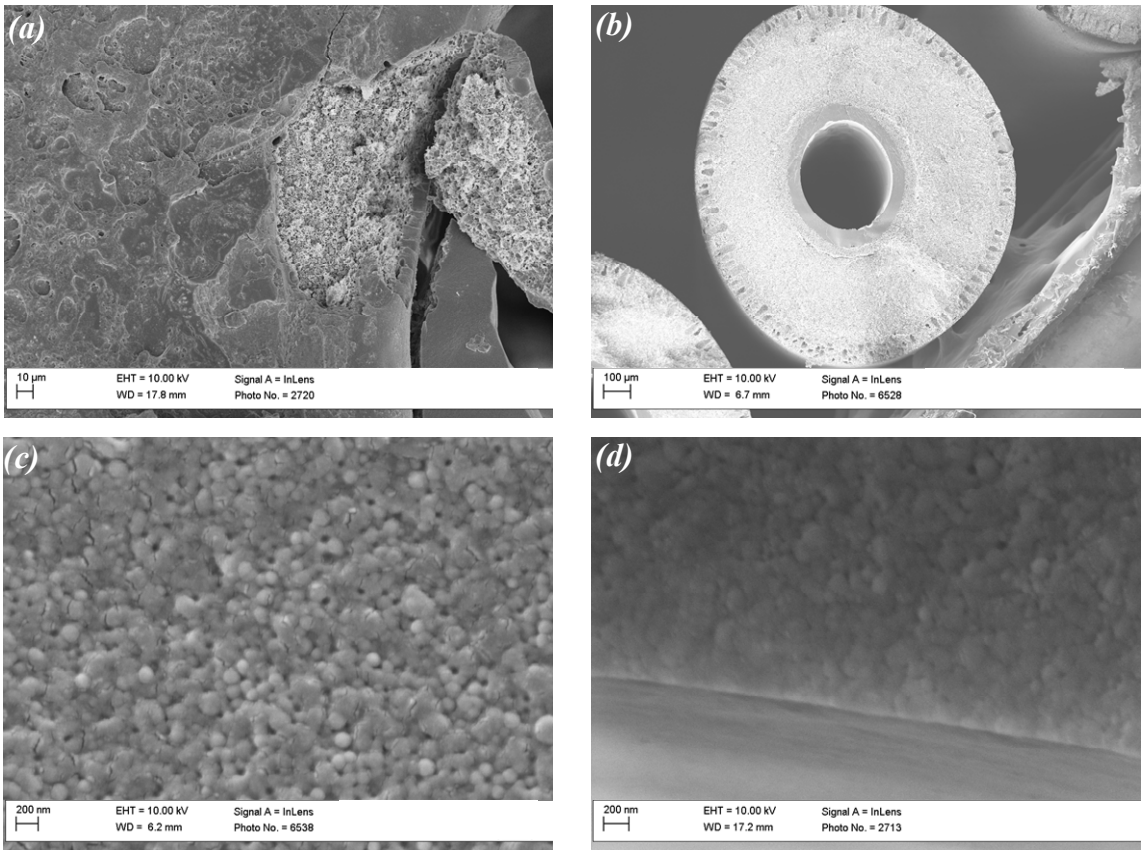

Figure 6.11: SEM images for PVDC-coated fiber sorbents. (a) Face-seal of fiber sorbent showing matted PVDC structure as well as large defect, revealing the CA/13X structure underneath. (b) Fiber sorbent with PVDC lumen layer. (c) High magnification of PVDC layer cast from aged latex. (d) High magnification of PVDC layer cast from fresh latex.

6.2.3.2 "Wet" Mode

The "wet" drying mode removed the fissures in the fiber faces (Fig 6.12*a*), as can be seen in Figure 6.12. However, under further magnification, poor film formation is still observed for the aged latex. Partial particle deformation is observed (Fig 6.12*c*), but complete coalescence into a film is still clearly unsuccessful. SEM images also show that film cast from the fresh latex suffers from similar issues with particle deformation and intercalation (Fig. 6.12*d*).

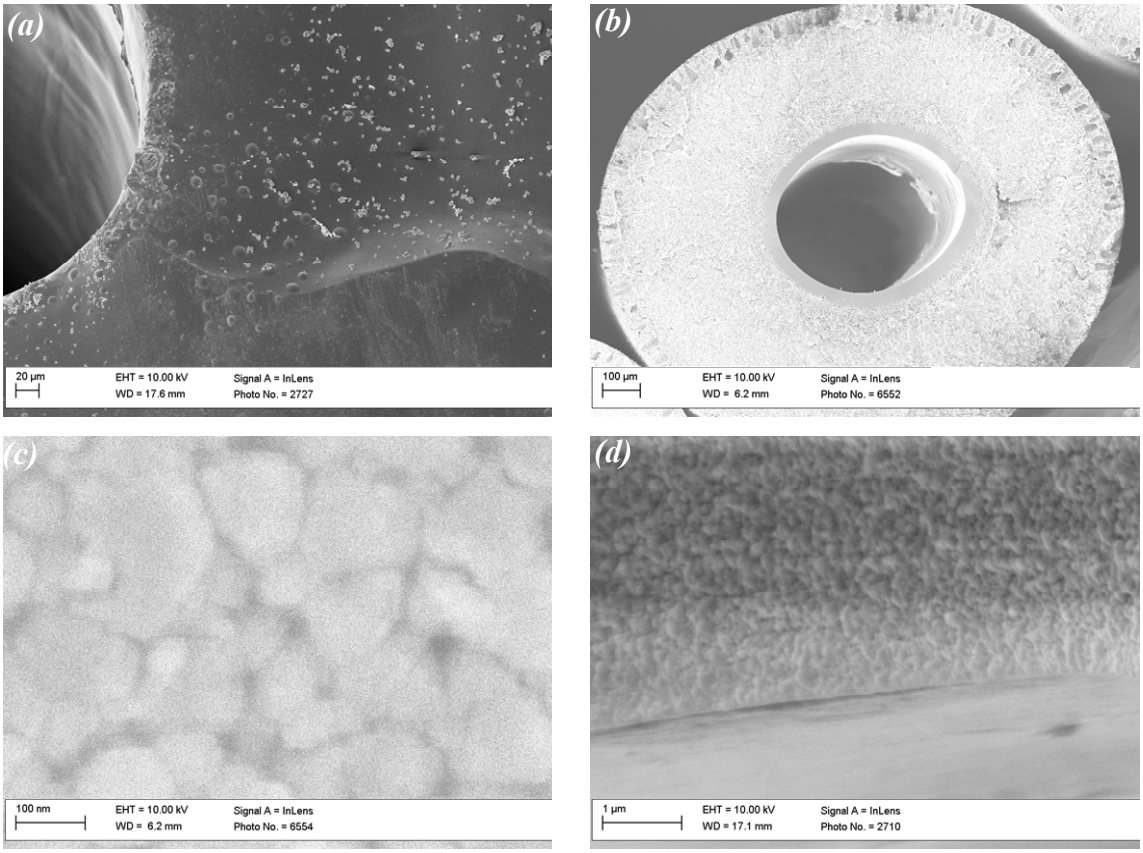

Figure 6.12: SEM of PVDC-coated fiber sorbents dried using the "wet" drying mode. ***(a)*** **Fiber face showing smooth PVDC without any visible cracks from drying.** ***(b)*** **PVDC-coated fiber sorbent.** ***(c)*** **High magnification of PVDC lumen layer from aged latex, showing poor particle coalescence.** ***(d)*** **High magnification of PVDC lumen layer from fresh latex, showing poor particle coalescence.**

Permeation results (Table 6.3) reveal that the aged latex barrier layer is defective, with a helium permeance of 6.8 GPU, while the fresh latex barrier layer has helium fluxes at 1.45 GPU, which cannot readily be inferred via SEM images. Most likely, the fresh PVDC particles do coalesce slightly better than the aged particles, resulting in a less porous lumen layer. Unfortunately, despite the marked improvement over the "dry" mode, even the fresh latex barrier layers dried in the "wet" mode are still much too defective for use in an actual RTSA operation with zeolite 13X as the CO_2 sorbent.

6.2.3.3 "Graded" Drying

The "graded" drying mode proved to be much more promising. SEM images reveal no fissures in the faces of the fiber, and upon further magnification, the aged latex exhibits highly deformed particles, but still under-developed particle-particle intercalation (Figure 6.13*a* and *b*) is seen throughout the PVDC lumen layer. Interestingly, the fresh PVDC lumen layer exhibits poor particle deformation and intercalation throughout the bulk of the lumen layer (Figure 6.13*c*), yet the innermost radius of the lumen layer was found to have a "gradient" of particle deformation: the particles closest to the innermost radius deformed and intercalated the most, resulting in a very thin (~50nm) PVDC skin layer. Permeation results are the most telling (Table 6.3), as the fibers with the PVDC lumen layer from the aged latex formed under "graded" drying exhibit a factor of 2 decrease in permeace over the "wet" mode, reducing the helium permeance to approximately 3.3 GPUs. Finally, fresh PVDC dried with the "graded" mode yielded low helium permeances (0.21 GPU), indicating again that fresh latex and reasonably slow drying conditions are required to create a dense layer. However, the layer is still partially defective, as the selectivity through the layer is only marginally above Knudsen selectivity.

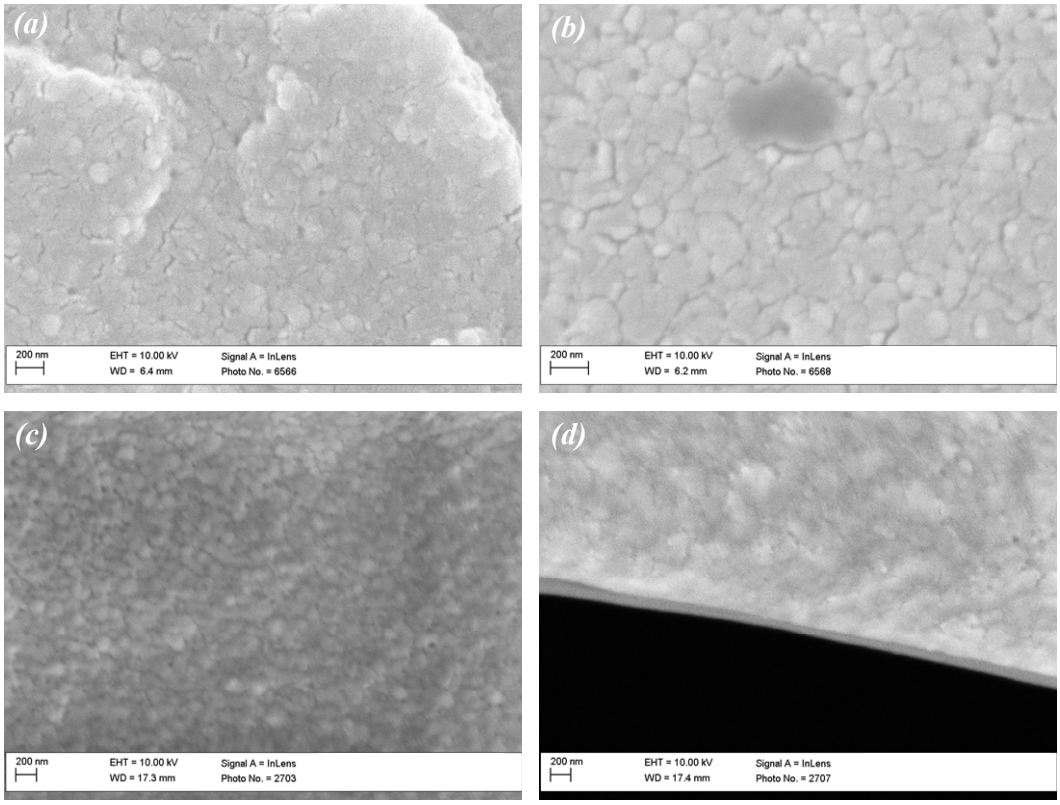

Figure 6.13: High magnification SEM images of PVDC lumen layer made with "graded' drying mode. *(a)* PVDC lumen layer from aged latex, showing good particle deformation, but poor intercalation. *(b)* Higher magnification image showing poor intercalation in aged latex film. *(c)* Middle of the PVDC lumen layer from fresh latex showing poor particle deformation and intercalation. *(d)* High magnification image of innermost radius of the PVDC lumen layer from the fresh latex showing a continuous, thin skin.

Table 6.3: Permeation results for CA/13X/PVDC fiber sorbents

	Drying Method					
Fibers	"Dry"		"Wet"		"Graded"	
Latex Sample	**Helium Permeance (GPU)**	**He/N_2 Selectivity**	**Helium Permeance (GPU)**	**He/N_2 Selectivity**	**Helium Permeance (GPU)**	**He/N_2 Selectivity**
2-year aged	63.8±0.9	2.1±0.03	6.8±0.55	1.94±0.26	3.26±0.02	2.8±0.27
Fresh	41.9±1.8	2.2±0.19	1.45±0.01	1.98±0.19	0.21±0.01	2.8±0.20

T=35°C, test pressures = 20 psig. Error bars represent 1 standard deviation.

6.2.4 Toluene-assisted drying of nascent PVDC barrier layer

The previous section showed that when using fresh latex and "graded" drying, low permeances were obtained, and SEM images showed the presence of a thin skin PVDC layer that was found to be slightly defective via permeation experiments. However, while the results presented above are encouraging, another method was devised to allow for even lower fluxes through the lumen-side barrier layer and that perhaps circumvents the main limitation of casting a latex dispersion onto a porous support. A large column of toluene was added to the top of the water column that humidified the nitrogen stream for the "graded" drying mode. Toluene was chosen due to its immiscibility with water, thereby allowing the nitrogen to be saturated in both water and toluene. Furthermore, toluene was chosen due to the fact that is a known swelling solvent for PVDC[13]. As discussed in the next section, the reasoning behind this is that by *controllably* softening the PVDC particles with toluene, particle deformation can occur at lower pressures, thereby allowing the lumen layer to form a dense, continuous layer. As can be seen in SEM images in Figure 6.14, a dense, apparently defect-free skin layer has been formed with the toluene-assisted drying mode for *both* the aged and fresh latex. Helium permeation confirms the SEM images, as the flux is immeasurably low (< 0.03 GPU).[**] Water permeation experiments (see Chapter 3 for details) on the toluene-assisted PVDC coated fiber sorbents revealed no water permeation through the layer at

[**] The reliable limits of measurement in the isobaric permeation system are ~0.01-0.03 GPUs, and these fibers are most likely less permeable than that. Ideally, installing these fibers into an isochoric system would yield the actual permeance. However, due to the fact that the end-caps of the fibers must be perfect as well as the lumen layer, Swagelok® fittings are avoided when working with these fiber modules (normal Swagelok® fittings were found to destroy the end-caps as confirmed by SEM and permeation), and Ultra-torr® fittings are used in lieu of the standard fittings in the isobaric system. Unfortunately, Ultra-torr® fittings are not "leak-proof" enough to be used in the high-vacuum isochoric systems, and ultimately the leak-rate in the isochoric system was all that could be detected.

25°C after 5 days. These apparently defect-free fibers made via the toluene-assisted drying mode were used to create the modules for the work performed in Chapter 7.

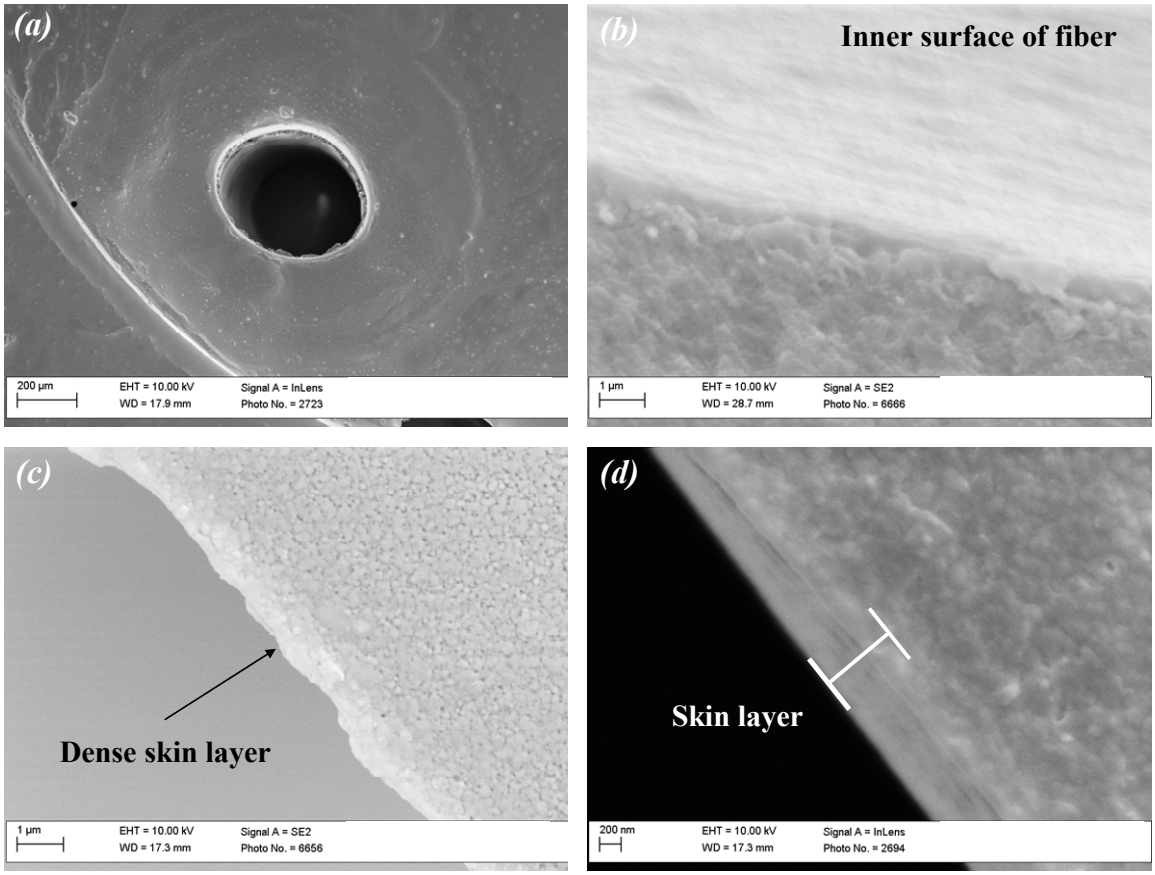

Figure 6.14: SEM images of PVDC-coated fibers that were dried using toluene, water vapor and nitrogen ("toluene-assisted graded drying mode"). *(a)* Fiber face showing smooth, crack-free PVDC coating. *(b)* Magnification of aged latex PVDC lumen layer showing cross-section of skin layer as well as the inner surface of the fiber. *(c)* SEM image of aged PVDC lumen layer clearly showing a dense skin. *(d)* High magnification SEM image of fresh PVDC lumen layer showing a thick (300-500 nm) skin layer.

6.3 PVDC Film Formation Hypothesis

The preceding sections experimentally investigated the barrier properties of films cast from old and new PVDC latex dispersions onto porous substrates of varying character while drying the nascent films at three different rates. While the literature

discusses in detail film formation theories onto ideal substrates (there are at least two large review papers on the topic)[5,14], there are very few proposals as to how latex films form when cast onto porous substrates[6,7]. Chapter 2 outlines the current consensus on how latex films form on ideal surfaces, and can be summarized as a shrinking meniscus during drying that collects and orders the disperse PVDC particles, followed by large interfacial tension forces between the air and the evaporating water which lead to particle deformation and finally polymer-polymer interdiffusion.

As was clear in the preceding section, the drying rate of the latex must be sufficiently slow to allow for a continuous, albeit porous, film to form (as opposed to a highly cracked or crazed film). Any form of dry convective sweep or vacuum drying will rapidly pull the interstitial water out of the latex. While this forms apparently dense sections (via SEM, Figure 6.3) throughout the film, the rapid film formation proves to be too much stress for the rapidly solidifying film, thereby causing stress-relief fractures. In the fibers, the cylindrical substrate most likely mitigates these stress-relief fractures to some extent, but on the faces of the fibers—which are equally crucial to barrier layer performance due to lumen layer bypass—the same stress-relief fractures can occur. Only in the "graded" drying mode (or the expanded toluene-assisted graded drying mode) is the nascent latex given enough time to sufficiently relax out the stresses that occur as a result of film formation.

The effect of the substrate is a much more nebulous factor in the film formation process. The smooth glass substrate was used as a control, and as expected, the PVDC

film (from the fresh latex) was found to coalesce into a dense, continuous structure much as the literature predicts[4,15,16]. As discussed in Section 6.1.2, PVDC laticies cast onto the hydrophobic polycarbonate substrate were completely defective. In this hydrophobic case, capillary forces are thwarted by the inability of the PVDC latex to wet the surface. The areas where the PVDC beads up likely form continuous dense films, as the hydrophobic substrate acts much like a smooth glass substrate. However, as the latex does not continuously coat the substrate mask due to the lack of wetting, the permeance data simply returns the flux through the porous substrate.

The porous, hydrophilic nylon 6,6 and cellulose acetate/13X supports yielded the most puzzling results. While the formed films appeared dense, albeit with a globular morphology, the permeation results indicate a film that is between 100-1000x more defective than the control films cast on the ideal substrates. Most likely, the hydrophilic porous substrate exhibits strong capillary action (Figure 6.15*a*), which pulls a large portion of the latex serum through the substrate. As a result, the evaporating-meniscus-driven ordering that occurs in the control film likely does not occur to the same extent on the hydrophilic porous substrates (Figure 6.15*b*). This reduction in particle mobility would have the effect of "flash vitrification" of the particles in place after the latex has been cast onto the substrate. Without the particles being packed closely together via a slowly shrinking/receding meniscus, the interfacial tension between the air and interstitial water will be much lower compared to the control films (Figure 6.15*c*). In the extreme case, the particles will not undergo deformation, but instead will only undergo polymer interdiffusion at the points where the particles are touching (Figure 6.15*d*). The toluene-

assisted drying softens the polymer particles during the interfacial tension-induced particle deformation step, allowing for particle deformation to occur even at lower pressures.

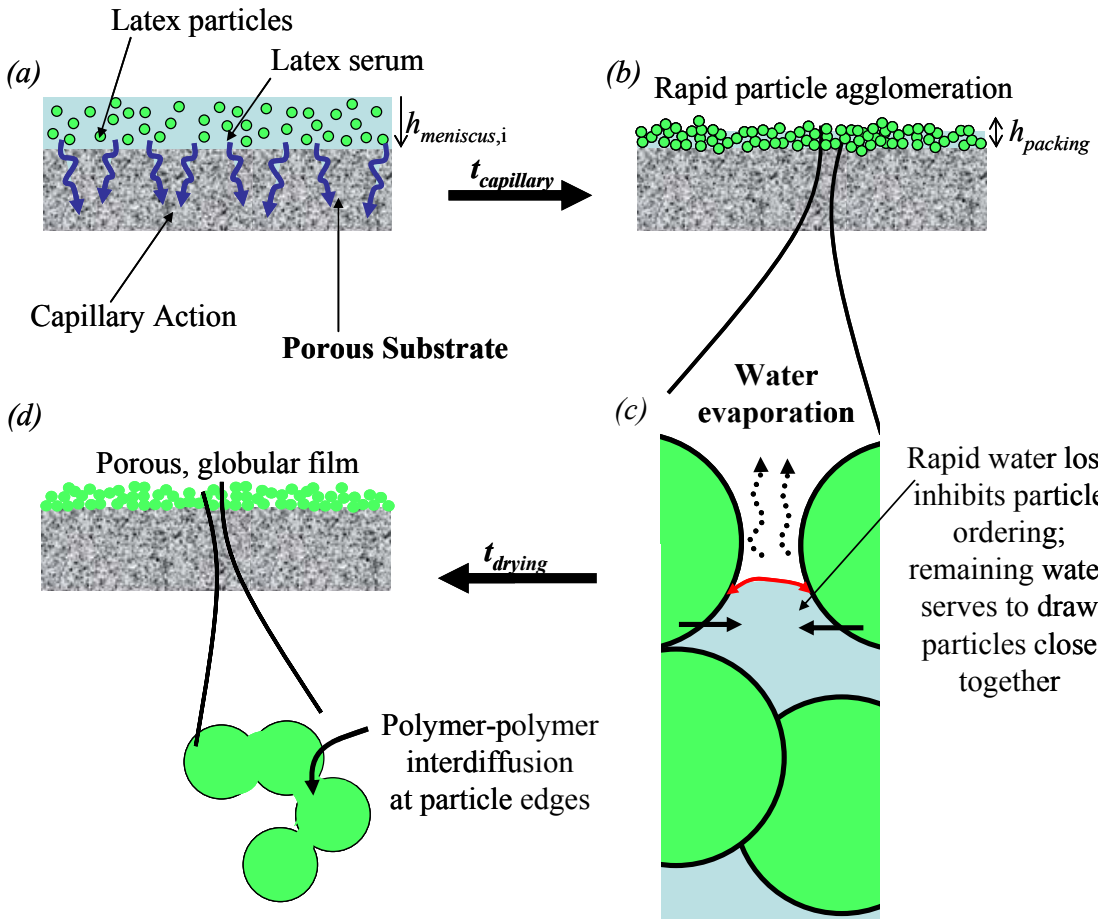

Figure 6.15: Schematic hypothesizing a film formation mechanism when a latex dispersion is cast onto a porous, hydrophilic substrate.

Finally, the latex age plays a dramatic role in the film formation. The hypothesis established in the above discussion still holds. The aged PVDC clearly develops crystallinity over time as evidenced by XRD and DSC, and most likely loses a volatile leveling agent over time as well. As a result, the polymer particles will have a higher T_g than the fresh latex particles, significantly reducing the ability of the particles to deform

and reducing polymer-polymer interdiffusion. This lack of particle deformation and intercalation as a result of the additional crystallinity and the rapid particle agglomeration results in a porous film that is also extremely brittle. Interestingly enough, the toluene-assisted drying softens the particles enough to allow for normal particle deformation and interdiffusion to occur, as evidenced by the formation of a skin layer and the immeasurably low helium permeances.

6.4 Conclusions

This chapter established basic guidelines and principles for creating defect-free lumen side barrier layers on fiber sorbents. Film experiments were performed in support of this goal, with the effect of drying rate, substrate hydrophobicity, substrate porosity (porous versus non-porous), and latex age being studied via film casting observations, SEM images, and helium/nitrogen permeation experiments, as well as DSC and XRD experiments. The main findings are that capillary forces in the hydrophilic cellulose acetate/13X matrix quickly dehydrate the nascent PVDC film, locking the particles in place much farther apart relative to a film cast on an ideal substrate. This additional spacing between the particles reduces the interfacial forces which causes less particle deformation—less particle deformation implies less polymer-polymer interdiffusion is occurring, resulting in a defective film. A drying method utilizing toluene as a swelling agent was utilized to soften the PVDC particles to compensate for the reduction in interfacial forces, thus allowing for a defect free skin to be formed on the lumen side barrier layer.

6.5 References

1. Korkikov, A.P.; Kosaraju, P.B.; Sirkar, K.K. Interfacially polymerized hydrophilic microporous thin film composite membranes on porous polypropylene hollow fibers and flat films, *Journ. Memb. Sci.*, **2006**, 279, 588- 560.
2. Suzuki, H.; Tanaka, K.; Kita, H.; Okamote, K.; Hosiro, H.; Toshimune, Y.; Kusuki, Y. Preparation of composite hollow fiber membranes of poly (ethylene oxide)-containing polyimdie and their CO_2/N_2 separation properties, *Journ. Memb.Sci.*, **1998**, 146(1), 31-37.
3. Lively, R.P., Chance, R.R., Kelley, B.T.., Deckman, H.W., Drese, J.H., Jones, C.W., Koros, W.J., *Industrial & Engineering Chemistry Research* **2009** *48* (15), 7314-7324.
4. Sweeting, O.J. *The Science and Technology of Polymer Films*, John Wiley & Sons, Inc.: New York, NY **1971**.
5. Steward, P.A.; Hearn, J.; Wilkinson, M.C. An overview of polymer latex film formation and properties, *Adv. Coll. & Interfacial Sci*., **2000**, 86, 195-267
6. Pan, S.X.; Davis, H.T.; Scriven, L.E. Substrate effects on binder migration in drying porous coatings, *Coatings, Conference Proceedings*, TAPPI Press, Atlanta, GA, **1996**, 115-133.
7. Cairncross, R.A. Modeling Drying During Low-Speed Coating of Porous & Continuous Films, *IS & TS 50th Annual Conference*, **1997**, 554-558.
8. Brown, G.L. Formation of films from polymer dispersions, *Journal of Poly. Sci.*, **1956**, 22 (102), 423-434.
9. Bieleman, J.; Hajas, J.; Dören, K. Flow-Levelling and Coalescing Agents, in *Additives for Coatings* (ed J. Bieleman), **2007**,Wiley-VCH Verlag GmbH, Weinheim, Germany.
10. Bragg, W.L. The Diffraction of Short Electromagnetic Waves by a Crystal, *Proceedings of the Cambridge Philosophical Society*, **1913**, 17, 43–57.
11. Schiers, J. *Compositional and Failure Analysis of Polymers: a practical approach*, **2000**, John Wiley & Sons, Hoboken, NJ, 122-123.

12. McKelvey, S. A. Formation and characterization of hollow fiber membranes for gas separation (fiber breaks, macrovoids). University of Texas, Austin, *Ph.D. Dissertation* **1997**.
13. Osborn, K.R.; Jenkins, W.A. *Plastic films technology & packaging applications*, **1992**, CRC Press, p. 98-99.
14. Keddie, J.L. Film formation of latex, *Materials Science & Engineering*, **1997**, 21, 101-170.
15. Wang, Y.; Kats, A.; Juhue, D.; Winnik, M.A.; Shivers, R.R.; Dinsdale, C.J. Freeze-fracture studies of latex films formed in the absence of surfactant, *Langmuir*, **1992**, 8(5), 1435-1442.
16. Chevalier, Y.; Pichot, C.; Grailat, C.; Junnicot, M.; Wang, K.; Maquet, J.; Lindner, P.; Cabone, B. Film formation with latex particles, *Colloid and Polymer Science*, **1992**, 270(8), 806-821.

Chapter 7

Sorption Performance of Hollow Fiber Sorbents

After establishing the RTSA concept in Chapter 4, developing a reliable method for spinning high-loaded fiber sorbents in Chapter 5, and creating a defect-free PVDC lumen layer in Chapter 6, Chapter 7 aims to be the culmination of the previous work by testing the sorption properties of the fiber sorbents in a simulated RTSA. The chapter begins by discussing the equilibrium, kinetic, cyclic and chromatographic uptake of CO_2 by bare (PVDC-free) fiber sorbents. From here, chromatographic experiments on coated, actively cooled, fiber sorbents will be discussed, and finally, a proof-of-concept RTSA cycle with cycling cool and hot water will be presented.

7.1 Equilibrium Uptake of CO_2 in Hollow Fiber Sorbents

Sorption in the hybrid fiber sorbents occurs primarily in the solid sorbents or other sorbent materials embedded in the fiber wall, and sorption uptake can be described in terms of a Langmuir isotherm,

$$C_i = \frac{C'_{H,i} b_i p_i}{1 + b_i p_i} \qquad \textbf{(1)}$$

where C_i is the amount of sorbate in the molecular sieve (cc[STP]/cm^3 sorbent), $C'_{H,i}$ is the pore saturation parameter of the molecular sieve sorbent (cc[STP]/cm^3 sorbent), b_i is the pore affinity for the sorbate (psi^{-1}), and p_i is the sorbate partial pressure (psi)[1,2].

Pressure decay sorption experiments[3,4] were performed to determine sorption kinetic times and sorption equilibrium in the sorbents. Sorption experiments on the fiber sorbents were compared with literature results for CA[5], and were adjusted to the measurement temperatures. The fiber sorbent and zeolite 13X (activated at 115°C) sorption isotherms at 45°C and 100°C are displayed in Figures 7.1 *a* and *b*, respectively. The isotherms under-report the Henry's Law regime when compared with literature values[6-8]. The current pressure decay apparatus is not ideal for studying such low-pressure uptake, as the pressure transducers in the apparatus become increasingly more inaccurate at lower pressures. Nonetheless, the equilibrium uptake measurements indicate that from a long-time point of view, the pores in the 13X crystals are not blocked or plugged by the cellulose acetate matrix or any residual NMP (spinning solvent).

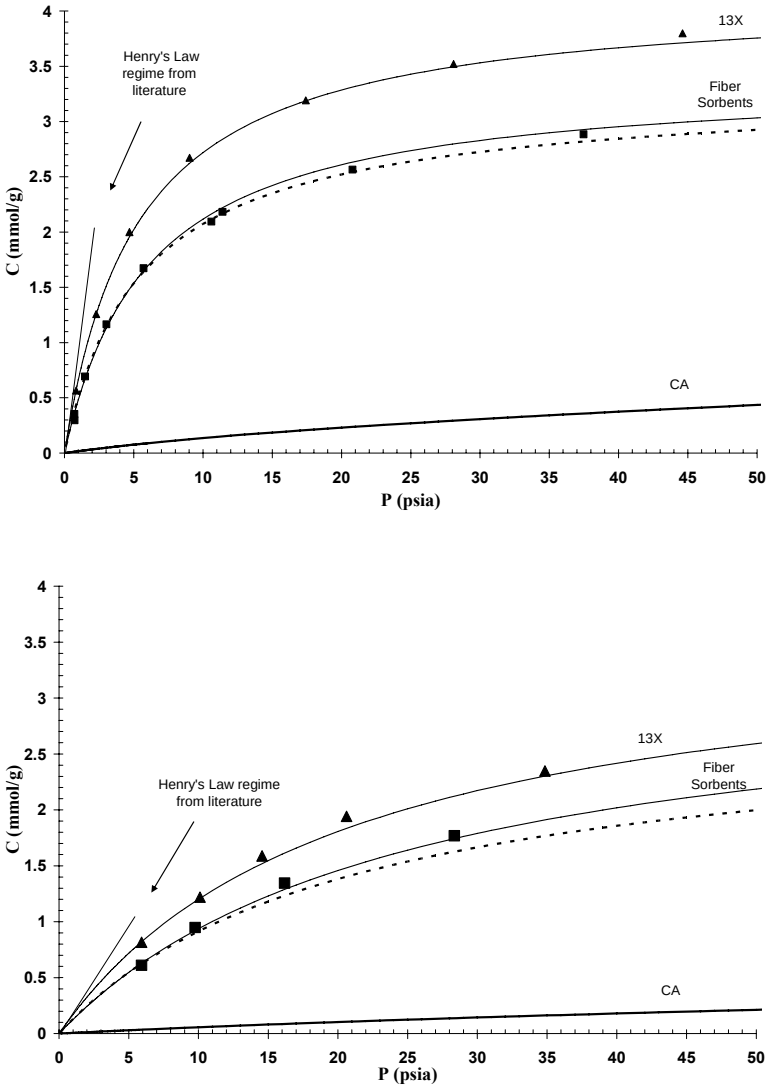

Figure 7.1 ***(a, top)*** **CO_2 sorption isotherm on fiber sorbents, 13X, and cellulose acetate at 45°C.** ***(b,bottom)*****: Isotherm at 100°C. Triangles indicate sorption isotherms for 13X, squares indicate 13X fiber sorbents. The dashed line indicates the predictions for 13X fiber sorbents based off a simple weighted average of the CA and 13X sorption capacities.**

7.2 Kinetic Uptake of CO_2 in Hollow Fiber Sorbents

Using the first exposure from the equilibrium experiments, sorption kinetics on the sorbent fibers were performed, and as shown in Figure 7.2, the fiber sorbents

achieved greater than 95% equilibration in under four seconds; however, the 13X crystals lagged behind the fiber sorbents in apparent response time. This is likely due to the fact that the 13X crystals are packed closely together in a stainless steel thimble, whereas the fiber sorbents are loosely packed into the sorption cell, allowing for greater heat dissipation in the fiber case. While both responses are compromised by the non-isothermicity caused by the intense sorption enthalpy, the results show relatively rapid sorption equilibration, and subsequent TGA results discussed in the next section support this as well. The rapid uptake of CO_2 by the fiber sorbents shows that CO_2 access to the 13X pores is not likely occluded appreciably by the cellulose acetate matrix.

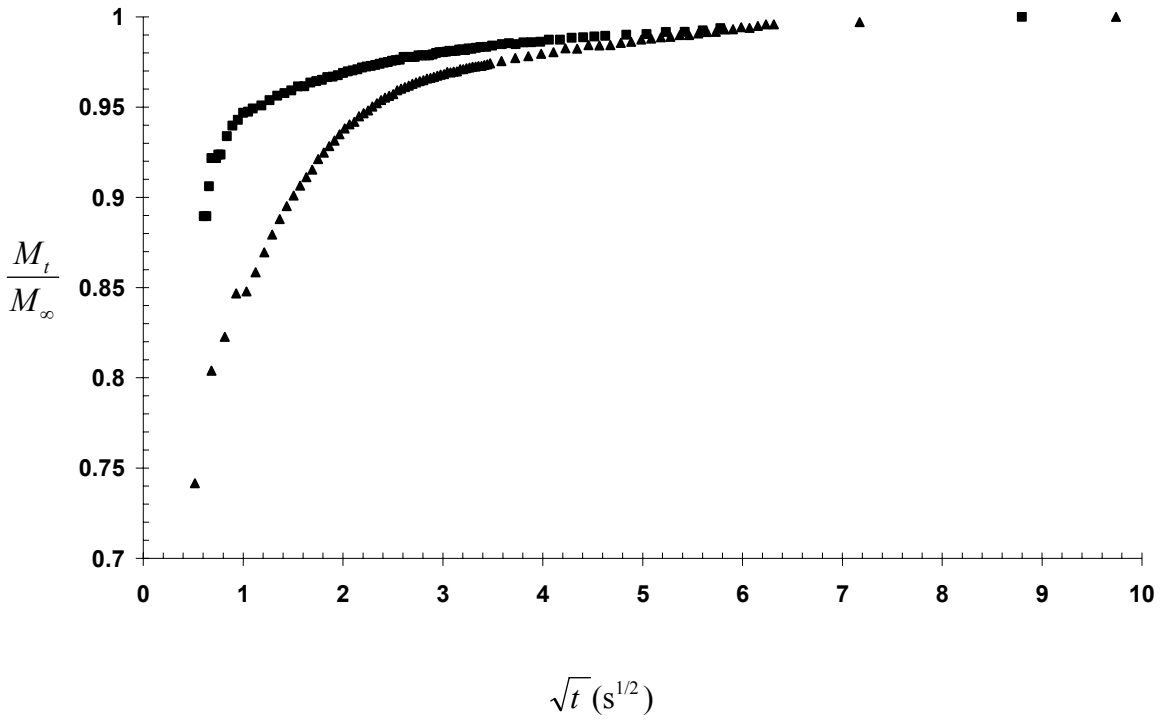

Figure 7.2: CO_2 response time comparisons between pure 13X and sorbent fibers embedded with 13X at 45°C. Closed squares indicate fiber sorbent responses, and closed triangles indicate 13X crystal responses.

7.3 Cyclic Thermal Performance of Hollow Fiber Sorbents in CO_2 Atmosphere

7.3.1 Zeolite 13X Control

To determine the validity of the cyclic TGA experiment (see Chapter 3 for details), 13X was conditioned under flowing helium at 400°C, and then cycled between 100°C and 45°C. The 400°C mass, with appropriate buoyancy corrections, was taken as the baseline mass, thereby enabling sorption capacities of zeolite 13X to be calculated. Figure 7.3 shows the cyclic portion of the thermal program as well as the mass gain/loss versus time (rephrased as CO_2 capacity) . The CO_2 capacities match well with values reported in the literature[9].

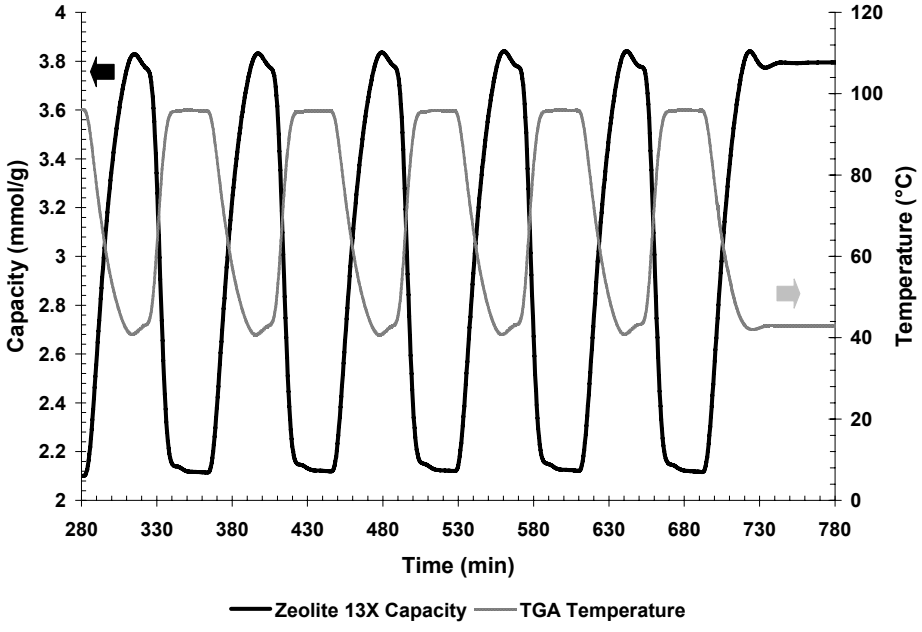

Figure 7.3: Thermal cycling of Zeolite 13X in CO_2 atmosphere (14.7psia) after 400°C activation.

7.3.2 Fiber Sorbents CO_2 Uptake in TGA

Due to the particular polymer matrix supporting the zeolites, a 400°C conditioning is not possible when studying the fibers; therefore, a low temperature activation must be used. However, this is consistent with the planned used of the sieves, so this working capacity is relevant. A temperature of 115°C was used as the baseline temperature, and repeated thermal cycles between 100°C and 45°C were performed on the 13X crystals and the fiber sorbents (Figure 7.4). The regenerability of the fiber sorbents can clearly be seen to be associated with the embedded 13X sorbents. Furthermore, the cellulose acetate matrix does not hinder CO_2 diffusion into and out of the embedded zeolite 13X, as can be seen by the near-perfect matching of the mass and temperature signals. The ability of the fiber sorbents to rapidly cycle in CO_2 environments without any apparent change in CO_2 capacity indicates that the fibers do not significantly degrade, at least not over the 48 hours of continuous cycling studied here.

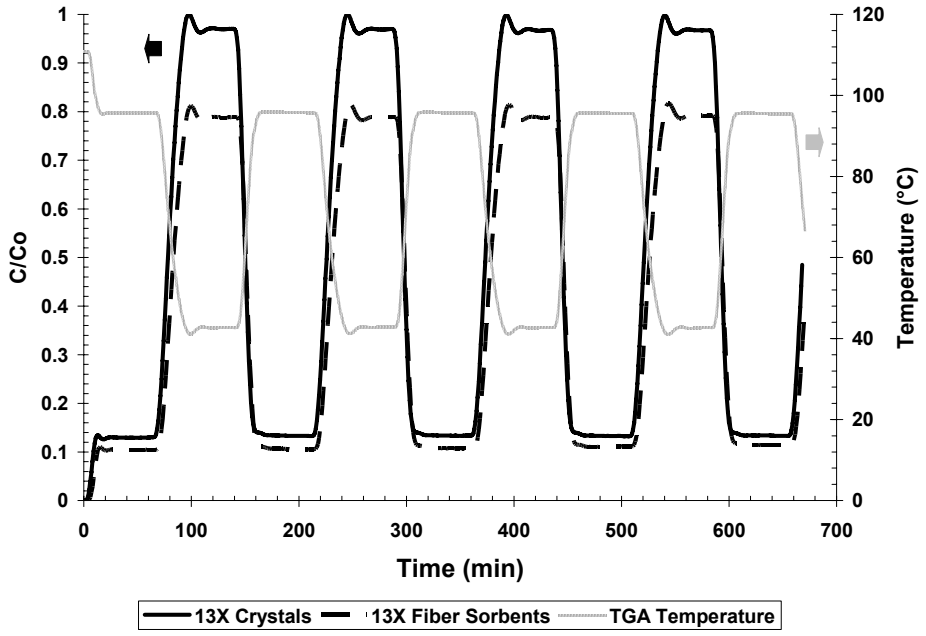

Figure 7.4: Thermal cycling of zeolite 13X and 13X fiber sorbents in a CO_2 atmosphere (14.7 psia) after 115°C activation with C_0 arbitrarily set to be the maximum zeolite 13X capacity at 45°C.

7.4 Uptake of CO_2 by Bare Hollow Fiber Sorbents in Parallel Flow Module

7.4.1 External Film Resistance Reduction

An initial design consideration in the fiber sorbent system for post-combustion CO_2 capture was minimization of the flue gas pressure drop across the hollow fiber module. To test if this was viable, two different fiber modules with separate void fractions were tested in the multicomponent adsorption system in a parallel flow configuration (see Chapter 3 for details). The sorption performance of a five fiber module with a void fraction (interstitial module volume over total module volume) of 0.40 was compared against a six fiber module with a void fraction of 0.28 at various

flowrates. Figure 7.5 shows the CO_2 breakthrough curves for the five fiber module at flowrates of 25 sccm, 75 sccm and 150 sccm, with the helium tracer at 150 sccm shown for reference (the tracers for 25 sccm and 75 sccm were approximately the same and have been removed for clarity). A useful term when discussing mass transfer resistances is the "degree of spreading" (in centimeters), which normalizes the velocity of the mass transfer zone (v_{MTZ}) by the slope of the breakthrough curve at 50% equilibrium, which can be seen, viz.[10],

$$v_{MTZ} = \frac{L_{Bed}}{\mu_1}$$

$$\text{Degree of Spreading} = \frac{v_{MTZ}}{\left(\frac{dy_{CO2}}{dt}\right)_{50}} \qquad \textbf{(2)}$$

where μ_1 (seconds) is the first moment of the breakthrough curve. The first moment for a step function is defined as[11],

$$\mu_1 = \int_0^\infty \left(1 - \frac{y(t)}{y_o}\right) dt \qquad \textbf{(3)}$$

where $y(t)$ (mol%) is the instantaneous fractional concentration as measured by the mass spectrometer and y_o is the equilibrium fractional concentration (mol%). In adsorption chromatography, the first moment can best be thought of as the average retention time of an adsorbate within the adsorbent bed[11]. When comparing the 25 sccm CO_2 breakthrough curve to the helium tracer (Figure 7.5), a significant degree of spreading was qualitatively observed, indicating either external resistances or internal sorption resistances (i.e., mesopore diffusion resistance or micropore diffusion resistance,

discussed later). This degree of spreading did not change significantly despite a factor of five increase in superficial velocity past the fiber (see Table 7.1).

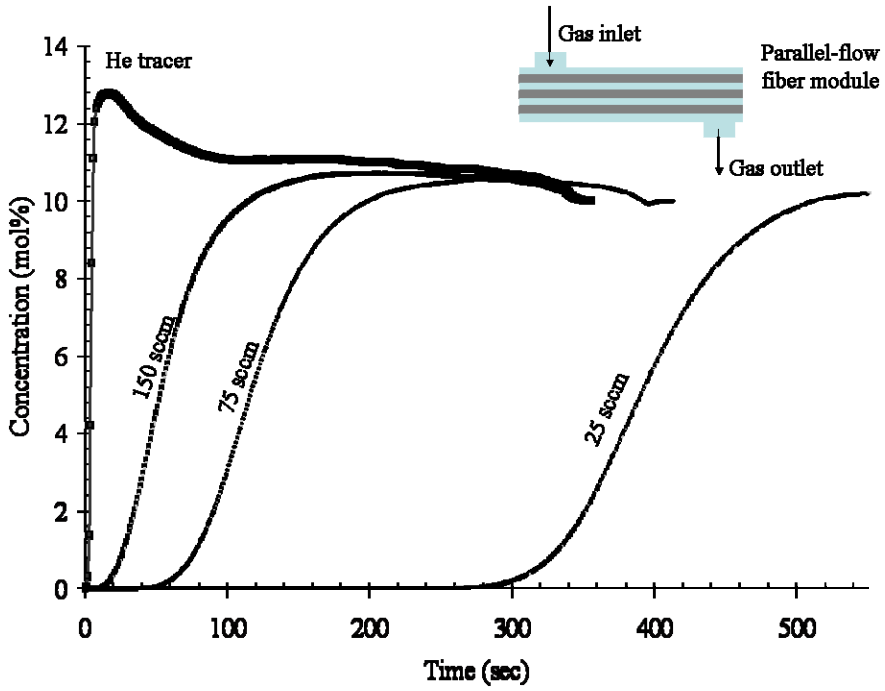

Figure 7.5: CO_2 breakthrough experiments for five fiber module (void fraction=0.40). System temperature is 45°C. Flow configuration is parallel flow. No cooling water was used in the bores. Bed length is 36.2 cm.

Figure 7.6 displays the CO_2 breakthrough curves for the six fiber module (void fraction of 0.28) at four different flowrates: 200 sccm, 160 sccm, 80 sccm, and 40 sccm with the helium tracer at 200 sccm displayed for reference (again, the tracers for 40, 80 and 160 sccm were approximately the same). Due to the high CO_2 adsorption capacities of 13X at these conditions as well as the He/CO_2 stream being exposed to a clean bed, a helium overshoot is observed, where helium filling the void space of the zeolites is displaced by the moving CO_2 front, resulting in the slight increase in He concentration observed (a phenomenon known as "roll-up[12]"). As can be seen, the CO_2 breakthrough

curves begin to "sharpen" as the superficial velocity past the fibers increases. This is also reflected by a decreasing "degree of spreading" (seen in Table 7.1) as superficial velocity increases for the lower void fraction module. Though the modules were tested at similar superficial velocities, the higher packed modules would exhibit higher local Reynolds numbers than the less-packed modules, thereby sharpening the breakthrough front more noticeably at equivalent superficial velocities, as explained in Chapter 2, Section 2.3.1.1[13].

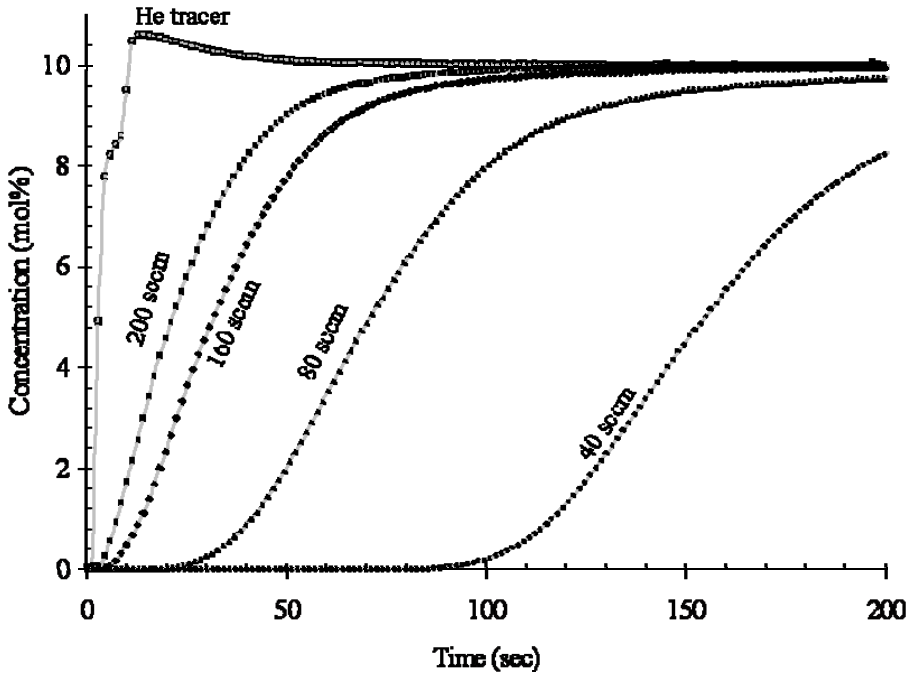

Figure 7.6: CO_2 breakthrough curves for six fiber module (void fraction=0.28). System temperature is 38°C. Flow configuration is parallel-flow, fibers have neoprene barrier layer present. No cooling water was used in the bores of the fibers. Bed length is 23.4 cm.

The loosely packed module would be expected to exhibit this same trend in sharpening at yet higher flowrates which are currently unachievable in the experimental setup. While a loosely packed fiber module was originally envisioned as the ideal arrangement for a fiber sorbent contactor used in RTSA systems, the results of these

experiments indicate that without tightly packed fibers, external mass transfer limitations will limit the overall efficiency of the bed since a sharper breakthrough wave is more desirable in actual operation.

Table 7.1: Degree of sharpening as a function of module void fraction and superficial velocity

Module Void Fraction	Gas	Superficial Velocity (cm/s)	Degree of Spreading (cm)	$\frac{\text{Degree of Spreading}}{L_{Bed}}$
$\varepsilon = 0.28$	CO_2	47.5	2.3	9.8%
		38.0	2.8	12.0%
		19.0	4.0	17.1%
		9.5	5.0	21.5%
	He	47.5	0.3	1.2%
		38.0	0.4	1.9%
		19.0	0.9	4.0%
		9.5	1.2	5.1%
Module Void Fraction	Gas	Superficial Velocity (cm/s)	Degree of Spreading (cm)	$\frac{\text{Degree of Spreading}}{L_{Bed}}$
$\varepsilon = 0.40$	CO_2	36.8	7.0	19.3%
		18.4	8.1	22.5%
		6.1	7.2	19.8%
	He	36.8	0.3	0.9%
		18.4	0.5	1.3%
		6.1	0.8	2.2%

As can be seen in Table 7.1, the CO_2 front spreads over approximately 20% of the bed at all superficial velocities studied for the "loosely" packed module ($\varepsilon=0.40$), while the spread is reduced to 10% at high velocities for the tighter packed module. These curve spreads indicate via the LUB method (Chapter 2) that the fiber sorbent modules will have to be oversized by 10-20%; this can be reduced via increased packing density[††] or increased superficial velocity. Clearly, a debate between capital expenditures and

[††] A void fraction of 0.28 is the close-packed limit of aligned cylinders.

operating expenditures arises here, as an increase in flue gas superficial velocity will decrease necessary bed sizes, but will increase the energy requirements of the CO_2 capture system.

7.4.2 CO_2 Sorption Capacity in Fiber Sorbents, Uncooled

The CO_2 sorption capacities of the fiber modules were measured 500 seconds after CO_2 breakthrough was observed by integrating the area bounded by the helium tracer curve and the CO_2 breakthrough curve. Figure 7.7 shows the capacities measured by the breakthrough experiments as a function of the superficial velocity past the fiber. The "apparent" fiber sorbent capacity for CO_2 decreases with an increase in superficial velocity. Clearly, if infinitely long times were used, all of the fiber sorbents would display equal capacity. This phenomenon could be explained by either a bed "bypass" or due to heat effects within the fiber sorbents. Since the breakthrough experiments showed no signs of helium (or CO_2) bypass, heat effects were identified as the likely cause of the loss of capacity. Without cooling water in the bores of the fibers, the sorption enthalpy will heat the zeolites within the fiber wall, thereby slowing the adsorption kinetics down (again, if given enough time the equilibrium capacity of 13X at the experimental temperature will be observed). The heat generated within the fibers is predominantly carried away by the shell-side gas and conducted through the fiber walls into the module wall (this is the main heat loss). At lower superficial velocities, the heat of sorption delivery rate is likely to be lower than or equivalent to the heat conduction rate, whereas at higher superficial velocities, the heat of sorption delivery rate is much higher than the

heat conduction rate. In essence, at lower superficial velocities, the fibers behave nearly isothermally (and film resistance becomes the dominating resistance) and at higher superficial velocities the fiber wall temperature becomes the dominating resistance to sorption. In actual operation, the cooling water in the bores of the fiber would carry away the heat of sorption and allow the fibers to remain isothermal even at higher superficial velocities.

To test this hypothesis, 5mm lengths of fiber sorbents were added to a water-jacket cooled packed bed filled with glass chips and the breakthrough experiments were repeated. As can be seen in Figure 7.7, the capacity of the fiber segments in the packed bed was maintained despite increases in the superficial velocity through the bed—the slight increase in capacity observed is a result of the higher CO_2 pressures in the bed required to achieve the higher superficial velocities. The fibers, diluted in glass chips and in contact with the actively cooled column walls, were able to maintain a nearly isothermal level over the course of the sorption experiment. The capacities measured were consistent with 75% of the 13X CO_2 capacity at the same conditions (Appendix D).

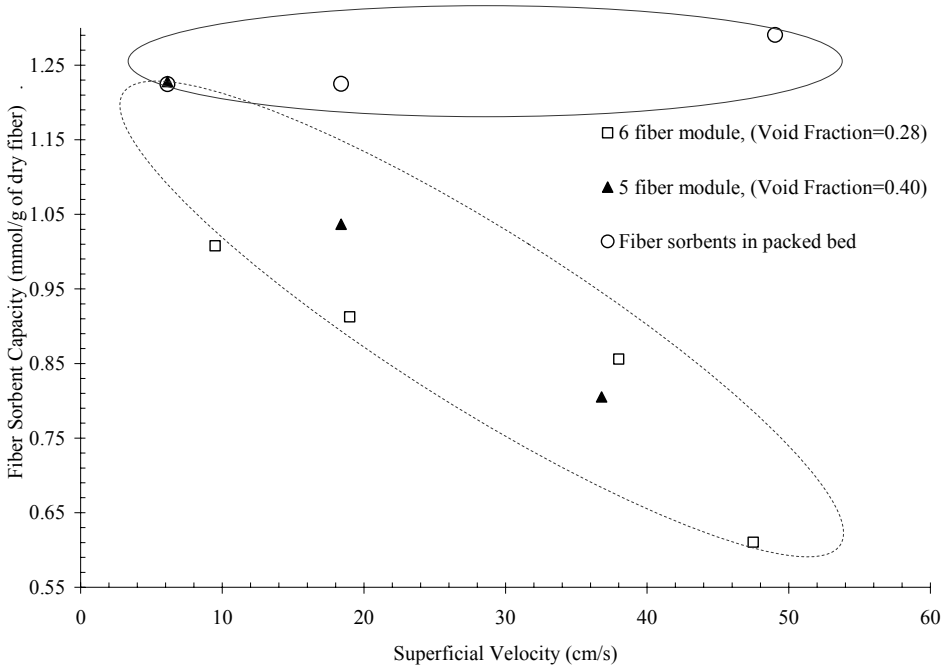

Figure 7.7: Sorption capacities of fiber sorbents 500 seconds after breakthrough time as a function of gas superficial velocity compared to sorption capacities of chopped fiber sorbents in packed bed with active cooling. The dashed-circle region indicates general trend of capacity loss with increasing superficial gas velocity for the fiber modules, while the solid-circle region indicates that the capacity of the fibers in the packed bed configuration remain nearly constant.

7.5 Effect of Cooling Water on Sorption Performance of Hollow Fiber Sorbents

One of the main motivations behind the use of hollow fiber sorbents is the ability to perform rapid thermal cycles which, in the absence of cooling, are quite non-isothermal due to the zeolite's heat of sorption release. Without cooling water, the fiber sorbent bed will lose capacity at higher CO_2 flowrates, as demonstrated in Section 7.4.2. As established in the previous section, a high CO_2 velocity is desired not only for rapid cycles and bed size reduction (due to the fact that each bed is processing more CO_2 per minute), but also for minimization of an external boundary layer. Cooling water running

through the bores of the fibers allow for this advantage to be realized. A second, arguably greater advantage of fiber sorbents is the ability to transfer the sorption enthalpy released to the cooling water flowing through the bores of the fibers for integrated heat management[14]. In order for both of these to be achieved, an understanding of the effect of cooling water and cooling water flowrate on the sorption capacity must be developed as well as an understanding of the effect of the cooling water flowrate on the amount of sorption heat captured by the cooling water. To explore this effect, a six-fiber module with a PVDC layer made via toluene-assisted drying was used and tested in a similar fashion to the experiments in the preceding section; deionized water at 38°C (the experimental temperature) was flowed through the bores of the fibers at 1500 mL per hour, the maximum flowrate that was attainable in the current RTSA system. In another set of experiments, the flowrate of the flue gas through the module was set at 200 sccm, the highest flue gas flowrate possible in the current setup, and the water flowrate in the bores was varied from 45 mL per hour to 1500 mL per hour.

7.5.1 Effect of Cooling Water on CO_2 Capacity

In Section 7.4.2, a hypothesis about the decrease in "apparent" CO_2 capacity as a result of increasing flue gas flowrate was developed. Primarily, the heat delivery rate at the faster gas velocities is much higher than for the slower gas velocities, resulting in a larger thermal spike in the fiber sorbent walls, which has the effect of temporarily decreasing the zeolite sorption capacity. The experiments in the previous section were revisited with a fine needle thermocouple nested into the middle of the fiber module (see

Chapter 3, Figure 3.8). These experiments were performed in order to have a meaningful comparison with fibers that were actively cooled. Figure 7.8 shows the thermal front data that were captured at three different flue gas flowrates for the uncoated fiber sorbents. The data have been normalized by the highest temperature spike that was observed at 160 sccm. The main reason for this normalization is that the maximum fiber temperature recorded was approximately 4°C, as opposed to the predicted 40°C thermal spike.‡‡ This difference in temperature is most likely the result of the 6 fibers within the module being in intimate contact with the walls of the module; these walls essentially act as a heat sink, which diminishes the magnitude of the thermal wave measured. These heat losses will be a recurring theme throughout the chapter.

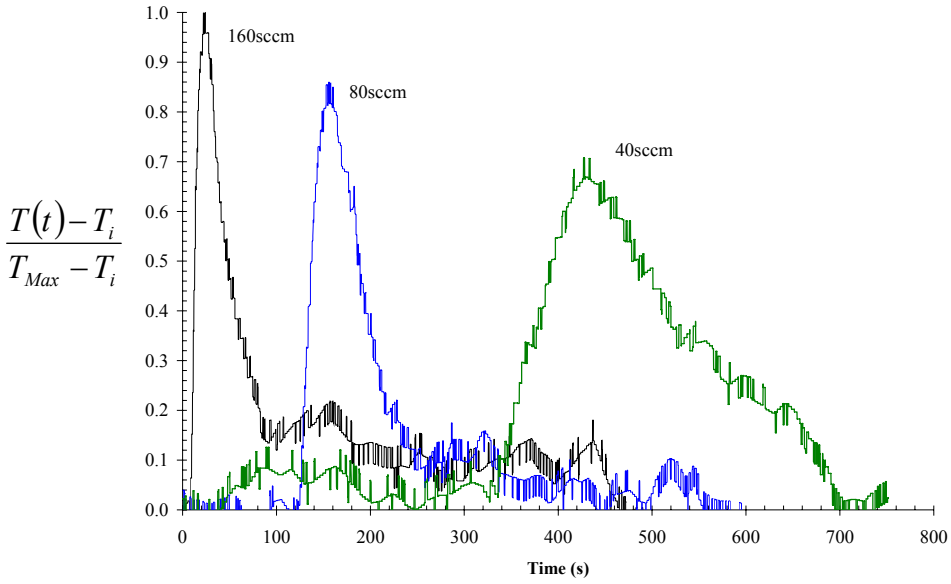

Figure 7.8: Thermal fronts measured at the middle of the six fiber module at three different flue gas flow rates. Bed length is 23.4 cm. The ordinate axis is the temperature signal normalized by the highest temperature observed at the highest flue gas flow rate.

‡‡

$$\Delta T_{13X} = \frac{n_{CO2}(0.1atm, 35°C)\cdot \Delta H_{CO2/13X}}{m_{13X}\cdot C_{P,13X}} = \frac{0.9mmol\ CO_2}{g\ 13X}\cdot\frac{36J}{mmol\ CO_2}\cdot\frac{g\ 13X\cdot °K}{0.8J} = 40.5°C$$

As can be seen in Figure 7.8, the overall intensity of the thermal wave decreases with decreasing flue gas flowrate, and the thermal wave itself becomes more diffuse. This is in line with the hypothesis in Section 7.4.2, as the heat delivery rate (via the CO_2 heat of sorption) is clearly much slower—or more diffused—at lower velocities, hence the higher breakthrough capacities. Once cooling water was flowed through the bores, the thermal front data (Figure 7.9) confirms that there is a drastic reduction in heat released when cooling water is used, lending credence to the heat-effect induced capacity loss hypothesis in Section 7.4.2.

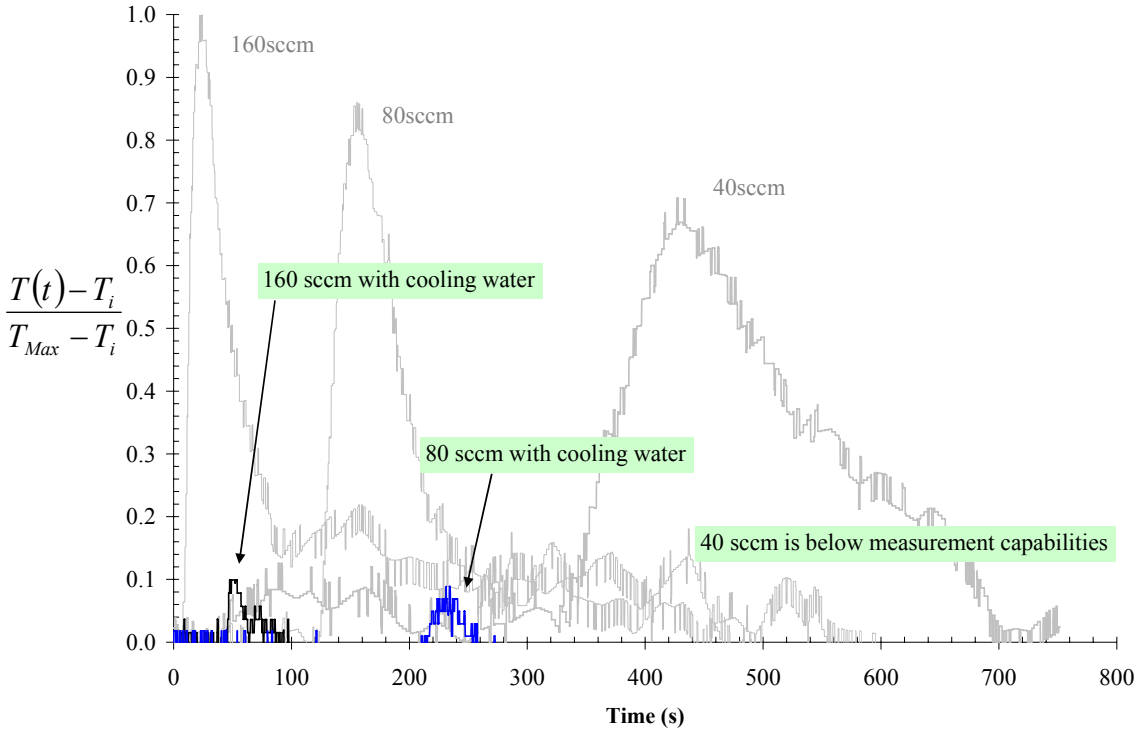

Figure 7.9: Thermal fronts in actively cooled fiber sorbent modules (cooling water flow rate = 1500 mL/hr) as a function of flue gas flow rate shown in color. Gray thermal fronts correspond to uncooled fiber sorbents at varying flue gas flowrates.

Figure 7.10 illustrates the capacity loss associated with an increasing rate of heat release (i.e., an increasing superficial velocity) for uncooled fiber sorbents, while the

"expected" capacity is roughly maintained once cooling water is flowed through the bores of the fibers. Ideally, the difference in uncooled capacities versus cooled capacities should grow as the flue gas flow rate is increased, provided the cooling water flowrate is increased sufficiently to match the increased heat delivery rate. As can be seen in Figure 7.10 this trend is realized within the range of velocities that were able to be tested.

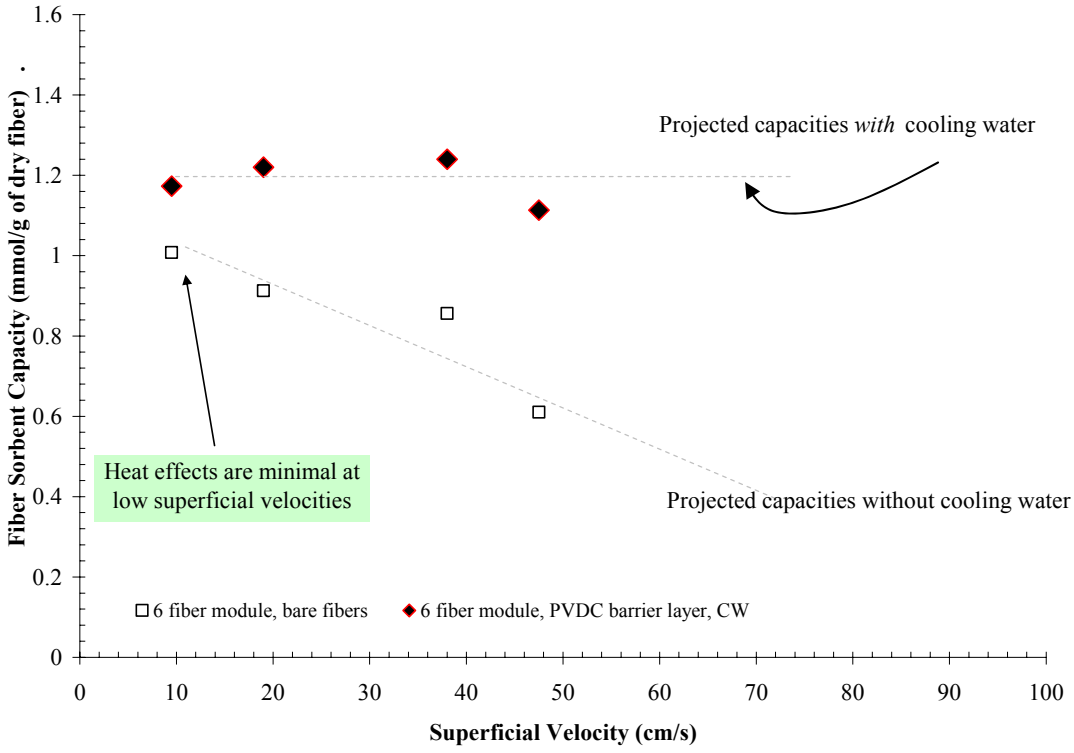

Figure 7.10: Capacity of uncooled fiber sorbents (open squares) as a function of flue gas superficial velocity, and capacity of actively cooled fiber sorbents (closed diamonds) as a function of flue gas superficial velocity. Cooling water flow rate was set at 1500 mL/hr.

Another possibility for the marked decrease in capacity with increased velocity is that the CO_2 front velocity is fast enough to cause internal mass transfer resistances to become dominant (as in, the contact time between the CO_2 and the fibers is longer than the internal mass transfer time).

However, this can easily discounted by the following estimate[10]:

$$\text{No external mass transfer resistance:}$$
$$t_{90} = \frac{0.5 \cdot l_{wall}^2}{D_{eff}} = \frac{0.5 \cdot \left(400x10^{-4}\, cm\right)^2}{0.004 \cdot cm^2 / s} = 0.2 \text{ seconds}$$
$$\text{Severe external mass transfer resistance:}$$
$$t_{90} = \frac{5.7 \cdot l_{wall}^2}{D_{eff}} = \frac{5.7 \cdot \left(400x10^{-4}\, cm\right)^2}{0.004 \cdot cm^2 / s} = 2.3 \text{ seconds} \qquad \textbf{(4)}$$

These estimates show that even in an extremely externally mass transfer limited case (which, according to Section 7.4, 50 cm/s flue gas superficial velocity is not), 90% sorption occurs in approximately 2 seconds. The above experiments show that cooling water in the bores is quite necessary to maintain sorption capacities at the high flue gas flowrates required for post-combustion CO_2 capture.

7.5.2 Effect of Cooling Water on Front Velocity

A key pair of parameters for designing a full scale RTSA system is the velocity of both the thermal front through the fiber bed and the concentration front through the fiber bed. These parameters can be estimated by taking the bed length over the time required to reach the midpoint in either the CO_2 front or the temperature front (the time for the temperature front must be multiplied by two, as the thermocouple is in the middle of the bed). Figure 7.11 shows these front velocities in the fiber module as a function of the superficial flue gas velocity.

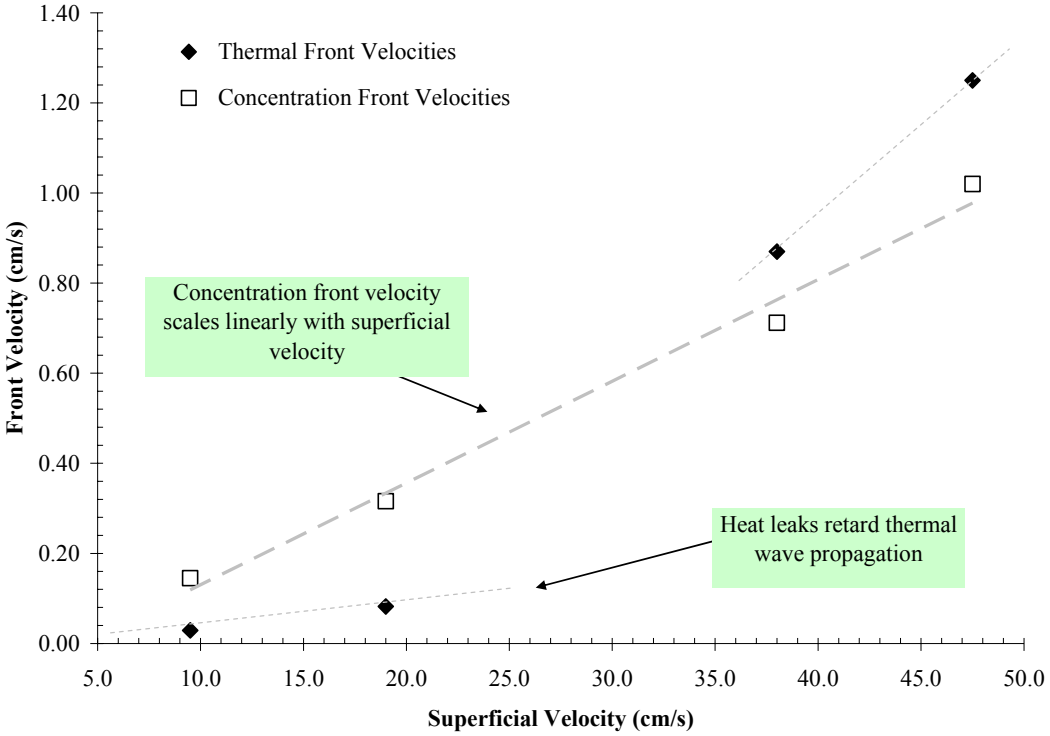

Figure 7.11: Concentration (open squares) and thermal (closed diamonds) front velocities as a function of flue gas superficial velocity.

Chapter 2 described that in the case of fiber sorbents, the thermal wave should always propagate faster than the concentration front. Surprisingly, at low flue gas feed flowrates (low superficial velocities), the concentration front leads the thermal front, while at high feed flowrates, the thermal front propagates faster than concentration front. As discussed in Chapter 2, both the thermal and concentration front propagation velocities scale linearly with the feed gas superficial velocity. While the concentration front experimentally scales linearly with superficial velocity (as expected), the thermal front appears to have a discrete step in front velocity between 20 cm/s and 35 cm/s. The most likely cause of this is that the heat delivery rate (which, in theory, also scales linearly with the flue gas flowrate) is quite low for the slower superficial velocities. In

the presence of significant heat leaks, the already weak thermal front at these low flowrates will be significantly diffused, causing the midpoint temperature rise to occur much later than it would in the absence of these heat leaks. At the higher feed flowrates, the thermal spike in the fibers is much more intense, and the midpoint is likely more accurately measured (though heat leaks are still significantly diffusing the thermal front). Ideally, once the fibers are actively cooled with cooling water, the CO_2 front velocity will be slowed due to the increase in capacity as a result of the fibers being more isothermal. Figure 7.12 shows that the concentration fronts were indeed slowed by flowing cooling water through the bores; an average of a 38% reduction in front velocity was recorded. In the absence of severe thermal leaks, the reduction in front velocity via active cooling is expected to be even more substantial, as the uncooled fibers will become significantly hotter, thereby accelerating the front velocity.

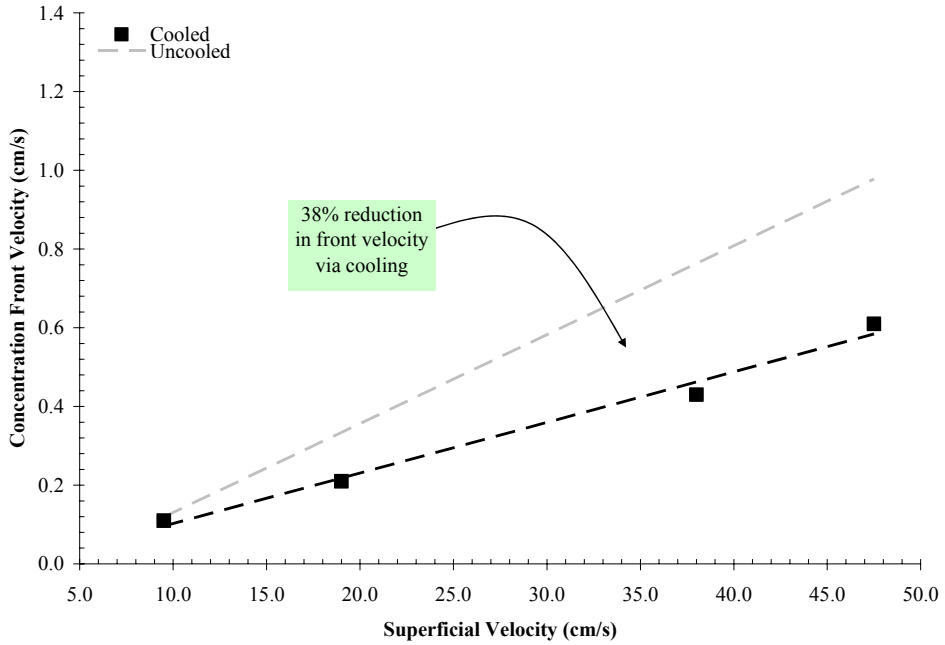

Figure 7.12: Concentration front velocities for cooled (squares) fibers and uncooled fibers as a function of flue gas superficial velocity. Cooling water flow rate was set at 1500 mL/hr.

Clearly, relative to the uncooled case, the fibers are kept almost entirely isothermal by the cooling water flowing at 1500 mL per hour through the bores of the 6 fibers. Furthermore, the 38% reduction in CO_2 front velocity allows for longer cycle times relative to an uncooled bed of the same size, thus reducing operating expenses[§§]. The above results clearly show that cooling water is necessary to achieve one of the main advantages of fiber sorbents: retained sorption capacity at high CO_2 flowrates, allowing for rapid cycles which thereby minimize the CO_2 capture system size.

7.5.3 Effect of Cooling Water Velocity on Heat of Sorption Capture

7.5.3.1 Cooling water velocity effect on fiber sorbent capacity

The secondary motivation behind fiber sorbents is the ability to capture via cooling water the heat of sorption released by the CO_2-zeolite interaction, as discussed in Chapter 4. To investigate the possibility of this, the flue gas flowrate was set at 200sccm, as this was the most thermally intensive flowrate studied (and was the maximum flowrate attainable in the system) while the water flowrate through the bores was varied from 45 mL per hour to 1500 mL per hour. A needle thermocouple at the outlet of the module was used to measure the temperature rise in the cooling water, while a needle thermocouple placed at the inlet to the bores of the fibers measured the input water temperature. This allowed for observation of the temperature rise in the cooling water,

[§§] For two beds of the same size, the one with longer cycle times will exhibit the lowest operating costs. The best way to think of this is that each bed will require the same amount of energy to cool the bed (or heat the bed) per cycle, and the one with a longer cycle time will have require less work, or in other words, less operating expenses.

and by integrating the outlet thermal wave, the total amount of heat transferred to the cooling water could be estimated.

Figure 7.13 shows the results of the experiment described above. As can be seen there is a steady decrease in the observed capacity (capacity after 150 seconds) as the cooling water velocity was increased. Of course, this is counterintuitive, as the cooling water velocity increase should keep the fibers more isothermal, resulting in the equilibrium CO_2 capacity being maintained. The most likely explanation is that, as part of the experimental procedure, the fiber module stayed online continuously at 38°C with shell-side N_2 (or flue gas) and flowing bore-side water for 5 days, where trace amounts of water were able to permeate through the barrier layer and slowly reduce the capacity of the 13X. To estimate the amount of water that is permeating through the barrier layer, the following calculation can be used (a water permeance of 0.03-1.0 GPU has been used for this estimate),

$$\dot{m}_{H2O} = P_{H2O,PVDC} \cdot A_s \cdot p^*_{H2O}(38°C) =$$

$$= 0.03 \cdot 10^{-6} \frac{cm^3(STP)}{cm^2 \cdot s \cdot cmHg} \cdot 14.0 cm^2 \cdot 4.97 cmHg \quad \textbf{(4)}$$

$$= 2.08x10^{-6} \frac{cm^3(STP)}{\text{s}}$$

$$\dot{m}_{FlueGas} = 200 \cdot \frac{cm^3(STP)}{\text{min}} = 3.3 \cdot \frac{cm^3(STP)}{s}$$

$$y_{H2O} = \frac{\dot{m}_{H2O}}{\dot{m}_{FlueGas} + \dot{m}_{H2O}} = \frac{2.08x10^{-6}}{3.3 + 2.08x10^{-6}} = 0.62\,ppm \quad \textbf{(5)}$$

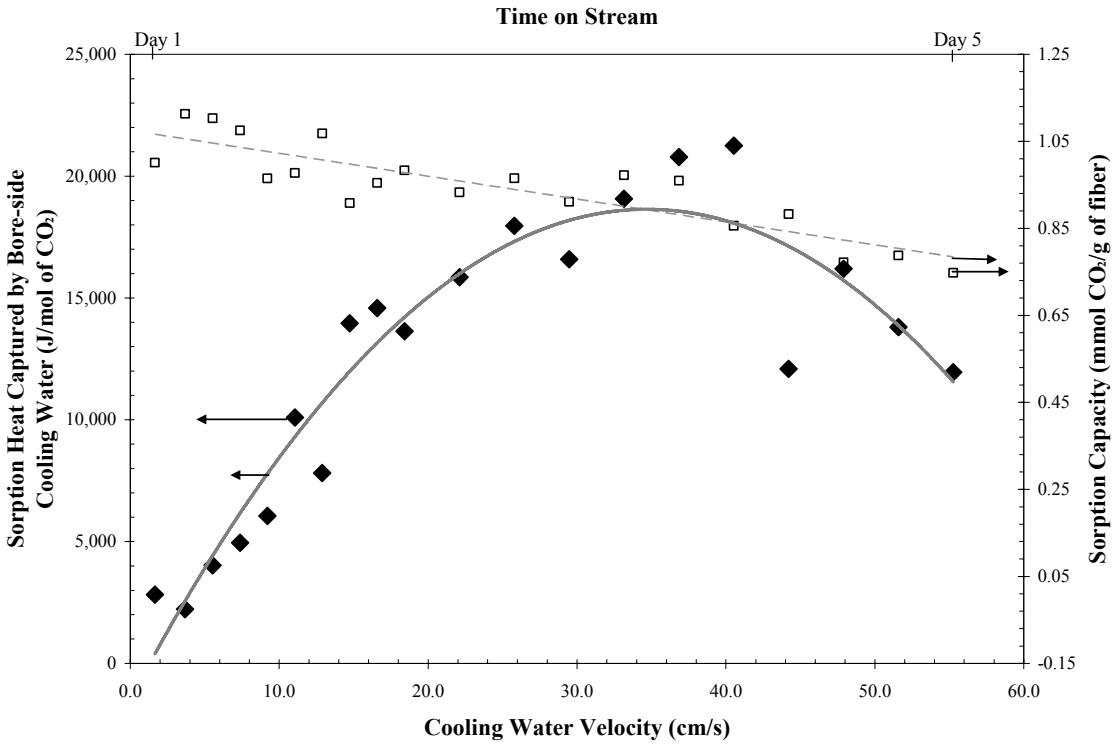

Figure 7.13: Effect of cooling water velocity on the sorption capacity of the fiber sorbents (open squares) and the sorption heat capture by the cooling water (closed diamonds).

As can be seen in the previous calculation, the equilibrium concentration of water in the gas phase on the shell-side of the sorbent is between 0.6-21ppm[***]; 21 ppm is a high-end estimate, as water permeation experiments that spanned 5 days (see Chapter 6 for details) never revealed any water in the gas phase—21 ppm is well within the range of the mass spectrometer. However, this estimate assumes that the permeating water mixes perfectly with the flowing shell-side gas. Most likely, there is a radially moving water concentration front in the fiber wall. Water permeating through the barrier layer will initially encounter freshly activated 13X at the very inner radius of the fiber; the local concentration of water at this location is unknown. The 13X will quickly come to

[***] 21 ppm calculation not shown; simply scale the 0.62 ppm by the ratio of the water permeances considered (0.03 GPU-1.0 GPU).

equilibrium with whatever the local water concentration is, and due to the highly chemisorbing nature of water, will not likely (or not quickly) go to the final global equilibrium water concentration of 0.6-21ppm. As such, the bed will slowly lose capacity the more time it is on stream, which has been demonstrated. Of course, if zeolite 13X-based fiber sorbents are used in industrial applications, the fiber beds can be periodically taken off-stream and regenerated with hot nitrogen.

7.5.3.2 Heat of Sorption Capture via Cooling Water

While the loss in capacity is certainly important for long term industrial use (and is more a fault of the proof-of-concept 13X than the fiber sorbent platform), the above experiment also revealed that there is an optimum water velocity for capturing the sorption heat via the water in the bores. As can be seen in Figure 7.13, at the maximum heat captured, approximately 22,000 joules of sorption heat per mole of CO_2 captured has been transferred to the water, out of a maximum of 36,000 joules per mole (the heat of sorption of CO_2 on 13X). It is difficult to tell whether the remaining energy not captured is lost to the heat leaks present in the system, or is actually the upper limit that can be achieved due to heat transfer through the fiber sorbent walls. While it is quite difficult to estimate how the heat captured should scale with the cooling water velocity, the observations can be logically explained. Figure 7.14 shows the normalized outlet water temperature for three different water flowrates; the flowrates were chosen to represent high velocity/low heat capture (1500 mL/hr), low velocity/low heat capture (100 mL/hr), and high velocity/high heat capture (1100 mL/hr).

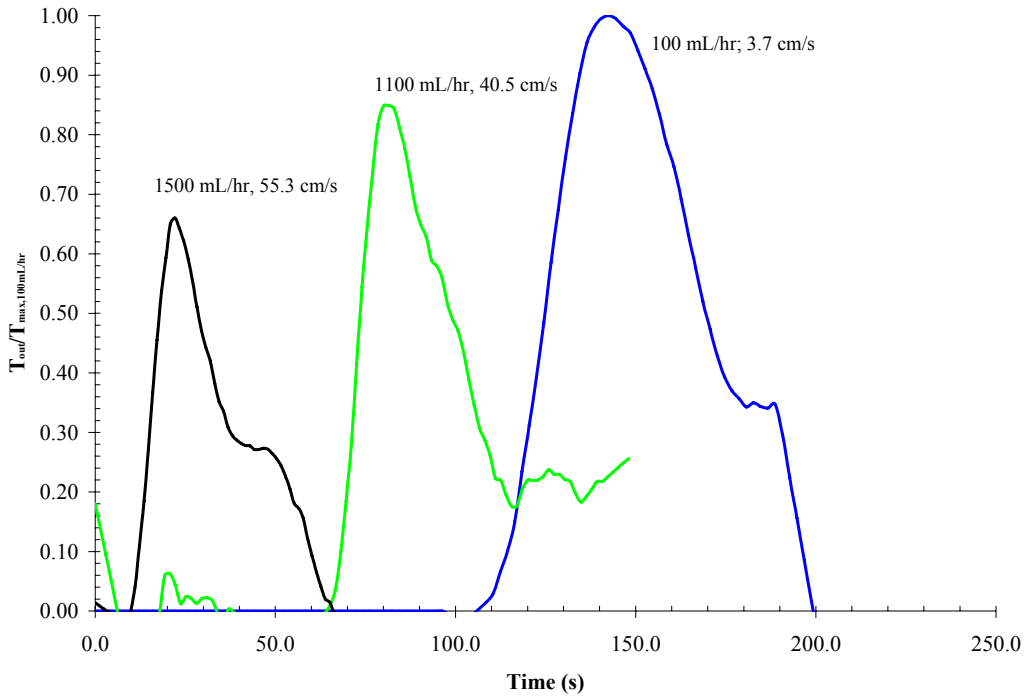

Figure 7.14: Normalized thermal fronts in bore-side cooling water measured at module outlet.

As can be seen in Figure 7.14, the low water flowrate results in the largest temperature increase in the outlet water, and also the largest area of the three curves. As the water flowrate is increased, the temperature rise in the cooling water becomes less pronounced. However, as the cooling water flowrate is increased, the temperature front becomes increasingly more sharp, which has important implications for efficient power-plant heat integration. Even though the slowest water flowrate has the largest temperature rise, only a small amount of water is heated, whereas at the higher flowrates, similar temperature rises (16% less and 34% less, respectively) are observed, but much larger quantities of water are heated, hence the increase in sorption heat captured. One possible explanation for the above results centers around the fact that, at high water velocities, the thermal front propagation will lag significantly behind the water velocity (Fig. 7.15, Table 7.2).

Table 7.2: Front velocities within hollow fiber sorbent module

Front	Velocity (cm/s)
Carrier Gas	47.50
Water, 100 mL/hr	3.70
Water, 1100 mL/hr	40.53
Water, 1500 mL/hr	55.30
CO_2	0.98
Thermal, fiber	1.28

If rapid heat transfer is assumed (which is likely in the thin fiber walls), the thermal front will transfer its heat to a plug of the rapidly moving cooling water. This plug will move well ahead of the thermal front in the fiber in the high water velocity scenario, creating a driving force for heat transfer from the water to the fiber wall (as the plug of hot water moves away from the thermal front in the fiber wall, the water plug is actually hotter than the fiber wall), causing the hot plug of water to become cool, as illustrated in Figure 7.15. Finally, once the thermal front nears the end of the fiber length, the hot plug of water will arrive at the ends of the fiber at the thermocouple, where the heat the water has picked up can be measured. However, in the high water velocity scenario, there is less time for heat transfer between the length of the thermal front in the fiber wall and the flowing cooling water, resulting in lower water outlet temperatures. At the slowest water velocities, the water propagates through the bore of the fiber only marginally faster than the thermal propagation front in the fiber wall. This gives the plug of water much more contact time with the hot fiber wall, causing its temperature to rise

considerably. However, since the water flowrate is quite slow, the total amount of sorption heat that is captured in the cooling water is reduced relative to the high flowrate scenarios. Figure 7.15 gives an overview of this hypothesis.

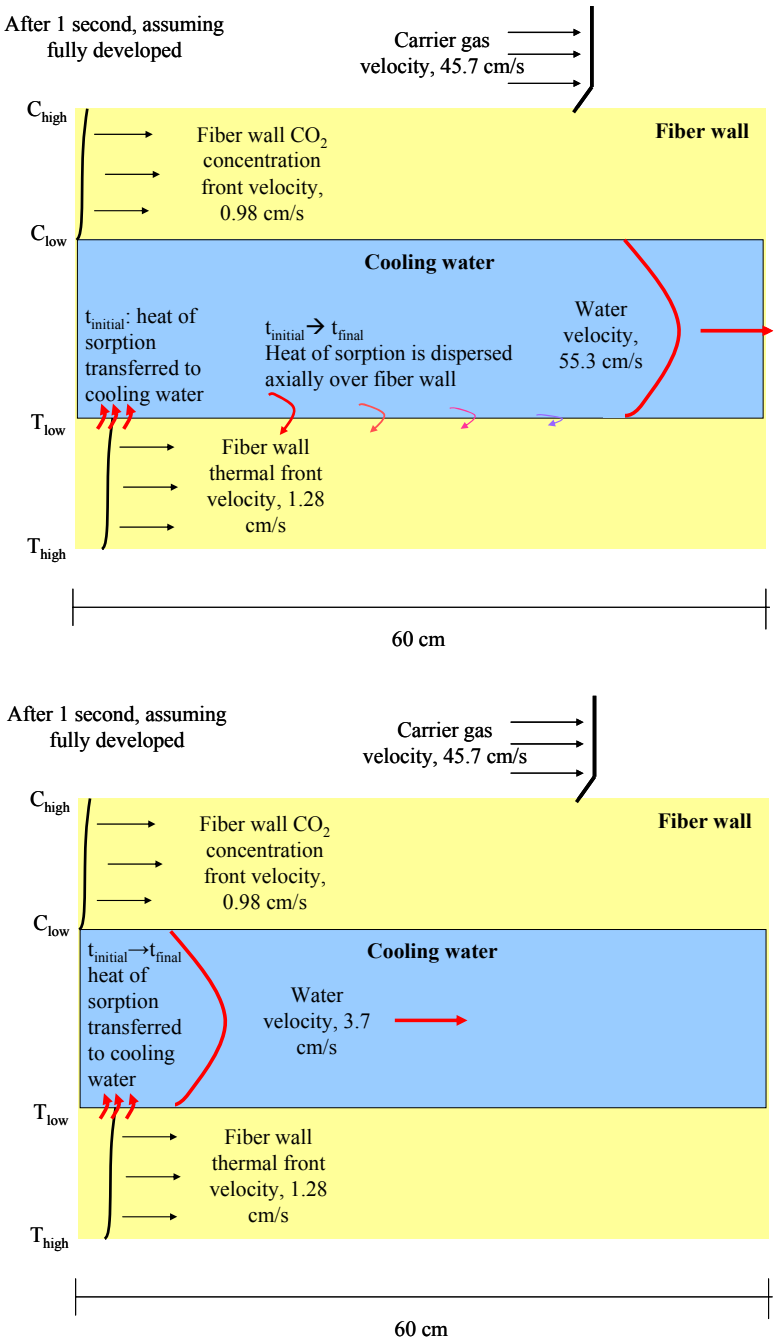

Figure 7.15: Cartoon representing front propagation axially through the fiber in two extreme cases: Rapid water velocity *(top)* and slow water velocity *(bottom)*.

These results indicate that an optimum exists for the cooling water flowrate; this optimum has been identified on the lab scale, but it requires considerable analysis to predict. While it is difficult to extrapolate exact values, this situation will likely extend to industrial scales as well: low water velocities will generate the hottest water, but also will generate less useful heat due to the small amounts of water used. On the other hand, extremely high water velocities will move much too fast to heat the water as much as the low velocity case. To achieve the most useful energy from the heat of sorption release (a key factor discussed in Chapter 4), the water velocity must be carefully balanced between water temperature rise and total amount of water heated.

7.6 Desorption of CO_2 from Fiber Sorbent Modules using Hot Water

7.6.1 Challenges of Recovering a Pure Product using TSA

The previous section focused entirely on the sorption side of the RTSA cycle, with emphasis on investigating the optimum water flowrate to ensure isothermal operation and/or maximum heat of sorption capture. Of course, capturing the CO_2 optimally does nothing for reducing CO_2 emissions if the fibers are regenerated without producing a pure CO_2 product. In this regard, there are serious difficulties associated with recovering a pure CO_2 product via a TSA process. Typically, adsorption processes are split depending on whether trace or bulk contaminants need to be removed. For trace contaminants (< 1 mol%), TSA is preferred; during regeneration (which occurs infrequently) the bed is simply heated with an inert purge, and the desorbing product is

condensed and collected[15]. For bulk contaminants (5-25 mol%), PSA is preferred[15]. However, PSA has already been ruled out as a post-combustion CO_2 capture technique due to the immense compression and/or vacuum requirements that go along with the enormous amount of flue gas.

This mismatch in desorption mode—bulk contaminant (CO_2, 10 mol%) and thermal swing desorption—creates a challenging situation for recovering a pure CO_2 product from fiber sorbents. The ideal case requires a sharp thermal step from 38°C to 100°C in the inlet water temperature, while the flue gas feed to the bed is shut off, and the vent to the bed is left open. If the sharp step is attained, the CO_2 will rapidly desorb as the thermal front moves through the fiber bed; the desorbing CO_2 will push the interstitial gas axially down the shell-side of the module. As the thermal wave leaves the fibers, the module will ideally be primarily CO_2, which can be seen assuming perfect mixing, viz.,

$$
\begin{aligned}
&C_{swing,38-100°C,13X} = 0.6 \cdot \frac{mmol\ CO_2}{g\ 13\text{X}} \\
&m_{13X,6\ fiber\ module} = 0.32\ g\ 13\text{X} \\
&m_{CO2,desorbing} = 0.19 mmol \text{ at } 38°\text{C and } 1\text{ atm} = 5.2 cm^3 \text{ of } CO_2 \\
&V_{interstitial} = 1.74 cm^3 \\
&y_{CO2} = \frac{m_{CO2,desorbing}}{m_{CO2,desorbing} + V_{interstitial}} = 74.9 mol\%
\end{aligned}
\qquad \textbf{(6)}
$$

At this point, the module feed should be opened to nitrogen (product gas from the sorption step) while hot water is still flowing through the bores. This will serve to push a

plug of CO_2 out. After the plug has been collected, cooling water can be switched back on, cooling the fibers back down and preparing for the next sorption step.

The above purity (74.9mol%) assumes that the desorbing CO_2 mixes with the interstitial gas in a perfect continuous stirred tank reactor (CSTR) fashion, which is the worst case. The *best* case is achieved when the desorbing CO_2 can displace the interstitially held gas in perfect plug flow reactor (PFR) form, thus attainting nearly pure CO_2 that can be collected via the aforementioned N_2 sweep.

7.6.2 CO_2 Desorption from 6-fiber Modules

An experiment was performed to simulate this ideal desorption mode. In this experiment, the fiber bed was saturated with 10 mol% CO_2 at 1 atm total pressure and 35°C. Next, the feed to the module was closed as the gas was switched to nitrogen, while simultaneously hot water at 100°C was pushed through the bores of the fiber. At the peak fiber temperature observed, the feed valve was switched back on to flush nitrogen over the fibers and ideally push out a plug of CO_2. Figure 7.16 shows the results of the desorption experiment. Initially, before 100 seconds (in the "Equilibrium" period), the fiber bed is saturated with CO_2 and no water is flowing. The inlet water temperature thermocouple is measuring stagnant water that is located between the 38°C module and the 100°C heat exchanger.

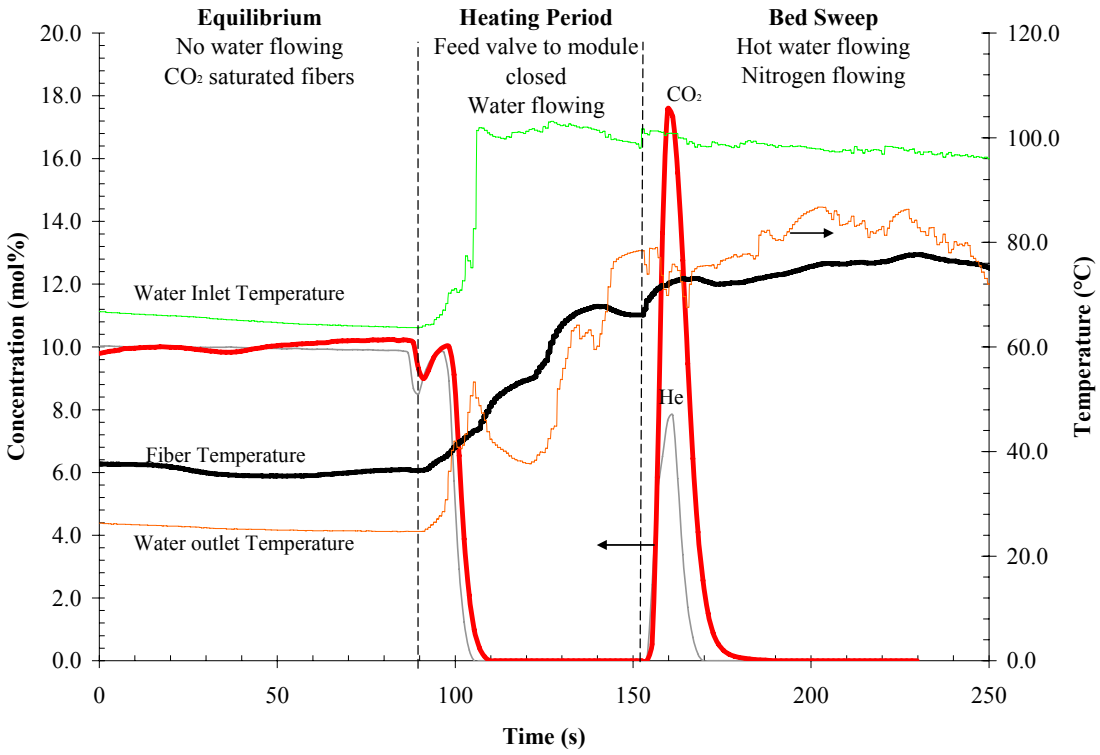

Figure 7.16: Temperature and concentration profiles for a CO_2 desorption experiment.

After the equilibrium period, hot water begins to push through the bore (1500 mL per hour) during the heating period. Unfortunately, due to the small scale of the experiments, a sharp thermal front could not be attained, despite many repeated attempts and system adjustments. While the inlet water certainly has a sharp thermal front (although it could be sharper—the front still spreads over 10 seconds), the fiber temperature front is severely dispersed. The main cause of this is that the fibers have both contact with the 100°C water in the bores and contact with the 38°C module wall. In essence, there is a large thermal heat sink in contact with every fiber in the module; the only way to avoid this is to construct modules that are much bigger in diameter. If sufficiently large modules are constructed, the majority of the fibers will be in contact only with other fibers, and only a small percentage will be in contact with the module

wall. This configuration should allow for a sharp thermal step in the fibers. Unfortunately, modules of this scale are currently beyond the scope of this project.

After a minute-long heating period, the fibers have risen to approximately 72°C. The outlet water temperature roughly matches the fiber temperature. Finally, the feed gas is turned back on to push the desorbed CO_2 out of the bed in the sweep step. Unfortunately, only an 18mol% CO_2 product has been recovered. However, to determine whether the desorption step works conceptually, the illustration in Figure 7.17 can be used.

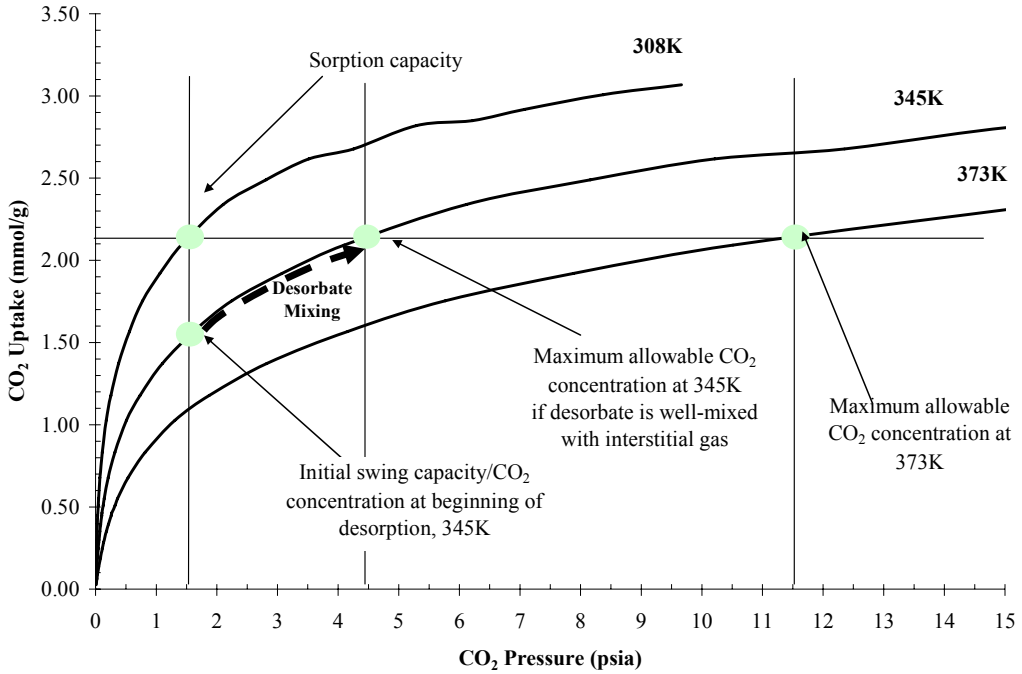

Figure 7.17: Fiber sorbent CO_2 sorption isotherms[16] showing possible desorption routes. If the CO_2 desorbs slowly due to a weak thermal step, subsequent mixing with interstitial gas in the module drives the CO_2 partial pressure up the isotherm via the "desorbate mixing" arrow.

This figure illustrates that if the CO_2 contained within the sorbents were to desorb and mix perfectly with the interstitial gas (worst case CSTR mode), that approximately 31

mol% purity should be expected (4.5 psia CO_2 partial pressure) . Of course, the poor thermal step results in a desorbing CO_2 front that is highly diffuse and mixes not only with the void space in the module (~2 cm^3), but possibly also the dead space downstream of the module (~8 cm^3). Furthermore, if there exists any zones for mixing between the module and the mass spectrometer, the purity of the CO_2 plug will be diminished significantly. Initially, the CO_2 will desorb from the fibers into a 10mol% CO_2 atmosphere, and due to the weak thermal step more CO_2 desorbs mixing in CSTR fashion, causing the interstitial CO_2 concentration to increase, thereby decreasing the driving force for CO_2 desorption. Most likely, the lack of purity is a result of these three factors working in tandem; the weak and dispersed thermal step reduces the swing capacity of the fibers and spreads the desorbing CO_2 out over more interstitial volume, while the nitrogen sweep can dilute the CO_2 purity if there are any mixing zones downstream of the module. Chapter 8 will discuss improvements to the RTSA system that should allow for higher purity CO_2 to be effectively captured in the desorption step.

7.7 Full RTSA Cycle

7.7.1 Fiber Sorbent Cooling Step

With the addition of a cooling step to bring the hot fibers back to the sorption temperature, a full thermal cycle can be emulated on the lab scale in a stepwise fashion. Unfortunately, a full rapid thermal cycle was not possible to perform on such small scales, as the sensible heat of the module and experimental apparatus significantly hinders the

ability of the fibers to be rapidly cycled between two extreme temperatures. The final step not addressed in the preceding discussions is the cooling step, which serves to remove the sensible heat in the fibers via cooling water while the exterior of the fibers are blanketed in nitrogen. Again, due to the large sensible heat of the experimental apparatus, this step is difficult to test in a rapidly cycling experiment. Therefore, an experiment was designed to simulate the cooling step. After the heating and desorption step—previously discussed—the fiber module heat tape was set to 110°C and allowed to thermally equilibrate. Cooling water at 25°C flowing at 1500 mL per hour was then turned on as the heat tape was shut off. The water inlet temperature, outlet temperature, and fiber temperature were monitored continuously. Figure 7.18 shows the results of this experiment.

Until a time of 32 seconds, the water in the system is stagnant (hence the high temperatures measured—the water thermocouples are close to the fiber module's heat tape), at which point the water begins to flow at 1500 mL per hour. A clear drop in the fiber temperature is observed, as is a long, slowly cooling tail. The long tail is most definitely a result of the natural cooling of the experimental apparatus from 110°C to ambient conditions. Despite the large heat leaks in the system, a sharp peak in the outlet water temperature was observed as the cooling step begins. However, this peak most likely corresponds to the plug of stagnant hot water that was present in the fibers bores before the experiment started. A water temperature greater than the feedwater temperature was observed at the outlet of the fiber, indicating that sensible heat was transferred over the length of the module.

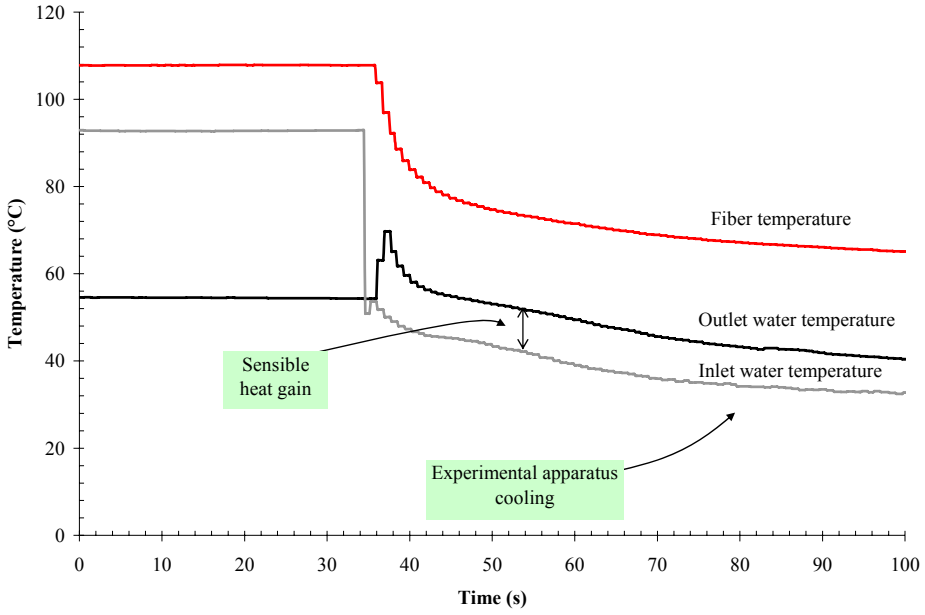

Figure 7.18: Cooling step in fiber sorbent RTSA cycle.

Of course, one of the principal energy saving mechanisms that was employed in Chapter 4 was the transfer of sensible heat from the fibers to the cooling water, essentially requiring cool water put in the front of the module to come out of the module as hot water. Unfortunately, it is difficult to decouple the sensible heat of the experimental system from the sensible heat of the fibers in the current setup. Therefore, the cause of the sensible heat gain in the cooling water is unknown. As larger modules are developed and constructed, this mechanism can be studied in detail.

7.7.2: Simulated Full RTSA Cycle

Finally, a picture of a full RTSA cycle may be assembled from the various parts described above. Figure 7.19 is the temperature and concentration response of the fiber

sorbent system for each step within the cycle. These results came from a single experimental run, but downtime required to heat and cool the experimental apparatus have been removed from the figure to show the performance of the system in the relevant portions of the cycle. The conditions used for this experiment were: 160sccm flue gas and nitrogen sweep flow rate and a 1500 mL/hr water flowrate.

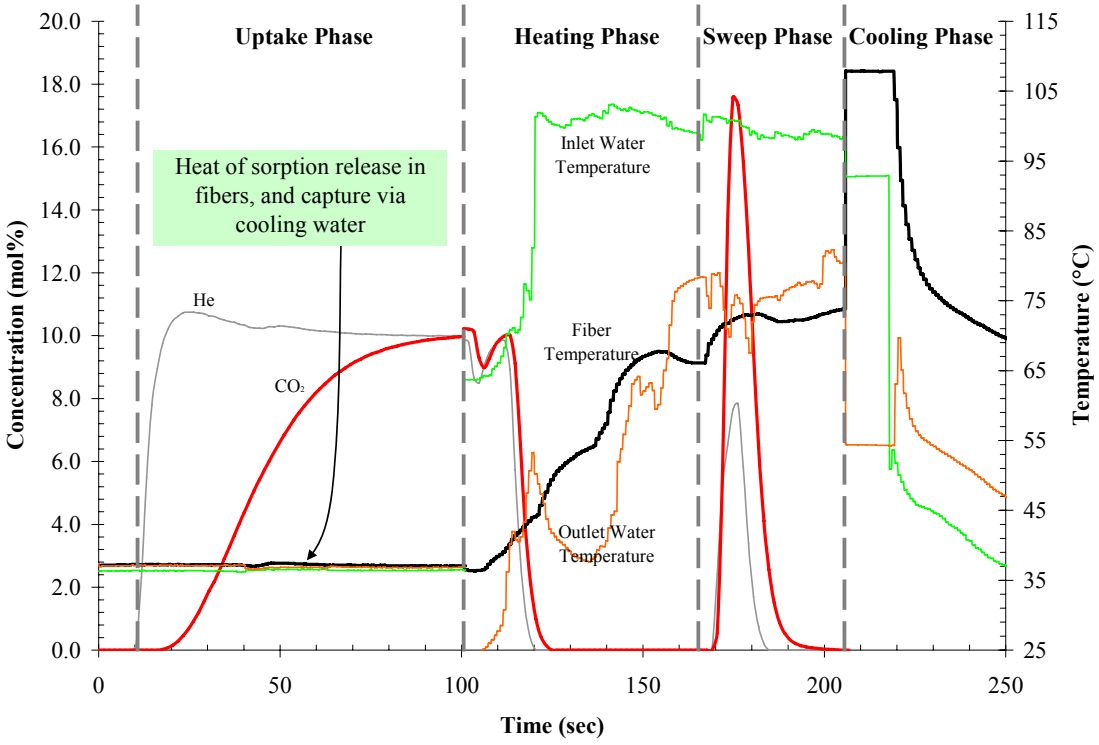

Figure 7.19: Simulated full fiber sorbent RTSA cycle. Due to severe thermal leaks associated with working on such small scales, there is a significant thermal lag between each step due to the experimental apparatus. The 4 phases of the full cycle have been "stitched" together to illustrate the important points.

A rough approximation of the full cycle time can be estimated for these conditions by taking the sum of the four phases. In this instance a full cycle time of 250-300 seconds can be expected, which is in line with the 70 second-per-phase estimate from Chapter 4. Ideally, for the industrial scale, all four phases would require the same

amount of time to allow for a four-bed, pseudo-steady state operation to take place. As can be seen in Figure 7.19, the uptake phase (or the sorption step) is by far the longest, requiring a full 100 seconds to complete. However, the vast majority of this 100 seconds is for the bed to come to complete equilibrium with the flowing CO_2. In the industrial case, the bed length would ideally be over-designed to account for the length of unused bed, and the sorption step would end when 1 mol% CO_2 has broken through the bed, which corresponds to a 90% capture of the power plant's CO_2. If this cut-off point had been used, the uptake phase would be approximately 25 seconds, instead of 100 seconds, putting it more in sync with the other phases. The heating phase also exhibits a longer-than desired operating time. As discussed above, due to the constraints of using small, six fiber modules, creating a thermal step in the fibers is difficult due to the large amount of heat leaks in the system. If the fiber temperature matched the inlet temperature step, the heating phase could be much shorter. While the full RTSA cycle is far from ideal, the general concepts of a fiber-based rapid thermal cycle can be gleaned from this rough sketch of a full cycle.

7.8 Effect of Oxygen on Fiber Sorbent Performance

In realistic flue gas conditions, oxygen is typically present up to 5 mol% within the CO_2-rich flue gas[17]. Therefore, any sorbent system which might be considered for post-combustion CO_2 capture must be tested for stability in the presence of oxygen. Oxygen exposure at high temperatures was unintentionally performed before tests similar to the ones described in the previous section. Before the experiment, the fiber sorbent

module was activated at 110°C under dry nitrogen. However, the bores of the fiber were not blanketed with nitrogen; ambient air was unintentionally left in the bores of the fibers. This effectively treated the fiber with 20 mol% oxygen at 110°C for 24 hours. Sorption capacity experiments (in the multicomponent fiber sorbent chromatography system) were performed on this oxygen-treated module, similar to the experiments in Figure 7.7 and Figure 7.10.

As can be seen in Figure 7.20, the fiber sorbent CO_2 capacity drops substantially after the fibers were exposed to oxygen at 110°C. Furthermore, the capacity does not show the same dependence on superficial velocity as the fresh fiber module, which was linked to the heat released during sorption. While 13X is calcined in air (indicating that it is likely stable in air at 110°C) the loss in capacity must nonetheless be attributed to the 13X.

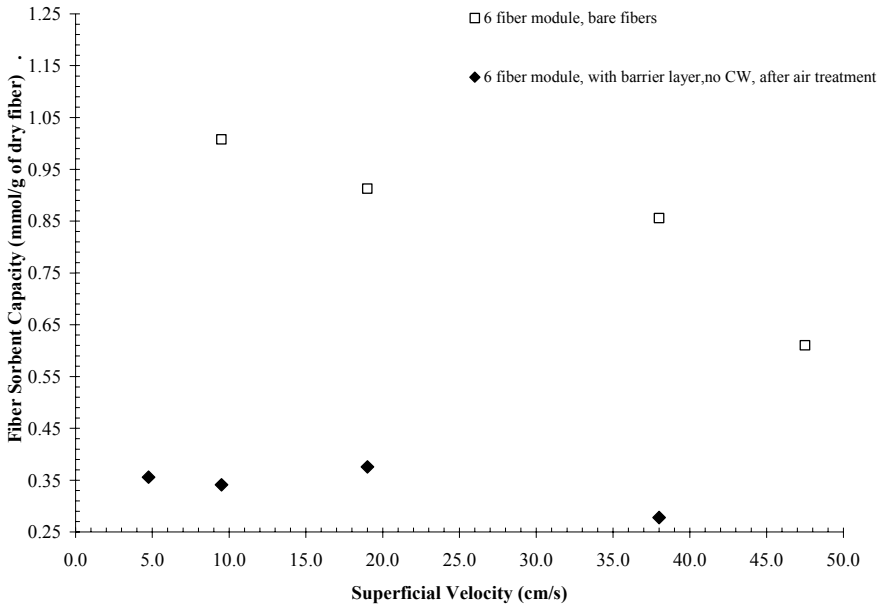

Figure 7.20: Fiber sorbent CO_2 capacity as a function of superficial velocity before and after 110°C air treatment.

It is known in the literature that under exposure to oxygen and heat, polyvinyl chlorides and polyvinylidene chlorides will undergo a process known as dehydrohalogenation, as illustrated in Scheme 1[18].

Scheme 1:

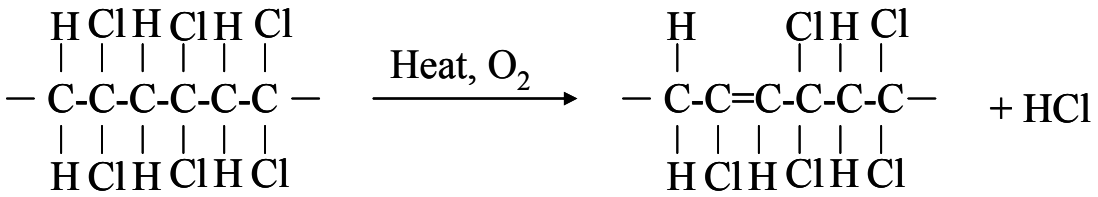

Under certain conditions (in the case of PVDC, 90°C is sufficient[18]), the PVDC layer will evolve hydrochloric acid (HCl) which will diffuse away from the barrier layer towards the bore and the zeolite-containing core structure. The current hypothesis explaining the lack of CO_2 capacity in the fiber sorbents after the oxygen treatment is that the evolving HCl attacks the 13X, perhaps destroying the crystal structure via dealumination[19]. To test this, a packed bed of coagulated PVDC was heated to 110°C under flowing air. Downstream of this bed was a 13X column, also heated at 110°C under the effluent from the PVDC bed. The effluent from the two-bed train was monitored with the mass spectrometer. After 24 hours, the 13X was removed, and XRD was performed on the 13X sample. The mass fraction spectrum clearly showed a peak pattern consistent with HCl (not shown here), while the XRD results (Figure 7.21) show that the crystal structure of the 13X has been altered significantly.

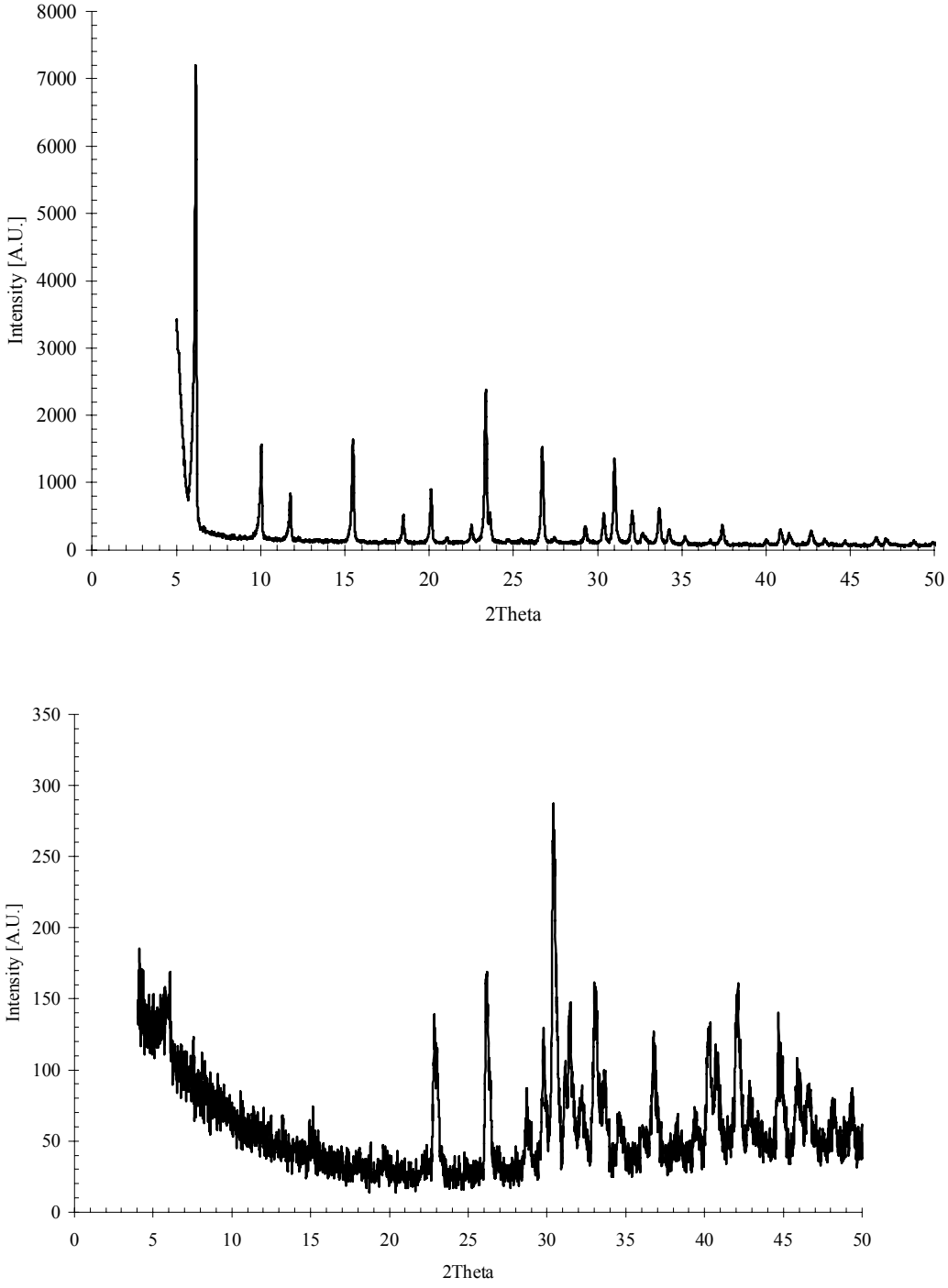

Figure 7.21: ***(top)*** **X-ray diffraction pattern of as-received zeolite 13X (dried at 110°C).** ***(bottom)*** **X-ray diffraction pattern of zeolite 13X that was placed downstream of a hot (110°C), air-exposed PVDC bed.**

The d-spacing in the HCl-treated 13X clearly shifts upwards relative to the fresh 13X after exposure to high temperature HCl. Furthermore, the pattern seems to indicate the HCl-treated 13X has developed an amorphous region. This experiment gives strong support to the hypothesis that HCl evolving via a dehydrohalogenation mechanism from the oxygen-exposed PVDC attacks the 13X, thereby destroying its crystal structure and its CO_2 sorption capacity.

The results presented above do not bode well for the future of PVDC as the barrier layer of choice in an industrial post-combustion CO_2 capture scenario, as the continuous oxygen exposure and thermal swings will likely render the sorbents inactive over a short period of time. However, for the purposes of demonstrating many of the new concepts that fiber sorbents introduce, PVDC works quite well, provided the flue gas streams studied are oxygen-free.

7.9 Conclusion

This chapter presented the sorption properties of the cellulose acetate/13X fiber sorbents in various modes: equilibrium, kinetic, cyclic, and chromatographic. From an equilibrium perspective, the spinning process and cellulose acetate support do not seem to affect the sorption capacity of the 13X, which was further confirmed with kinetic analysis, as the fiber sorbents sorbed CO_2 just as fast as bare 13X crystals. Cyclic measurements in a TGA show that the fiber sorbents do not appear to lose capacity over 48 hours of continuous thermal cycling. Finally, the fiber sorbents were assembled into

parallel flow modules, and installed into a custom-made chromatographic system. It was found that the hollow fiber sorbent modules need to be tightly packed with fibers and high gas velocities must be used in order to reduce external boundary layers which limit mass transfer. The addition of flowing cooling water in the bores of the fibers allowed the fibers to maintain sorption capacities as expected, even at high gas velocities. Thermal front and concentration front velocities were measured, and the cooling water velocity was varied to determine the optimum velocity required to capture the majority of the heat released during sorption. Full RTSA cycle experiments were attempted, but due to the small scales studied, heat leaks were the dominating form of heat transfer, often obscuring the heat transfer between the water and fiber sorbents. Nonetheless, a slightly more pure CO_2 was able to be generated via a thermal wave/inert sweep desorption mode. Finally, the effects of oxygen on the fiber sorbent were studied. PVDC was found to evolve HCl under high temperature (110°C) oxygen exposure, which subsequently attacked the 13X, rendering the fiber sorbents inactive. This last conclusion likely renders PVDC as a "no-go" for barrier layer in actual industrial applications. However, other emulsion-based polymers exist that exhibit much higher oxygen and temperature resistance than PVDC. Polyacrylonitrile (PAN), for instance, is available as an emulsion[20], and has outstanding gas barrier properties[21], as well as high thermal resistance[21] and oxidative resistance[22]—future directions for the barrier layer are discussed in Chapter 8. The lessons learned in Chapter 6 for creating defect free lumen-side barrier layers will aid in initial research that extends those principles to a new emulsion-based polymer.

7.10 References

1. Ruthven, D.M.; Farooq, S.; Knaebel, K.S. *Pressure Swing Adsorption*. John Wiley & Sons, Inc.: Hoboken, NJ, **1994**.
2. Yang, R.T. *Gas Separation by Adsorption Processes*, Butterworth Publishers: Stoneham, MA, **1987**.
3. Koros, W.J.; Paul, D.R.; Design considerations for measurement of gas sorption in polymers by pressure decay, *Journal of Polymer Science, Polymer Physics Ed.* **1976**, 14, 1903.
4. Chandra, Preeti. Multi-component Transport of Gases and Vapors in Poly(Ethylene Terephthalate). Georgia Institute of Technology, GA, *Ph.D. Dissertation* **2006**.
5. Stern, S.A.; Kulkarni, S.S. Solubility of methane in cellulose acetate-conditioning effect of carbon dioxide. *Journal of Membrane Science* **1982**, 10, 235-251.
6. Brandani, F.; Ruthven, D.M.; *Ind. Eng. Chem. Res.*, **2004**, 43, 8339-8344
7. Li, P.; Tezel, F.H.; *Journal of Colloid and Interface Science*, **2007**, 313, 12-17
8. Hyun, S.H.; Danner, R.P.; *J. Chem. Eng. Data,* **1982,** 27, 196-200
9. Chue, K.T.; Kim, J.N.; Yoo, Y.J.; Cho, S.H.; Yang, R.T. Comparison of Activated Carbon and Zeolite 13X for CO_2 recovery from Flue Gas by Pressure Swing Adsorption. *Industrial & Engineering Chemistry Research* **1995**, 34, (2), 591-598.
10. Hines, A.L.; Maddox, R.N. *Mass Transfer: Fundamentals and Application*. Prentice-Hall, New Jersey. **1985**.
11. Ruthven, D.M..; *Encyclopedia of Separation Technology Volume 1,* John Wiley and Sons, Inc., New York, NY, **1997**.
12. Ruthven, D.M. *Principles of Adsorption & Adsorption Processes*, Wiley-Interscience, **1984**.
13. McCabe, S.; Smith, J., *Unit Operations of Chemical Engineering.* McGraw-Hill, New York, NY, **1993**.
14. Lively, R.P.; Chance, R.R., Koros, W.J. Enabling Low-Cost CO_2 Capture via Heat Integration, *Industrial & Engineering Chemistry Research* **2010**, 49(16), 7550-7562.

15. Yang, R.T. *Gas Separation by Adsorption Processes*, Butterworth Publishers: Stoneham, MA, **1987**.
16. Sirwardane, R.V.; Shen, M-S.; Fisher, E.P.; Poston, J.A. Adsorption of CO_2 on Molecular Sieves and Activated Carbon, *Energy & Fuels,* **2001**, 15(2), 279-284.
17. Cost and Performance Baseline for Fossil Energy Plants. Volume 1: Bituminous Coal and Natural Gas to Electricity, NETL Technical Report Number DOE/NETL-2007/1281, August **2007**.
18. Grant, D.H. The pyrolysis of poly (vinylidene chloride) in solution, *Polymer*, **1970**, 11(11), 581-596.
19. Elaiopoulus, K.; Perraki, Th.; Grigoropoulou, E. Monitoring the effects of hydrothermal treatments on the structure of a natural zeolite through a combined XRD, FTIR, XRF, SEM & N_2-porosimetry analysis, *Micro. & Meso. Mats.*, **2010**, 134, 29-43.
20. Harrison, S.A.; Brown, W.E. Mixture of Acrylonitrile polymer and butadiene copolymer, *U.S. Patent*, **1951**, #2,538,779.
21. Sweeting, O.J. *The Science and Technology of Polymer Films*, John Wiley & Sons, Inc.: New York, NY **1971**.
22. Nunes, S.P.; Peinemann, K-V.*Membrane Technology in the Chemical Industry*, **2006**, Wiley-VCH, p. 36.

Chapter 8

Dissertation Conclusions, Summary and Future Directions

This dissertation developed a new form of hybrid sorbent that has the potential as a path forward for post-combustion CO_2 capture. The research conducted and presented in this dissertation on these hollow fiber sorbents has five main conclusions:

1) Hollow fiber sorbents can combine the advantages of traditional and novel solid sorbents while mitigating the extent of typical processing deficiencies such as bed pressure drop, heat management, and particle attrition. From an energetic perspective, hollow fiber sorbents are one of the low-cost paths for CO_2 capture due to the unique ability of the hollow fiber sorbents to behave as an "adsorbing heat exchanger." This allows the sorption enthalpy within the fibers to be transferred to the heat transfer fluid flowing through the bore, thereby generating useful heat.

2) Spinning fibers with high zeolite loadings is a consistent process that does not stray too far from conventional hollow fiber membrane spinning. Complete control over the pore morphology and the effect the zeolites have upon the pore morphology are still challenges to be overcome, yet the current state-of-art creates highly porous and permeable fibers.

3) Creating a *defect-free* lumen barrier layer within a fiber using an emulsion-based polymer is possible. This had never been done before in the literature, and proved to be a difficult process to optimize, but once optimized, yielded an excellent barrier layer. Ultimately, a more fundamental study on the film formation properties of an emulsion cast onto a porous substrate is needed to fully understand the mechanics behind film formation and the subsequent gas and vapor permeation properties.

4) The sorption properties of the fiber sorbents are equivalent to those of the solid sorbent contained within—the support material does not seem to occlude CO_2 access to the solid sorbent appreciably. Cooling water in the bores of the fibers is necessary for maximum performance from the hollow fiber sorbents. The cooling water velocity can be tuned to capture as much of the fiber sorption enthalpy as possible, though arriving at this optimum water velocity is a tedious process. Studying the complete RTSA cycle and recovering a pure CO_2 product is beyond the current capabilities of the system due to large heat leaks. Larger fiber sorbent modules are needed to better understand the physics of the RTSA cycle.

5) Plant-wide heat integration is absolutely crucial for CO_2 capture for *any* CO_2 capture technology. Fiber sorbents enable this goal more than any other form of CO_2 capture due to the sorption system and heat exchange system being integrated within each individual fiber.

8.1 Dissertation Overview

This thesis presented a new post-combustion CO_2 capture platform in the form of hollow fiber sorbents. These sorbents are based on supporting microporous solid sorbents—zeolites are used in this work—within a porous polymer hollow fiber which is then coated on the lumen-side by a barrier polymer. These fibers are ideally assembled into a parallel flow module that has power plant flue gas flowing on the shell-side of the fibers, with cooling water flowing through the bore-side to mitigate the intense sorption enthalpy that is released when the CO_2 sorbs into the solid sorbents. To recover a pure CO_2 product, the feed to the fiber module is closed, while hot water is pushed through the bores of the fibers to create a desorbing "wave" of CO_2 that pushes out the interstitially held flue gas. This heating and cooling cycle is continuously repeated to form a rapid thermal swing adsorption cycle.

8.2 Summary

8.2.1 Objective 1

Chapter 1 presented the objectives which guided the research discussed in this dissertation. The first objective was:

1. *Develop a conceptual framework for the capture of CO_2 via hollow fiber sorbents, and compare it against existing and emerging CO_2 capture technologies.*

Chapter 4 presented a high level, energy based analysis on the fiber sorbent capture system. The analysis broke the energy costs associated with CO_2 capture into three different penalties: *1)* intrinsic energy penalties, *2)* auxiliary energy penalties, and *3)* compression energy penalties. For the fiber sorbent systems, the auxiliary energy penalties (i.e., draft fans, sensible heat of the solids) were found to be dominant, while the compression costs and the intrinsic costs (i.e., the heat of sorption) were found to be equivalent to each other and less serious than the auxiliary penalties. In comparison to other proposed CO_2 capture technologies, fiber sorbents were found to be the most energetically favorable, except for chilled ammonia operated in slurry mode. The slurry mode ammonia plant has considerable uncertainties associated with its real difficulties in handling slurry feeds. Moreover, even these two technologies (fiber sorbents and chilled ammonia) were found to be highly parasitic to the host power plant. To circumvent these seriously limiting energy penalties, a plant-wide heat integration strategy was developed that essentially transferred the heat of sorption released by the CO_2 capture system to the plants feedwater, thereby allowing the capture system to operate as a feedwater preheater. This and other heat integration strategies allowed for a marked reduction in the overall parasitic nature of the CO_2 capture system. These preliminary calculations show that fiber sorbents have the potential to be favored path forward for low-cost CO_2 capture.

8.2.2 Objective 2

Another objective presented in Chapter 1 was concerned with the creation of a hollow fiber sorbent including a lumen side barrier layer:

2. *Develop methods for the creation of high-sorbent-loaded composite hollow fibers and the formation of an impermeable lumen layer.*

Chapter 5 presented an analysis on spinning high-solids-loaded fiber sorbents while creating a highly porous polymer support layer. Zeolite 13X was used as a proof-of-concept solid sorbent while cellulose acetate was chosen as the support polymer. The dry-jet, wet-quench spinning process was adapted for spinning hollow fiber sorbents, and the effect of spin temperature, draw ratio, bore fluid flowrate, and bore fluid composition on pore formation were studied via permeation porosimetry. Permeation porosimetry was found to be limited by the dominating resistance through the fiber wall, causing the technique to probe the smaller pore sizes rather than the large pores that the bulk of the fiber seems to exhibit based on SEM inspection. Mercury porosimetry returned the complete pore size distribution, with the majority of the pores being slightly smaller than the crystal size of the supported zeolites. In general, at this stage of the technology it is difficult to make an *a priori* prediction regarding the effect of spinning conditions on the fiber pore properties due to complications contributed by the high loadings of zeolite. This fact notwithstanding, this preliminary work yielded some general rules of thumb for future hollow fiber sorbent spinners: *1)* higher temperatures result in more stable spin lines, but lower permeances, *2)* solvent-rich bore fluids result in higher permeances, more circular bores, and more stable spin lines, *3)* non-solvent-rich bore fluids result in higher permeances, but non-circular bores and more *unstable* spin lines, *4*) the fiber diameter scales linearly with the draw ratio used, and *5*) approximately 30% zeolite in solution is the maximum zeolite concentration that is spinnable.

Chapter 6 investigated the ability of an aqueous latex dispersion to form a continuous, defect-free film within a hollow fiber sorbent to create the lumen-side barrier layer. The goal of achieving a defect free lumen layer turned out to be among the most challenging in this project. Much of the initial work on coating hollow fiber sorbents resulted in defective barrier layers, and as a result, a simplified study using flat films was conducted to elucidate the mechanisms at play during the film formation process. Polyvinylidene chloride films (latex-based) were cast onto cellulose acetate and 13X composite substrates and the effect of drying rate on the film formation was studied. It was found that rapid drying techniques are unsuitable for creating a barrier film, and instead, slow drying rates must be used to form an adequate (albeit still defective) film. To investigate the effect of the porous substrate on latex film formation mechanics, the PVDC latex was cast onto glass substrates, hydrophilic porous substrates, and hydrophobic porous substrates using slow drying conditions. As expected, the glass substrates yielded a defect-free film when fresh latex was used. On the other hand, the porous substrates yielded defective films even with fresh latex suspension. Capillary forces between the latex and porous substrate were hypothesized to be responsible for the defective films. Essentially, the aqueous latex serum was withdrawn rapidly from the latex, causing the particles to jam and vitrify in place, rather than allowing the particle ordering that typically occurs on normal nonporous substrates. This rapid vitrification results in decreased surface forces between the interstitial water and the air above the film, which thereby results in less particle deformation upon water evaporation. To counter this, a swelling agent was added into the drying gas mixture that served to soften the polymer particles, which allowed the particles to be deformed and rearranged even in the

face of low surface forces. This allowed for the creation of 200-500 nm thick, defect-free barrier layer inside the fiber sorbents, which exhibited immeasurably low gas and water permeances.

8.2.3 Objective 3

Once the fiber sorbents had been created in their entirety, the sorption properties of the materials were tested. Chapter 1 stated that the third objective of this dissertation was,

3. Demonstrate proof-of-concept CO_2 capture experiments simulated flue gas.

Chapter 7 detailed the experimental results on the sorption properties of the fiber sorbents from an equilibrium, kinetic, cyclic, and chromatographic perspective. The supporting cellulose acetate matrix was found to not occlude CO_2 access to the zeolites in any way, nor was the matrix found to degrade over continuous thermal cycling. The fiber sorbents were found to exhibit significant external mass transfer limitations for low flue gas velocities, a situation which was remedied by tighter fiber packing and higher flue gas velocities. In the absence of cooling water, the fibers were found to be highly non-isothermal, and the resulting breakthrough CO_2 capacities were found to decrease as the flue gas flowrate increased. Upon addition of cooling water flowing through the bores of the fibers, the breakthrough CO_2 capacity was found to be maintained at all flue gas flowrates studied. The cooling water velocity was varied within the fiber sorbents, and

the amount of sorption enthalpy transferred to the water was measured. An optimum was found to exist that was the balance of large amounts of heat transferred to small amounts of water, and small amounts of heat transferred to large amounts of water. Desorption of CO_2 from the fibers was accomplished via a hot-bore, inert-sweep combination. The small scales that were used in these studies resulted in severe heat leaks that significantly diffused the thermal step entering the fiber sorbents, resulting in a low purity CO_2 product. A full RTSA cycle was attempted many times, but again the heat leaks associated with the small scales used resulted in a cycle that had many long lag times as a result of the experimental apparatus having to be heated and cooled. Finally, the oxygen-sensitivity of the PVDC barrier layer was found to be quite high, resulting in the layer dehydrohalogenating with the off-gas of this process badly damaging the CO_2 sorption capacity of zeolite 13X. While a fully operating rapid thermal swing adsorption system is far from a reality, the preliminary experiments in Chapter 7 provide insight onto the necessary measures that must be taken to retrieve meaningful data on the process.

8.3 Future Directions

This thesis describes significant progress towards the possibility of using fiber sorbents as a viable CO_2 capture platform. The fibers were estimated to be energetically favorable, and were found to be readily spinnable, and preliminary sorption experiments pointed towards the possibility of using these fibers in rapid thermal swing adsorption mode. However, much of the work presented in this thesis was exploratory in nature,

with the final route to a fully operating fiber sorbent system still yet to be discovered. Some possible avenues to achieving this goal are detailed below.

8.3.1 Extending fiber sorbent process design

While Chapter 4 presented a high-level energetic analysis of the fiber sorbent system, much more extensive work is needed to arrive at a "final" estimate for the cost of CO_2 capture. Most notably, the work here has focused on operating expenses, with little regard paid to the capital expenditures required for building such a system. These capital expenditure estimates are not trivial: costs of composite fiber sorbents in plastic modules are unknown, as well as the costs of the extensive piping and valving required to operate the CO_2 capture system. In regard to the piping and valving systems, a detailed process flow diagram including valve timing and "auxiliary" units that were ignored in the analysis here needs to be developed. This process flow diagram will be difficult to develop, as the plant-wide heat integration requires clever matching between plant feedwater and fiber sorbent bed. This hurdle notwithstanding, once developed, this process flow diagram will serve as a "treasure map" for all future fiber sorbent projects, guiding future research by pointing to areas within the process that can be optimized, either energetically, or from a footprint/capital expenditures perspective.

8.3.2 Tuning the fiber sorbent pore size

Chapter 5 sought to characterize the effects of some spinning parameters on the fiber sorbent pore size, with the ultimate goal being to maximize the transport rate of gas through the fiber wall. While success was achieved in this endeavor, little predictive power was produced from the results due to the myriad of factors at play. Ideally, a hollow fiber sorbent spinner should be able to plan spins and spinning parameters based on some desired fiber pore morphology. Although this work sought to establish pores as large as possible, scenarios could be envisioned that seek to make the pores as small as possible instead. To arrive at a fully tunable fiber sorbent pore size, more work is needed. Much work has been performed in the microfiltration field[1-3] that allows for some predictive properties when using pure polymer spinning solutions, and these results may be able to guide future fiber sorbent spins. The effects of the zeolite—including both zeolite size, loading, and chemical composition—need to be more extensively studied, as the bulk of the pores in the fiber sorbent wall are a result of inter-particle voids. The formation of pores in the polymer sections of the fiber needs to be more fully investigated as well. This can be achieved by spinning at more temperatures and at a variety of zeolite loadings, and by spinning at a wider range of draw ratios at a variety of zeolite loadings. Furthermore, a fully temperature-dependant polymer-solvent-non-solvent ternary phase diagram should be developed, which will aid in the interpretation of the spinning results. Finally, these experiments should be repeated for two other "standard" spinning polymers—Ultem® and Matrimid®—to determine how predictive the results from the cellulose acetate/13X experiments are.

8.3.3 Addition of other solid sorbents to the fiber sorbent

Throughout the course of the thesis, zeolite 13X was used as a proof-of-concept sorbent for CO_2. This was done in order to allow for meaningful comparison between the composite fiber sorbent sorption properties and the well-studied zeolite's properties. However, zeolite 13X is not a "silver bullet" for CO_2 capture due to its extreme water-sensitivity. Chapter 4 presented two other options for solid sorbents: Silicalite-1® and solid-supported amines. Much of the work in Chapter 5 will need to be repeated to spin fiber sorbents with new zeolites (in the case of silicalite). Some preliminary experiments on this task can be found in Appendix E for cellulose acetate and silicalite. However, for novel sorbents, such as solid-supported amines, metal-organic frameworks (MOFs), and functionalized polymers, the spinning process will likely need to be greatly altered, as many of the sorbents are not stable in the presence of liquid water[4] (though they are typically stable in water vapor[5]), indicating that they may not be viable in the current spinning process. Ideally, some form of framework for the process of incorporating a new sorbent into the polymer matrix can be developed, which will guide future researchers seeking to combine the advantages of a novel sorbent and the hollow fiber platform.

8.3.4 Fiber sorbents in VSA mode

Chapter 4 illustrated that the costs associated with heating and cooling the water that has exited the fiber sorbent modules is the most significant cost associated with fiber

sorbents. Before the heat integration strategies were formulated, a new avenue for CO_2 capture utilizing fiber sorbents (but no cooling water) was developed. Instead of actively flowing water through the bores during the sorption/desorption step, a phase change material with a melting point in the range of the flue gas temperature—such as eicosane (T_m=36.1°C)—is envisioned for placement in the bores of the fibers permanently. This material mitigates the sorption enthalpy by transferring it to the fusion enthalpy of the phase change material, while the fiber sorbents are regenerated via a vacuum (vacuum swing adsorption). While pressure swing adsorption was initially ruled out due to the large costs of compression associated with flue gas, vacuum swing adsorption has the advantage that only a tenth of the compression costs are necessary (as the vacuum is only operating on the sorbed CO_2, not all of the flue gas). An initial sketch of this idea, along with some preliminary experiments, can be found in Appendix F. This avenue of research needs to be more extensively studied to determine its viability for CO_2 capture, as well as for other separations where a PSA/VSA is more appropriate.

8.3.5 Moving onto PAN for the fiber sorbent barrier layer

Chapter 7 showed that PVDC as a barrier layer is unlikely to be useful in a real setting by itself due to its low oxygen resistance. However, much of the work performed on PVDC paves the way for extension to other emulsion-based polymers. One emulsion-based polymer in particular, polyacrylonitrile (PAN), has excellent oxygen and temperature resistance, and moderately low water vapor permeances[6,7]. One route, which utilizes water-resistant solid sorbents in the polymer matrix, uses PAN as the sole barrier

layer for the fiber sorbents. This layer of PAN would be created using extensions of the latex post-treatment techniques developed in Chapter 6. Another route, which utilizes water-sensitive solid sorbents in the polymer matrix, uses a PAN barrier layer as the primary barrier layer that is attached to the fiber wall, and a thin PVDC inner lining on the lumen-side of the PAN barrier layer. This composite barrier layer protects the inner layer (PVDC) from oxygen via the thick PAN layer, and protects the fiber wall from large amounts of permeating water via both the PAN and PVDC layer. Both of these avenues need to be explored experimentally to determine their viability as a fiber sorbent barrier layer.

8.3.4 Scaling up RTSA system to study heat effects

One of the main issues that was encountered throughout the work presented in Chapter 7 was the heat leaks that were present throughout the small-scale RTSA system. This prevented a detailed analysis of the heat transfer properties throughout the fiber sorbent, leaving properties such as thermal diffusivity through the fiber wall still unknown. Furthermore, these heat leaks prevented a rapid thermal cycle from occurring due to the sensible heat of the experimental apparatus. To combat these heat leaks, the entire experiment needs to be scaled up. Initially, fiber sorbent modules need to be constructed out of 3/8" nylon PFA Swagelok® fittings. This change alone will approximately double the surface area to volume ratio of the fiber module, which was identified as a primary source of heat leaks within the system (essentially, in the ¼" modules, every fiber is in contact with the module wall, while in the 3/8" module, only

half of the fibers are in contact with the module wall). From here, the modules should be eventually scaled up to 1" nylon PFA modules. However, there is great difficulty associated with making these modules at lab scales, as great amounts of fibers are required to make the modules, and the current potting techniques do not scale well into these large modules. Furthermore, the latex post-treatment step will need to be appropriately tuned for such a large module. This scaling up within the laboratory is necessary in order to prove that fiber sorbents are able to be operated in a rapid thermal swing cycle and are able to generate a pure CO_2 product.

8.4 References

1. Tasselli, F.; Drioli, E. Tuning of hollow fiber membrane properties using different bore fluids, *Journ. Memb. Sci.*, **2007**, 301 (1-2), 11-18.
2. Yang, Q.; Chung, T-S.; Santoso, Y.E. Tailoring pore size & pore size distribution of kidney dialysis hollow fiber membranes via dual-bath coagulation approach, *Journ. Memb. Sci.*, **2007**, 290(1-2), 153-163.
3. Qin, J.J.; Li., Y.; Lee, L.S.; Lee, H. Cellulose acetate hollow fiber ultrafiltration membranes made from CA/PVP 360 K/NMP/water. *Journal of Membrane Science* **2003**, 218, 173-183.
4. Cassiers, K.; Linssen, T.; Mathieu, M.; Bejelloun, M.; Schrijnemakers, K.; Van Der Voort, P.; Cool, P.; Vansant, E.F. A Detailed Study of Thermal, Hydrothermal, & Mechanical Stabilities of a Wide Range of Surfactant Assembled Mesoporous Silicas, *Chemistry of Materials*, **2002**, 14(5), 2317-2324.
5. Li, W.; Choi, S.; Drese, J.H.; Hornbostel, M.; Krishnan, G.; Eisenberger, P.M.; Jones, C.W. Steam-stripping for regeneration of supported amine-based CO_2 adsorbents, *ChemSusChem*, **2010**, 3(8), 899-903.

6. Sweeting, O.J. *The Science and Technology of Polymer Films*, John Wiley & Sons, Inc.: New York, NY **1971**.
7. Stannett, V.T.; Ranade, G.R.; Koros, W.J. Characterization of water vapor transport in glass polyacrylonitrile by combined permeation & sorption techniques, *Journ. Memb. Sci.*, **1982**, 10(2-3), 219-233.

Appendix A

Cross Flow System Design

A.1 Overview

This appendix presents some rough estimates of a cross-flow module for post-combustion CO_2 capture. The analysis uses 13X as the sorbent, and assumes a dehydrated flue gas feed. The numbers presented here were the guiding calculations from the beginning periods of the research. Similar calculations can be used to size a parallel flow module (not shown here).

A.2 System Development

A.2.1 Bed Dimensions

The system must process $1x10^6$ scfm of flue gas at 50°C and 1.5 atm. The other design constraints are that we need to have <1mol% CO_2 in the exiting flue gas. Also, a high purity (>90mol% CO_2) product stream is desired.

$$\dot{V} = \left(\frac{50+273}{273}\right)\left(\frac{1}{1.5}\right)x10^6 = 0.79x10^6 \; actual \; cfm \qquad \textbf{(1)}$$

The manifold is sized in order to allow a large enough cross-section to minimize flue gas pressure drop. Fibers as long as possible are used to aid in this large cross-section. The bed length is set at 4.5 m.

$$L=4.5m \; (13.56ft)$$

$$H=6m \; (18.9ft)$$

$$W=25m \; (82ft)$$

To minimize the flue gas pressure drop, the amount of fibers in the manifold sparse. A void fraction of 60% is used in this case.

$$\varepsilon_{Bed}=0.60$$

From this the fiber volume can be calculated:

$$(1-\varepsilon_{Bed})V_{chamber}=V_{fibers}=(1-0.6)x(450x600x2500 \; cm^3)=2.7x10^8 \; cm^3 \; of \; Fibers \qquad \textbf{(2)}$$

A.2.2 Fiber Dimensions

Next, the fibers are set at realistically spinnable values.

$$OD=1000 \; microns$$

This determines how many fibers are needed:

$$V_{fibers}=N_{fibers}\pi R_o^2 H_{fibers} \quad \textbf{(3)}$$

$$N_{Fibers}=\frac{V_{Fibers}}{\pi R_o^2 H_{Fibers}}=\frac{2.7x10^8\,cm^3}{\pi(500x10^{-4})^2\,cm^2\,600cm}=57.3x10^6\ fibers \quad \textbf{(4)}$$

To maximize the amount of sorbent in the fiber, a thick fiber wall is desired:

$$ID=400\ microns$$

A.2.3 Sorbent Requirements

Now the amount of required sorbent can be calculated. The sorbent is zeolite 13X. Envision a polymer "mesh" supporting the sieves and assume a polymer/sieve ratio of:

$$\frac{V_{Polymer}}{V_{Sieve}}=0.44$$
$$\frac{m_{Polymer}}{m_{Sieve}}=0.25 \quad \textbf{(5)}$$

A relationship relating the sieve volume to the volume of the fiber wall and the fiber porosity can be easily derived:

$$1.44V_{sieve}=(1-\varepsilon_f)\, N_{fibers}\, \pi\, H_{fiber}\, (R_o^2-R_i^2) \quad \textbf{(6)}$$

A fiber wall porosity of *0.25* should be achievable:

$$V_{sieve} = \frac{(1\text{-}0.25)\cdot(57.3x10^6)\cdot\pi\cdot(600cm)\cdot\left[(500x10^{-4}cm)^2\text{-}(200x10^{-4}cm)^2\right]}{1.44} = 11.8x10^7\ cm^3\ of\ 13X \quad \textbf{(7)}$$

Therefore, the polymer volume is:

$$V_{polymer}=5.2x10^7\ cm^3\ of\ polymer$$

The bed capacity, assuming 90% saturation at the end of the cycle is (35°C sorption temperature):

$$Capacity=(C_{35°C}-C_{100°C})\, m_{sorbent} \quad \textbf{(8)}$$

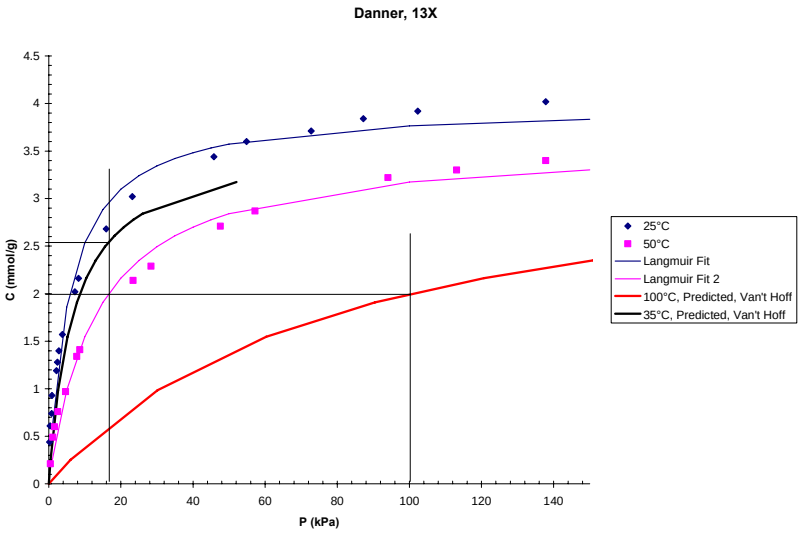

Figure A.1. 13X Isotherms adjusted to 35°C and 100°C[1]

In the worst case (CSTR mixing), the desorption at 100°C will happen at 1 atm of CO_2.

$$C_{35°C,\ 0.15atm}=2.55\ mmol/g$$

$$C_{100°C,1atm}=1.98\ mmol/g$$

From this, the total amount of CO_2 the fiber bed holds can be calculated, viz.,

$$n_{CO2} = (2.55-1.98)\frac{mmol\cdot CO_2}{g13X}\frac{9.45x10^7\,cm^3 13X}{}\frac{1.6g}{cm^3} = 4.08x10^6\,g$$

A.2.4 Flue gas pressure drop

Using the amount of CO_2 entering the system per minute, the cycle time (δt) can be calculated:

$$n_{flue=}1x10^6\,scfm\frac{lbmol}{359scf}\frac{454mol}{lbmol} = 1.27x10^6\,mol/\min$$

$$\dot{m}_{CO2} = 0.15x1.27x10^6\,mol/\min\,44\frac{g}{mol} = 8.35x10^6\,g\,CO_2/\min$$

$$\delta t = \frac{4.08x10^6\,g\,CO_2/cycle}{8.35x10^6\,g\,CO_2/\min}60\frac{\sec}{\min} = 29.28\sec$$

The superficial velocity of the flue gas can now be calculated:

$$v_{Flue} = \frac{V_{Flue}}{\varepsilon_{Manifold}A_{x,flue}} = \frac{0.79x10^6\,acfm}{0.60\cdot(600x2500)/30.48^2/60} = 18.58\,fps \qquad \textbf{(9)}$$

Finally, the pressure drop of the flue gas can be estimated. The Reynolds number first needs to be calculated.

$$\mathrm{Re} = \frac{D_V v_{Flue} \rho_{flue}}{\mu_{flue}} = \frac{(1000x10^{-4}\,cm)\cdot(18.58\,fps\cdot 30.48)(1.022x10^{-3}\,g/cm^3)}{2.0x10^{-4}\,g/cm-s} = 289 \quad \textbf{(10)}$$

This is of the order of magnitude of the transition region for flow through a fiber bed[2], which is a conservative estimate, since the correlation used in this region returns a considerably higher pressure drop than the laminar regime (Perry's 6th Edition (5-52)):

$$\Delta P_{Flue} = \frac{4 f_f N_r \rho_{flue} v_{Maxe}^2}{2 g_c}\left(\frac{\mu_s}{\mu_b}\right)^{0.14} \quad \textbf{(11)}$$

N_r is a measure of how many obstacles a typical "packet" of gas will bump into in its run through the manifold. This can be roughly estimated as:

$$N_r = \frac{(1-\varepsilon_{manifold})\cdot 2R_o \cdot N_{fibers}}{\tau \cdot W_{manifold}} \cdot L_{manifold} = \frac{(1-0.88)(1000x10^{-4}\,cm/100)(41.6x10^6)(12m)}{3\cdot(25m)} = 1{,}375 \quad \textbf{(12)}$$

The friction factor can be read off the diagram in the same section (5-52) of Perry's 6th Edition:

$$f_f = 0.05$$

Finally, the pressure drop in the bed can be estimated:

$$\Delta P_{Flue} = \frac{4(0.05)(1{,}375)(1.022 kg/m^3)(18.58\, fps \cdot 0.3048 m/ft)^2}{2} = 0.59 atm$$

This ΔP exceeds the upper limit of 0.1 atm, but to achieve adequate packing density, it appears that this higher ΔP may be necessary. By using a higher capacity sorbent, the number of fibers within the fiber bed can be reduced. *In that case, it is easy to envision adding "guard layers" to the front of the manifold that essentially sorb water*, NOX, or other compounds. This is entirely possible since there exists plenty of leeway in the cycle time.

A.2.5 Energy Balances

Now we can perform the energy balance for the desorption step to determine how much steam we'll need. First we'll find how much heat is required for desorption.

The energy balance around the fiber module can be performed. For the desorption step, the fibers must be both heated and the sorption enthalpy must be paid for.

$$Q_{REQ'D} = n_{CO2}\Delta H_S + m_{13X}C_{P,13X}\Delta T_{13X} + m_{poly}C_{P,poly}\Delta T_{poly} \quad \textbf{(13)}$$

$$n_{CO2} = \frac{92{,}620 mol \cdot CO_2}{cycle}$$

$$\Delta T_{poly} = 65K$$

$$\Delta T_{13X} = 65K$$

$$\Delta H_S = 36{,}000 J/mol$$

$$C_{P,13X} = 800 J/kg - K$$

$$C_{P,poly} = 1{,}600 J/kg - K$$

$$m_{13x} = 11.8x10^7 cm^3 13X \cdot \frac{1.6g}{cm^3} = 189{,}000kg\ 13\text{X}$$

$$m_{poly} = 5.2x10^7 cm^3 \frac{1.2g}{cm^3} = 62{,}400kg \text{ polymer}$$

$$\Rightarrow Q_{REQ'D} = 12.1x10^9 J/cycle$$

For the system to be in equilibrium, the amount of heat removed by the steam will have to equal the amount of heat required for desorption. We assume the steam will condense and cool 60°K.

$$Q_{Steam} = \dot{m}_{steam}\Delta H_{Vap}\delta t + \dot{m}_{steam}C_{P,Steam}\Delta T_{Steam}\delta t = Q_{REQ'D} \quad \textbf{(14)}$$

$$\Delta H_{Vap} = 2{,}250{,}000 J/kg$$

$$\delta t = 29.28 \sec$$

$$C_{P,Water,40-100°C} = 3000 J/kg - K$$

$$\Delta T_{Steam} = 60K$$

$$\Rightarrow \dot{m}_{steam} = \underline{\underline{10{,}502 kg/\min}}$$

Another scenario is the use of hot water to desorb the CO_2:

$$Q_{Sdesorb} = \dot{m}_{water} C_{P,water} \Delta T_{water} \delta t = Q_{REQ'D} \quad \textbf{(15)}$$

$$\delta t = 29.28 \sec$$

$$C_{P,Water,40-100°C} = 3000 J / kg - K$$

$$\Delta T_{water} = 60 K$$

$$\Rightarrow \dot{m}_{steam} = \underline{\underline{138{,}000 kg / \min}} = 36{,}500 gpm$$

Next, the amount of cooling water in the bore can be estimated. Assume a 25°C feed, 35°C exhaust cooling water during the sorption step to keep the fibers at a constant temperature.

$$Q_{Sorption} = \dot{m}_{flue} C_{P,Flue} \Delta T_{Flue} + \dot{n}_{CO2} \Delta H_s + \frac{m_{13X} C_{P,13X} \Delta T_{13X}}{\delta t} + \frac{m_{poly} C_{P,poly} \Delta T_{poly}}{\delta t} \quad \textbf{(16)}$$

$\Delta T_{poly} = 10K$

$\Delta T_{13X} = 10K$

$\Delta H_S = 36{,}000 J/mol$

$C_{P,13X} = 800 J/kg - K$

$C_{P,poly} = 1{,}600 J/kg - K$

$m_{13x} = 11.8x10^7 cm^3 13X \cdot \frac{1.6g}{cm^3} = 189{,}000kg$ 13X

$m_{poly} = 5.2x10^7 cm^3 \frac{1.2g}{cm^3} = 62{,}400kg$ polymer

$\dot{m}_{flue} = 1x10^6 scfm \frac{lbmol}{359scf} \frac{454mol}{lbmol} \frac{(0.15(44) + 0.85(30))g}{mol} \frac{1kg}{1000g} = 4.06x10^4 kg/\min$ of flue

$C_{P,Flue} = 1042 J/kg - K$

$\Delta T_{Flue} = 10K$

$\dot{n}_{CO2} = 1.90x10^5 mol - CO_2/\min$

$\Delta H_s = 36{,}000 J/mol$

$\Rightarrow Q_{Sorption} = 12.4x10^9 J/\min$

Since the heat added via sorption needs to be removed by the water in the bore, we can set those heats equal and determine the amount of water necessary:

$$Q_{Water} = Q_{Sorption} = \dot{m}_{Water} C_{P,Water} \Delta T_{Water} \quad \textbf{(17)}$$

$C_{P,Water} = 4{,}184 J/kg - K$

$\Delta T_{Water} = 10K$

$\Rightarrow \dot{m}_{Water} = 1.78x10^5 kg/\min = \underline{\underline{47{,}100gpm}}$

A.2.6 Water Pressure Drop

Finally, since water has the highest flowrate in the bore, we'll use that to see if the pressure drops in the bore are reasonable:

We need the velocity of the water first.

$$v_{Water} = \frac{\frac{\dot{m}_{water}}{\rho_{water}}}{A_{x,Total}} = \frac{\frac{1.78x10^5\, kg/\min}{1000 kg/m^3}}{(57.3x10^6)(\pi \cdot (200x10^{-4}\, cm/100)^2)} = 41.29 cm/s$$

$$\mathrm{Re} = \frac{v_{Water}\rho_{water}D_i}{\mu_{Water}} = \frac{(41.29 cm/s)\cdot(1 g/cm^3)\cdot(400x10^{-4}\, cm)}{(0.01 g/cm-s)} = 165$$

Now we employ Hagen - Poiseuille to determine our pressure drop in the bore. The flow is steady - state, laminar, and incompressible.

$$v_{Water} = \frac{R_i^2 \Delta P}{4\mu L_{Fiber}} \qquad \textbf{(18)}$$

$$\Delta P_{Water} = \frac{v_{Water}\cdot 4\mu L_{Fiber}}{R_i^2} = \frac{41.29 cm/s \cdot 4 \cdot (0.01 g/cm-s)(600 cm)}{(200x10^{-4}\, cm)^2 \cdot 10} = 17.25 psia$$

A.2.7 Heat & Mass Transfer in the Fiber Sorbents:

Since the assumption that mass transfer was in local equilibrium at time scales much shorter than the time scales of the overall system, it would be wise to check whether this is true or not. First, external mass transfer resistances need to be accounted for. The first step is to find a mass transfer coefficient:

Re=289, which is in the laminar regime for these correlations.[2]

Laminar flow :

$$\frac{k_c d}{D_{AB}} = \left[0.04\,\mathrm{Re}^{1/2} + 0.06\,\mathrm{Re}^{2/3}\right]\left[\frac{\mu}{\rho D_{AB}}\right]^{0.4} \qquad \textbf{(19)}$$

Re = 289

$$D_e = \frac{D_{AB}\varepsilon_{fiber}}{\tau} \qquad \textbf{(20)}$$

$D_{CO2-N2} = 0.2 cm^2/s$

$\tau \sim 2$

$\varepsilon_{fiber} = 0.25$

$D_e = 0.025 cm^2/s$ (This is the effective diffusion coefficient in the fiber wall)

$$k_c = \frac{0.025 cm^2/s}{1200 x10^{-4} cm}\left[0.04(289)^{0.5} + 0.06(289)^{2/3}\right]\left(\frac{2x10^{-4}}{1.3x10^{-3}\cdot 0.025}\right)^{0.4} \approx 1.4 cm/s$$

From here the ratio of external to internal mass transfer limitations, α, can be estimated. A low α indicates external mass transfer limitations[3]:

$$\alpha = \frac{k_c l}{K D_e} \qquad \textbf{(21)}$$

$$K = \frac{0.29 gCO_2}{cm^3 13X - atm}\frac{mol}{44g}\frac{1atm}{1.01bar}\frac{83.14}{}\frac{323K}{} = 160$$

$$\alpha = \frac{1.4 cm/s (440x10^{-4} cm)}{160(0.025 cm^2/s)} = 0.02$$

This indicates external mass transfer limitations exist even in the cross-flow pattern. Of course, these can be combated by higher superficial velocities, or higher fiber packing densities.

An additional assumption is that local thermal equilibrium exists within the fiber wall. Let's check the validity of that assumption. It can be shown that the cooling step (during sorption) will take the longest to equilibrate.

In this evaluation we assume that the water is being fed into the bore at a constant 35°C, and the flue gas is constantly contacting the outer surface of the fiber at 50°C. We also assume that the thermal conductivity of the fiber is approximately constant, and we can use the Heisler Charts (Welty-Wicks)[4] to determine the time for equilibrium. Finally, we also assume that the conduction through the polymer composite wall is the limiting thermal resistance ($\alpha_{13X} >> \alpha_{polymer}$).

As a limiting case, we can assume that the flow in the bore is laminar and fully developed, thus :

$$Nu = 3.44 = \frac{h(R_i)}{k_{water}}, \text{ Welty - Wicks} \qquad \textbf{(22)}$$

$$k_{water} = 0.64 \frac{W}{m \cdot K}, \text{ Welty - Wicks}$$

$$\Rightarrow h = \frac{3.44 \cdot (0.64 W / m \cdot K)}{(440 x 10^{-4} cm / 100)} = 5{,}000 \frac{W}{m^2 K}$$

The effective thermal conductivity of the fiber wall is a weighted average of the thermal conductivities of the polymer and estimated to be roughly *2.45 W/(m K)*. Combined with the above value of *h* and the wall *440* micrometer wall, this gives a value *m* very close to unity[4]. This suggests that the resistance to transfer via conduction and convection are similar, and both are rather small.

We want the entire fiber wall rapidly adjust to a uniform temperature set by the bore fluid temperature, and using the worst case (polymer thermal diffusivity ~ *7.93x 10^{-5} m^2/s*)[5], one can estimate the required time for a *440* micron slab by using:

$$\frac{\alpha_{polymer} \cdot t_{equilibrium}}{l^2} = 6$$

$$\alpha_{polymer} = 7.93x10^{-5} m^2 / s \text{ (Polymer Handbook)} \quad \textbf{(23)}$$

$$t_{equilibrium} = \frac{6(440x10^{-4} cm/100)^2}{7.93x10^{-5} m^2 / s} = 0.015 \sec$$

As expected, the above estimate certainly suggests that rapid thermal equilibration will be achieved with the bore fluid due to the very small value of the wall thickness and the relatively high thermal diffusivity.

Another assumption worth checking is whether the time it takes for the CO_2 to locally sorb into the sieve embedded in the wall is significant. If we envision the 13X particles to be 3 micron spheres, we can calculate how long it will take for the sieves to reach 99% capacity. A good estimate of $D_{CO2\text{-}13X}$ is *~1.8x10^{-5} cm^2/s* (Pressure Swing Adsorption, Ruthven, D.M[6].). From Hines and Maddox again, Figure 4-17[3]:

$$0.75 = \sqrt{\frac{D_{AB} t}{R^2}}$$

$$t = \frac{0.75^2 (1.5x10^{-4} cm)^2}{1.8x10^{-5} cm^2 / s} = 6.1x10^{-4} \sec$$

A.3 References

1. Hyun, S.H.; Danner, R.P.; *J. Chem. Eng. Data,* **1982,** 27, 196-200.
2. *Perry's Chemical Engineers' Handbook*. 6th ed.; McGraw-Hill, Inc.: **1984.**
3. Hines, A.L.; Maddox, R.N. *Mass Transfer: Fundamentals and Application*. Prentice-Hall, New Jersey. **1985**.
4. James R. Welty, C. E. Wicks, Robert E. Wilson, Gregory L. Rorrer, *Fundamentals of Momentum, Heat, and Mass Transfer*. 4th ed.; John Wiley & Sons: New York City, **2001**.
5. Brandrup, J.; Immergut, Edmund H.; Grulke, Eric A.; Abe, Akihiro; Bloch, Daniel R. *Polymer Handbook*, 4th ed., John Wiley & Sons, Hoboken, NJ., **1999.**
6. Ruthven, D.M.; Farooq, S.; Knaebel, K.S. *Pressure Swing Adsorption*, Wiley-VCH, **1993.**

Appendix B

Alternative Lumen Layer Creation Methods

B.1 Overview

Throughout the course of the research presented in this thesis, many different methods were employed to create the lumen layer within the fibers. While PVDC ultimately proved to be the most successful water barrier, two other approaches, rapid interfacial polymerization and Neoprene®-based laticies, were considered with mixed success.

B.2 Rapid Interfacial Polymerization

B.2.1 Background

One of the few literature mentions of creating a lumen layer within a microporous fiber utilized a rapid interfacial polymerization method[1]. This method essentially involves an interfacial condensation of a polymer at room temperature. Typically, an aqueous solution of diamine is brought into contact with an organic, water-immiscible

solution of a diacid halide[2]: the diamaine and diacid halide will react at the interface and polymerize continuously to form a polyamide. An example of this reaction can be seen in Scheme 1.

Scheme 1:

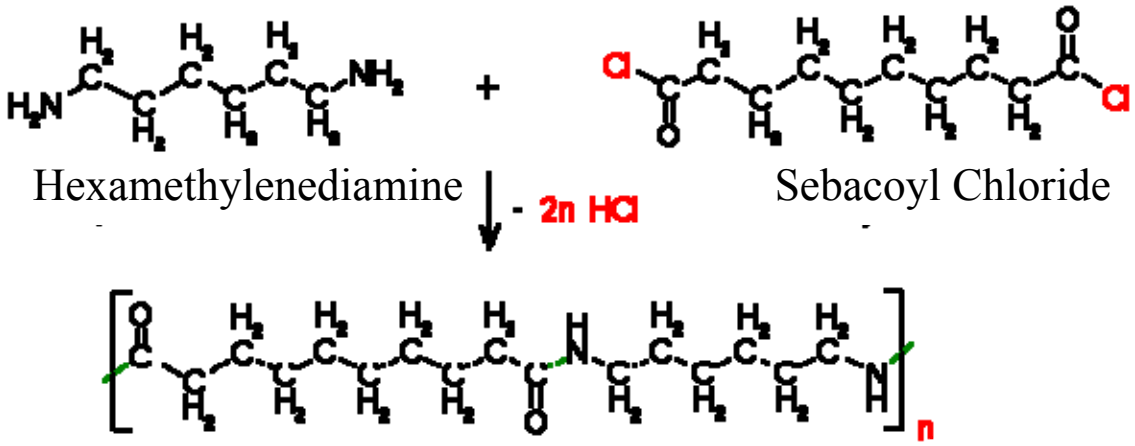

Ideally, the reaction between the two monomers occurs quite rapidly (i.e., the first diamines in contact with the acyl chlorides are quickly acylated, while the subsequent diamines find acyl chloride terminated oligomers, and the reaction proceeds[2]), thereby forming a nascent film. The prevailing hypothesis is that the diamine diffuses through the nascent layer to continue to find fresh acyl chloride for as long as the reaction is allowed to proceed. The product HCl diffuses out of the nascent layer and dissolves into the aqueous solution.

This work chose hexamethylene diamine and sebacoyl chloride as the monomers to form the polyamide nylon 6,10, which is known as a much better barrier than the typical nylon 6,6.[3]

B.2.2 Materials and Methods

Hexamethylene diamine (Sigma-Aldrich, 98% purity, reagent grade) and sebacoyl chloride (Sigma-Aldrich, 99% purity) were used as the monomers. Hexamethylene diamine (HMD) was mixed with DI H_2O to form a 0.5M aqueous solution, while sebacoyl chloride (SC) was mixed with hexane to form a 0.2M organic solution.

Fibers were potted according to the normal procedure (Chapter 3), and the 0.5M HMD solution was flowed through the bores of the fibers at 300 mL/hr using a 1L Isco® syringe pump for 2 minute. Next, hexane was flowed through the bores of the fibers for 1 minute at 300 mL/hr using a 100 mL Isco® syringe pump. Finally, the 0.2M SC solution was pumped through the bores of the fibers at 100 mL/hr for 1 hour using a 100 mL Isco® syringe pump. The bore of the fiber was then cleared with argon at 20psig for 1 hour. In other experiments, the SC solution was placed into the bore first, followed by a water purge, then an HMD solution wash. A conceptual overview of the experiment can be seen in Figure B.1.

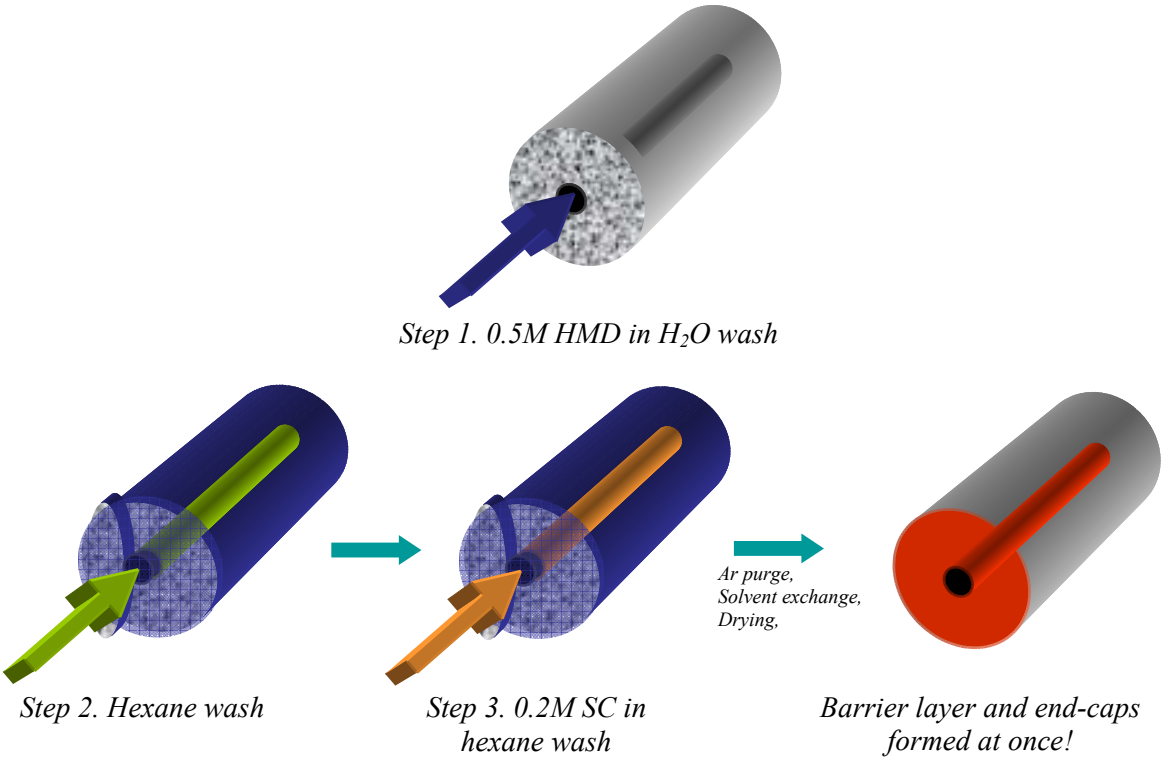

Figure B.1: Overview of rapid interfacial polymerization of nylon 6,10 within fiber sorbents.

To remove excess HCl from the fibers and to carefully remove water from the pores, a solvent exchange procedure similar to the one used after fiber spinning was adopted (Chapter 3). The fibers were soaked in a water bath for 1 day, followed by a methanol bath for 1 day, then allowed to air dry.

Permeation and SEM experiments were performed as described in Chapter 3.

B.2.3 Results and Discussion

The post-treatment experiments were simple to do, and consistently resulted in a thin inner lumen layer. However, as can be seen in Figure B.2, the layer formed was quite thin, even ethereal, and exhibited poor adhesion to the cellulose acetate layer (Fig B.2, *top left* and *top right*). Upon closer examination, the adhered portions of the layer exhibited good coverage over the rough cellulose acetate/13X support (Fig B.2, *bottom left*). A dense skin appears to form in the polyamide layer (Fig B.2., *bottom right*) with a porous polyamide structure underneath.

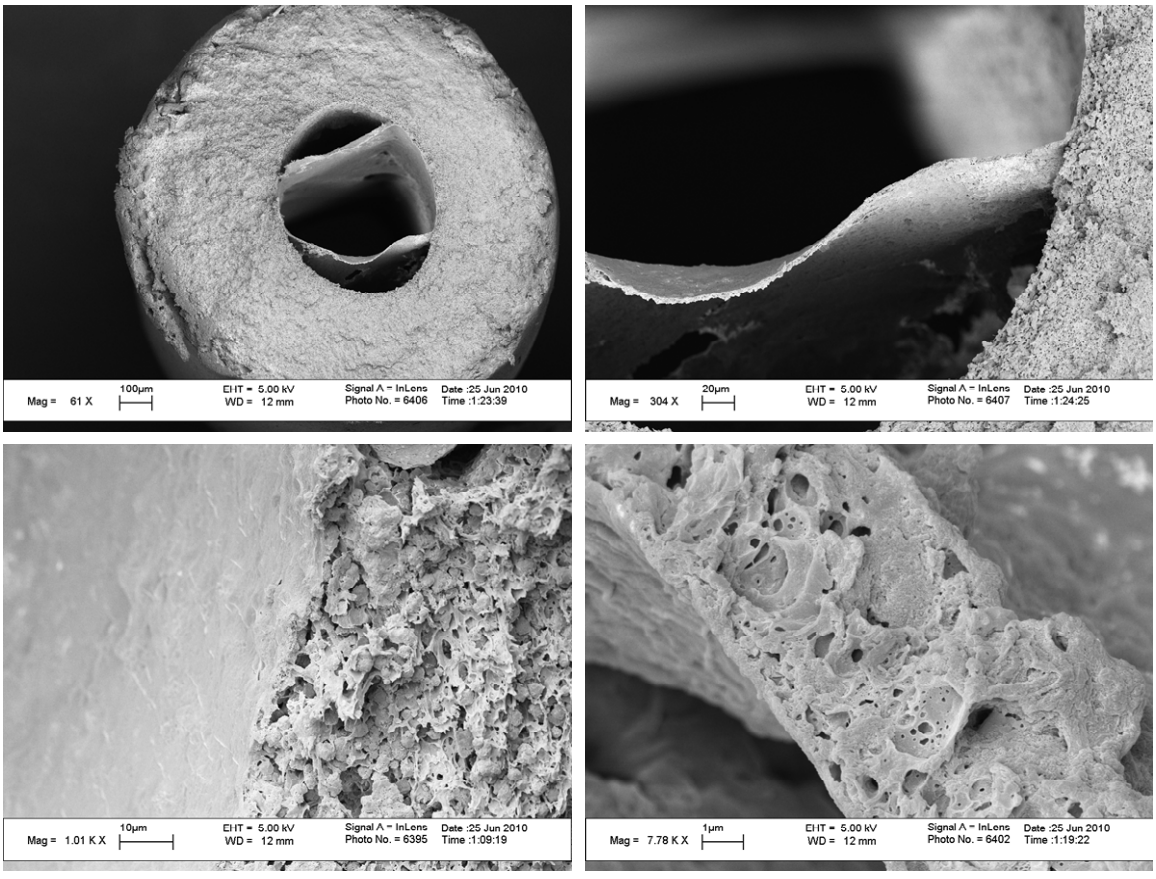

Figure B.2: *(top left)* SEM image of nylon-6,10 coated fiber sorbent, *(top right*) image showing polyamide delamination from fiber sorbent, *(bottom left)* image showing good polyamide coating in adhered area, *(bottom right)* image showing cross section of delaminated film.

The layers created via the interfacial polymerization method were quite weak: the layers visibly moved when a slight gust passed the fibers. Due to this, the permeation measurements conducted on these fibers typically yielded the CA/13X permeance (10^4 GPU). However, one module was made in the same fashion as described above that exhibited remarkably low nitrogen permeances (0.4 GPU), and an SEM of the fiber can be seen in Figure B.3 (the layer likely slightly delaminated due to SEM sample preparation). Unfortunately, selectivities could not be obtained on this fiber: when the feed gas was switched to oxygen (after the module was depressurized), the resulting oxygen permeance was found to be 110 GPU. When nitrogen was repeated again, the nitrogen permeance was also found to be 110 GPU, likely indicating that the ethereal polyamide layer ruptured during permeation. This "partial success" was encouraging, and many additional experimental attempts were made to re-create the adhered polyamide layer, but ultimately the result could not be reproduced.

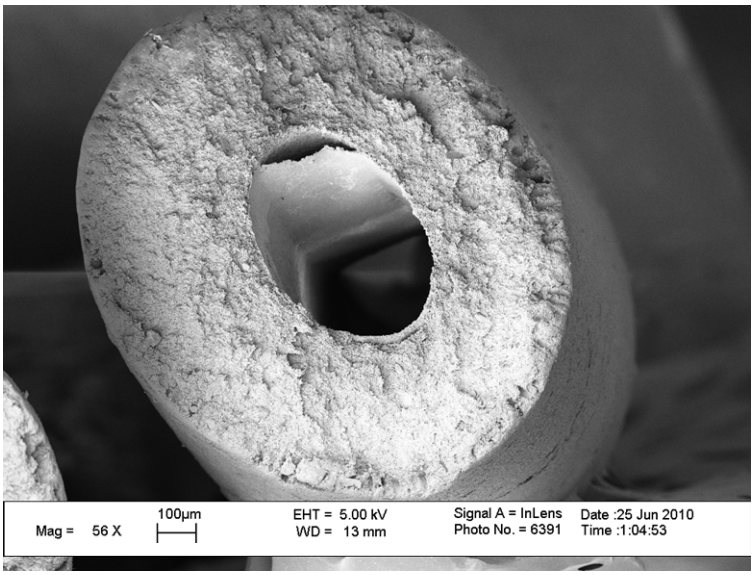

Figure B.3: SEM image of nylon-6,10-coated fiber sorbent showing good adhesion throughout the majority of the fiber.

B.3 Neoprene® Lumen Layers

In parallel with PVDC coatings, Neoprene® coatings on fiber sorbents were also investigated. It was with Neoprene® that lumen layer bypass was first identified (Chapter 6). Neoprene® coated fibers (of the same length) all exhibited the same nitrogen permeance (~3.0 GPU, indicating a defective layer). A simple experiment was devised to prove that lumen layer bypass was responsible for the defective measurements. Two fiber modules were made, one that was 52 cm long, and another that was 5.5 cm long. Both were coated with Neoprene® in the same fashion as described in Chapter 3 for the PVDC coatings. Table B.1 reveals the difference in nitrogen permeance between the two modules. If a module is defect-free, the *permeance* through the fiber will be the same regardless of the length, as the flux through the wall is normalized by the surface area for permeation. However, the *absolute flux* through the fiber will scale with the total surface area if the fibers are defect free (the fibers had the same OD and ID, only the length changed). If the fibers are defective, the absolute flux through the module no longer scales with the surface area of the lumen layer, but instead with the size of the defect. In this simple experiment, neither fiber had end-caps present, which in theory allows for lumen layer bypass to occur. Despite the order of magnitude difference in length, both the "short" and "long" module exhibit the *same defective area* at the ends of the fibers, so an *equivalent* absolute flux is expected in both the "short" and "long" modules. As can be seen, the nitrogen absolute flux through the two modules varies by a factor of 2, while the oxygen absolute flux through the two modules is quite similar. This

simple experiment indicated that lumen layer bypass was most likely the culprit for the defects.

Table B.1: Permeation results for "short" and "long" Neoprene® coated fiber modules.

Module	Module Length (cm)	Apparent Nitrogen Permeance (GPU)	Nitrogen Flowrate (mL/hr)	Apparent Oxygen Permeance (GPU)	Oxygen Flowrate (mL/hr)
"Long" Module	52.0	0.12 +/- 0.03	3.8 +/- 0.9	0.16 +/- 0.06	8.00 +/- 1.07
"Short" Module	5.5	2.26 +/- 0.08	7.45 +/- 1.45	3.23 +/- 0.61	9.65 +/- 0.85

To further confirm the presence of lumen layer bypass, a Neoprene®-coated fiber module was made (N_2 permeance: 3.23 GPU) that then had one fiber end epoxied close, while the other half of the fiber was coated in epoxy (Fig B.4), effectively increasing the defect path length by a factor of 10 (one defect path is closed via the end-cap epoxy, and the other end-defect has had its length extended by a factor of 5 due to the shell-side epoxy). The nitrogen permeation experiments were reduced to 0.15 GPU after the epoxy was placed within the module, indicating that lumen layer bypass likely was the dominating defect.

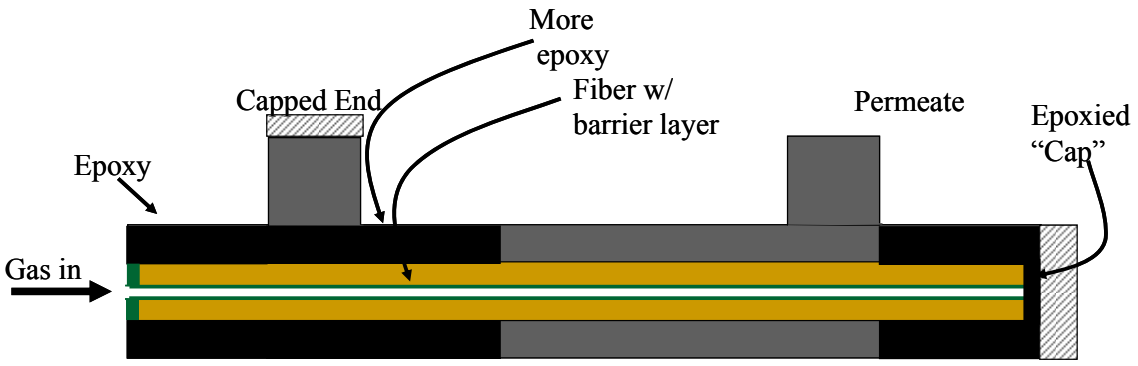

Figure B.4: Schematic of module that was coated with epoxy at end of fiber as well as on the outside of fiber to test for lumen layer bypass.

Of course, epoxying the module shut does not allow for the module to be used in an RTSA setting. Once lumen layer bypass was identified as a real concern, many different methods were attempted to try and cap the defective fiber ends: spray capping, latex dip capping, shell-side vacuum with the face under latex, epoxy capping with flowing bore-side gas, and water hammer. The last method, water hammer, was found to be a reliable and repeatable method for removing lumen layer bypass. In this method, the bore of the fiber module is rapidly (every 30 seconds) switched between 60psig, 25°C water and 15psig saturated steam (Fig B.5.) 200 times, then repeated on the other side of the module. The current hypothesis is that the combination of heat and pressure compacted the cellulose acetate/13X matrix at the faces of the fibers, thereby making a dense CA/13X end cap. Oxygen and nitrogen permeation before and after water hammer can be seen in Table B.2. As can be seen in Table B.2., the total nitrogen flux went down after water hammer, as did the oxygen and nitrogen permeance. Most encouragingly, the lumen layer exhibited an O_2/N_2 selecitivity of approximately 2, indicating that the lumen layer exhibited a few minor pinhole defects, but no major defects.

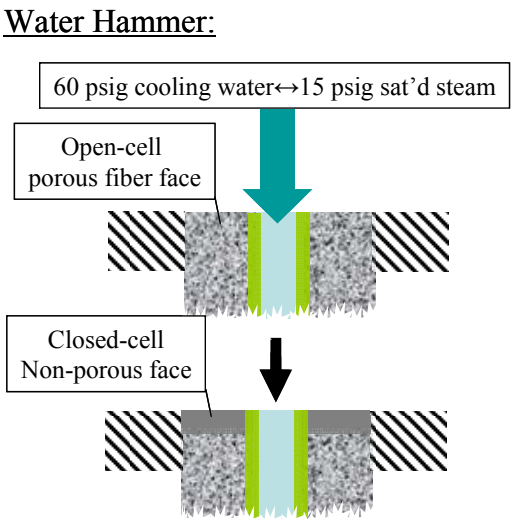

Figure B.5: Schematic showing the current hypothesis behind water hammer removing lumen layer bypass.

Table B.2: Permeation properties of Neoprene®-coated fiber before and after water hammer

Module	Module Length (cm)	Apparent Nitrogen Permeance (GPU)	Nitrogen Flowrate (mL/hr)	Apparent Oxygen Permeance (GPU)
No thermal cycles	5.5	2.40 +/- 0.04	7.84 +/- 0.13	2.46 +/- 0.20
200 thermal cycles	5.5	0.50	1.63	0.94

Finally, these Neoprene®-coated fiber sorbents were sent to ExxonMobil to be tested in a multicomponent adsorption system there. Unfortunately, upon the addition of high-temperature water (100°C), the lumen layer became completely defective. It was later discovered that the Neoprene® latex did not have any crosslinking agents contained within the serum; uncrosslinked Neoprene® apparently degrades near 110°C[4] (Neoprene® films cast from the latex were put into an oven at 110°C overnight, and were

found to be brittle and black afterwards). As mentioned in Chapter 3, Tiarco Chemicals supplied a Neoprene® compounding mixture that required mixing with the Neoprene® latex. Films were cast from this mixture, and after drying at ambient conditions, were crosslinked at 141°C for 1 hour[4]. After the same overnight 110°C treatment, the films were found to be light brown, rubbery, and retained the same permeation properties that were exhibited before the thermal treatment. Water permeation experiments on these films yielded a water permeability of 914 barrers, which was remarkably close to the literature values for water permeation in Neoprene®[3,5].

The latex/compounding mixture was then coated onto the fiber sorbents in the same manner described in Chapter 3. However, the mixture was significantly more viscous than the as-received latex, causing multi-fiber modules to exhibit plugged fibers (1-2 fibers out of 6 were typically plugged). The coated fibers were successfully crosslinked, and were then sent through the water hammer protocol. Due to the high water permeabilities intrinsic to Neoprene®, the Neoprene® layers were set aside in favor of PVDC to be used in conjunction with the water-sensitive zeolite 13X.

Finally, it was found that if the module ends had a Swagelok® nut attached, the act of attaching the post-treated fiber module to a system (i.e., using a wrench to tighten the module end nut onto a fitting connected to a permeation system) damages the end cap of the fiber sorbent (Fig B.6.). As a result, all of the experiments performed involving fiber sorbent modules were carried out using Ultra-torr® fittings to connect the modules to the various experimental apparatuses.

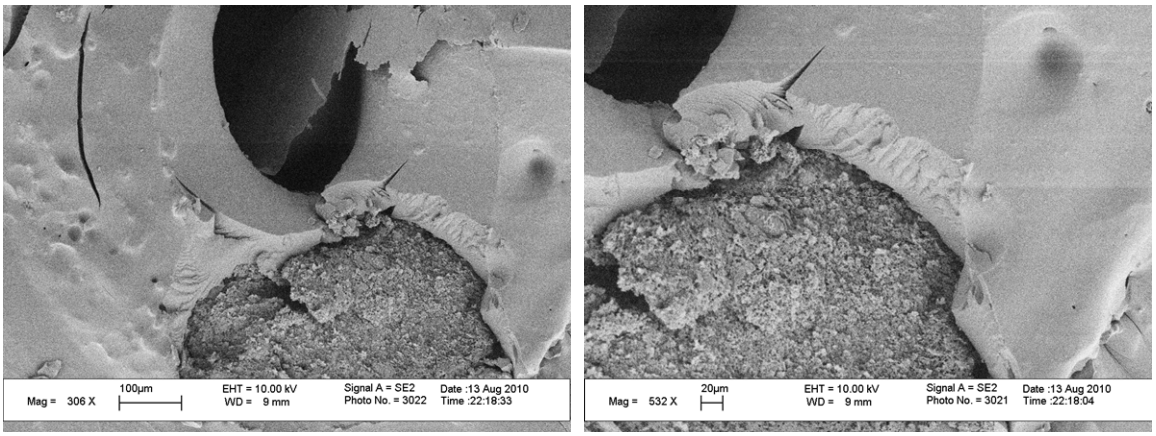

Figure B.6: SEM images showing damage to a fiber sorbent end-cap as a result of Swagelok® fittings.

B.4 References

1. Korkikov, A.P.; Kosaraju, P.B.; Sirkar, K.K. Interfacially polymerized hydrophilic microporous thin film composite membranes on porous polypropylene hollow fibers and flat films, *Journ. Memb. Sci.*, **2006**, 279, 588- 560.
2. Morgan, P. W.; Kwolek, S.L. Interfacial Polycondensation. II. Fundamentals of Polymer Formation at Liquid Interfaces, *Journal of Polymer Science*, **1959**, Vol. XL, 299-327.
3. Sweeting, O.J. *The Science and Technology of Polymer Films*, John Wiley & Sons, Inc.: New York, NY **1971**.
4. Kovacic, P. Bisalkylation Theory of Neoprene Vulcanization, *Ind. & Eng. Chem.*, **1955**, 47(5), 1090-1094.
5. Brandrup, J.; Immergut, Edmund H.; Grulke, Eric A.; Abe, Akihiro; Bloch, Daniel R. *Polymer Handbook*, 4th ed., John Wiley & Sons, Hoboken, NJ., **1999.**

Appendix C

Dual Layer Spinning

C.1 Overview

Aside from post-treating the fiber sorbent to form the internal barrier layer, the only other method for creating the dense lumen layer is by co-spinning a barrier polymer simultaneously with the zeolite-laden core dope. To facilitate this, a novel dual layer spinneret was designed and constructed. Once the spinneret was constructed, polyacrylonitrile was spun as the barrier polymer and cellulose acetate/13X was used as the fiber sorbent solution.

C.2 Spinneret Design

Due to the unique requirements for an interior barrier layer, a dual layer spinneret was designed and constructed such that the thin sheath layer (traditionally the outer opening of the annulus) of the annulus was the innermost opening. The spinneret was made with the intent of accepting three operating fluids, a bore fluid (ρ=1.0 g/cc, μ=1 cP, nominal flow rate=60 mL/hr), a polymer core dope (ρ=1.2 g/cc, nominal μ=150,000 cP,

nominal flow rate=180 mL/hr) and a polymer sheath dope (ρ=1.2 g/cc, nominal μ=75,000 cP, nominal flow rate=10 mL/hr). The spinneret was designed on the basis that pressure drop of the fluids should be low (less than 500 psia), pressure rated to 3300 psia, and the ease of needle alignment and disassembly. The basis of construction was two monolithic spinnerets in series (Figure C.1). The conical wells offer points of mixing so that a well mixed solution enters the annulus. The annulus was designed to be long enough for the fluids to reach a fully developed profile before extrusion. The annulus dimensions are shown in Figure C.2. COMSOL© computational fluid dynamics software was used to determine flow profiles in the spinneret (Figure C.3). The spinneret was constructed by the Georgia Tech Research Institute Machine Services, and the schematic is given in Figure C.4-C.7. As a note, to determine the dimensions of the "extended" and "recessed" composite spinnerets (two other spinnerets used in the Koros Research Group), simply switch the annular opening dimensions of the core and sheath compartment.

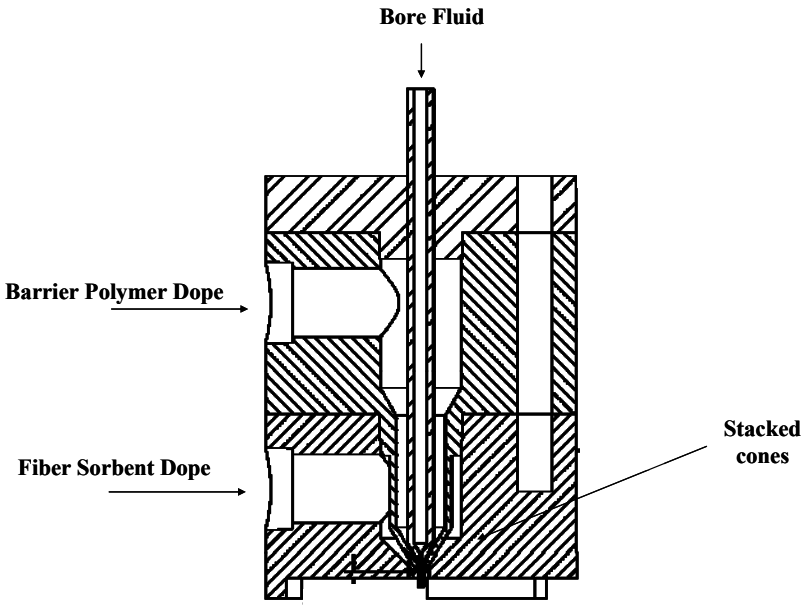

Figure C.1: Composite "inverted" spinneret

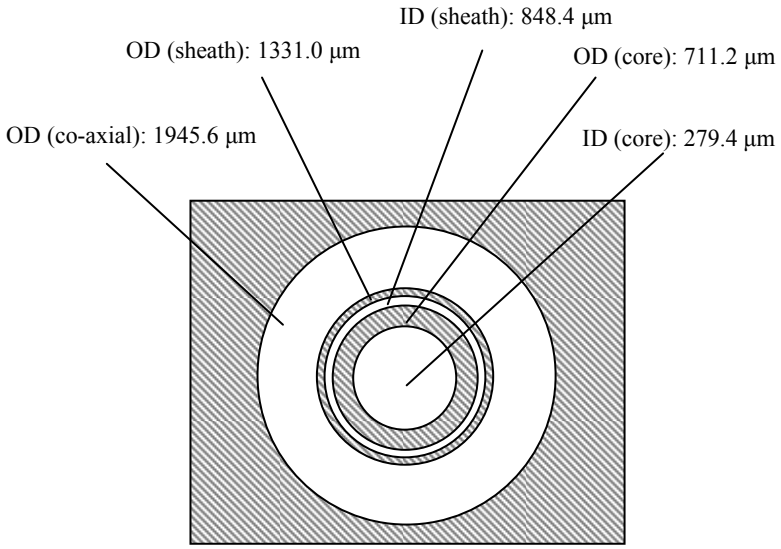

Figure C.2: Simplified schematic of spinneret showing annulus dimensions

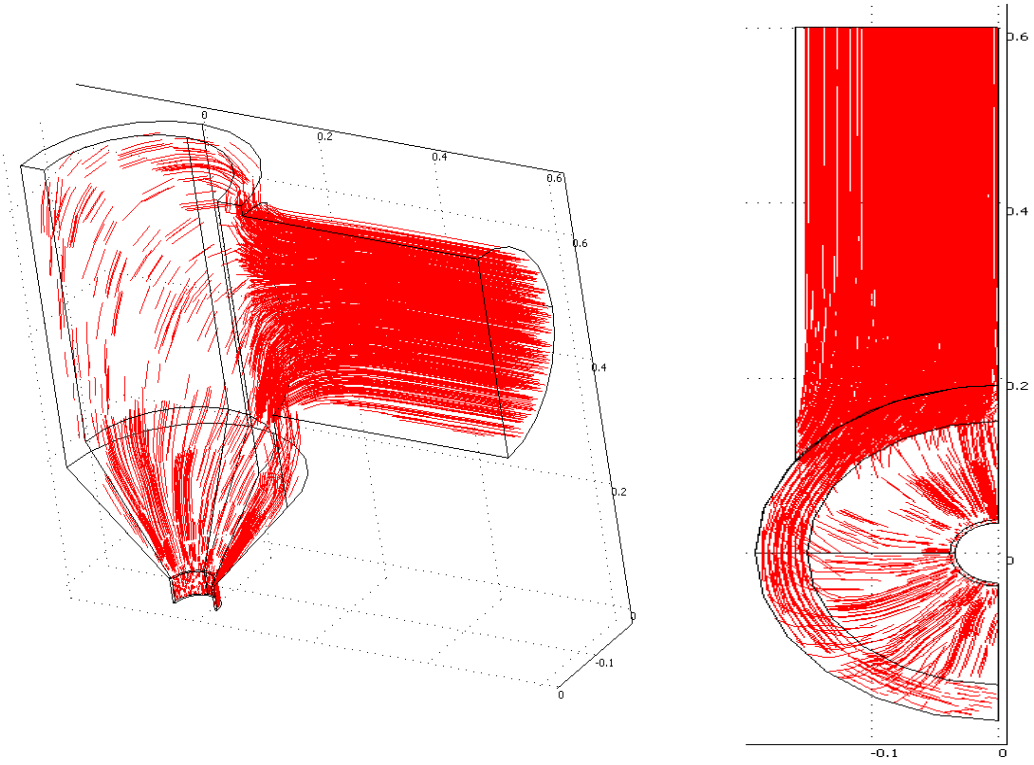

Figure C.3: Flow distribution profiles in barrier layer compartment from COMSOL®.

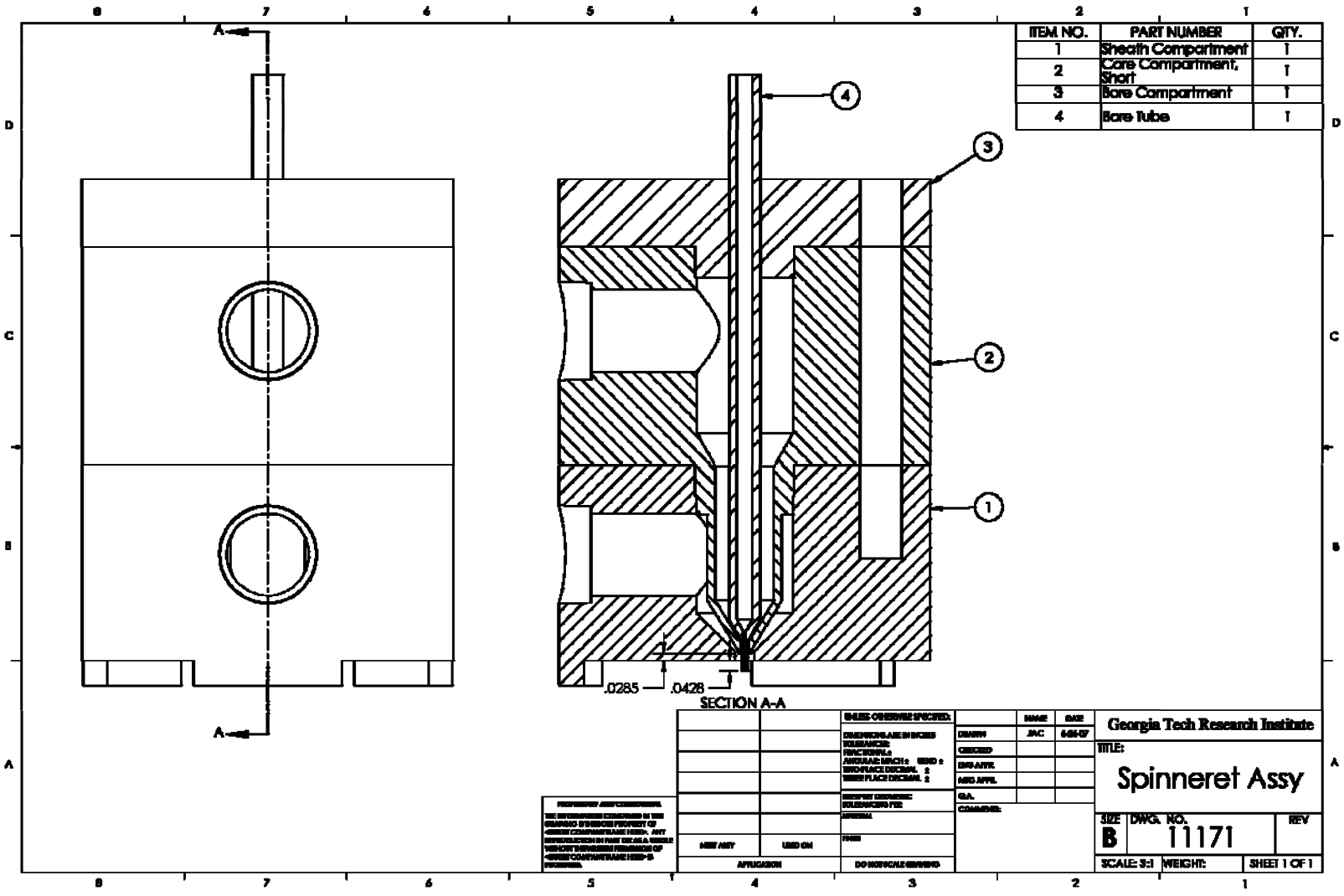

Figure C.4: "Inverted" composite spinneret machining schematic 1.

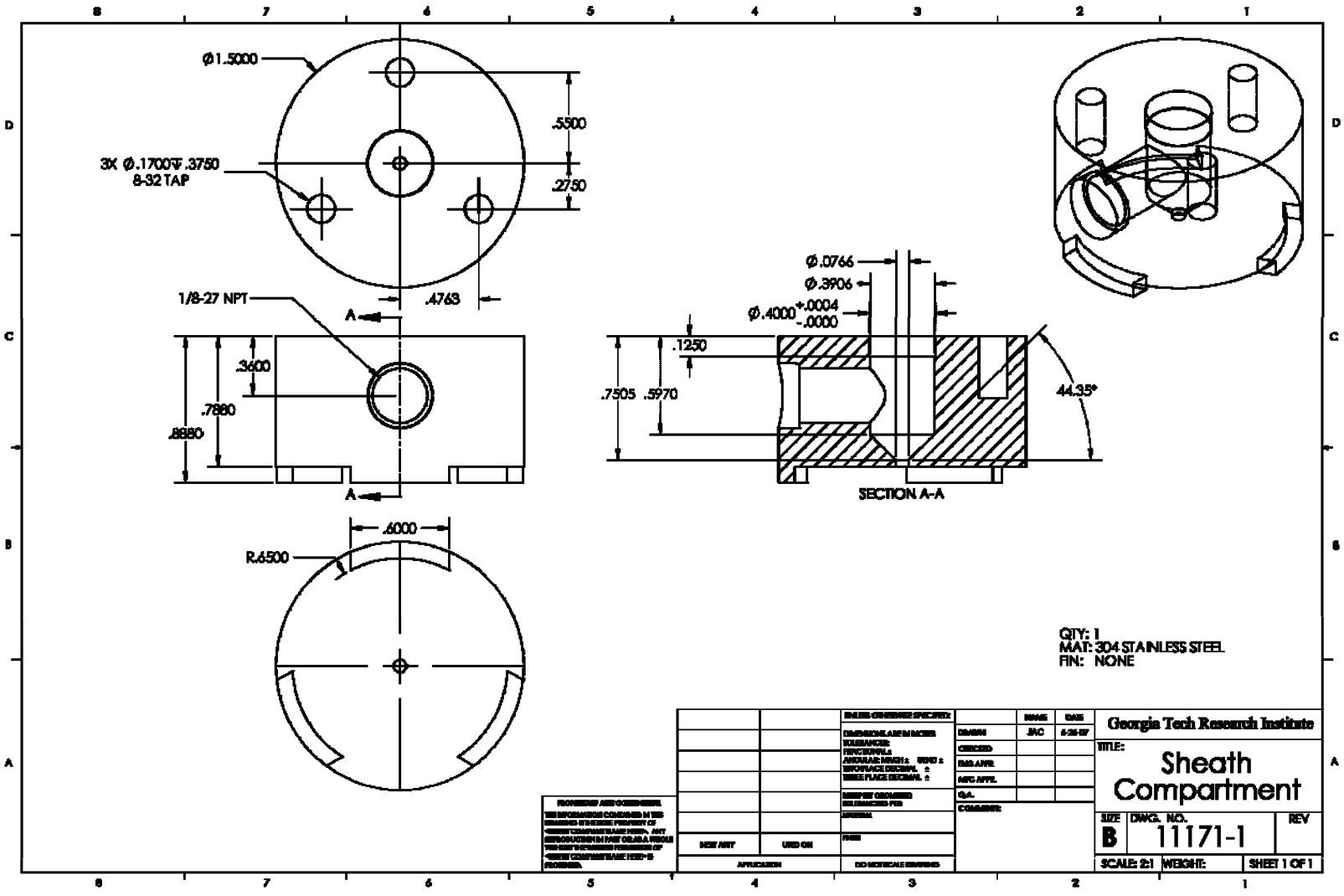

Figure C.5: "Inverted" composite spinneret, barrier layer compartment schematic.

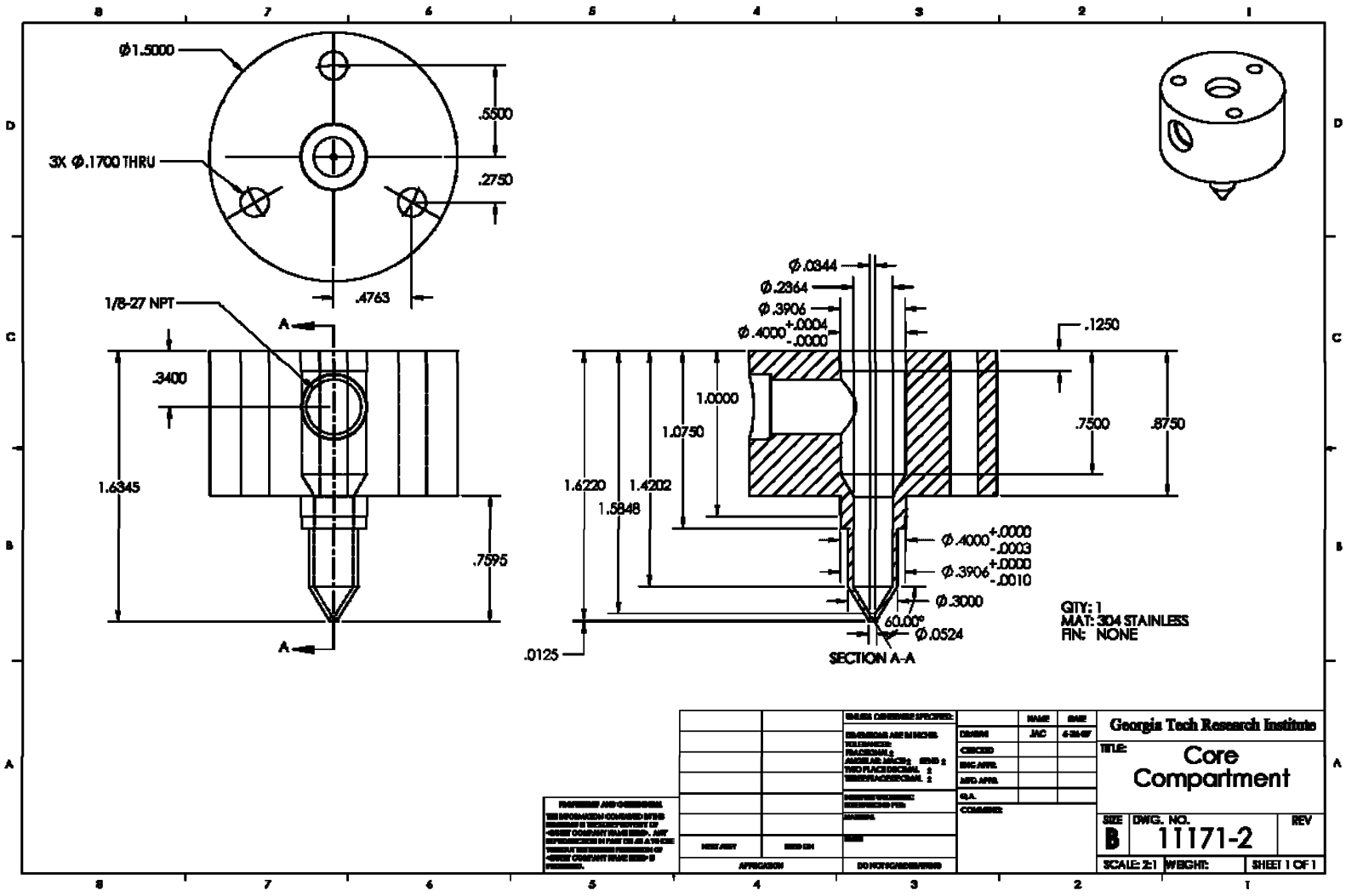

Figure C.6: "Inverted" composite spinneret, fiber sorbent dope compartment schematic.

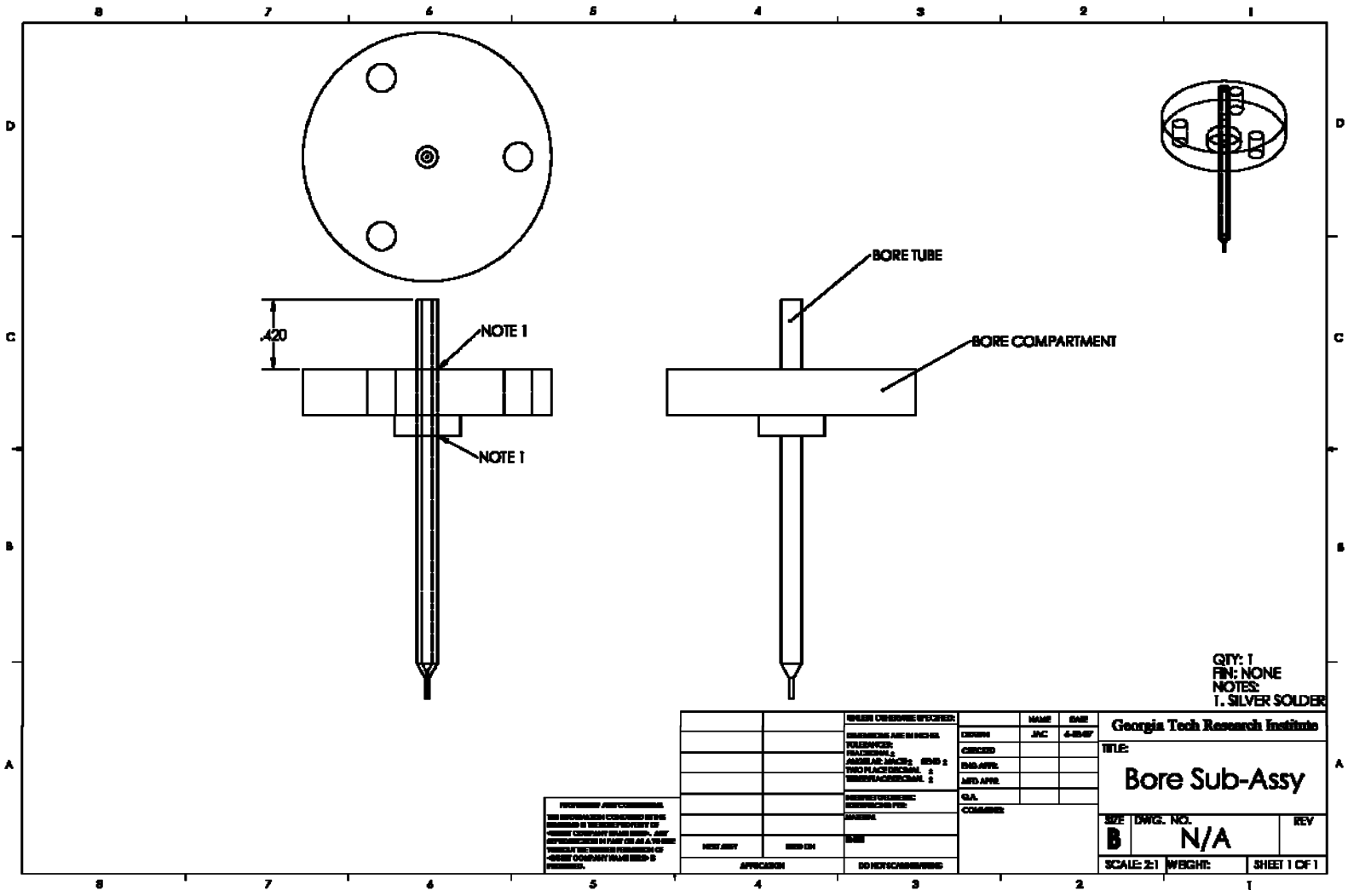

Figure C.7: "Inverted" composite spinneret, bore needle schematic.

C.3 Spinning Experiments

The spinning experiments were conducted using the same fiber sorbent dope discussed in Chapter 5. The barrier layer dope composition is listed in Table C.1.

Table C.1: PAN barrier layer dope

Component	Wt%
PAN	15
Water	1
NMP	84

The spinning conditions used can be seen in Table C.2.

Table C.2: Dual layer spinning conditions

Spinning Parameters	
Core Flow Rate	1000 mL/hr
Lumen Flow Rate	100-200 mL/hr
Bore Flow Rate	250-500 mL/hr
Bore Composition	80/20 NMP/H_2O
Operating Temperature	25°C
Take-up Rate	11.7. m/min
Air Gap	3 cm

Spinning the dual layer fibers was quite similar to spinning single layer CA/13X fibers. However, upon examination under the SEM, the lumen layer was found to be completely delaminated from the fiber sorbent structure, indicating that PAN and CA are immiscible (Fig C.8).

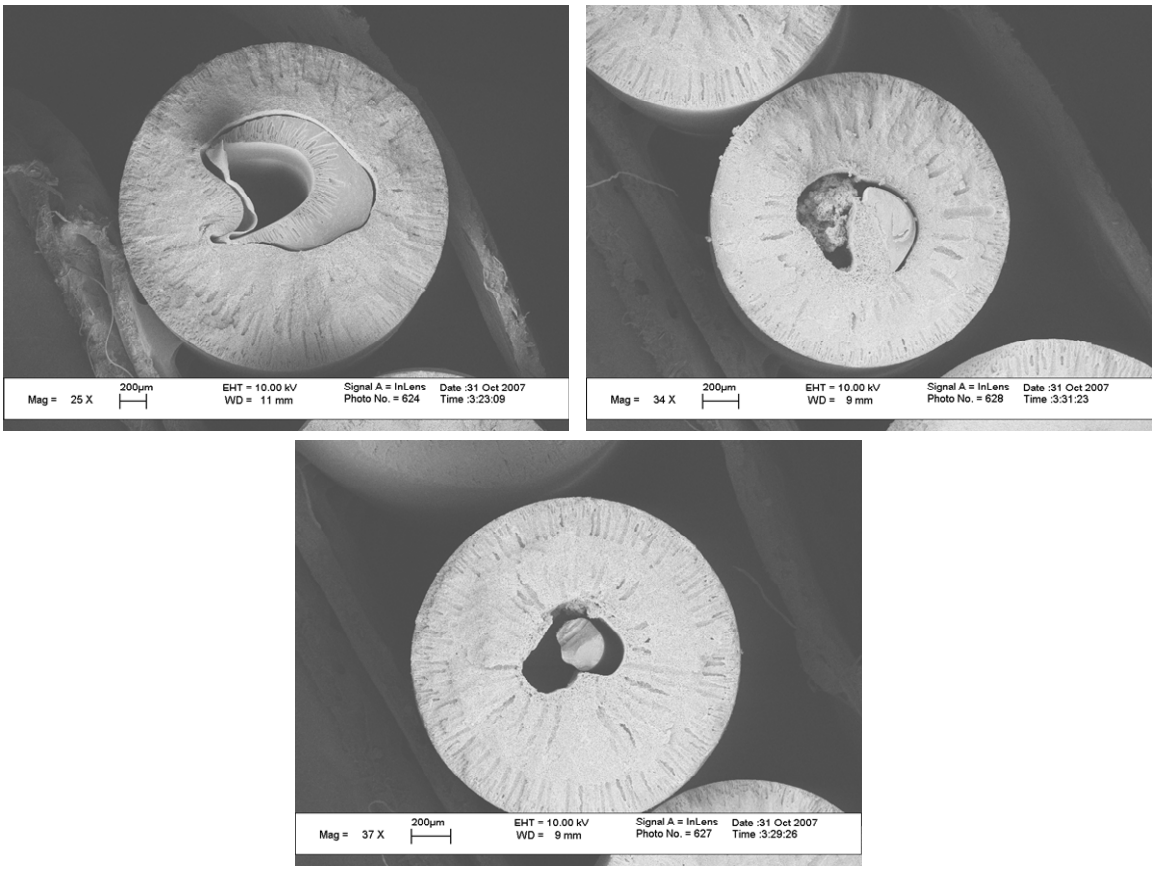

Figure C.8: SEM images showing immiscibility between CA (outer structure) and PAN (inner structure).

Appendix D

Water and Carbon Dioxide Competitive Adsorption in Silicalite

D.1 Introduction

Broadly, there are two routes for post-combustion CO_2 capture technologies[1]: absorption systems and adsorption systems. Absorption systems typically involve thermally cycling a chemical solvent for CO_2, stripping the CO_2 from the power station's flue gas and regenerating the solvent to create a pure CO_2 stream. These processes range from traditional amine based solvents, such as monoethanol amine (MEA)[2], to new processes based on chilled ammonia[3], and to new and novel solvents such as ionic liquids[4]. Adsorption processes, on the other hand, typically involve the use of porous solid particles that exhibit a selective affinity for one gas species over another. These processes are usually divided into two groups: chemisorption systems and physisorption systems. Chemisorption systems rely on strong interactions between the adsorbent and adsorbate—typically a chemical reaction between the surface and CO_2 occurs. Typical chemisorbents involve a mesoporous support with functional groups impregnated or covalently tethered to the surface of the support[5]. Physisorption processes rely on weak attractions between the sorbent surface and the CO_2.

From an energetic perspective, physisorption processes have the lowest heat of sorption requirements, and correspondingly have the potential to drive down post-combustion CO_2 capture costs when compared to chemical processes. Unfortunately, zeolites, the physisorbents typically considered, exhibit a stronger affinity for water vapor over CO_2. Since coal-fired power station flue gas is saturated with water[2], physisorption processes will likely require costly dehydration steps, effectively negating the energetic bonus inherent in the physisorbents. However, the more silicaceous a zeolite is, the lower its affinity for water compared to CO_2[6]. This appendix seeks to demonstrate that CO_2 capture capacity of pure-silica MFI (or silicalite) in competitive $N_2/H_2O/CO_2$ kinetic adsorption is substantially the same as its dry CO_2 capture capacity, which has the potential to allow fully water-saturated operation and elimination of expensive dehydration steps.

D.2 Background

Silicalite, more formally referred to as Silicalite-I, is a nominally 100% silicaceous analog of the ZSM-5 series of zeolites, is highly hydrophobic and has a high affinity for organic molecules[8]. The zeolite possesses multiple intersecting channels in all three dimensions, with pore openings approximately 5.5Å in diameter. Depending on the synthesis route and crystal size, the zeolite can exhibit a near perfect crystal structure with few defect sites, or it can exhibit multiple grain boundaries and defect sites[9]. Water adsorption in silicalite has been studied previously and typical capacities were found to be quite low relative to alumina-containing zeolites.[10-14]

Kinetic and equilibrium adsorption measurements are often performed with chromatographic methods[15]. A carrier gas, typically an inert or relatively non-adsorbing gas, is fed across a packed bed of sample towards a detector, until the gas is switched to a mixture of an inert tracer gas, the carrier gas, and an adsorbate of interest. In this way, the inert tracer gas allows for the removal of the effects of bed spreading and dispersion on the adsorbate signal. By integrating the tracer signal and the adsorbate signal with respect to time, the area bounded by the two resulting curves yields the sorbed concentration (when the sample mass is accounted for), as demonstrated in Chapter 2.

The chromatographic method provides a simple means for determining adsorption equilibrium parameters as well as kinetic parameters[15]. In this experiment, an inert gas flows through a cylindrical cell packed with the adsorbent of interest dispersed in an inert substrate to reach steady state, thereby providing the baseline signal. The inert substrate provides isothermal conditions and minimizes pressure drop in the cell, even for small sorbent particle sizes. A square or pulse input of feed (with adsorbing components and non-adsorbing "tracers") is introduced at the cell inlet and the resulting concentration front of this input is measured continuously at the cell exit. Passage of the feed through the cell influences the exit concentration in two ways: the mean residence time of the adsorbing components in the cell is altered by the affinity of the adsorbate for the adsorbent and the input signal spreads out as it propagates, owing to several factors:

1. Axial dispersion, related to non-ideal mixing in the bed
2. Film resistance at the sorbent particle surface

3. Intra-particular resistances, including macropore and micropore diffusion resistances, and adsorption resistance

The affinity of the adsorbing component for the sorbent, in the linear region of the adsorption isotherm, characterized by the Henry's Law Constant *K*, is obtained directly from the difference in the mean residence times of the adsorbing component and the tracer. The residence time, $\bar{t}$ (s), is simply the normalized first moment μ_1 of the tracer exit signal.

$$\bar{t} = \mu_1 = \frac{\int_0^\infty t \cdot C(L,t)dt}{\int_0^\infty C(L,t)dt} \quad \textbf{(1)}$$

where *C(L,t)* is the measured concentration of tracer at exit. *K* is directly proportional to the difference in μ_1 of the adsorbate and tracer as[15]:

$$K \cdot \frac{\varepsilon_b L_{bed}}{u} = \frac{\mu_1 - (\mu_1)_{inert}}{\left[\frac{(1-\varepsilon_b)\cdot(1-\varepsilon)}{\varepsilon_b}\right]} \quad \textbf{(2)}$$

where ε_b is the bed porosity, ε is the zeolite void fraction, *u* is the superficial velocity (cm/s) of the feed gas in bed, and L_{bed} (cm) is the length of the bed.

The spread of the exit signal about its mean is measured as μ_2'(s^2), the second moment of the signal relative to its mean:

$$\mu_2^{'} = \frac{\int_0^{\infty} (t-\mu_1)^2 \cdot C(L,t)dt}{\int_0^{\infty} C(L,t)dt} \quad \textbf{(3)}$$

μ_2' is directly proportional to the dispersive resistances within the bed, one of which is the micropore diffusion resistance of the adsorbate through the zeolite[16].

$$\mu_2^{'} \frac{L_{bed}}{2u} = \frac{D_L}{u^2} + \frac{\varepsilon_b}{(1-\varepsilon_b)} \cdot \left(\frac{r_c^2}{15K \cdot D_c} \right) \quad \textbf{(4)}$$

$$\frac{\mu_2^{'}}{\bar{t}^2} = \frac{2D_L}{uL_{bed}} + 8 \cdot \left(\frac{D_L}{uL_{bed}} \right)^2 \quad \textbf{(5)}$$

Here, D_L is the axial dispersion coefficient (cm^2/s) calculated as per equation 5, r_c is the radius of zeolite particles, and D_c (cm^2/s) is the micropore diffusivity of sorbate through the particle. The above expression, which is applicable to low flow rate situations, ignores macropore and external film resistances and can be used to estimate the micropore diffusivity of CO_2 through the zeolite.

Another technique that is useful for adsorption characterization is thermal gravimetric analysis (TGA). This method measures the mass uptake (or loss) of adsorbate within a sample, and allows for control of the sample temperature. Multicomponent sorption can be determined in a limiting case by first exposing the sample to an inert carrier gas and measuring the corresponding gas uptake, and then introducing an adsorbate gas (such as H_2O), followed by the final adsorbate gas (such as

CO_2)[17]. In this manner, at equilibrium, the sorption values of CO_2 (for instance) may be estimated as,

$$m_{uptake,\ CO2} = m_{uptake,Total} - m_{uptake,\ H2O} - m_{uptake,\ inert} \quad \textbf{(6)}$$

which allows for a "minimum" uptake of CO_2, with the assumption that CO_2 does not displace any already adsorbed water. Finally, the TGA technique allows for temperature cycling, enabling analysis of cyclic stability and cyclic uptake.

D.3 Materials and Methods

D.3.1 Materials

Zeolite 13X (1-3 micron particles, Sigma-Aldrich) was used as a zeolitic standard for the multicomponent sorption system. The zeolites were dried at 230°C prior to use to remove any potential contaminants. Nitrogen physisorption, wide angle X-ray diffraction, and elemental analysis were used to confirm the zeolite's physical properties in comparison to known values.

D.3.2 Silicalite Synthesis

We elected to use silicalite synthesized in our laboratories rather than commercial samples in order to have consistent particle size and quality. The following materials

were purchased from commercial sources and used as-received: tetrapropylammonium hydroxide (TPAOH, 40wt% aqueous solution, Alfa Aesar), and tetraethylorthosilicate (TEOS, 98%, Sigma-Aldrich). The synthesis of 200 nm silicalite followed the procedures established by Schoeman et. al[18], and has been reported elsewhere—we repeat the essential details here for completeness. The precursor solution had a molar ratio of 1.0 TEOS/0.36 TPAOH/ 20 H_2O, where TEOS is the silica source and TPAOH is the structure directing agent (SDA). The precursor solution was mixed at room temperature for 24 hours before being added to a 700 mL autoclave reactor (HR-700, Berghof Inc). The hydrothermal reaction was performed at 150°C and stirred for 96 hours. The suspension recovered from the reaction vessel was centrifuged at 8000 rpm and the supernatant was removed. The solids were redispersed into DI H_2O by sonication and centrifuged again. This sonication-centrifugation cycle was repeated until the supernatant pH fell below 8.0. The recovered solids were then dried at room temperature, followed by calcination at 550°C for 8 hours. Scanning electron microscopy, X-ray diffraction, and nitrogen physisorption were performed on the Silicalite particles, and have been published elsewhere[9].

D.3.3 Competitive Sorption System Construction

A multicomponent competitive adsorption system was built to test the zeolites in both dry and wet simulated flue gas feeds (Figure D.1). The zeolites were stored in a 100% relative humidity (RH) saturation chamber for 2 weeks prior to use, thereby circumventing the complicating issue of water sorption onto the zeolites during the

sample preparation stage. Samples of the water-saturated zeolites were dried at 400°C under He in a Netzsch STA 409 thermal gravimetric analysis (TGA) instrument to determine the total water uptake by the zeolites, which was removed in the calculation of the sorption capacities reported here. Samples were dispersed in a packed column with sand (Sea Sand, Fisher) with a loading of 5wt% zeolite, and loaded into the adsorption system. The samples were dried at 125°C for 2 days under vacuum in the system. After drying, the bed was purged with 20.0 sccm of dry nitrogen and brought to the adsorption temperature (either 35°C or 120°C). The bed was then rapidly switched to a 10mol% He/10 mol% CO_2/80 mol% N_2 feed at 20.0 sccm—which was either dry or bubbled through a saturation column (held at the adsorption temperature). In this protocol, He acts as the inert tracer, N_2 acts as the carrier gas, and CO_2 and H_2O act as the adsorbates of interest. Such low flow rates were chosen, in comparison with other experiments in the literature[19], to keep bed pressure drop at a minimum so that water condensation could be avoided. The outlet concentrations were measured using a Pfeiffer Vacuum QMS 200 Omnistar® Mass Spectrometer. Once the signals stabilized after breakthrough, the bed was rapidly switched back to dry N_2, thus completing the square impulse required to perform the method of moments analysis listed above. After the N_2 signal stabilizes, the bed was heated back to 125°C and dried under vacuum for 24 hours. Every adsorption run was repeated three times. To confirm the capacities reported, the experiment above was repeated, but with a humid N_2 stream pre-saturating the bed before the introduction of humid CO_2. Mass flow controllers were used to precisely hold the purge and feed gases at 20.0 sccm. The upstream of the system was held at a constant temperature by heaters at 35°C, while the bed was wrapped in heat tape and held at the desired

experimental temperature. The immediate downstream of the bed was held at 130°C, allowing for rapid switching between wet and dry mode. This procedure was adopted, since in the absence of downstream heating, water vapor desorbing from zeolites tends to become supersaturated and condense on the non-heated walls. The feed gas and the purge gas are each fed through an independent water bubbling column, thereby removing any lag time associated with saturating a single column with CO_2 and then un-saturating it with N_2.

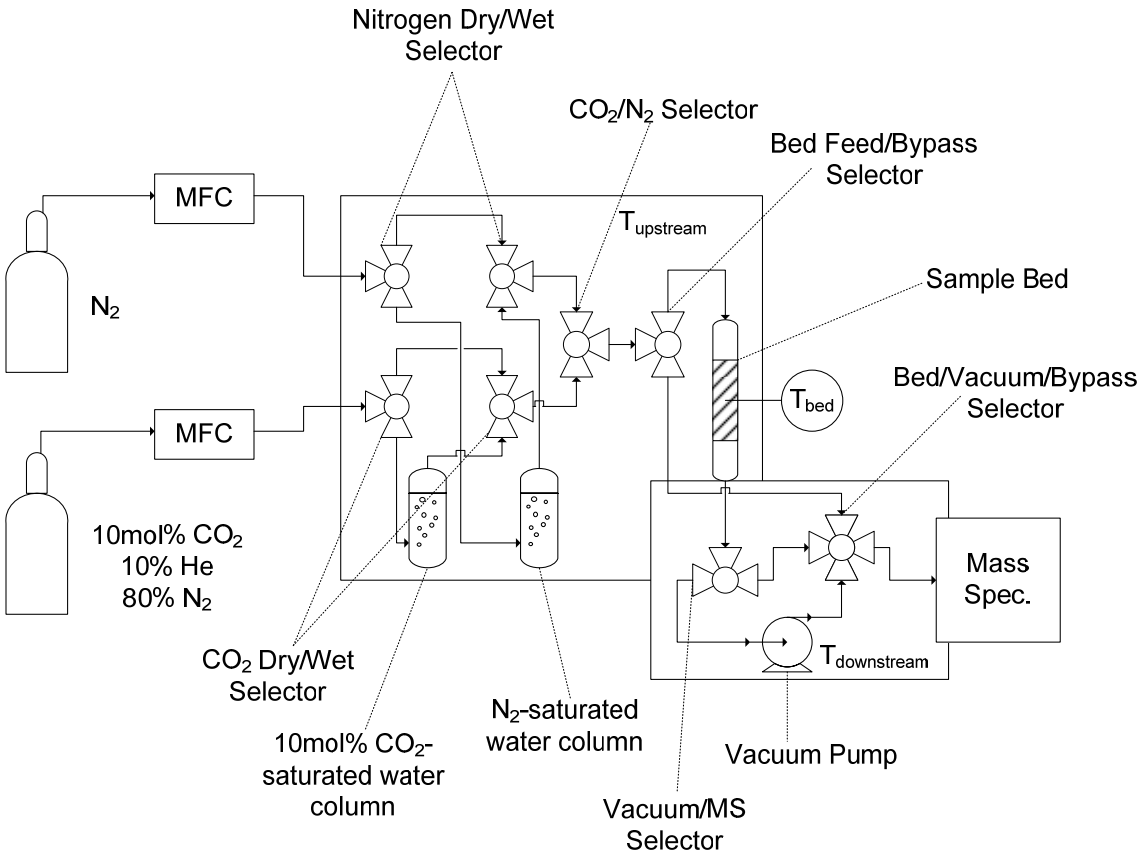

Figure D.1: Multicomponent competitive adsorption system.

D.3.4 Cyclic Thermogravimetric Analysis

TGA was used to analyze the regenerability and response rates of the silicalite samples in constant thermal cycles under a humid CO_2 atmosphere. A Netzsch STA 409 TGA was used to allow for control of heating and cooling ramp rates and thermal soak times. Helium gas was dried with liquid nitrogen and sent to the TGA to dry the zeolite samples at 115°C for 36 hours (36 hours was used to allow for sufficient drying time, as determined by the mass loss stabilization). After the drying step, the TGA was cooled to 100°C, and the purge gas was switched using a three-way valve to 10mol% CO_2/90mol% He, which was either dry or bubbled through a room temperature saturation column. The zeolites were then cycled between 45°C and 105°C for 24 hours under this humid 10mol% CO_2 atmosphere. The cycling portion of the experiment was repeated with the following sweep gases: helium, water-saturated helium, 10mol% CO_2/90mol% He, and finally, water-saturated 10mol% CO_2/90mol% He.

D.4 Results and Discussion

The multicomponent competitive sorption apparatus was first tested using zeolite 13X and 200nm silicalite in dry CO_2 and N_2 conditions to confirm the accuracy of the system relative to reported literature values. Table D.1 lists the capacity values for the two zeolites at the two temperatures considered, as well as the dimensionless Henry's Law constants.

Table D.1. Summary of Dry CO_2 sorption properties on zeolites 13X and silicalite: 0.1 atm of CO_2, 0% RH, dried at 125°C

Zeolite	Temperature (°C)	K	Capacity (mmol/g)	Swing Capacity	$K_{(literature)}$	Literature capacity (mmol/g)
13X	35	985 ± 13.3	1.78 ± 0.07	0.89 ± 0.03	20200[7,16]	2.1[20]
	120	661 ± 11.8	0.89 ± 0.02		480[7]	1.34[21]
Silicalite	35	207 ±15.3	0.34 ± 0.03	0.16 ± 0.009	350[22]	0.3[23]
	120	113 ± 9.5	0.09 ± 0.007		30[17]	< 0.1[23]

Experimental results are the average of three experiments with standard deviations indicated.

The Henry's Law constants were determined from Equations 1 and 2. The results for silicalite generally match the values given in the literature[7,16]. The capacities and Henry's Law constants reported here for 13X are lower than those found in the literature. This discrepancy probably reflects the lower drying temperatures used in this study (limited to 125°C, chosen to represent a low temperature drying step likely used in a post-combustion CO_2 capture scenario) relative to other research, since only by drying at very high temperatures can strongly chemisorbed species be removed (namely water), as demonstrated previously[7,24,25]. Furthermore, as the CO_2 feed conditions in this study are somewhat outside the Henry's Law regime, the Henry's Law coefficients determined by the chromatography technique will be lower than the true infinite dilution coefficients. Strongly chemisorbing sites significantly affect the sorption capacity in the Henry's Law regime; when these sites are occupied, the apparent capacities and Henry's Law constants for weaker sorbates will be lower as a consequence. Lower drying temperatures are of

more interest in a post-combustion CO_2 capture scenario, as the regeneration step for solid-adsorbents is typically the most energy intensive due to the high temperatures required; Table D.1 shows that meaningful capacities are still retained despite the low temperature zeolite drying step.

Table D.1 also lists the swing capacities of the zeolites; where the swing capacity is defined as

$$\Delta C = C_{CO2,\ High\ Temperature} - C_{CO2,\ Low\ Temperature} \quad \textbf{(7)}$$

which may be found by either a thermal adsorption-desorption cycle, or repeating the adsorption experiment at the higher temperature (the latter was used in this work). The swing capacity of a sorbent effectively determines the amount of sorbent required, bed sizing, and by extension, bed pressure drops (another energy penalty associated with packed bed systems). As expected, 13X has a much larger swing capacity in dry CO_2 conditions than silicalite. This is mainly attributed to the former's counter-balancing ions interactions with the large quadropole moment of CO_2[7], as opposed to the much weaker van der Waals interactions present in the CO_2-silicalite system[16]. As such, in dry conditions, a Silicalite-based packed bed process would require 3.5 times as much sorbent as a 13X system, demonstrating the importance of the swing capacity.

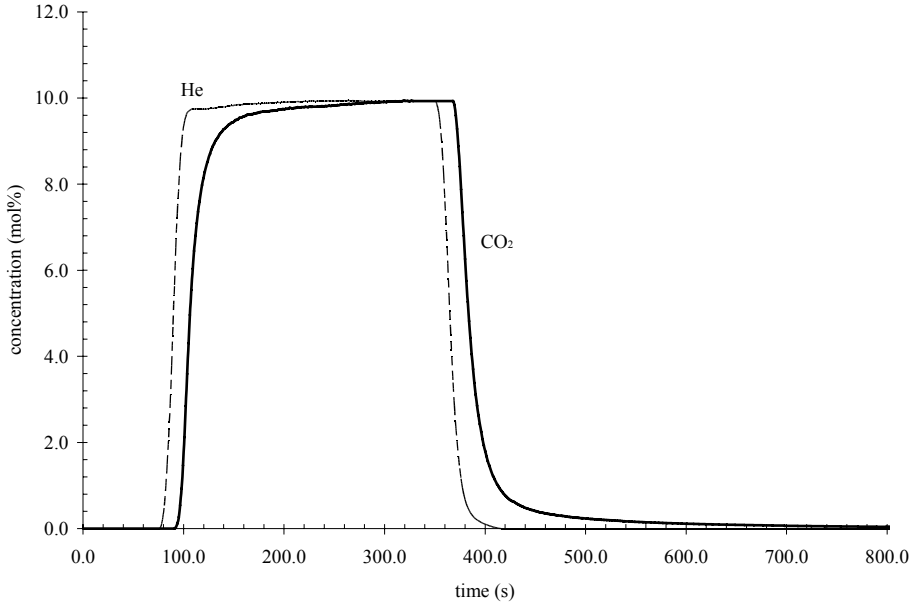

Figure D.2: Typical multicomponent sorption system response to square input

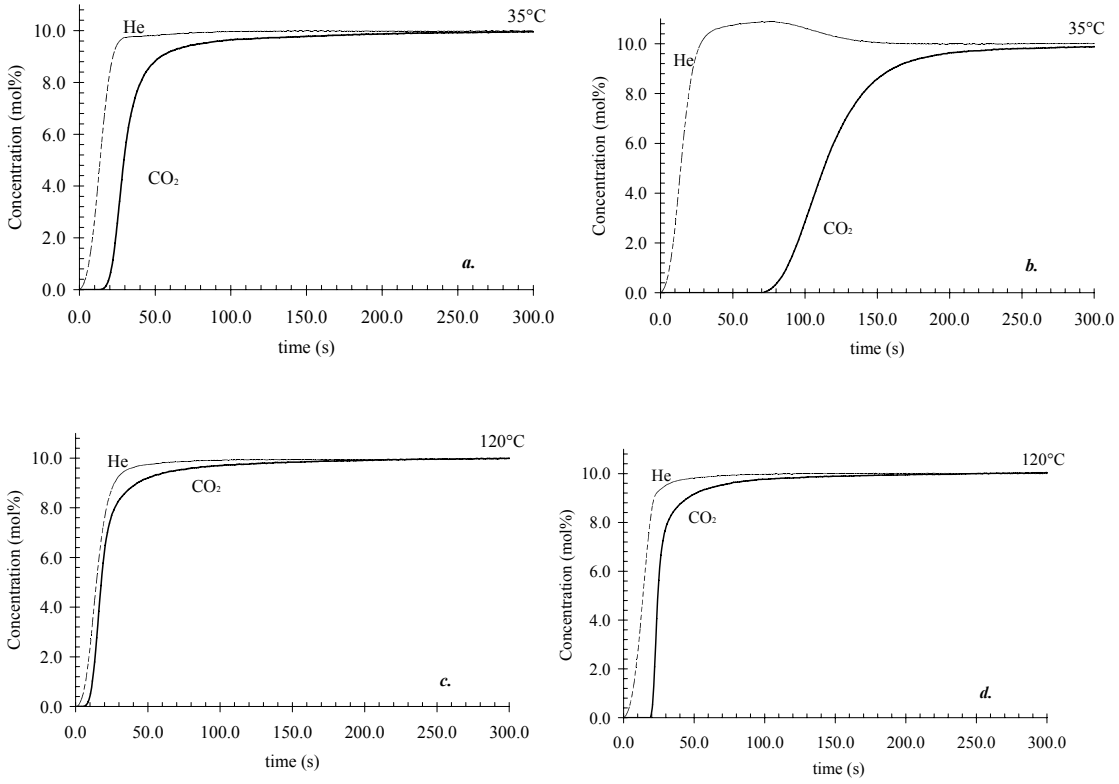

Figure D.3: Breakthrough curves for silicalite and 13X at 35°C (*a* and *b*, respectively), and 120°C (*c* and *d*, respectively). Feed and purge flow rates were set at 20.0 sccm.

Figure D.2 shows a representative square input which was used to perform the method-of-moment analysis, and Figure D.3 shows typical breakthrough curves for 13X and silicalite at the two temperatures. Due to the high CO_2 adsorption capacities of 13X at these conditions as well as the He/CO_2 stream being exposed to a clean bed, a roll-up phenomenon is observed, where helium filling the void space of the zeolites is displaced by the moving CO_2 front, resulting in the slight increase in He concentration observed. By using Equation 5 and taking the ratio of the second moment and the squared first moment, the axial dispersion in the system can be accounted for, in theory allowing for determination of zeolite micropore diffusion coefficients. Earlier work[16,26] has shown that more than 98% of the diffusion resistance is the internal or micropore diffusion, with external mass transfer resistances making up the remainder. Of the three resistances (axial dispersion, external mass transfer resistance, and micropore diffusion), the axial dispersion resistance was the dominant resistance in this work due to the very low flow rates; therefore micropore diffusion coefficients determined here are not accurate. There exists a trade-off between the ability to determine the diffusion coefficients and the possible water loading in the feed stream; that is, at higher flow rates axial dispersion is minimized, yet higher pressure drops occur resulting in water condensing within the bed.

When saturated CO_2 is fed to the zeolites, two very different responses are exhibited. As can be seen in Figure 5b, zeolite 13X exhibits characteristics of strong competitive adsorption; initially adsorbed CO_2 is slowly displaced by the more strongly adsorbing water, so rising CO_2 concentration is seen until the H_2O breakthrough occurs, where equilibrium is reached—an expected result in competitive adsorption[27].

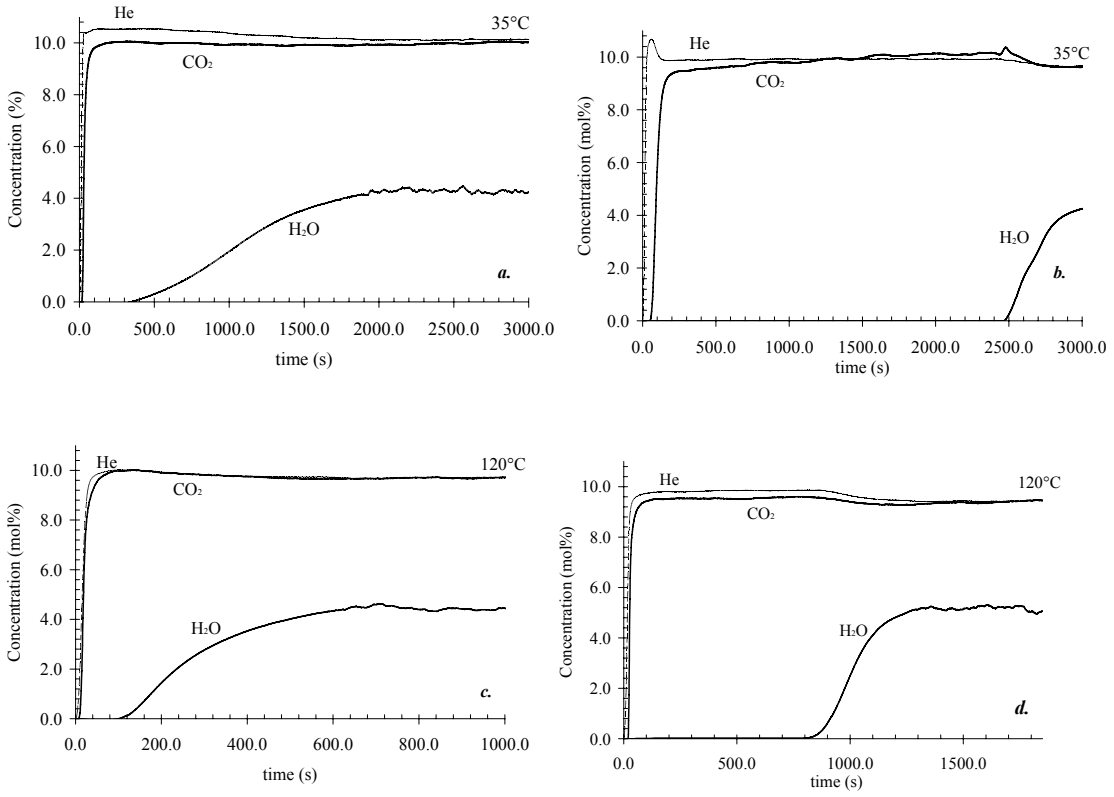

Figure D.4: Breakthrough curves for silicalite and 13X at 35°C (*a* and *b*, respectively), and 120°C (*c* and *d*, respectively) in humid CO_2 feeds. Flowrate is 20.0 sccm

Table D.2: Summary of wet CO_2 sorption properties on zeolites 13X and silicalite: 0.1 atm of CO_2, 100% RH at 35°C, dried at 125°C

Zeolite	Temperature (°C)	*K*	Capacity (mmol/g)	Swing Capacity (mmol/g)
13X	35	38.4 ± 6.5	0.09 ± .02	--
	120	210 ± 9.9	0.32± .03[a]	
Silicalite	35	355 ±36.3	0.35 ± 0.002	0.29 ± 0.005
	120	129 ± 16.5	0.06 ± 0.002	

[a]*Equilibrium capacity at very long times (~48 hours)*

In comparing Figures D.4*a* and D.4*c* with the dry CO_2 (Figures D.3*a* and D.3*b*), it is clear that Silicalite shows very little of the competitive adsorption effects seen in the CO_2/H_2O/13X system. The lack of competitive adsorption in silicalite (or the presence of competitive sorption in 13X) can be easily seen by comparing Tables D.1 and D.2. The CO_2 sorption capacities in the presence of competitive water sorption remain virtually unchanged. This fact suggests that CO_2 and water vapor do not compete directly for sites in the homogenous regions of the silicalite pore volume. Interestingly, the Henry's Law constant for wet CO_2 at 35°C is almost twice that of dry CO_2 at 35°C; the increase in experimental error observed is a result of the overall length of the wet runs versus the dry runs (due to water sorption). This protraction in run times makes determination of the first moments inherently less accurate. As the equilibrium capacities for CO_2 at 35°C are observed to be equivalent for dry and wet conditions, and the apparent diffusion coefficient can be assumed to decrease under wet conditions, we believe that water hinders CO_2's transport into the zeolites, thereby extending the observed first moment which, and may cause an erroneous increase in the estimated Henry's Law constant by Equation 2.

Table D.2 lists the swing capacities between 35°C and 120°C for the two zeolites in wet CO_2 feeds. As can be seen in comparison between Table D.1 and Table D.2, silicalite has approximately the same swing capacity in wet feeds as dry feeds, whereas 13X loses almost all ability to swing CO_2 on and off due to the strong effects of water and the strong temperature dependence of water sorption on 13X (the "reverse swing capacity" observed is the final equilibrium capacity seen after very long times, and would

not be viable in typical operating conditions). Water sorption is more temperature dependent than CO_2 sorption; as temperature increases CO_2 decreases less in equilibrium adsorption than H_2O. In a post-combustion CO_2 capture situation, where the feed stream is saturated with water, a 13X packed bed system would require expensive dehydration steps to be effective as a post-combustion CO_2 capture sorbent. The 35°C Henry's Law constant observed for 13X agrees well with values reported by previous researchers[7]. Again due to the stronger temperature dependence of water over CO_2, the Henry's Law constant actually increases as temperatures are raised sufficiently under wet conditions.

Cyclic TGA experiments were performed to ascertain the effect of water accumulation on silicalite over many thermal cycles, as well as the performance of the zeolite in these continuous cycles. The TGA was cycled continuously for 24 hours (after 36 hours of drying at 115°C in dry He) between 45°C and 100°C. The preceding swing temperatures were selected to reflect flue gas feed conditions (45°C) and typical low-grade steam temperature for desorption (100°C). Figure D.5*a* shows the dry CO_2 sorption cycles. Figure D.5*b* shows that silicalite maintains a constant working capacity throughout the extended thermal cycling in the 9.67mol% CO_2/3.3% H_2O/87.03% He atmosphere. The swing capacities are plotted on the right-hand ordinate of Figure D.5, and are correspondingly lower than those determined via the multicomponent competitive sorption instrument. This is expected due to the difference in swing temperatures used (a ΔT of 95°C in the multicomponent sorption device as opposed to a ΔT of 65°C in the TGA). Furthermore, the equilibration time for water is much longer than for CO_2, and is

significantly hindered by the continual thermal cycling, hence the upward trend in the uptake.

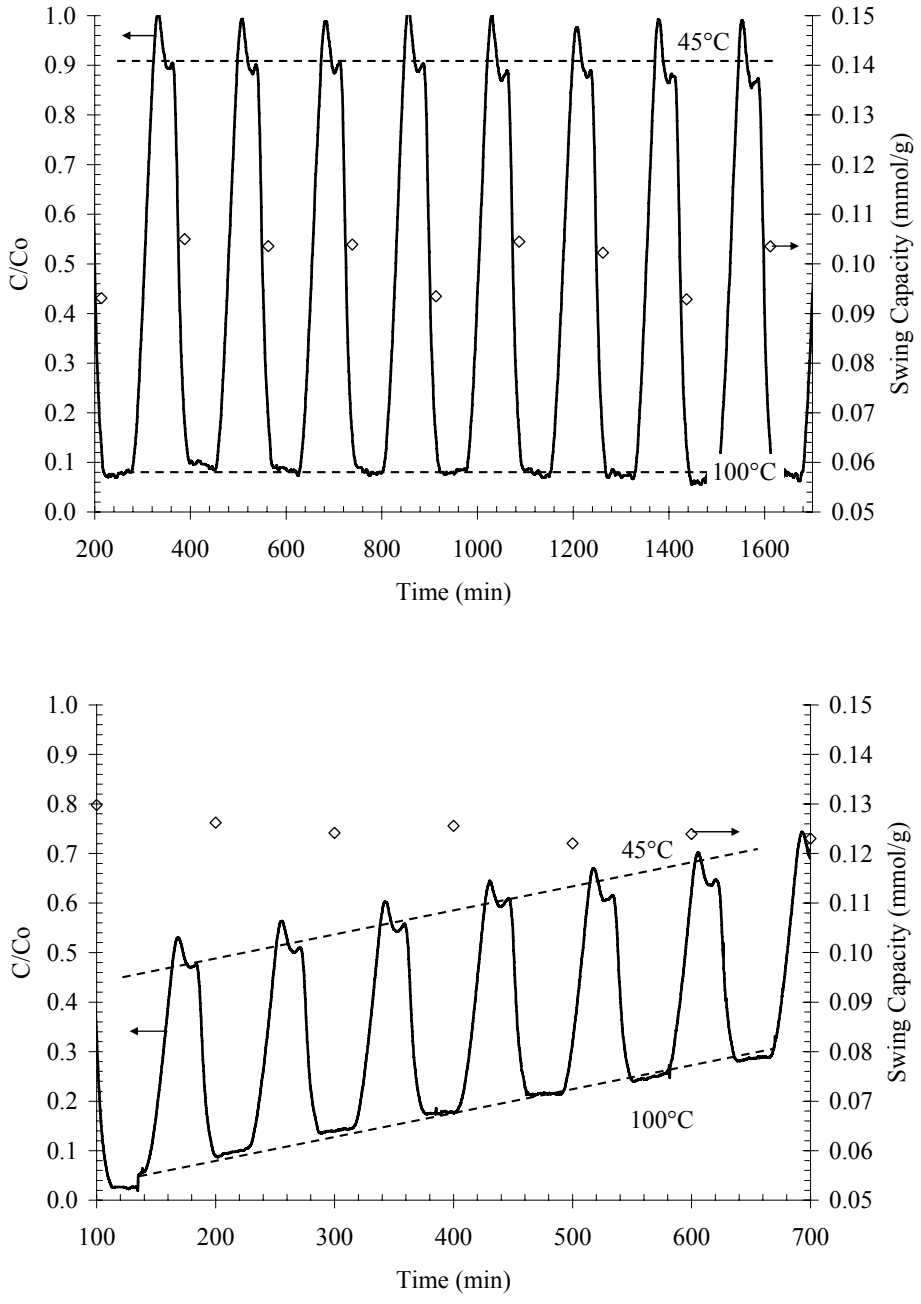

Figure D.5: *a (top)*, 10mol% CO_2 in He, cycled continuously between 45°C and 100°C in the TGA. Temperature curves are not shown, rather, the dashed lines represent the top and bottom of the thermal cycle. Points represent the difference in capacity from the low temperature to the high temperature. *b (bottom)*, Water-saturated CO_2 (10mol%) in He, cycled continuously in the TGA. Left-hand ordinate is non-dimensionalized by the highest capacity observed.

D.5 Conclusions

The results from multicomponent chromatography and TGA both indicate that CO_2 sorption on silicalite was essentially unaffected by the addition of water vapor. In practice, this implies that a solid sorbent system based on Silicalite would be able to operate equally well in both dry and wet feeds, and certainly will operate more effectively than typical hydrophilic zeolitic adsorbents, such as 13X, in wet feeds. This effectiveness in wet feeds, combined with silicalite's reported low heat of sorption (~25 kJ/mol), potentially positions Silicalite as a favorable solid adsorbent for CO_2 capture from an energetic perspective. Also, silicalite may well be more tolerant of SO_X in flue gas than 13X or amine adsorbents[28]. However, there are several issues associated with silicalite—and packed bed systems in general—that may prevent them from becoming a standard in flue gas CO_2 capture. Low swing capacities, high packed bed pressure drops, and competitive adsorption of $SO_X/CO_2/H_2O/N_2$ on silicalite are all issues that still need to be addressed for silicalite to be truly considered as a potential sorbent for post-combustion CO_2 capture. Many of the issues associated with packed bed adsorption systems for post-combustion CO_2 capture can be potentially removed by the use of fiber sorbent adsorption systems.[17]

D.6 References

1. Carbon Dioxide Capture and Storage; **2002**; pp 21-37.
2. Cost and Performance Baseline for Fossil Energy Plants. Volume 1: Bituminous Coal and Natural Gas to Electricity, NETL Technical Report Number DOE/NETL-2007/1281, August **2007**. http://www.netl.doe.gov/energy-analyses/pubs/Bituminous%20Baseline_Final%20Report.pdf
3. Gal, E.; Olson, S. **2006**. Chilled ammonium process (CAP) for post combustion CO2 capture. In: Presented at the 2nd Annual Carbon Capture and Transportation Working Group Workshop, Palo Alto, March 23.
4. Figueroa, J.D.; Fout, T.; Plasynski, S.; McIlvried, H.; Srivastava, R.D. *Int. Journal of Greenhouse Gas Control,* **2008**, 2, 9-20
5. Choi, S.; Drese, J.; Jones, C. *ChemSusChem* 2009, **2**, 796.
6. Olson, D.H.; Haag, W.O.; Borghard, W.S.; *Micropor. Mesopor. Mater.* **2000**, 35-36, 435-446
7. Brandani, F.; Ruthven, D.M.; *Ind. Eng. Chem. Res.*, **2004**, 43, 8339-8344
8. Flanigen, E.M.; Bennett, J.M.; Grose, R.W.; Cohen, J.P.; Patton, R.L.; Kirchner, R.M.; Smith, J.V.; *Nature*, **1978**, 271, 512-516
9. Cheng, C-H.; Bae, T-H.; McCool, B.A.; Chance, R.R.; Nair, S.; Jones, C.W.; *J. Phys. Chem.*, **2008**, 112, 3543-3551
10. Trzpit, M.; Soulard, M.; Patarin, J.; Desbiens, N.; Cailliez, F.; Boutin, A.; Demachy, I.; Fuchs, A.H.; *Langmuir*, **2007**, 23, 10131-10139
11. Giaya, A.; Thompson, R.W.; *Microporous Mesoporous Materials*, **2002**, *55*, 265-274
12. Soulard, M.; Patarin, J.; Eroshenko, V.; Regis, R-C.; *Proc.14th Int. Zeolite Conf*, **2004**, 1830
13. Oumi, Y.; Miyajima, A.; Miyamoto, J.; Sano, T.; *Stud. Surf. Sci. Catal.*, **2002**, 142, 1595
14. Olson, D.H.; Haag, W.O.; Borghard, W.S.; *Microporous Mesoporous Materials*, **2000**, 35-36, 435
15. Do, D.D.; *Adsorption Analysis: Equilibria and Kinetics*, Imperial College Press, London, UK, **2008**.
16. Li, P.; Tezel, F.H.; *Journal of Colloid and Interface Science*, **2007**, 313, 12-17
17. Lively, R.P., Chance, R.R., Kelley, B.T.., Deckman, H.W., Drese, J.H., Jones, C.W., Koros, W.J., *Industrial & Engineering Chemistry Research* **2009** *48* (15), 7314-7324

18. Schoeman, B. J.; *Stud. Surf. Sci. Catal.* **1997**, *105*, 647.

19. Delmas, M.P.F.; Ruthven, D.M.; *Microporous Materials*, **1995**, 3, 581-592

20. Hyun, S.H.; Danner, R.P.; *J. Chem. Eng. Data,* **1982,** 27, 196-200

21. Barrer, R.M.; Gibbons, R.M.; *Trans. Faraday Soc.,* **1965,** 61, 948-961

22. Harlick, P.J.E.; Tezel, F.H.; *Micro and Meso Mat.,* **2004,** 76, 71-79

23. Zhu, W.; Hrabanek, P.; Gora, L.; Kapteijn, F.; Mouljin, J.A. *Ind. Eng. Chem. Res,* **2006**, 45, 767-776

24. Ward, J. W.; Habgood, H.W.; *J. Phys. Chem.,* **1966,** 70, 1178-1182

25. Bertsch, L.; Habgood, H.W.; *J. Phys. Chem.*, **1963**, 67, 1621-1628

26. Triebe, R.W.; Tezel, F.H.; *Gas Sep. Purif.*, **1995**, 9, 223-230

27. Ruthven, D.M..; *Encyclopedia of Separation Technology Volume 1,* John Wiley and Sons, Inc., New York, NY, **1997**.

28. Lin, Y.S.; Deng, S.G.; *Sep. and Purif. Tech.*, **1998**, 13, 65-77

Appendix E

Spinning Cellulose Acetate/ZSM-5 Fiber Sorbents

E.1 Overview

As explained in Appendix D, silicalite sorbents are attractive for a post-combustion CO_2 capture scenario due to the sieves ability to retain CO_2 capacities even in the presence of saturated flue gas streams. As a proof-of-concept that the fiber sorbent platform can be extended to other sieves, a cellulose acetate/ZSM-5 (a silicalite analog with alumina in the framework) spin was conducted. From a dope composition perspective, changing from one zeolite to another is relatively easy, provided the chemical composition of the replacement zeolite is similar to the zeolite used to formulate the dope recipe.

E.2 Experimental Overview

An attempt at expanding the hollow fiber sorbent platform to other sorbents was made by spinning cellulose acetate fibers with embedded ZSM-5 particles (Zeolyst, CBV-3024E, Si/Al ratio of 30). Many unsuccessful attempts at spinning these fibers

were made using the "as-received" ZSM-5. These spins were unsuccessful because the fiber was not able to be drawn, only collected on the bottom of the quench bath, resulting in large, brittle fibers (Fig. E.1*a*). SEM (Fig E.1*b*) and light scattering experiments revealed that the ZSM-5 had a non-uniform particle size distribution, with a range of 250nm – 20 microns.

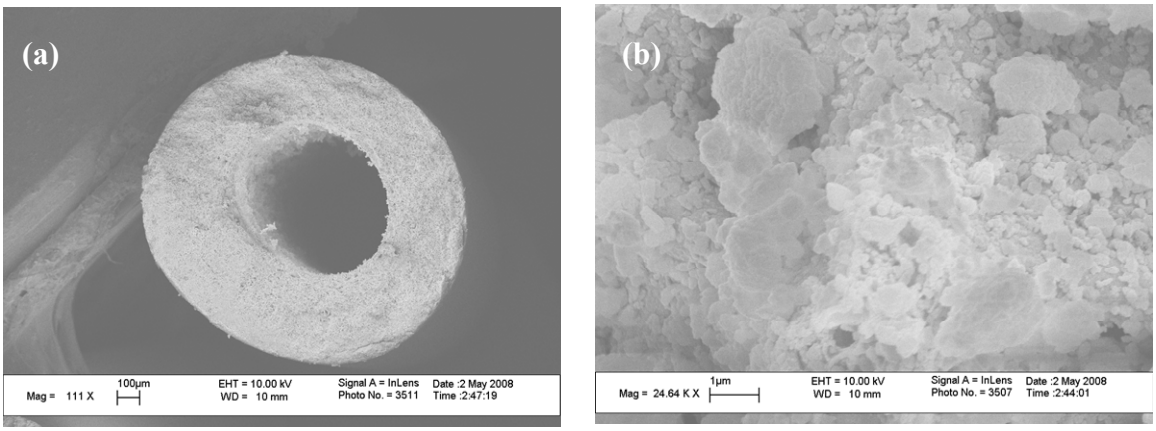

Figure E.1: a, SEM image of large CA/ZSM-5 fiber that was extruded into quench bath (no take up), b, SEM image of ZSM-5 sample from Zeolyst showing large particle distribution.

The ZSM-5 sample was put into a settling column, and the supernatant was recovered after an hour of settling. The supernatant was then centrifuged and heated to 110°C under vacuum to dry the size-classified ZSM-5 powder. After recovering enough 400nm particles (deduced via light scattering) to spin, the cellulose acetate/ZSM-5 spin was attempted again, this time successfully. The spin conditions can be seen in Table E.1. SEM images of the fibers and the pore structure can be seen in Figure E.2. These fibers were readily drawn up to extrusion rates of 500 mL/hr, though 1000 mL/hr was also likely possible, but the small amount of ZSM-5 sample limited the number of spin states that were able to be tried. Most surprising was the fact that the CA/ZSM-5 fibers (75wt% loading), once solvent-exchanged and dried, were able to be tied into double knots! This

marked improvement in mechanical properties relative to CA/13X could be a result of the smaller crystal sizes used, or the fact that smaller OD fibers were made.

Table E.1: Spinning dope compositions and parameters for cellulose acetate/ZSM-5

Spin Dope Composition			Spinning Parameters	
Component	**Core Dope (wt%)**		**Parameter**	
CA	14		Core Flow Rate	500 mL/hr
PVP	0		Bore Flow Rate	110 mL/hr
ZSM-5	30		Bore Composition	80/20 NMP/H_2O
NMP	49.3		Operating Temperature	25°C
H_2O	6.7		Take-up Rate	11.7. m/min
--	--		Air Gap	3 cm

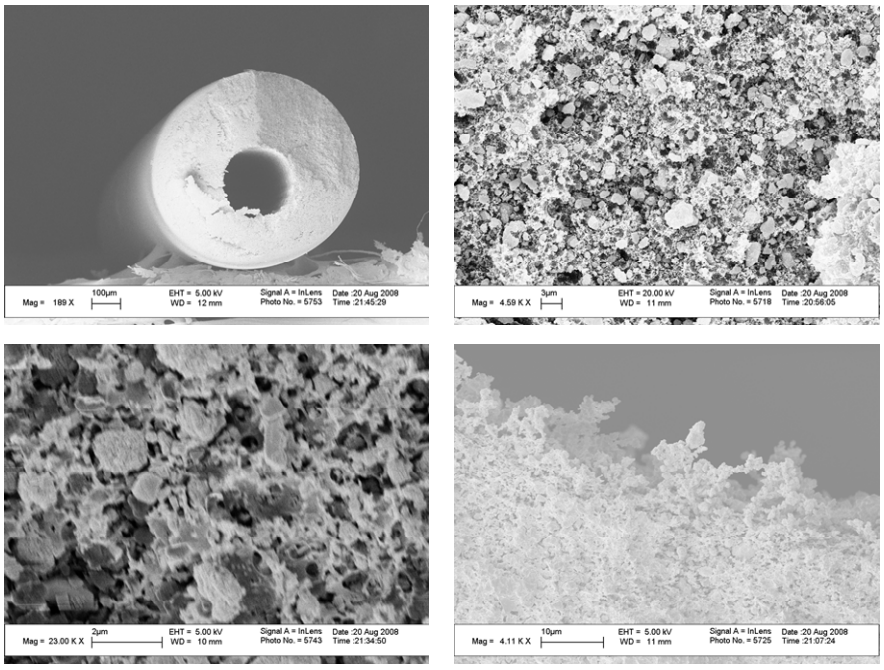

Figure E.2: SEM images of ZSM-5 fiber sorbents. a, ZSM-5 fiber sorbent cross-section, b, Image showing adequate size-classification, c, Image showing porous polymer structure supporting ZSM-5 crystals, d, Image showing inner radius of fiber sorbent.

The CO_2 sorption isotherm on the fiber sorbents was generated using a pressure-decay cell (Chapter 3), and the CO_2 uptake kinetics from the first expansion were recorded, and can be seen in Figure E.3 and E.4, respectively. The isotherm shows uptake that is consistent with the measurements for silicalite present in Appendix D. The uptake (Fig. E.4) shows rapid initial uptake, followed by a long shoulder. 70% uptake is seen to take 9 seconds, while 90% uptake is seen to take 64 seconds. The long shoulder is likely due to the non-uniform particle size distribution within the fiber sorbent (Figure E.2*b*), and the release of sorption enthalpy.

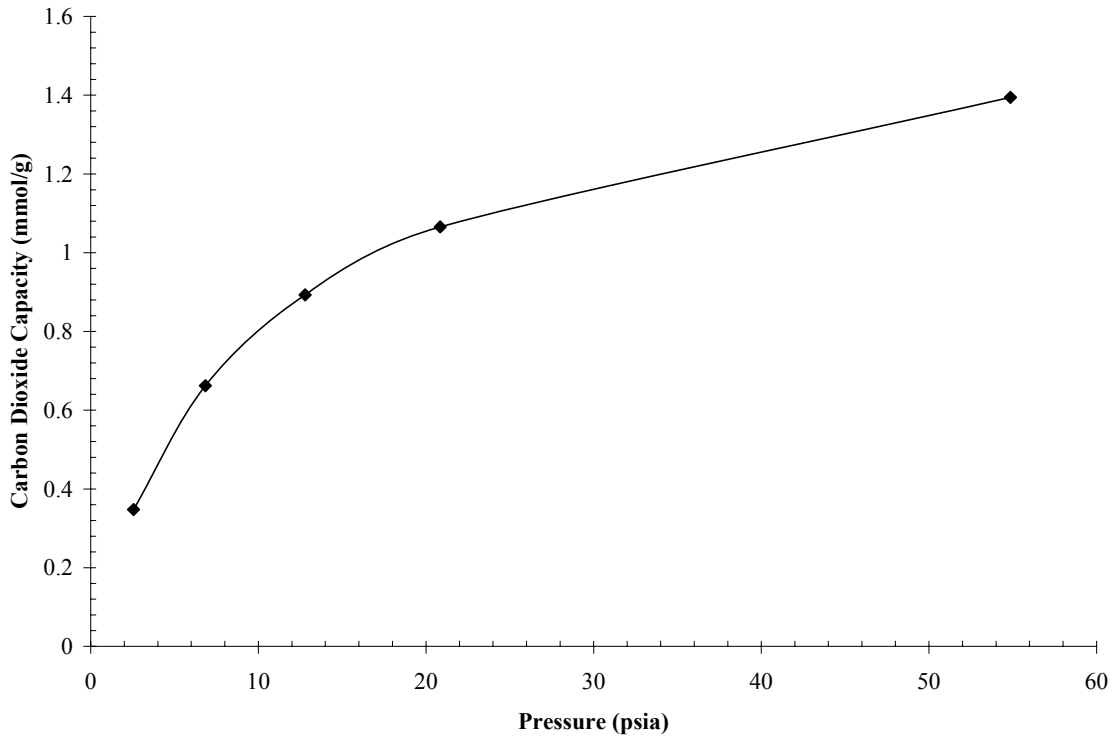

Figure E.3: CO2 sorption isotherm on CA/ZSM-5 (Si/Al~30) fiber sorbents at 45°C.

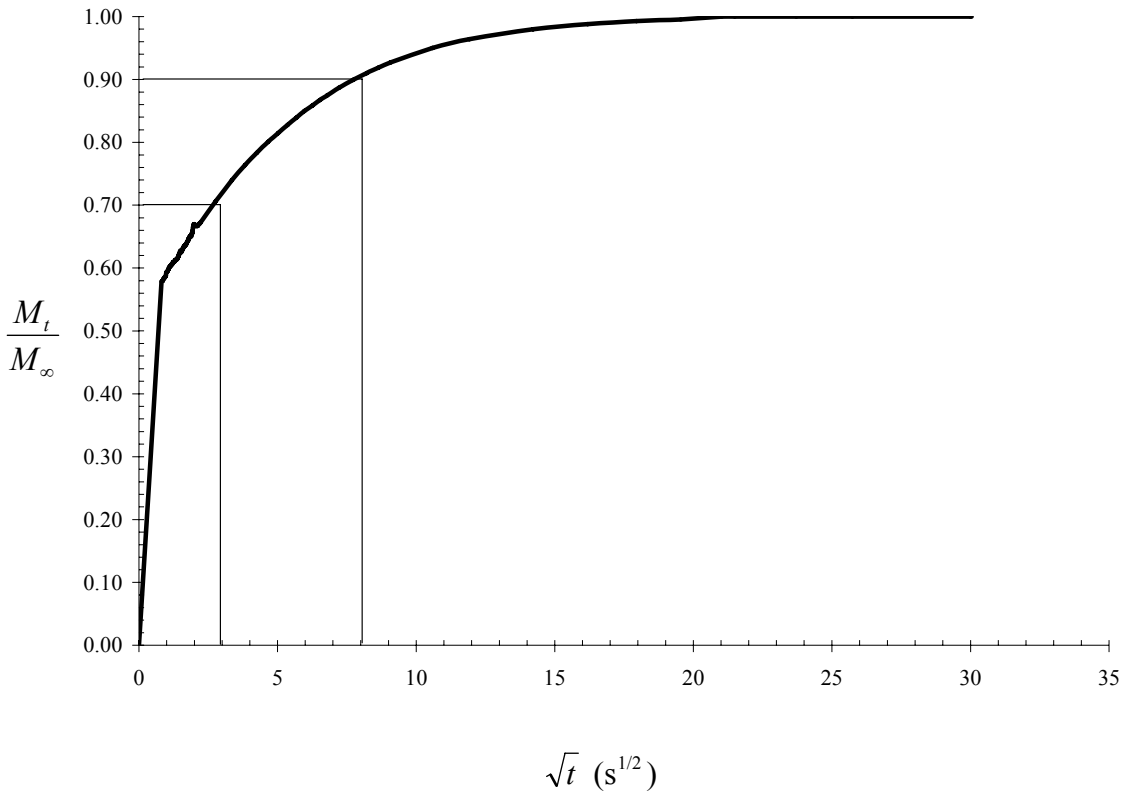

Figure E.4: CO2 uptake kinetics on CA/ZSM-5 fiber sorbents. Long shoulder is likely the result of a non-uniform particle size distribution and sorption enthalpy effects.

Appendix F

Eicosane-Filled Fiber Sorbents for Vacuum Swing Adsorption

F.1 Overview

Fiber sorbents also have the potential to be used in vacuum swing adsorption system, if a method is developed to mitigate the sorption and desorption enthalpies. According to Chapter 4, there is significant opportunity to reduce the operating costs of a fiber sorbent capture system by removing the need to cycle water continuously through the bores of the fibers. Of course, to regenerate the CO_2 without a thermal swing requires a pressure or vacuum swing—both of which have been discounted due to the immense size of the compression systems needed. This appendix addresses both concerns: the sorption enthalpy and the method of desorption. To tackle the first problem, a phase change material is entombed into the bores of the fibers (Figure F.1).

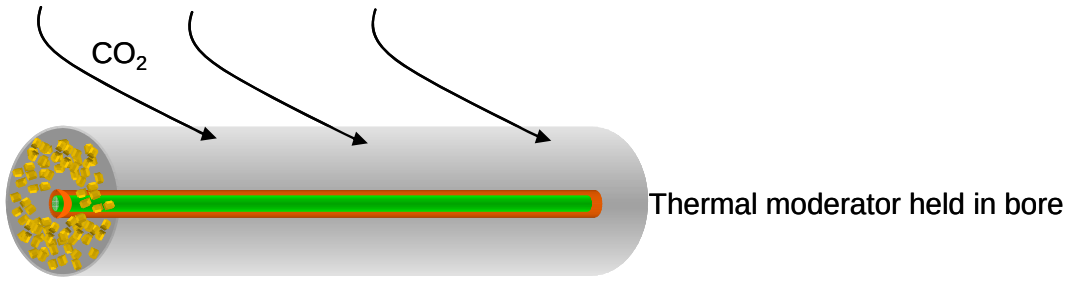

Figure F.1: Schematic of fiber sorbent with a phase change material (green) entombed in the bore

As the CO_2 sorbs into the zeolites within the fiber, the heat released is transferred to the phase change material. Ideally, the system is held at the melting/fusion temperature of the phase change material. In this scenario, any sorption enthalpy transferred from the fiber wall to the phase change material simply melts the solid phase change material (Fig F.2). For a typical phase change material—eicosane—the heat of melting is greater than the heat of sorption between CO_2 and 13X. It can be readily shown that the total amount of melting heat available in the core as a sink is greater than the heat of sorption as a source. Essentially, as the CO_2 sorbs, the fiber stays isothermal while the phase change material in the bore changes from a solid to a liquid. For the desorption step, when vacuum is pulled on the bed, the reverse phenomenon happens.

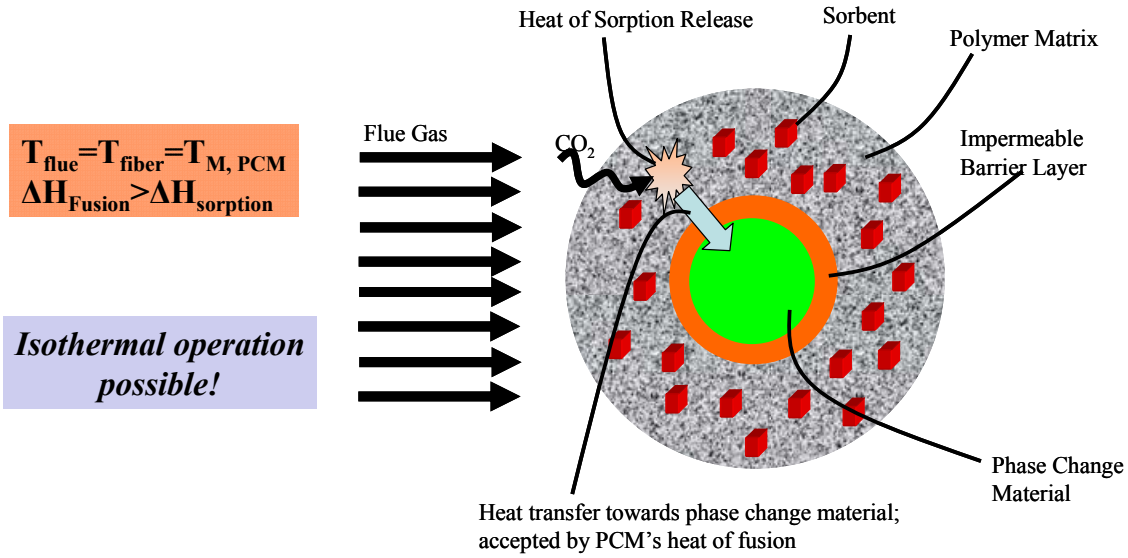

Figure F.2: Cartoon illustrating how fiber sorbents stay isothermal via sorption enthalpy transfer to phase change material's heat of melting.

The next challenge is how to pull vacuum on the fiber sorbent bed without putting a significant parasitic load on the power station. To achieve this, the plant's feedwater

pre-heating cycle is again used. For the desorption step, an identical module--devoid of fibers--is held at a weak vacuum (0.1-0.5 atm absolute), while a valve connecting the fiber module and the blank module is momentarily opened (Fig. F.3), thereby rapidly removing the interstitial flue gas contained within the fiber module. Next, a strong vacuum is pulled on the fiber module via a steam ejector (in a coal-fired power plant scenario), thereby desorbing the CO_2 from the fibers--the heat of fusion of the PCM is transferred to the heat of desorption of the fibers, thereby resolidifying the PCM. The CO_2 dissolved and entrained within the steam is carried along to the high-temperature and high-pressure feedwater preheater, where the steam is condensed as per normal plant operation. The head space, at steady state, contains wet CO_2, which can then be vented away and compressed for sequestration (Fig F.4). This integration with the plant minimizes any expensive vacuum equipment. Unfortunately, steam ejectors are quite difficult to design, so the full efficacy of this idea is not known yet.

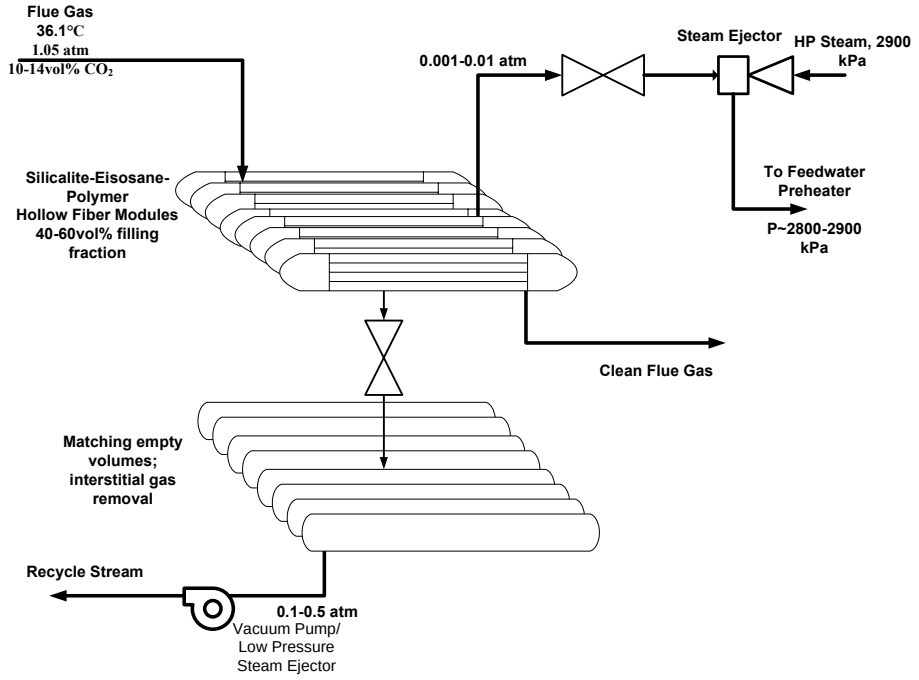

Figure F.3: Process overview of fiber sorbent vacuum swing adsorption process

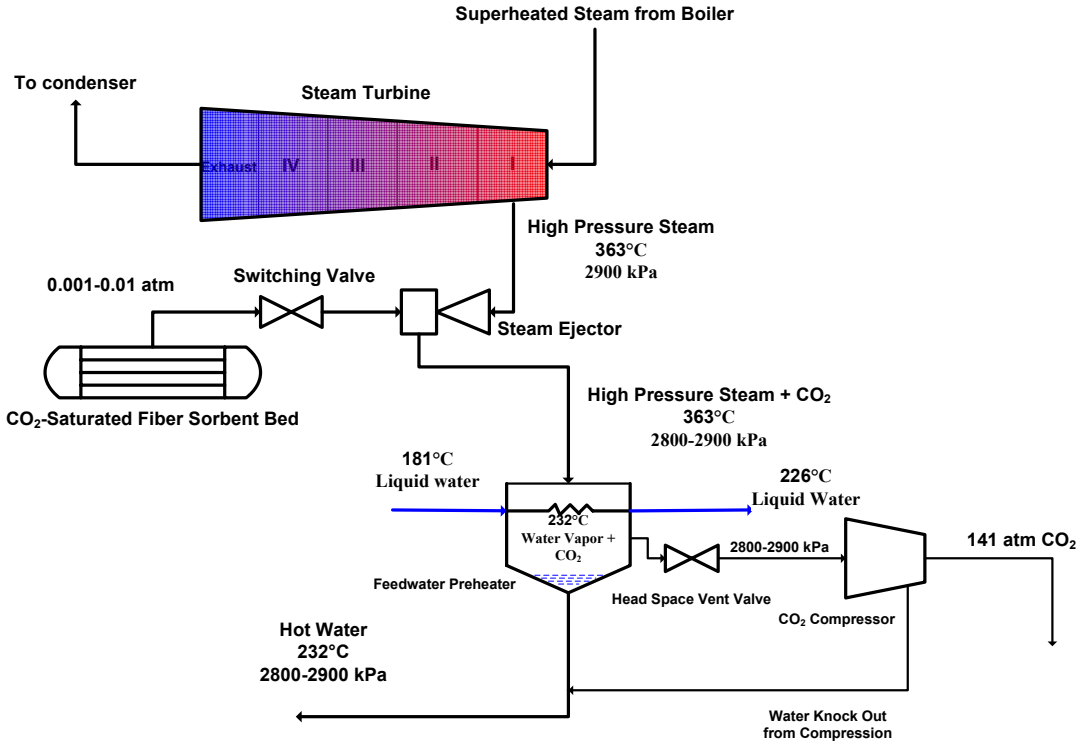

Figure F.4: PCM-hollow fiber sorbent CO2 capture bed integration with coal-fired power plant.

F.2 Experimental Procedure:

As a proof of concept, cellulose acetate and 13X hollow fiber sorbents were assembled into a module**,** and a compounded **N**eoprene® barrier layer was deposited on the lumen side of the fibers. These fibers were then heated to 45°C and attached to an Isco® Pump (also at 45°C) filled with Eicosane (Sigma-Aldrich). Eicosane was then pumped through the fibers at 1800 mL/hr, before the fibers were plugged and sealed with epoxy. The fibers were then cooled down and removed from the module, and broken into 2 cm pieces. The ends of these pieces were carefully blocked with epoxy. These pieces were then assembled into a plastic bed with a Omega® hypodermic needle thermocouple inserted in the middle of the bed. The bed was dried under N_2 at 125°C for 24 hours, and then cooled down to 36.1°C, the melting temperature of eicosane. The fibers were exposed to CO_2 and N_2, and the concentration breakthrough curves were measured with a mass spectrometer, and the thermal wave was measured using the hypodermic needle thermocouple. A bed of **N**eoprene®-coated cellulose acetate and 13X fibers (2 cm pieces with ends epoxied) with a neoprene coating (but no eicosane filling) was used as a control.

F.3 Supporting Calculations:

To illustrate the ability of the eicosane to isothermally accept the heat of sorption released from the zeolites, the volume of eicosane per fiber must be calculated, as well as the amount of heat released from the zeolites per fiber.

$$V_{eicosane}=\pi L_{fiber}(R_i^2)=3.14 \text{ x } (100cm) \text{ x } [(160x10^{-4}cm)^2]=0.08cm^3$$

$$m_{zeolite,fiber}=\omega_{zeolite}\rho_{fiber}\pi L_{fiber}(R_o^2-R_i^2)=$$

$$=0.75 \text{ x } (1.5 \text{ g/cm}^3) \text{ x } 3.14 \text{ x } (100cm) \text{ x } [(550x10^{-4}cm)^2-(160x10^{-4}cm)^2]$$

$$=0.98 \text{ g}$$

$$q_{silicalite,\ CO2,\ 36.1°C,10kPa}=0.3 \text{ mmol } CO_2/\text{g zeolite}$$

$$n_{CO2}=0.29 \text{ mmol } CO_2$$

$$\Delta H_{CO2\text{-}silicalite}=25 \text{ kJ/mol}$$

$$Q_{sorption}=(25 \text{ kJ/mol}) \text{ x } (0.29 \text{ mmol})/1000=7.31 \text{ J}$$

Heat of Fusion/Melting of Eicosane: $\Delta H_M=246.8$ kJ/kg

$$\rho_{eicosane}=0.787 \text{ g/cm}^3$$

$$\Delta H_M=194.3 \text{ J/cm}^3$$

$$Q_{melting}=V_{eicosane}\Delta H_{melting}=0.08cm^3 \text{ x } 194.3 \text{ J/cm}^3=15.5 \text{ J}$$

$$\rightarrow Q_{melting}>Q_{sorption}$$

This demonstrates the ability of eicosane to accept all of the heat of sorption towards it's own heat of melting, thus allowing the fibers to remain isothermal.

F.4 Results

Figure F.5 shows the thermal fronts and the concentration fronts for the control module as well as the eicosane module. As is clear, the eicosane module exhibits a longer CO_2 breakthrough time (modules are the same size), indicative of a reduction in heat effects. Furthermore, the breakthrough front is clearly sharper for the eicosane case, another indication that the fibers are more isothermal. Finally, the thermal front for the

eicosane fibers exhibits only 40% of the maximum temperature that was seen in the control case, and a factor of 8 reduction in the total amount of heat measured by the thermocouple. While these are still preliminary experiments, they provide encouragement for future research concerning fiber sorbents in VSA mode.

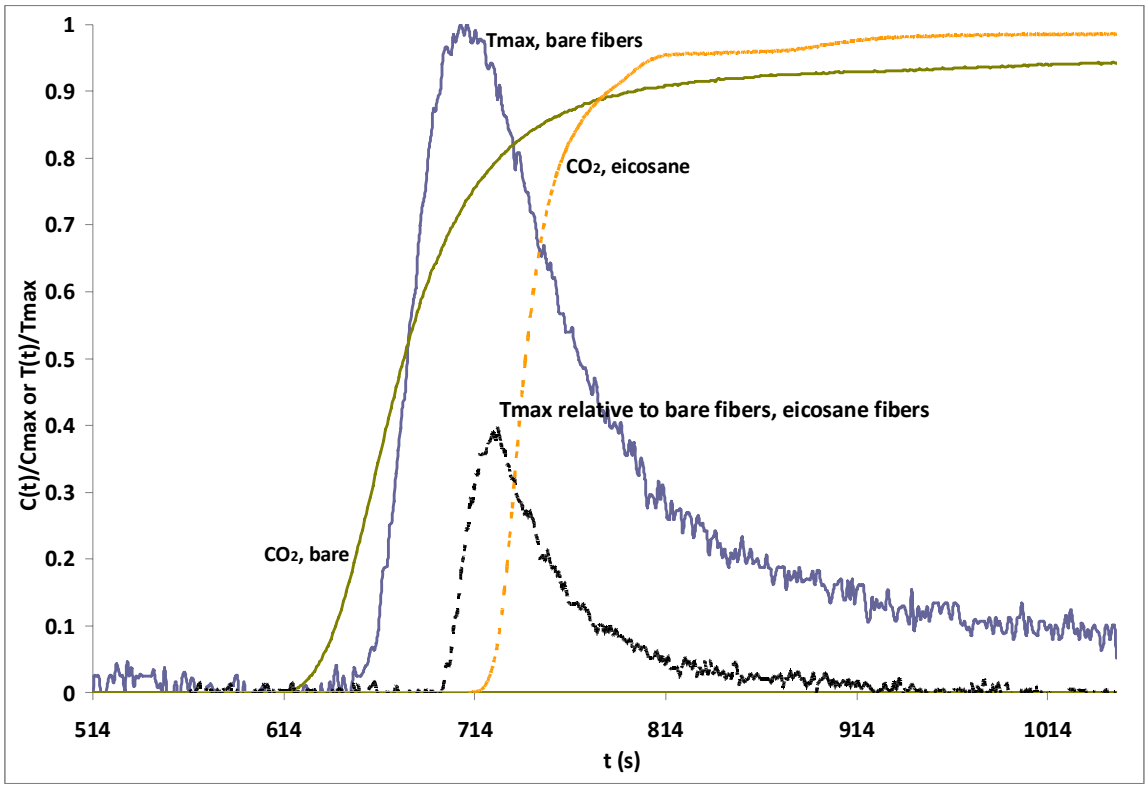

Figure F.5: Thermal and CO2 concentration fronts for normal (empty) fiber sorbents and eicosane-filled fiber sorbents. T=36.1°C, PCO2=0.1atm, 6-fiber parallel flow modules.